Fundamental Study of Electrospray Ionization Using Atmospheric Pressure and High-Pressure Ion Sources

大気圧及び高圧イオン源を用いたエレクトロスプレーイオン化の基礎研究

山梨大学大学院

医工農学総合教育部

博士課程学位論文

2023 年 9 月 14 日

韓忠保

Fundamental Study of Electrospray Ionization Using Atmospheric Pressure and High-Pressure Ion Sources

Doctoral Dissertation

Integrated Graduate School of Medicine, Engineering, and Agricultural Sciences

Faculty of Engineering

University of Yamanashi

September 14, 2023

ZHONGBAO HAN

Abstract

Generating ultra-fine charged droplets using electrospray is crucial for attaining high ionization efficiency for mass spectrometry. The size of the precursor charged droplets depends on the spray flow rate and the conventional wisdom holds that the electrospray of nanoliter per min flow rate (nanoelectrospray) is only possible using narrow capillaries with an inner diameter of ~1 micrometer or smaller. In Chapter 2, the electrospray of aqueous solutions with high electrical conductivities generated from a large off-line capillary of 0.4 mm i.d. has been performed using a high-pressure ion source. The electrical discharge is avoided by operating the ion source at high pressure. The highly stable Taylor cone can be tuned to a near-hydrostatic state that exhibits the "true nanoelectrospray" properties, i.e. high salt tolerance and minimal ion suppression. The $Q^{1/2}$ scaling law describing the electrospray current I and flow rate Q is found to be valid down to the nanoflow regime under a condition that is free of electrical discharge. The flow rate and the size of the initial droplets and ionization species can be controlled with the spray current as the indicator for the instantaneous flow rate. A continuous scan of the flow rate in this regime can trace the effect of droplet size in greater detail for a better understanding of the ionization process.

To date, such practical implementation is hindered by the lack of a suitable liquid pump and the reproducibility of microcapillaries-based systems. In Chapter 3, an offline nanoESI mass spectrometry with a continuously varying flow rate in a dynamic range of several hundred pL/min to ~100 nL/min was performed by precision scanning of the ESI high voltage (HV). The system is successfully applied to reveal the role of nanoflow rate on the average charge state of proteins, analysis of analyte mixture, and desalting effect. With the use of buffer solution with high electrical conductivity, a highly controllable oxidative modification was also observed by tuning the low flow rate.

The finding is discussed in detail in Chapter 4. The highly tunable oxidation can be performed in line with the nanoESI-MS analysis at the same ESI emitter without the use of oxidative reagents such as ozone, H_2O_2, and UV activation. Oxidations occur as the electrical field at the tip of the Taylor cone or the initially produced charged droplet reaches approximately 1.3 V/nm. The oxidized ion signal responds instantaneously to changes in flow rate, indicating that the oxidation is

highly localized. Using isotope labeling, it was found that the incorporated oxygen primarily originates from the gas phase, suggesting a direct oxidation pathway for the analyte-enriched liquid surface by the reactive oxygen atoms formed by the strong electrical field.

Acid-induced protein refolding is a phenomenon where a further increase in acidity in the most denaturing acidic solution will, on the contrary, lead to the refolding of the fully unfolded protein into a molten globule with a native-like compact conformation. The phenomenon takes place at ~pH 1 in strong acid aqueous solutions with high electrical conductivity and surface tension, a condition that is difficult to handle using conventional ionization methods for mass spectrometry. In Chapter 5, a method based on high-pressure electrospray (HP-ESI) is developed to produce well-resolved mass spectra for proteins in strong acids with a pH as low as 1. The refolding is indicated by a shift in the charge state from high charges to native-like low charges. The addition of salt to the protein in the most denaturing condition also reproduces the refolding, thereby supporting the role of anions in this phenomenon.

The electrospray under the steady cone-jet mode is highly stable but the operation state can shift to other pulsation or multi-jet modes owing to the changes in flow rate, surface tension & and electrostatic variables. In Chapter 6, a simple feedback control system is developed using the spray current and the apex angle of the Taylor cone to determine the error signal for emitter voltage correction. The system is applied to lock the cone-jet mode operation against external perturbations for online and offline electrospray. ESI-MS with feedback control is demonstrated to produce ion signal acquisition with long-term stability that is susceptible to emulated external disturbances.

A bipolar ESI source is developed to generate a simultaneous emission of charged liquid jets of opposite polarity from an electrodeless sprayer in Chapter 7. The sprayer consists of two emitters. The sprayer and the liquid delivery system are made of all insulators without metal components, thus enabling the total elimination of electrochemical reactions taking place at the liquid-electrode interface in the typical electrospray emitter. The voltage-current and flow rate-current relationships of bipolar electrospray were found to be similar to the standard electrospray. The application of bipolar ESI to the mass spectrometry of protein, peptide, and metallocene without the electrochemically induced oxidation/reduction is demonstrated.

In Chapter 8, endeavor was made to investigate the electrospray ionization inside the narrow channel of the ion inlet tube. An insulating emitter capillary made of fused silica with 0.2 mm outer diameter was inserted into the ion inlet tubes with 0.5 & 0.6 mm inner diameter to aspirate all the charged droplets. A custom-made ion inlet tube with two side holes near its entrance is used to observe the spraying condition. A stable operation under a flow rate of 1- 4 μL/min is found to be in the form of multi-cone-jet mode with two or more Taylor cones anchoring around the rim of the emitter. Comparison with the typical cone-jet and multi-jet mode operated several millimeters outside the inlet capillary shows signal enhancements for protein standards.

Contents

Chapter 1: General Introduction

1.1 Mass Spectrometry

Mass spectrometer

Mass spectrometry (MS) is a technique used to study the molecular structure, chemical composition, and relative abundance of substances. It achieves this by measuring the mass-to-charge ratio (m/z) and relative abundance of ions in a sample. The continuous development of mass spectrometry technology has resulted in its increasing importance in scientific research and practical applications. It can be applied in various fields, including metabolomics analysis, drug discovery and development, environmental pollutant detection, and more. In general, the structure of a mass spectrometer can vary based on different analysis requirements and various application areas.

A mass spectrometer consists of an ion source, ion transport system, mass analyzer, detector, and data acquisition system. The ion source operates at atmospheric pressure (1 bar), while the ion transport system (1-10^{-4} bar), mass analyzer (10^{-5}-10^{-10} bar), and detector (10^{-5}-10^{-10} bar) operate in a vacuum environment. The ionization source is the component responsible for converting the sample into ions. It can utilize various methods for ionization, such as electron impact ionization (EI)[1–3], chemical ionization (CI)[4–6], matrix-assisted laser desorption/ ionization (MALDI)[7,8], and electrospray ionization (ESI)[9]. The choice of ionization source often depends on the nature of the sample. The mass analyzer is an important component of the mass spectrometer, responsible for the ions separation and analysis based on mass-to-charge ratio (m/z). Common types of mass analyzers include linear quadrupole (Q), quadrupole ion trap (QIT), time-of-flight (TOF), linear quadrupole ion trap (LIT), Fourier transform ion cyclotron resonance (FT-ICR), and Orbitrap. Each type of mass analyzer operates on different principles and exhibits unique performance characteristics. Detectors in mass spectrometry are used to measure the relative abundance and mass-to-charge ratio (m/z) signals of ions. Commonly used detectors include Multi-Channel Plate (MCP) detectors, Photomultiplier Tubes (PMTs), and Micro Channel Plates (MCPs), among others. These detectors are designed to convert

ions into measurable signals, which are then amplified and recorded for data analysis. The choice of detector depends on factors such as the desired sensitivity and dynamic range. The data system is designed to convert the signals from the mass spectrum into mass peaks and provide corresponding data analysis functionalities. It plays a crucial role in extracting meaningful information from the raw data. During the analysis process, the sample undergoes an ionization process to convert it into ions. After ionization, the ions are accelerated by an accelerator and then deflected in a magnetic field or electrical field, allowing ions with different mass-to-charge ratios (m/z) to be separated. After the ions were separated, they were transported to the detector of the mass spectrometer, which measures the ions' mass-to-charge ratio and relative abundance. This data is typically presented in the form of a mass spectrum, where the x-axis represents the mass-to-charge ratio (m/z) and the y-axis represents the relative abundance.

Orbitrap analyzer

The mass spectrometry data in this thesis were obtained using an Orbitrap mass spectrometer. The core of the Orbitrap mass spectrometer is a mass analyzer called the Orbitrap. The Orbitrap mass analyzer is based on an orbit consisting of two concentric electrodes: inner and outer electrodes. In the mass spectrometer, ions are injected into the central region of the Orbitrap, where they orbit around the central axis. The ions' motion generates a resonant frequency, which is proportional to their mass-to-charge ratio. By measuring the oscillation frequency of the ions, their mass-to-charge ratio can be determined, resulting in high-resolution mass spectral data.

1.2 Electrospray ionization

Electrospray & Ionization mechanism

Electrospray ionization mass spectrometry (ESI-MS) is an indispensable tool for the analysis of a wide range of biomolecules such as peptides, proteins, and polymers. ESI is a so-called “soft ionization” technique since there is very little fragmentation. Upon the application of a high potential to the liquid at the ESI emitter, the strong electrical field cause the emission of charged droplets of the

sample solution, and the desolvation of droplets generates the gaseous ions of the solute.

When a conductive liquid meniscus anchored to the outlet of a capillary is charged, its free surface first deforms to attain a static shape in which the stress owing to the surface tension balances out the electrostatic stress and other external components. Further increase of the electrical potential causes the liquid meniscus to vibrate with the erratic ejection of bulk liquid droplets. However, upon reaching a certain critical potential, the liquid meniscus suddenly turns into a remarkably stabilized cone with a jet of fine droplets issuing from its apex[10,11]. With the presence of a heat bath (e.g. spraying under an atmospheric pressure ambient), the charged droplets emitted from the Taylor cone undergo solvent evaporation, and the shrinkage in droplets size raises the charge density. As the excess charge approaches the Rayleigh limit,[12] which is the maximum charge the surface tension of a spherical droplet of a given radius can hold, the instability of the precursor droplet initiates the release of secondary droplets with their radius much smaller from the precursor one. This Coulombic fission (henceforth referred to as Rayleigh fission) repeats down to the formation of late-stage droplets where the generation of gaseous ions takes place via the ion evaporation,[13] charged-residue,[14] chain ejection[15], or the recently proposed bead ejection[16] mechanisms.

Accompanying reactions for ESI: electrochemical and corona discharge

The flow of current in the electrospray of the solution involves ions, therefore the loop of the electrical circuit needs to be closed by electrochemical reactions at the electrode/solution interface. Owing to this reason, Kerbale et al. viewed the ESI source as "*an electrolytic cell of a special kind*"[17]. Although the presence of electrochemical processes in the electrode interface of electrospray is indisputable, there are debates on its importance on ESI[18]. From an electrohydrodynamic point of view, the details of the involving electrochemistry are not essential in predicting the physical behavior of electrospray. But from a mass spectrometric point of view, the electrochemical reactions alter the composition of the electrospray solution and affect the MS results, therefore its effects can not be taken lightly. In the positive ion mode, the consequence of the electrochemistry are i) corrosion of the electrode that releases the metal ions to the solution, ii) the oxidation of solvent or analytes, and iii) the neutralization (oxidation) of the anion of the analyte or buffer salts. The corrosion of electrodes can be prevented by the use of inert materials such as platinum but that will instead give rise to other

reactions such as the oxidations of solvent or analytes[19,20]. In the negative ion mode, the reduction can result in the deposition of metal ions on the electrode[21]. For an unbuffered solution, there could also be a change in pH caused by the inherent electrolytic process of the ESI source[19,20]. This intrinsic electrolytic effect of electrospray has also been exploited for analytical applications such as the detection of radical cations $M^{+\bullet}$ of porphyrins[22].

In the operation of ESI, apart from oxidation occurring near the electrodes, oxidation phenomena can also take place at the tip of the Taylor cone under specific conditions. For example, Electrical discharge (e.g. corona discharge) takes place when the potential at the ESI emitter or on the conductive liquid surface exceeds the threshold voltage for gaseous breakdown. The reactive oxygen species (ROS) generated by the discharge is known to cause the oxidation of analyte generated from ESI. Because the discharge could disrupt the stability of the electrospray and generate unwanted background ions, it usually needs to be avoided. The electrospray discharge relies on water samples with high surface tension. Therefore, in traditional electrospray, it is necessary to avoid using pure water samples and instead add additional organic solvents to reduce the surface tension. Another method like high-pressure ESI based on Paschen's law has been developed to prevent the discharge during the electrospraying of pure aqueous solution[23].

Relationship between flow rate and current & Nanoelectrospray

Flow rate is an important parameter in electrospray, as it influences the ionization process. When the electrospray operates in the Taylor cone mode, we have verified the relationship between the flow rate and the spray current, which follows popular $Q^{1/2}$ law. The popular $Q^{1/2}$ law is the one by Fernández de la Mora and Loscertales (FL) in which the electrospray current I is given with good accuracy by[24]

$$I = f(\epsilon_r)\left(\frac{\gamma K Q}{\epsilon_r}\right)^{1/2} \quad (1)$$

, where ϵ_r is relativity permittivity, γ is surface tension, K is the electrical conductivity of the liquid, and $f(\epsilon_r)$ is an empirically determined coefficient that varies with the relative permittivity of the liquid. For liquids such as aqueous solutions with $\epsilon_r > 40$, $f(\epsilon_r) = 18$. Eq. (1) is not influenced by the gas pressure of the ESI working environment, and it is not limited by online or offline conditions.

For highly conductive aqueous samples, the flow rate can reach as low as several hundred pL/min. Due to its high surface tension and large electrical conductivity, it is challenging to perform a stable electrospray of pure aqueous solutions under atmospheric pressure. In the case of traditional atmospheric pressure electrospray (AP-ESI), this challenge was addressed by reducing the size of the emitter top to several nanometers. The relationship between flow rate and electrical current in atmospheric pressure nanoelectrospray (AP-nanoESI) does not follow Eq. 1. However, it can be determined that the droplet size does not exceed the size of the emitter orifice.

Manners of operation: online and offline

The ESI can be operated in online and offline manners. The online operation employs a liquid pump such as a syringe pump or LC pump to deliver the solution to the sprayer, usually at a constant flow rate. Online operation is widely used in LC-MS and other routine analyses that require a constant supply of samples. For a given flow rate and HV, the electrospray condition can vary across different spraying regimes, i.e. dripping, pulsation/oscillation (in the kHz range), steady cone-jet, and multi-jet modes[25]. Among those regimes, the steady cone-jet mode is usually the preferred operating mode because it is highly stable as manifested by the stationary geometry of the liquid cone (Taylor cone) and a near-constant spray current. The apex angle of a static Taylor cone without pressure difference across the liquid-air interface is 98.6°[11]. The stable operation of cone-jet mode depends on the applied HV, surface tension, and electrical conductivity. In the offline electrospray, the liquid loaded inside the capillary sprayer or liquid reservoir is drawn to the emitter by the electrospray. Unlike the online operation where the flow rate is regulated by the pump, the liquid flow rate is controlled solely by the high voltage. Offline electrospray has been performed using pulled-glass nanoESI capillary[26], wet metallic wire or solid needle emitter[27,28], solid substrate[29], paper[30], and pipet tip[31]. Recently we also reported an offline nanoESI using micropipette tips with large i.d. for highly conductive aqueous solutions[32,33].

Chapter 2: Fundamental study of HP nanoESI: using novel ESI emitter

Summary

Generating ultra-fine charged droplets using electrospray is crucial for attaining high ionization efficiency for mass spectrometry. The size of the precursor charged droplets depends on the spray flow rate and the conventional wisdom holds that the electrospray of nanoliter per min flow rate (nanoelectrospray) is only possible using narrow capillaries with an inner diameter of ~1 micrometer or smaller. Here, the electrospray of aqueous solutions with high electrical conductivities generated from a large off-line capillary of 0.4 mm i.d. has been performed using a high-pressure ion source. The electrical discharge is avoided by operating the ion source at high pressure. The highly stable Taylor cone can be tuned to a near-hydrostatic state that exhibits the "true nanoelectrospray" properties, i.e. high salt tolerance and minimal ion suppression. The $Q^{1/2}$ scaling law describing the electrospray current I and flow rate Q is found to be valid down to the nanoflow regime under a condition that is free of electrical discharge. For a given solution, the flow rate and the size of the initial droplets and ionization species can be controlled with the spray current as the indicator for the instantaneous flow rate without changing the emitter capillary of different sizes. Application-wise, the nanoelectrospray with a large micropipette tip is easy to use, free of clogging when dealing with viscous and high salt buffer solutions, and with reduced surface interaction with the emitter inner surface. Acquisition of very clean mass spectra of proteins from concentrated solutions of nonvolatile salts such as phosphate-buffered saline is demonstrated.

Introduction

When a conductive liquid meniscus anchored to the outlet of a capillary is charged, its free surface first deforms to attain a static shape in which the stress owing to the surface tension balances out the electrostatic stress and other external components. Further increase of the electrical potential causes the liquid meniscus to vibrate with the erratic ejection of bulk liquid droplets. However, upon reaching a certain critical potential, the liquid meniscus suddenly turns into a remarkably stabilized cone with a jet of fine droplets issuing from its apex[10,11]. The cone, which is called the Taylor cone is

involved in electrospinning, electrospray, and liquid metal ion sources[34]. With the presence of a heat bath (e.g. spraying under an atmospheric pressure ambient), the charged droplets emitted from the Taylor cone undergo solvent evaporation, and the shrinkage in droplets size raises the charge density. As the excess charge approaches the Rayleigh limit,[12] which is the maximum charge the surface tension of a spherical droplet of a given radius can hold, the instability of the precursor droplet initiates the release of secondary droplets with their radius much smaller from the precursor one. This Coulombic fission (henceforth referred to as Rayleigh fission) repeats down to the formation of late-stage droplets where the generation of gaseous ions takes place via the ion evaporation,[13] charged-residue,[14] or the recently proposed chain ejection[15] mechanisms. Through electrospray ionization (ESI),[35] the soft mass spectrometry for large biomolecules (ESI-MS) has brought revolutionary impacts on analytical chemistry, biochemistry, and medicine.

In the absence of gravity and space charge effects, Taylor showed that a rigorous analytical solution exists for a semi-infinite cone in which the stresses due to surface tension and electrostatic balance out each other exactly at any point on its equipotential surface. In that special case, the pressure difference across the liquid-air interface is zero and the semi-vertical angle (or half apex angle) α of the pure Taylor cone is 49.3° (see Figure 2.1 inset for the assignment of α). That angle is also called Taylor angle α_T. In practice however, a true static Taylor cone has never been observed. Although the shape of the Taylor cone may appear stationary under a cone-jet mode, α is always smaller than the Taylor angle, and the deviation $|\alpha - \alpha_T|$ was found to increases with the solution flow rate.[36] The structure of a non-static Taylor cone so far cannot be described using a simple analytical form. Approximations using dimension analysis and empirical modeling led to the development of scaling laws that determine the electrospray current, and the size of the initial charged droplets using fundamental physical variables of liquid such as flow rate Q, relativity permittivity ϵ_r, density ρ, viscosity μ, surface tension γ, and electrical conductivity K. One example is the $Q^{1/2}$ law for spray current for the liquid with sufficient electrical conductivity.[24,37,38] The popular $Q^{1/2}$ law is the one by Fernández de la Mora and Loscertales (FL) in which the electrospray current I is given with good accuracy by[24]

$$I = f(\epsilon_r)\left(\frac{\gamma K Q}{\epsilon_r}\right)^{1/2} \quad (1)$$

, where $f(\epsilon_r)$ is an empirically determined coefficient that varies with the relative permittivity of

the liquid. For liquids such as aqueous solutions with $\epsilon_r > 40$, $f(\epsilon_r) = 18$. Eq. (1) has been well established for the micro-flow system that uses external liquid pumps for flow regulation. Under a cone-jet mode, the spray current is entirely determined by the liquid flow rate independent of the charging potential and other electrostatic parameters. The order of magnitude for the radius of the initial droplet R_o is given as[24]

$$R_o \sim \left(\frac{\epsilon_o \epsilon_r Q}{K}\right)^{1/3} \quad (2)$$

where ϵ_o is the vacuum permittivity. From the scaling laws, it is well known that fine and monodisperse droplets can be produced by decreasing the flow rate and by increasing the electrical conductivity.[24,37] However, the flow rate Q in Eq. (1) & (2) cannot be set to an arbitrarily small value. Experimentally, there exists a minimum flow rate $Q_{\min}$ to form the cone-jet and its order of magnitude is expressed as[24,39]

$$Q_{\min} \sim \frac{\epsilon_o \epsilon_r \gamma}{\rho K} \quad (3)$$

The physics behind its existence is still not well understood. It is also noted that the size of the emitter capillary does not enter Eq. (1) – (3). The validity of scaling laws is also not without a limit. Fernández de la Mora et al. cautioned their use for liquids with K > 1 S/m because the field strength can become so high that the direct emission of ions from the Taylor cone surface becomes possible.[40] S/m is Siemens/meter, the SI unit for conductivity. Scaling laws for the droplet emission at the nanometer scale are expected to follow those of the micrometer scale but concrete evidence and extensive research on this area is still lacking.

Nanoelectrospray (nanoES) refers to a variant of electrospray that uses fine capillaries,[26,41] typically with inner diameters < 20 μm as a means to restrict the liquid flow rate under 1000 nL/min. Flow rate regulation using precision liquid pumps and the application of backpressure to the capillaries are also used in practice. Although any flow regime below 1 μL/min is nowadays referred to as nanoelectrospray,[42] there exists a unique operation at 20 nL/min, in which Karas et al. called the "true nanoelectrospray" because it is "more than just a minimized-flow electrospray ionization source".[43] The unique feature is related to the generation of initial charged droplets of nanometer size that carry a high charge density, contain only one or a few analytes molecules per droplet and undergo a smaller number of Rayleigh fission to generate gaseous ions. As a result, the true nanoESI has a high tolerance to salt and minimal analyte ion suppression effect, i.e. the preference of surface-active

compounds for the competition of excess charge over the less surface-active one can be effectively reduced.[44] Recent developments on nanoESI have seen the further downsizing of the emitter using sub-micron capillaries.[45–47] However, besides the issue of reproducibility, fine capillaries are prone to blockages and require frequent replacement. Unwanted interactions of analytes with the inner surface of the capillary also becomes more pronounced with a smaller inner diameter.[48] Flow rate measured for capillary-based nanoESI also showed a discrepancy from $Q^{1/2}$ law for the.[49] Because the $Q^{1/2}$ law assumes a much smaller jet diameter with relative to the nozzle diameter, its adoption to very fine capillary system is not well justified in principle. Despite its popularity for >1 μL/min flow regime, the validity of the $Q^{1/2}$ scaling laws has not been extensively verified for i) ≥1 S/m aqueous solution, ii) flow regime of <20 nL/min, iii) operation in which the regulation of flow rate is done using high potential without external pumps, and iv) independence on emitter size for the generation of nanoESI equivalent droplets. This work attempt to address those issues by characterizing the Taylor cone of highly conductive aqueous solutions generated from a capillary of 0.4 mm i.d. (micropipette tip) which is large in the conventional sense. This work also focuses on the 100% aqueous solution which is the most common solvent in chemistry, yet the least friendly one for electrospray due to its high surface tension. Here, a condition that is completely free of electrical discharge is provided by performing the electrospray under a high-pressure (>1 atm) environment, a technique which has been developed in our laboratory previously.[23] The tendency for discharge depends on the mean-free path of electron and gas molecules. Increasing the pressure of gas surrounding the ESI electrodes shifts the onset potential for discharge to a higher value but leaves the onset voltage for ESI unchanged. Besides preventing the discharge for high surface tension solutions, the high-pressure operation enhances the performance of conventional nanoESI for native proteins,[50–52] and enables the electrospray of liquid kept at temperatures higher than the normal boiling point for high-throughput proteomics[53] and high-temperature liquid chromatography.[54,55] The reduced flowrate operation using gel-loading tips of 0.1 mm i.d. was noticed under the high-pressure,[56] but its nature and its relevance to the scaling law had not been explored previously.

Experimental section

A simplified schematic of the ion source is shown in Figure 2.1. Polypropylene pipette tips with a tip opening inner diameter of 0.4 mm (Eppendorf, Hamburg, Germany) were used as the electrospray emitters and the liquid reservoirs. The loaded liquid was made contact with the high potential by inserting a platinum wire (dia: 0.2 mm) into the pipette tip. The whole emitter tip was placed inside a high-pressure chamber which was consisted of an aluminum chamber and an insulating flange made of polyetheretherketone (PEEK). The ion source was attached with viewports for the microscopic inspection of the Taylor cone. The ion source could be operated up to 6 bar gauge pressure using dry air from an air compressor. To eliminate the electrical discharge, the ion source was pressurized to a default gauge pressure of 2.5 or 5 bar using compressed air.

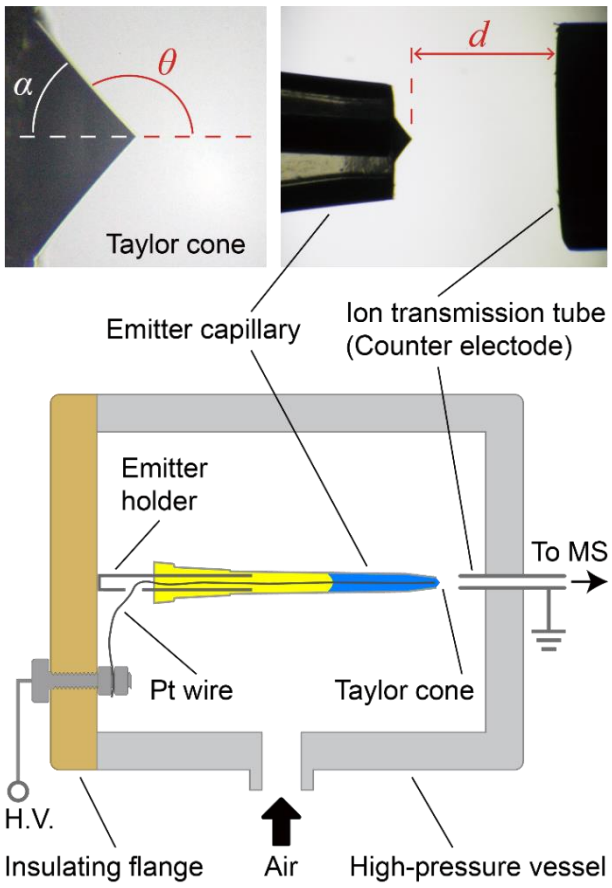

Figure 2.1. Simplified schematic of the high-pressure nanoESI source for highly conductive aqueous solution. Insets show magnified photographs of the Taylor cone, semi-vertical angle α, polar angle θ pointed to the equipotential surface, and electrode distance d measured from the surface of the counter electrode to the apex of the Taylor cone. Here α = 49°, d = 1 mm.

MS measurements were performed using a benchtop Orbitrap mass spectrometer (Exactive Plus, Thermo Fisher Scientific, Bremen, Germany). The default instrumental settings for the mass spectrometer were as follows: the temperature for the ion transport tube: 300 °C, S-lens voltage: 80%. The maximum ion injection time was 100 ms. The pressure in the fore vacuum was 1.4 mbar. The high-pressure ion source was coupled to the mass spectrometer using three different methods. Method I was the default one in which a 50 mm stainless-steel tube (i.d. 0.5 mm) was used to transport the ion to the atmospheric pressure side. Under the default ion pressure (2.5 bar gauge pressure), the gas flow rate measured at the atmospheric side was 4.8 L/min. The high-speed carrier gas containing the ions and fine droplets was directed towards to ion inlet of the mass spectrometer. The distance between the ion source outlet nozzle and the MS inlet was approximately 5 mm. Method II used a custom-made ion transmission tube of 0.5 mm i.d. to transmit the ions directly from the high-pressure chamber to the vacuum. A mechanical booster pump (ULVAC, Kanagawa, Japan) was added to the mass spectrometer to keep the first vacuum stage at 1.4 mbar. Method III was similar to Method II but an ion inlet tube of 0.25 mm i.d. was used and a higher ion source gauge pressure (~6 bar) was used to maintain the original gas throughput of the mass spectrometer. Schematics for coupling Methods I-III are shown in Figure 2.2. The ion source chamber and the liquid meniscus were at room temperature and the temperature of the operating air was monitored using a humidity/temperature sensor. Details of the measurement of spray current, solation flow rate, microscopic inspection of Taylor cone, and the chemicals are included.

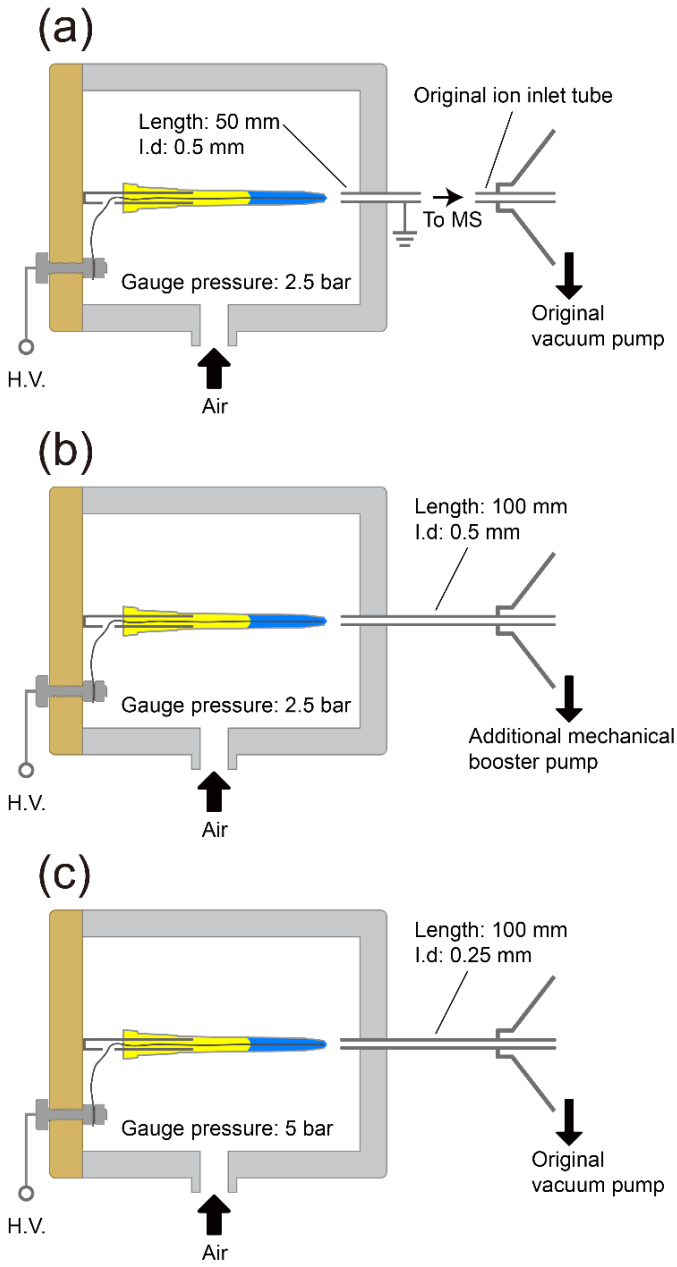

Figure 2.2. Coupling methods for connecting the high-pressure ion source to the mass spectrometer.
a) Method I: Default method in this study. At the default gauge pressure of 2.5 bar (~3.5 atm), the gas flow rate measured at the atmospheric pressure side was 4.8 L/min. The linear velocity of the gas flow inside the pressurized ion transmission tube was approximately 116 m/s. The length of the tube was approximately 50 mm, thus the residence time was ~0.4 ms.
b) Method II: A custom-made ion inlet tube of 0.5 mm i.d. is used to transmit the ions directly from the high-pressure ion source to the vacuum. A mechanical booster pump is added to the mass spectrometer to keep the first vacuum stage at ~1.4 mbar.
c) Method III: An ion inlet tube of 0.25 mm i.d. The ion source is pressurized to 5~6 bar gauge pressure to maintain the original gas throughput of the mass spectrometer.
The custom ion transmission tube was made of straight-cut stainless-steel tubes commercially available as consumables for GC application.

Results and Discussion

Electrical characteristics

The voltage-current characteristics of the Taylor cone were evaluated by ramping the potential applied to the liquid (see Figure 2.3). The onset of the electrospray was indicated by an abrupt increase in spray current with an overshoot during the ramping-up sequence. The current overshoot was sometimes followed by current fluctuation which may be related to the pulsation mode observed in the typical electrospray. The fluctuation stopped when the voltage swept past a certain threshold and a stabilized Taylor cone was formed. In the ramping-down sequence, a step decrease in spray current indicates the position of minimum current. It is noted that onset voltages (Vonset) to initiate the spray were 120V~200V higher than the minimum voltages (Vmin) that were needed to sustain the Taylor cone. We conjecture that during the ramping-up sequence, the volume of the liquid meniscus at the tip was not enough to form the Taylor cone at Vmin. A higher potential up to Vonset was needed to draw the liquid to the tip to surpass a minimum liquid volume. It was in contrast to the typical liquid pump-driven system where the onset of the pulsation mode is often several hundred volts lower than that of the cone-jet mode.

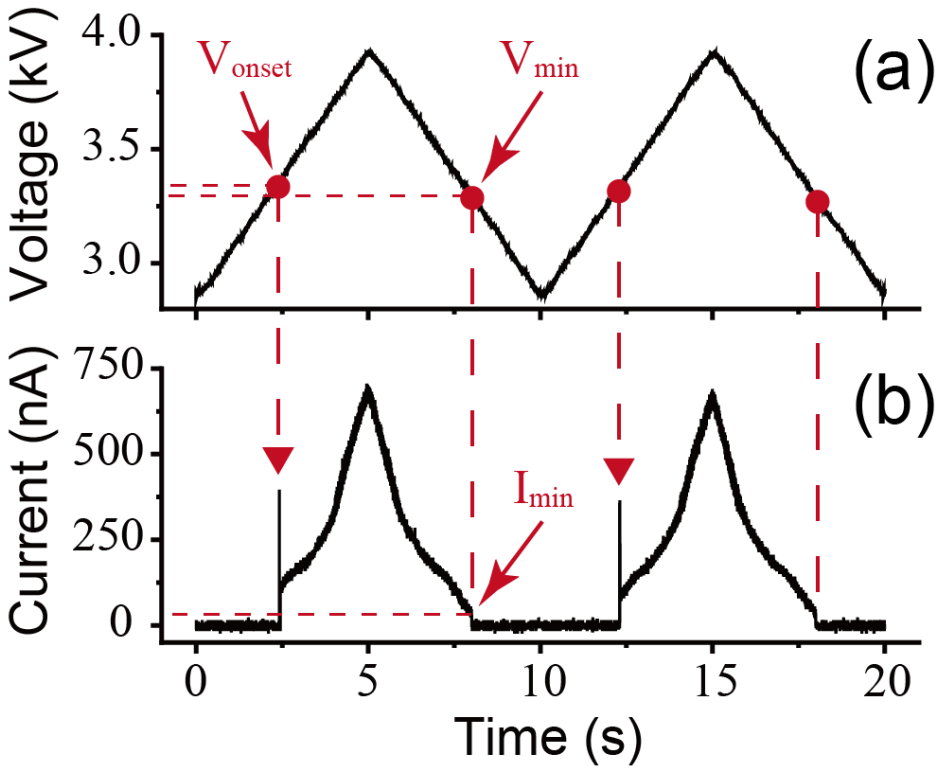

Figure 2.3. Response of electrospray current with the applied potential to the liquid. **a)** Ramping of applied potential. **b)** Recorded spray current. The onsets of spray current are indicated by the arrowed dashed lines. The voltages corresponding to the minimum currents are marked with dashed lines without the arrow. The solution here is 100 mM NaCl in water (K = 1 S/m).

Figure 2.4 shows the current-voltage characteristic curve (I-V curve) for the electrospray of various solutions of different electrical conductivities prepared by different concentrations of NaCl in water. The I-V curves are constructed from the instantaneous voltage and current data for a single Taylor cone formation event. The vertical arrows indicate the position of the onset potential. The deviation in minimum voltages was due to the small variation in distance d when the sample solutions were changed. The obtained I-V curve was found to be different from that of the typical electrospray. For the electrospray which is operated using external liquid pumps, there is an operating voltage window in which cone jet mode remains stable. In those situations, upon reaching the cone jet mode, the spray current nearly does not change with the voltage until the onset of multiple jet mode. Here, the characteristic current plateau of cone-jet mode was not observed. The hysteresis effect, i.e. different value of spray current under the same emitter potential which is found in the typical electrospray I-V curve was also absent. The observed experimental minimum currents were 76 ± 7 nA, 57 ± 5 nA, 33 ± 4 nA & 31 ± 5 nA for the electrical conductivities of 8.6, 1.0, 0.1, 0.01 S/m, respectively. These values were smaller than the minimum currents predicted using Eq. (2) & (3). Since Eq. (3) only gives an estimate for $Q_{\min}$, the improvement of the scaling law on this aspect is still necessary.

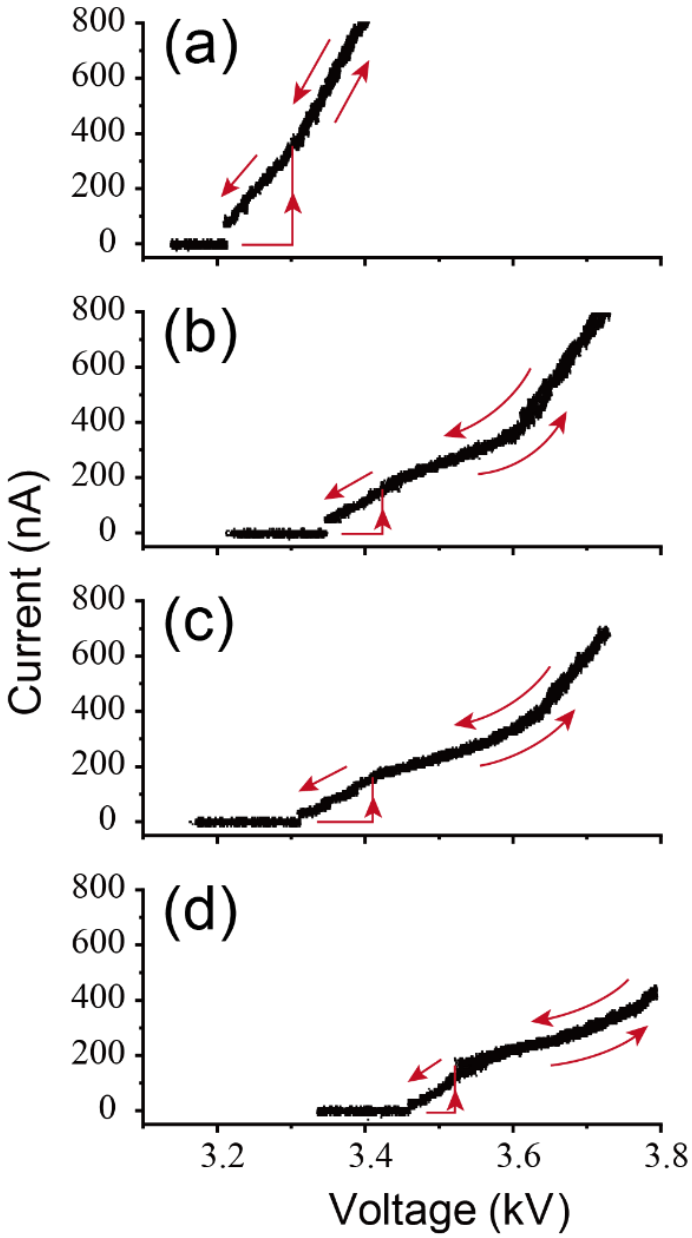

Figure 2.4. Current-voltage characteristic curve for the electrospray of **a)** 1 M, **b)** 100 mM, **c)** 10 mM, and **d)** 1 mM NaCl aqueous solution. Arrows indicate the direction of the current change. Electrical conductivities are 8.6 S/m (a), 1.0 S/m (b), 0.1 S/m (c), and 0.01 S/m (d).

The minimum spray current is related to the minimum flow rate that can be sustained by a Taylor cone. To perform the measurement, the high potential applied to the liquid was quickly ramped up to form the Taylor cone, and then slowly ramped down (1/volt per step) at a rate of 4 V/s while recording the spray current. The current value before the drastic drop of current accompanied by the collapse of the Taylor cone is assigned as the minimum electrospray current. Figure 2.5 shows the minimum electrospray current at different gauge pressures for 1 M Tris-HCl (K = 5.35 S/m), PBS (K = 1.58 S/m), 100 mM AA (K = 0.95 S/m), and 1 v/v % FA (K = 0.28 S/m). The minimum spray current was found to decrease with the operating pressure of the ion source. It was likely a space charge effect as the ion drifts slower under high pressure. A lower attainable spray current also indicated a reduced solution flow rate under a high-pressure condition, which is a welcoming effect for nanoESI. Assuming that the scaling law still holds, the minimum flow rate for 1M Tris-HCl which is the solution with the highest conductivity is approximately 180 pL/min, though direct verification by flow rate measurement was difficult due to the limitation set by the evaporation.

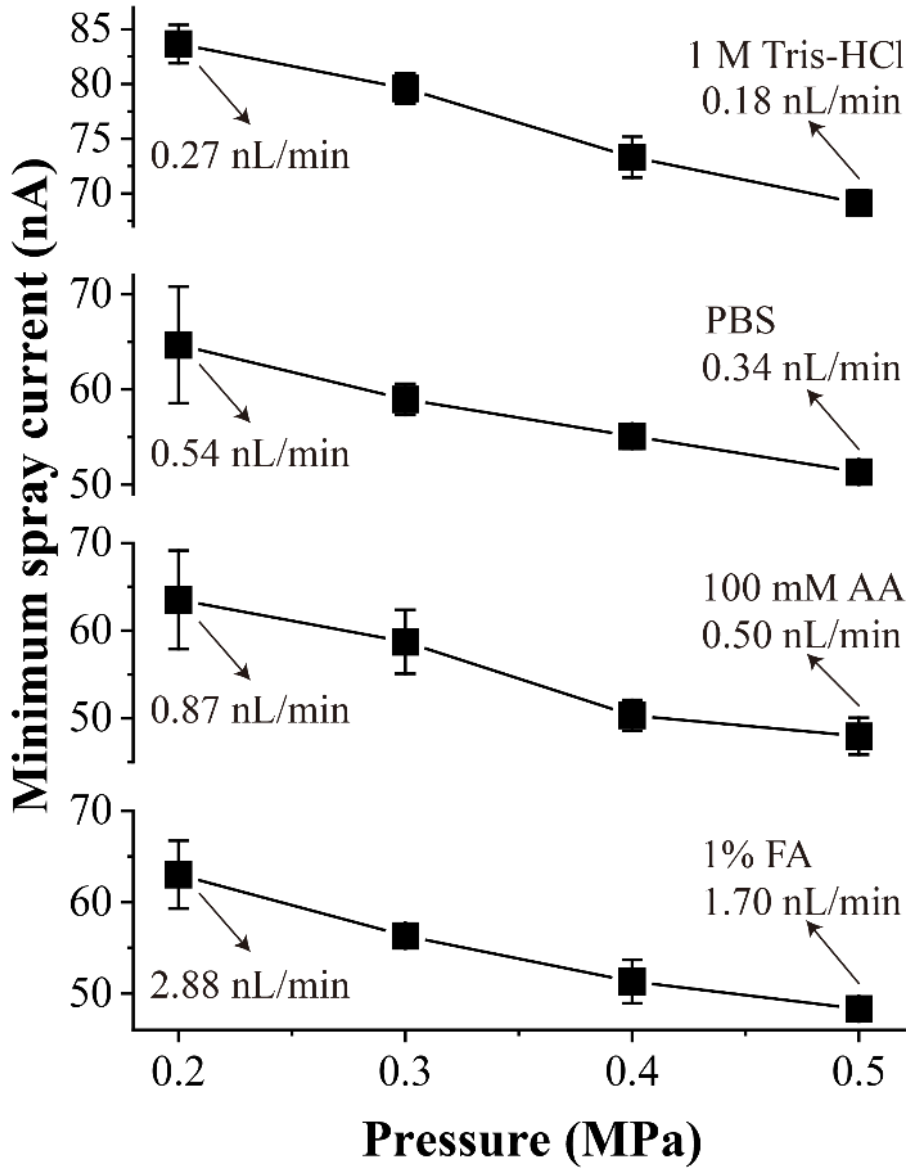

Figure 2.5. The minimum spray current measured at different gauge pressure for aqueous solutions of 1M Tris-HCl (5.35 S/m), PBS (1.58 S/m), 100mM ammonium acetate (AA, 0.95 S/m), and 1% v/v formic acid (FA, 0.28 S/m).

Structures of the Taylor cone

Microscopic images in Figure 2.6 show the shapes of the Taylor cones for aqueous solutions of different electrical conductivities (8.6 S/m to 0.001 S/m) at different spray currents. Each column represents the images for the solution of the same electrical conductivities, arranged from the top to bottom in ascending order for spray currents. The resolution of the magnifying lens was 700 nm. Illumination had also been performed using a green laser (wavelength: 532 nm) as shown in Figure 2.7. For spray currents below 500 nA, apparent jets with a diameter ≥1 μm were only observable for less conductive solutions (0.01 S/m and 0.001 S/m) using the optical method. At high current, the liquid meniscus took the shape of a cusp similar to those observed in liquid metal ion sources.[34] The semi-vertical angles of the Taylor cone α determined from microscopic images are plotted against the spray current in Figure 2.8. At the current near the minimum values, the shape of the Taylor cone approached an ideal shape with $\alpha \sim \alpha_T$ for $K > 0.01$ S/m . With the increase of current, α of the asymptotic cone reduced as expected with the current due to a higher solution flow rate, in agreement with the earlier report that used liquid pump for flowrate regulation.[36]

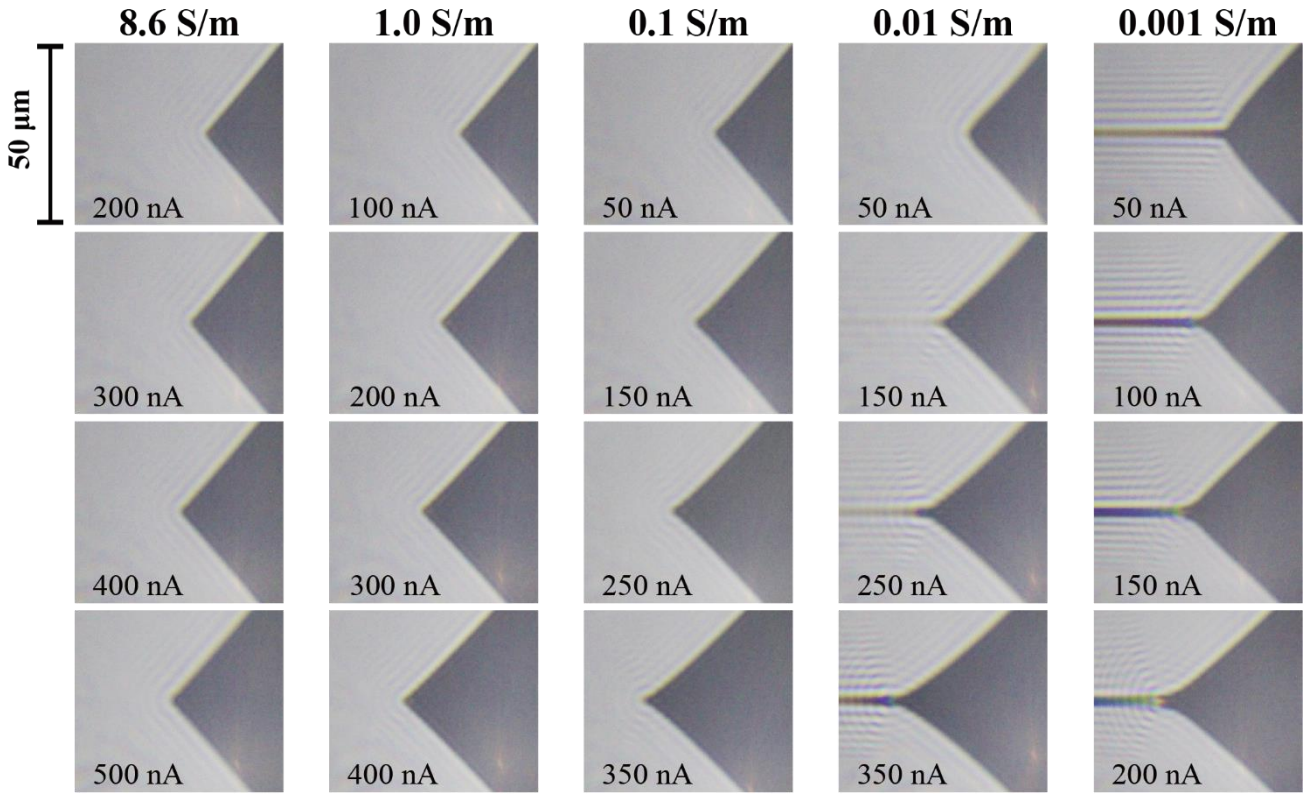

Figure 2.6. Structures of Taylor cone for NaCl aqueous solutions of different electrical conductivities at different spray currents. Columns from left to right: decreasing electrical conductivities (8.6 S/m to 0.001 S/m). Rows from up to down: increasing spray current.

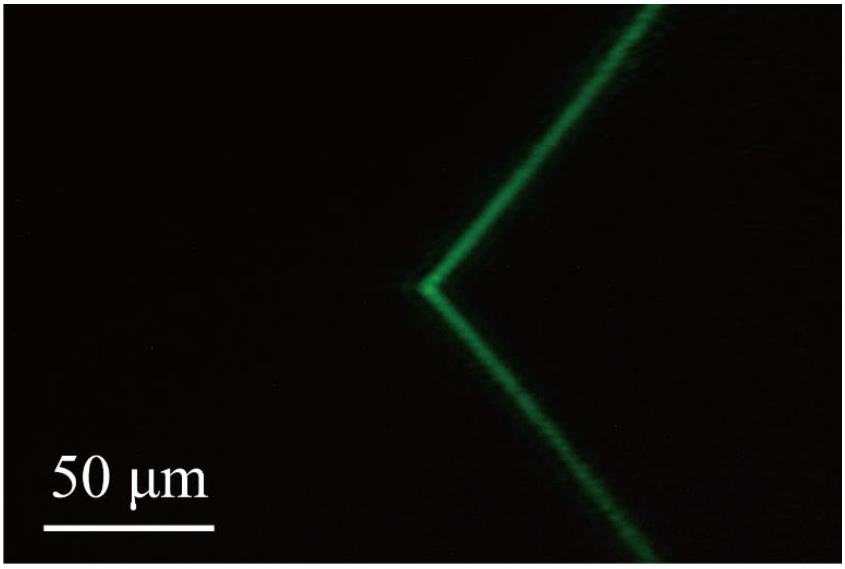

Figure 2.7. Microscopic image of an aqueous Taylor cone illuminated using a green laser (Nd: YAG, 2nd harmonics, 532 nm wavelength). A razor blade was used to block the main beam in front of the microscope to capture the scattered light from the edges of the Taylor cone. The apex angle is ~99°. Liquid: 1% v/v formic acid aqueous solution (electrical conductivity: 0.28 S/m).

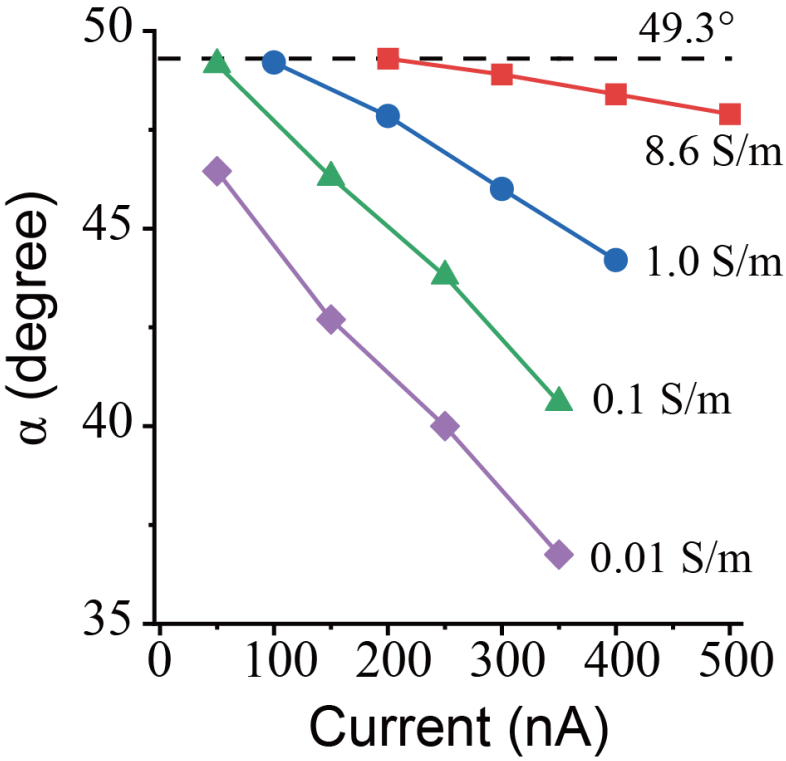

Figure 2.8. Semi-vertical angle of the Taylor cone α versus electrospray current for NaCl solutions of different electrical conductivities. The dashed line denotes the theoretical Taylor angle.

Flow rate-spray current relationship

Figure 2.9 shows the measurement of solution flow rates at different electrospray currents. The spray current was controlled solely by the applied voltage. Evaporation during the measurement was minimized by maintaining the relative humidity of the air supplied to the ion source at 90% using the bubbling method. The curves plotted using Eq. (1) are indicated as dashed lines. The values of surface tension under different NaCl concentrations were estimated using the model by Dutcher et al.[57] The measured values are in good agreement with the FL scaling law for Figure 2.9. Sources of error include the initial ejection of the relatively large droplet during the initialization of the Taylor cone, air drag, and the evaporation of water under 90% relative humidity. A rough estimation using the Hertz-Knudsen equation gave the evaporation rate at the order of ~1 nL/min which set the lower limit of our present measurement. The measurement of evaporation rate for a slightly charged liquid meniscus without forming the Taylor Cone gave a value is ~0.5 nL/min. We assume an error of ± 1 nL/min for the flow rate measurement in Figure 2.9. In sum, the results show that the $Q^{1/2}$ law can be safely applied for aqueous solutions down to several nL/min flow regimes, and the spray current was a reliable indicator of instantaneous flow rate if the system was free of electrical discharge. The anomaly in the spray current caused by the direct ion emission during the electrospray of formamide in a high vacuum[40] was not observed. Hereafter, the solution flow rate and the radius of the initial charged droplets are estimated based on Eq 1 and Eq 2 and the measured spray currents.

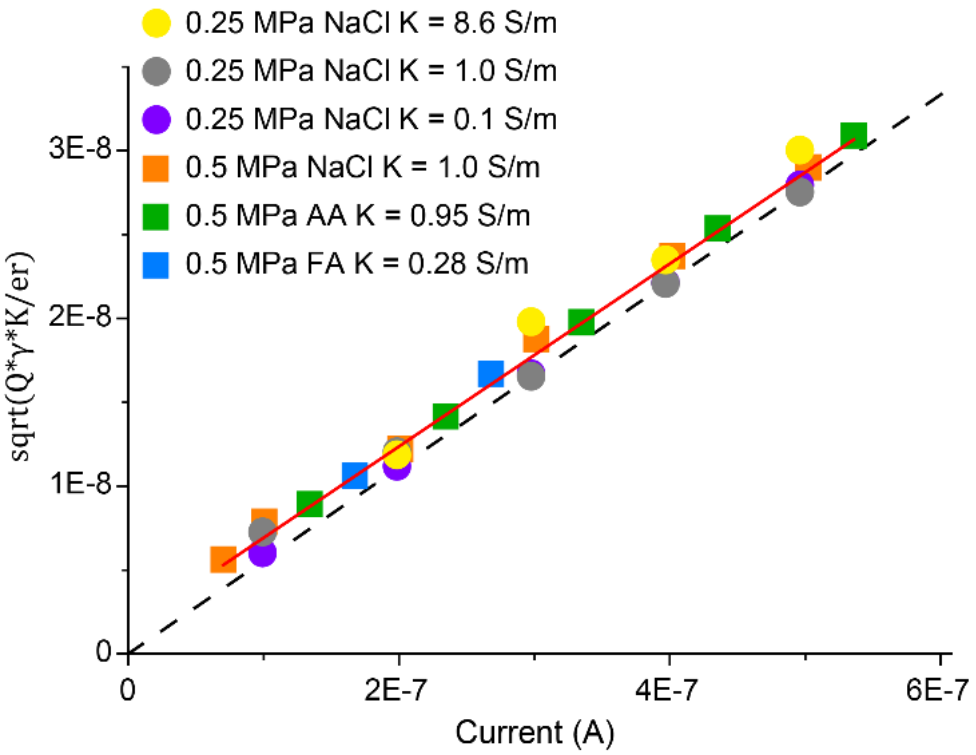

Figure 2.9. Validation of the scaling law for the spray current and the flow rate under the nanoflow regime. For aqueous solution, $I = 18\sqrt{\gamma K Q/\epsilon_r}$. ϵ_r is relativity permittivity, γ is surface tension, K is the electrical conductivity of the liquid. The dashed line depicts the theoretical curve. The result shows that the scaling law is independent of the ion source pressure. AA: ammonium acetate, FA: formic acid.

$BaBr_2$ as a probe for initial droplet size

The scaling law predicts a smaller initial droplet at a lower current but they are of submicron sizes and could not be measured directly in this study. Karas *et al.* proposed to use the ion signal of a suitable inorganic salt to reflect the size of initial droplets qualitatively.[44] They used barium bromide as the probe analyte and postulated that a smaller initial droplet would produce a higher ratio of $[Ba^{2+} + Ba^{+}]/[BaBr^{+}]$. Their MS analysis of 0.1mM $BaBr_2$ in ethanol using nanoelectrospray with fine capillaries had shown that the ratio did decrease with the increase of solution flow rate. Here, we performed a similar measurement, but to attain a suitable electrical conductivity, we used a 10 mM $BaBr_2$ aqueous solution (K = 0.24 S/m). The parameters of MS instruments were adjusted to optimize the detection of B^{2+} and $BaBr^{+}$. Ba^{+} was not detected in our measurement and there was also a significant contribution from the singly charged and doubly charged species of $[BaOH]^{+}$ and $[Ba_2(OH)_2]^{2+}$. The measurement of these ion signals at different spray currents (Figure 2.10) shows a similar trend obtained by Karas *et al.*, validating the spray current in our system as an indicator for flow rate and droplet size.

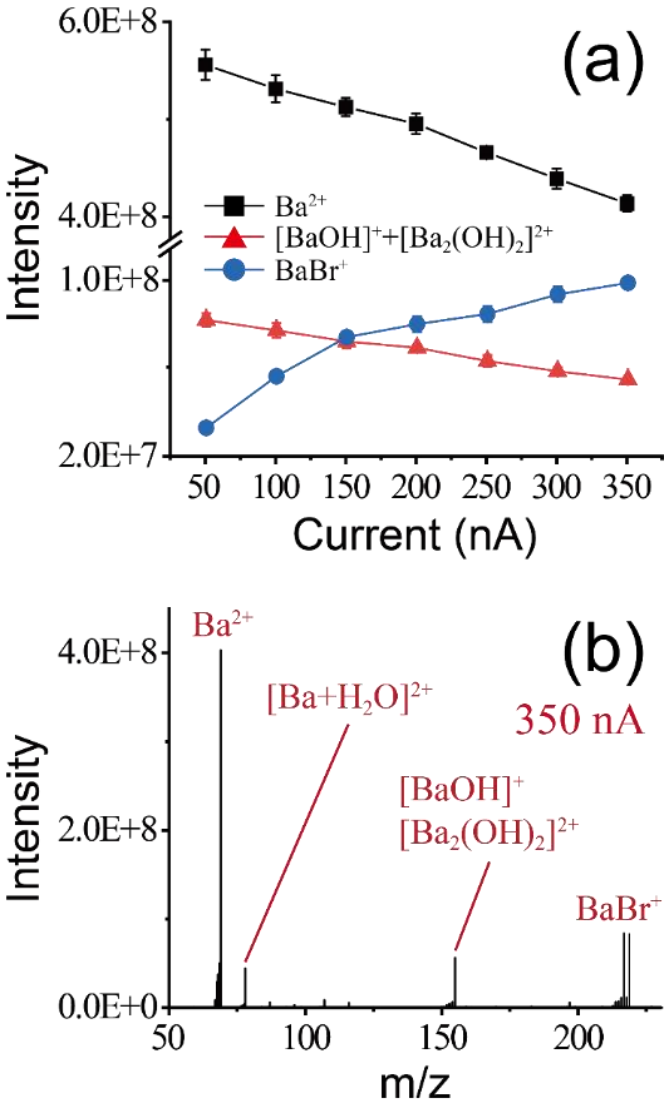

Figure 2.10. a) Ion signals for Ba^{2+}, $[BaOH]^{+}$ plus $[Ba_2(OH)_2]^{2+}$, and $BaBr^{+}$ acquired from 10 mM $BaBr_2$ in pure water solution at different spray currents. b) Mass spectrum obtained at spray current of 350 nA.

Effect of ion inlet temperature

In the typical operation of the conventional ESI sources, the heating of the ion inlet capillary of the mass spectrometer provides further desolvation to the droplets and prevents the clustering of ions with the solvent molecules during the adiabatic expansion. Droplets of sub-micrometer size generated by the true nanoelectrospray take a much shorter time to evaporate the solvent and undergo less number of Rayleigh fission to release the gaseous ions. This allowed the nanoESI emitter to be placed at ~1 mm or shorter to the ion inlet to aspirate most of the ions and required a much lower temperature for the ion inlet capillary than the typical >250 °C. Measurements were made to evaluate if the present electrospray operated at near minimum spray current also exhibits that property. To rule out the desolvation effect caused by the high-speed airflow when the droplets/ions were released to the atmospheric pressure region, the high-pressure ion source was connected directly to the MS vacuum via custom-made ion inlet tubes using Methods II & III. The sample in use was cytochrome c prepared in a 1% v/v formic acid aqueous solution (K = 0.28 S/m). The distance between the apex of the Taylor cone to the inlet is 0.8 mm. The spray current was maintained at 100 nA and the estimated flowrate and radius were 7 nL/min and 68 nm. Figure 2.11a shows the response of the total ion signal of cytochrome c over a wide range of ion inlet temperatures from 50 °C to 300 °C acquired using Method II. Overall, The near independence of ion signal on the inlet capillary temperature down to ~50 °C indicates a small initial droplet size as predicted by the scaling law. For comparison, a typical response of an ESI at a flow rate ~170 nL/min is depicted in Figure 2.11b, showing the rise in signal intensity with temperature before reaching a plateau at 250 °C.

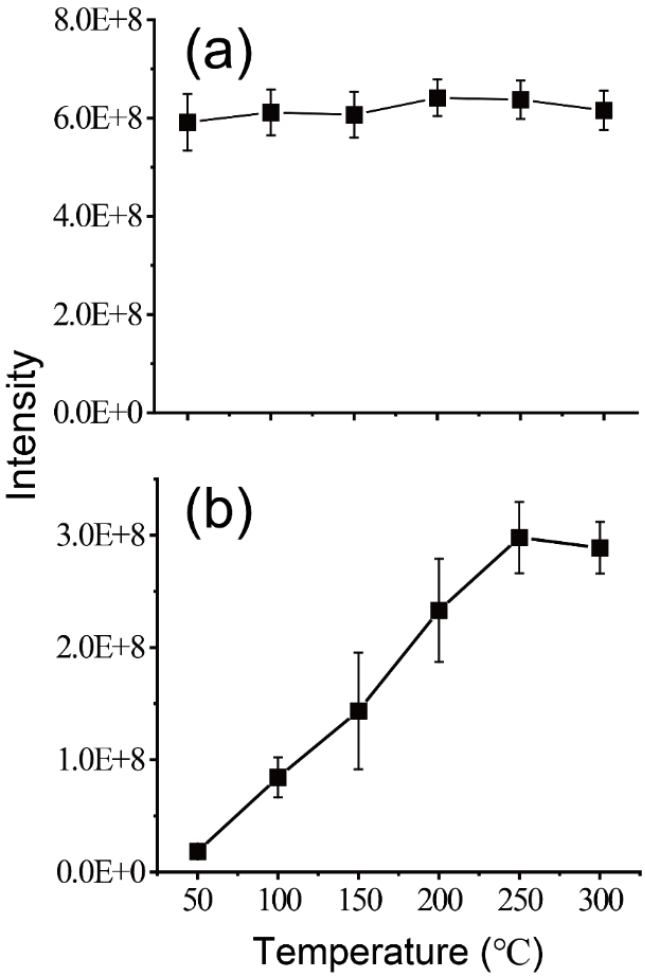

Figure 2.11. TIC of 2.5×10^{-6} M originated from cytochrome c acquired at different temperatures of the ion inlet capillary using different ion sources. **a)** Present HP-ESI ion source using pipet tip. **b)** Conventional ESI sprayer with a syringe pump. The liquid in (a) is a 1% v/v formic acid aqueous solution (K = 0.28 S/m). HP-ESI source in (a) is coupled to the mass spectrometer using coupling Method II. 50% methanol aqueous solution with 1% v/v formic acid is used in (b) to optimize the stability of the electrospray under atmospheric pressure. The distance between the apex of the Taylor cone to the inlet is 0.8 mm.

Sample in formic acid

Figure 2.12 shows the mass spectra of 2.5×10^{-6} M cytochrome c, β-lactoglobulin, lysozyme, ubiquitin, bradykinin, and angiotensin I in 1 % v/v FA aqueous solution (pH = 2.0) acquired at spray currents ranging from 60 nA to 400 nA, corresponding solution flow rates of 2.7 nL/min to 121.4 nL/min. The solution flow rates and the droplet radius were calculated using Equations 1 and 2. For cytochrome c, β-lactoglobulin and ubiquitin, the mass spectra show the presence of a bimodal distribution of charge state, and the average charge states shifted to a lower value at higher spray current. The CSD of Lysozyme is narrower compared to other proteins due to its compact structure with four disulfide bridges. The increase of lower charge species for protein was associated with the larger initial droplets generated at a higher flow rate, a trend that was typically observed in fine capillary nanoESI[45,58]. For proteins, the ion signals were higher at a lower current of 60~100 nA. For peptides, the ion intensities remained relatively constant within the range of measurement.

Sample in ammonium acetate

The mass spectra of the same proteins and peptides in 100 mM AA aqueous solution (pH = 6.7) are shown in Figure 2.13. Here, the sprayed current was varied from 60 nA to 700 nA, corresponding to a flow rate range of 0.8 nL/min to 110.3 nL/min. Except for -lactoglobulin, the mass spectra acquired at an optimum spray current of 60~100 nA show a narrow CSD. Overall, the average charge of the protein decreases as the flow rate increases but the variation is not as large as the case of 1% FA solution. Except for cytochrome c, the ion intensity reduced at a higher rate with the increase of spray current. Dimers of cytochrome c, lysozyme, and ubiquitin were also observed at higher spray currents (Figure 2.14). By comparison, the CSD of peptides was less sensitive to the solution flow rate.

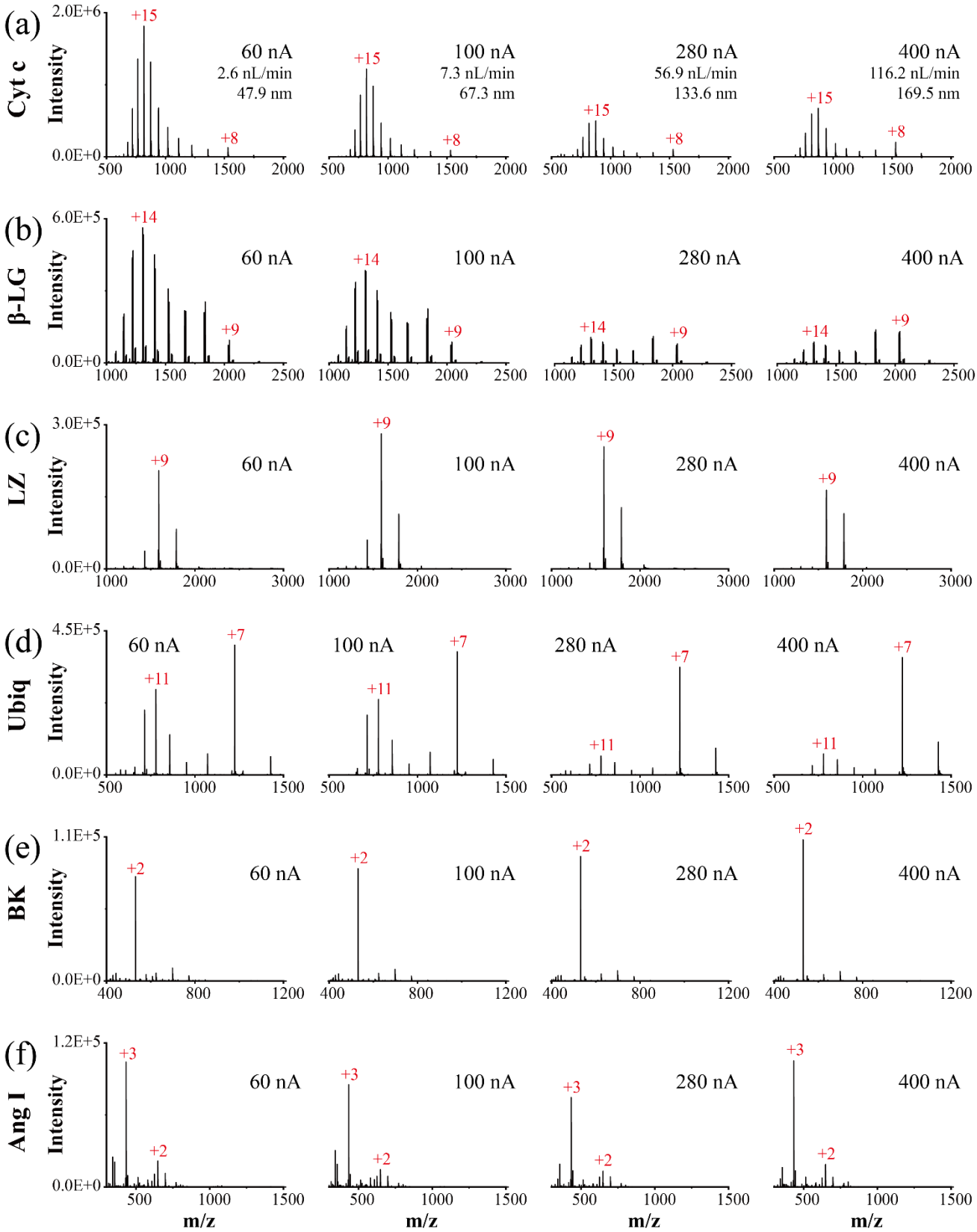

Figure 2.12. Mass spectra of 2.5×10^{-6} M cytochrome c (a), β-lactoglobulin (b), lysozyme (c), ubiquitin (d), bradykinin (e), and angiotensin I (f) in 1% formic acid aqueous solution acquired at different spray currents. Calculated flow rates and droplet radii are indicated in row (a).

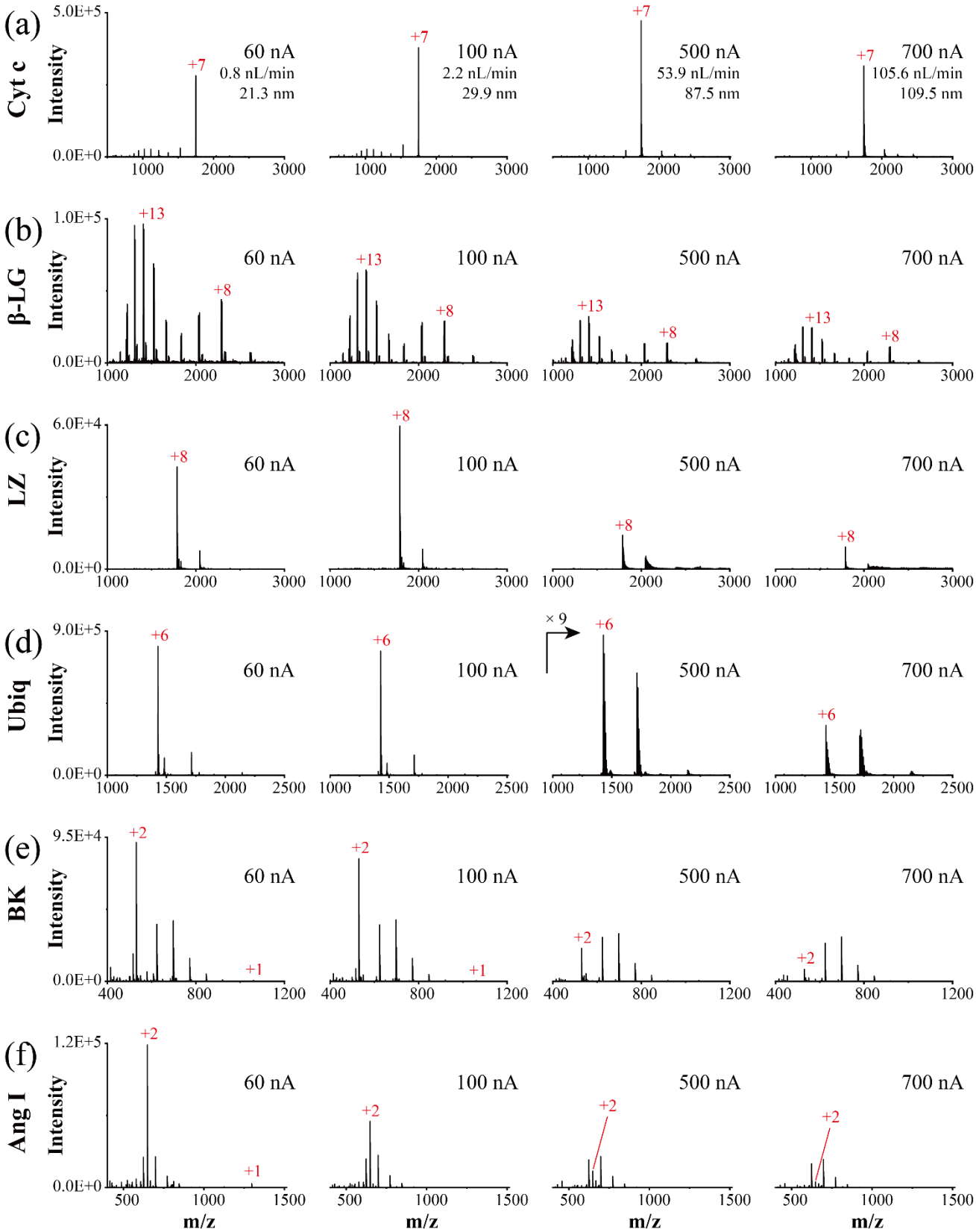

Figure 2.13. Mass spectra of 2.5×10^{-5} M cytochrome c (a), β-lactoglobulin (b), lysozyme (c), ubiquitin (d), bradykinin (e), and angiotensin I (f) in 100 mM ammonium acetate aqueous solution acquired at different currents.

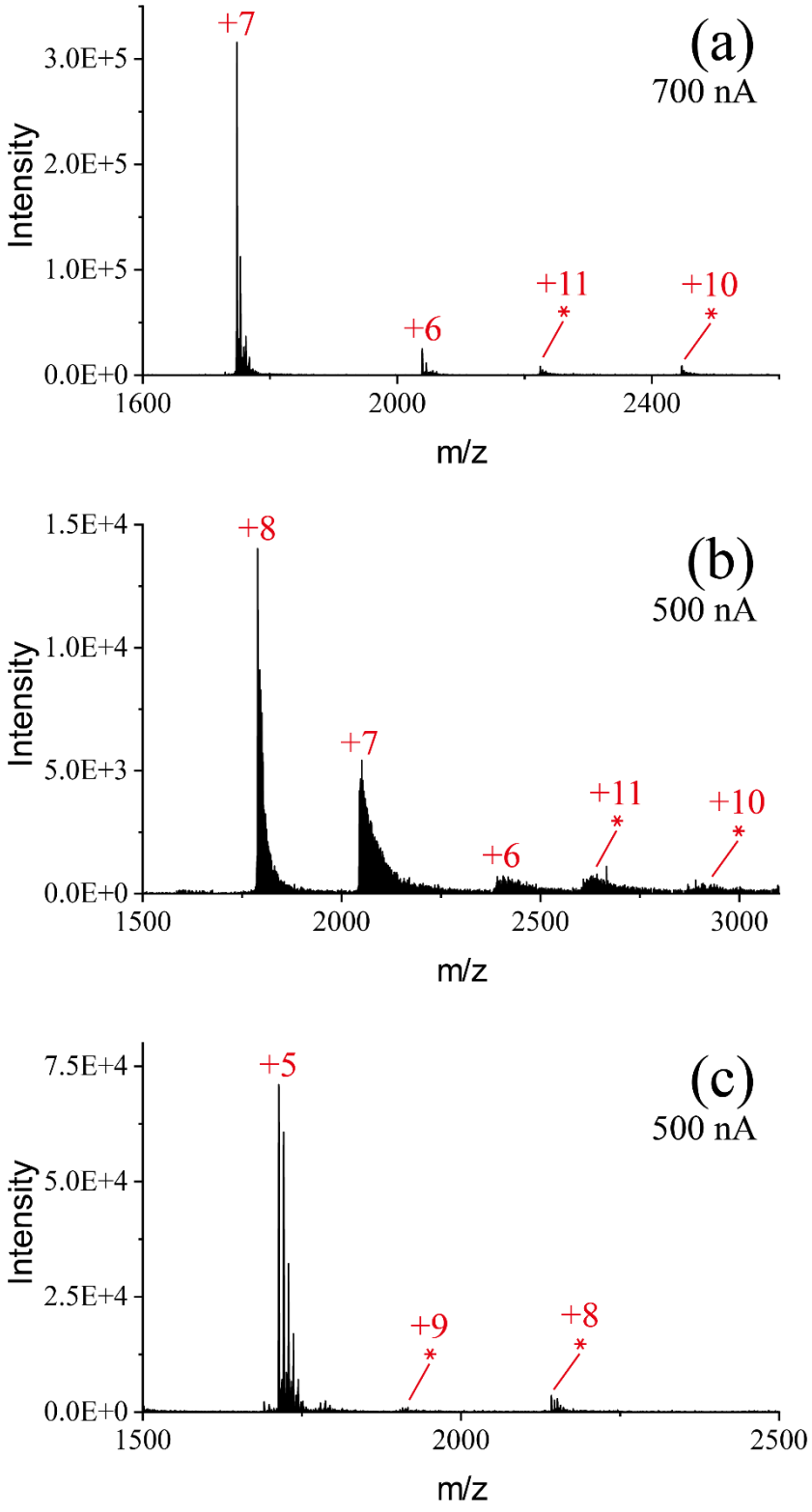

Figure 2.14. Mass spectra of 2.5×10^{-5} M cytochrome c (a), lysozyme (b), and ubiquitin (c) in 100mM ammonium acetate buffer and ubiquitin.

Sample in phosphate buffered saline

PBS is the typically used buffer for biological application, but due to its high concentration of nonvolatile salts, it is seldom used directly in ESI-MS. Figure 2.15 shows the mass spectra of 2.5×10^{-5} M cytochrome c, β-lactoglobulin, lysozyme, ubiquitin, bradykinin, and angiotensin I in PBS buffer (pH = 7) aqueous solution at various spray currents. The smallest tested spray current was 60 nA (corresponds to 0.7 nL/min). The largest spray current here was 500 nA (33.8 nL/min). Except for lysozyme, good mass spectra were acquired from the undiluted PBS by operating the ESI at a low spray current of 70~100 nA. For lysozyme, the PBS was diluted to 1/5 with pure water. The detected dominant ion species for protein and peptides are due to those of sodium adduction, but unlike the results obtained from AA, the CSD is not as narrow. The observed series of ion peaks are 22 Da apart, which correspond to the form of $[\mathrm{M}+(z-n)\mathrm{H}+n\mathrm{Na}]^{z+}$. Figure 2.16 shows the case of +2 state for angiotensin I. The degree of sodium and NaCl adduction depends on the size of the initial charged droplets. A larger droplet produced at a higher spray current increased the adduction of salt which reduced the peak height and the quality of the mass spectra. For all samples, the adduction of salt was reduced by generating smaller initial charged droplets at lower spray current operation. To a certain extent, in-source CID could also be used to remove adducts from the proteins to obtain narrower peaks (Figure 2.17).

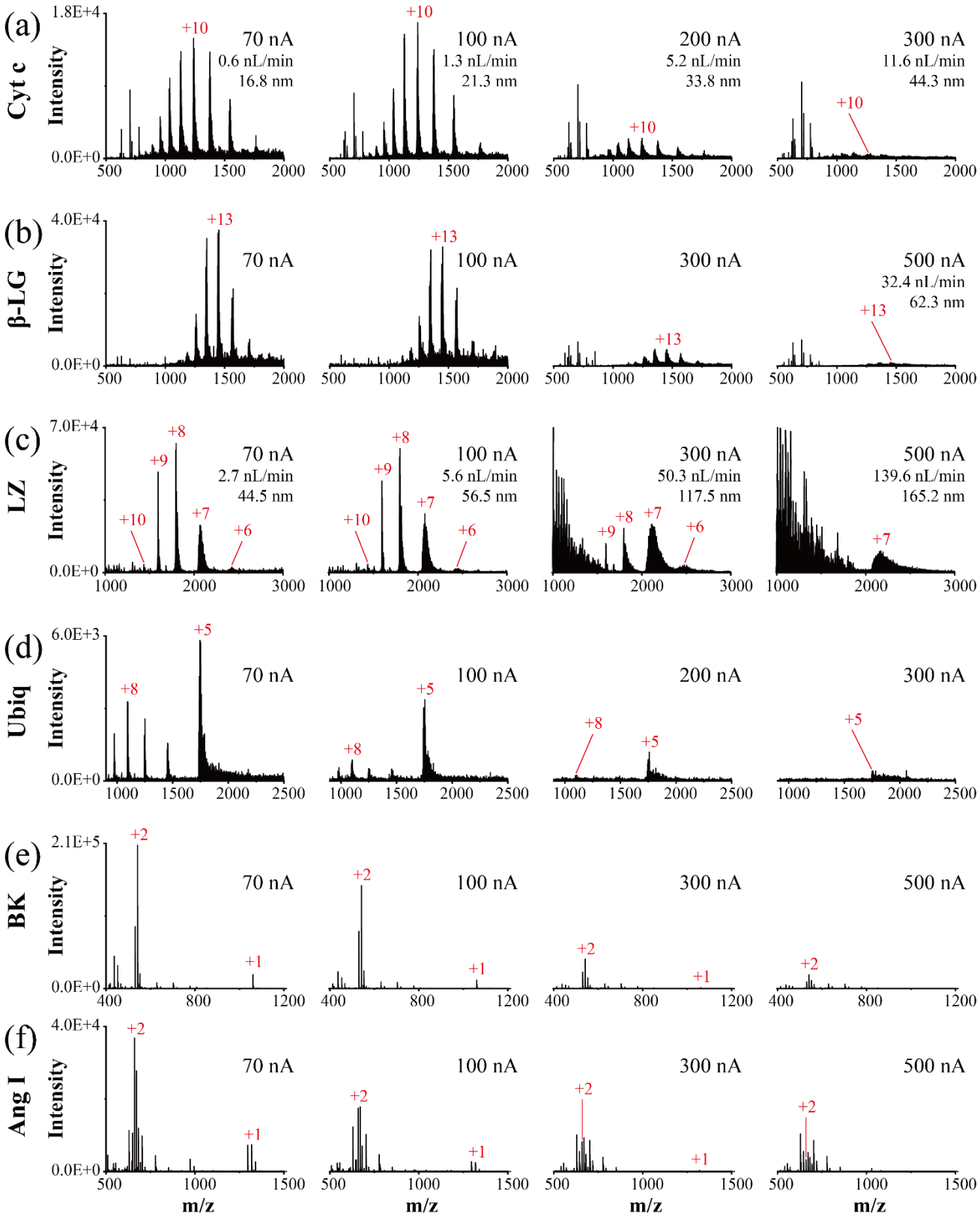

Figure 2.15. Mass spectra of 2.5×10^{-5} M cytochrome c (a), β-lactoglobulin (b), lysozyme (c), ubiquitin (d), bradykinin (e), and angiotensin I (f) in PBS buffer solution acquired at different spray currents.

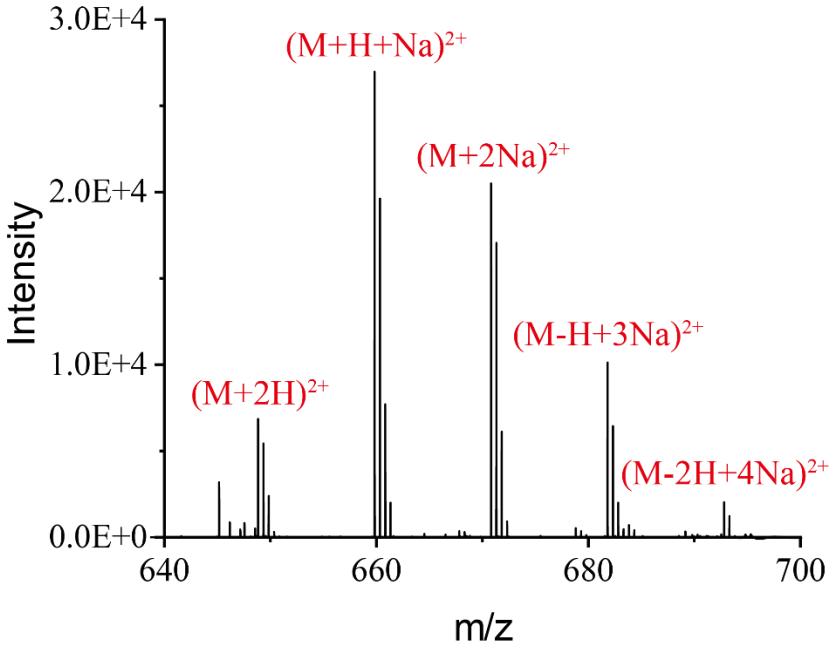

Figure 2.16. Mass spectra of 2.5×10^{-5} M angiotensin I in PBS buffer aqueous solution acquired at 60 nA.

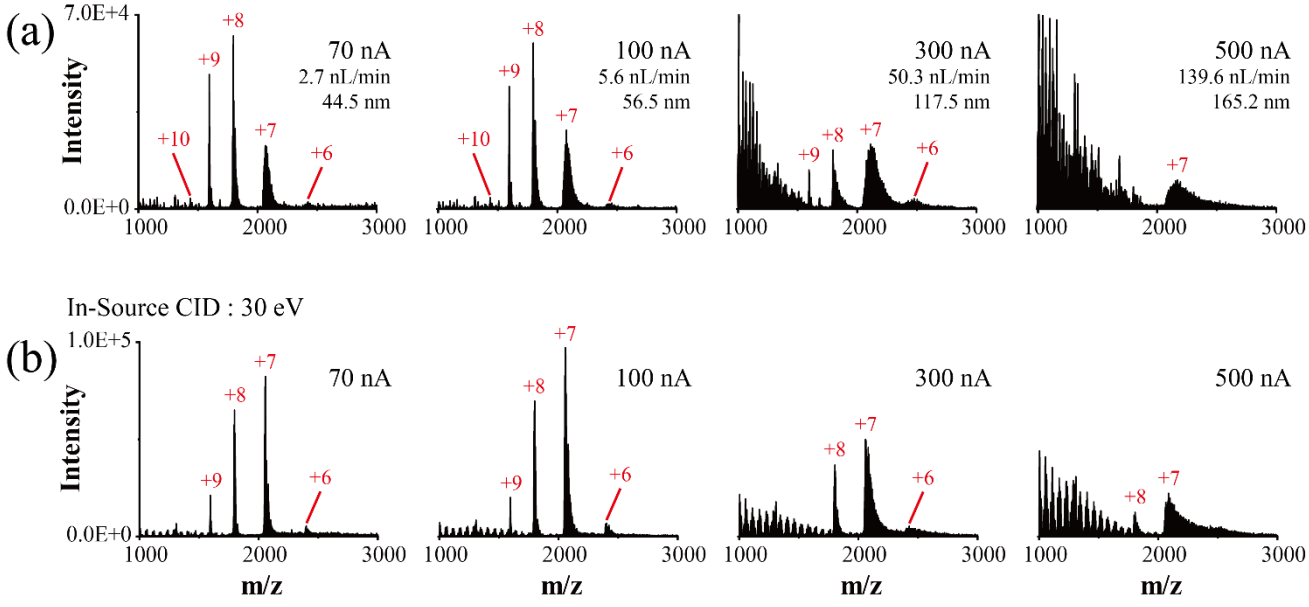

Figure 2.17. Mass spectra of lysozyme in PBS (1/5 dilution) obtained without (a) and with in-source CID (b) at different spray currents.

Sample in Tris-HCl buffer (1M)

Figure 2.18 shows the mass spectra of proteins and peptides, each of 2.5×10^{-5} M in 1 M Tris-HCl buffer aqueous solution at various spray currents. The solution of the highest electrical conductivity in this study (pH = 7). The lowest spray current at 100 nA corresponds to a flow rate of 0.4 nL/min. Tris-HCl is a strong buffer widely used for nucleic acids and proteins in many biochemical reactions and analyses such as electrophoresis. Here it is demonstrated that clean mass spectra could be obtained from the concentrated buffer of 1 M, a concentration that was relatively difficult to handle with conventional ESI or nanoESI due to high surface tension, electrical discharge, and plugging problems. Cluster ions originating from the Tris-HCl were present in the mass spectra, but the detection of proteins and peptides was not seriously affected. For cytochrome c, the CSD was narrower compared to that of PBS, but wider than that of AA. The dominant charge state is +9, which slightly lower than that of PBS, but higher than AA. For β-lactoglobulin, the CSD is narrower than those of PBS and AA. For lysozyme, the dominant charge state (+6) is smaller than that of AA (+8). For ubiquitin, the dominant charge state (+5) is similar to that of PBS but smaller than that of AA (+6).

Ion intensity and average charge state

In most cases, the strongest ion signal was observed at low spray current operation (<10 nL/min), but not always at the minimum current. Exceptions are for cytochrome c in AA where the highest intensity was obtained at around 50~60 nL/min. The ion signal for peptides in FA solution remained relatively constant over the tested range of ~1 to 120 nL/min.

The changes of the average charge state of proteins and peptides with the spray currents for various are summarized in Figure 2.19. The dominant charge state and the average charge state were primarily determined by the pH and the type of the buffer solution. Buffers of the nearly same neutral pH but different salts might not produce the same CSD. For example, the average charge state of the protein in PBS is always higher than that in AA and Tris-HCl. For cytochrome c and lactoglobulin in PBS, the average charge states were higher than those from AA. For ubiquitin, the charges number for the dominant peak of ubiquitin in PBS is lower than that of AA but a series of higher charge state species of the ubiquitin was also detected. For acidic solutions, the average charge state is higher at a

lower spray current. This was consistent with the capillary-based nanoESI where a higher average charge state is typically observed for smaller capillaries[45,58]. In some cases, the shift of the average charge state is due to the multi-modal distribution of the charge state. Williams et al. showed that the use of submicron emitter caused the appearance of another higher charge state series in addition to those seen in micrometer capillary, and the phenomenon was postulated to be caused by the unfolding due to the columbic interaction between the glass surface and the positively charged protein[59]. Multimodal CSD was also observed in the present study but the interaction of proteins with the surface could be ruled out because the material of the emitter was non-glass material, and the inner diameter was large enough. For the non-denaturing buffers, the variation of average charge with the flow rate was relatively small but the trend was not general.

Finally, the average charge numbers obtained using the non-denaturing buffer solutions are compared with the Rayleigh limit. The charged residue model (CRM) is believed to hold for large globular macromolecules such as proteins[14]. As such, the maximum charge transferred to an unfolded protein cannot exceed the Rayleigh limit, i.e. the maximum excess charge that can be sustained by the surface tension of a liquid sphere, Nevertheless, there is no single consensus value for the density of protein droplet at the last stage of evaporation. The protein density was taken as 1.0 g/cm^3 by Fernandez de la Mora for the hydrated protein[60]. Electrophoretic mobility measurement of protein aerosol suggested a density value of 0.6 g/cm^3. [61] Both values were used for the plots of the average charge number against the protein diameter in Figure 2.20. All average charges measured in our experiment fall below the Rayleigh limit if the protein density was taken as 0.6 g/cm^3.

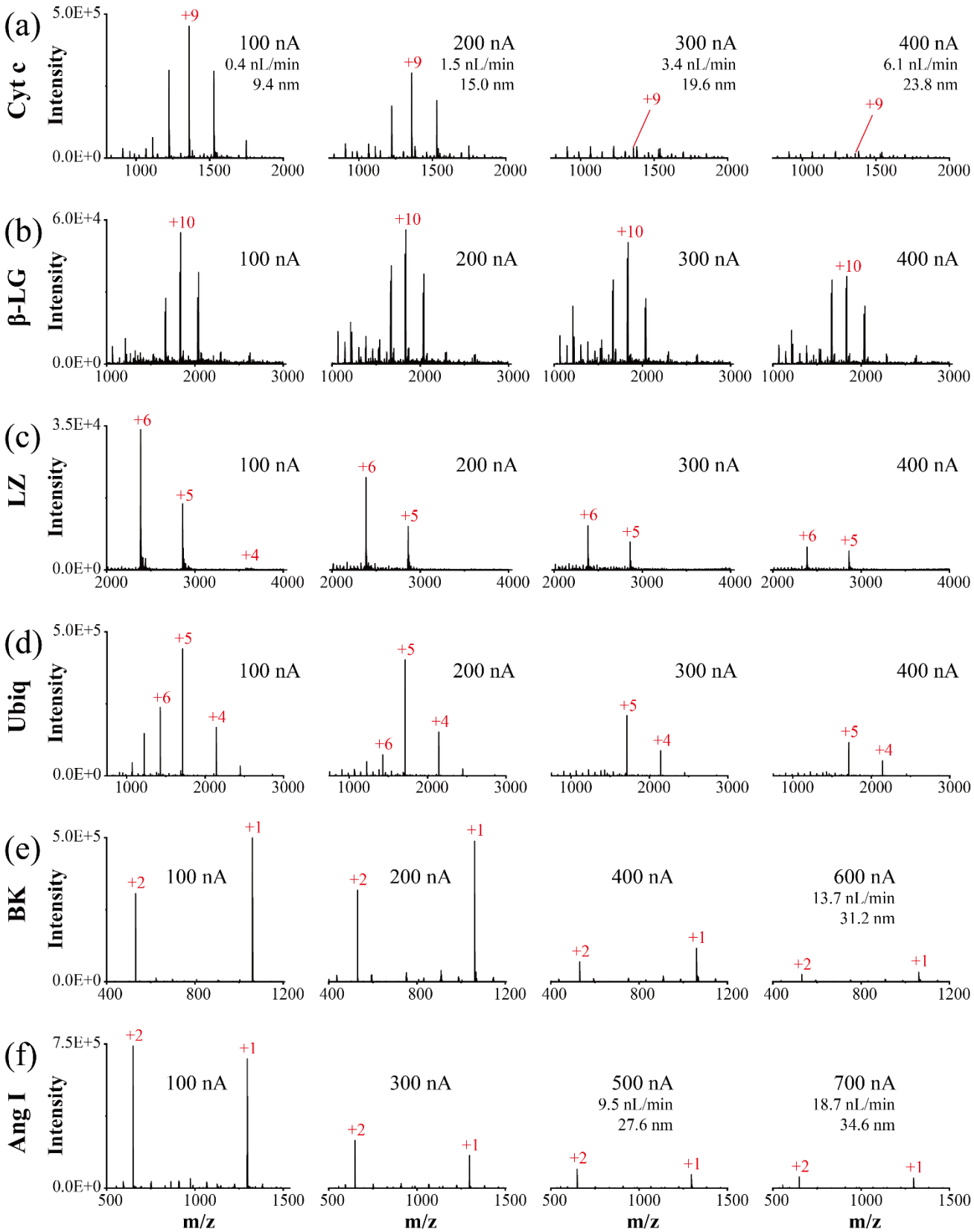

Figure 2.18. Mass spectra of 2.5×10^{-5} M cytochrome c (a), β-lactoglobulin (b), lysozyme (c), ubiquitin (d), bradykinin (e), and angiotensin I (f) in 1M Tris-HCl buffer aqueous solution acquired at different spray currents.

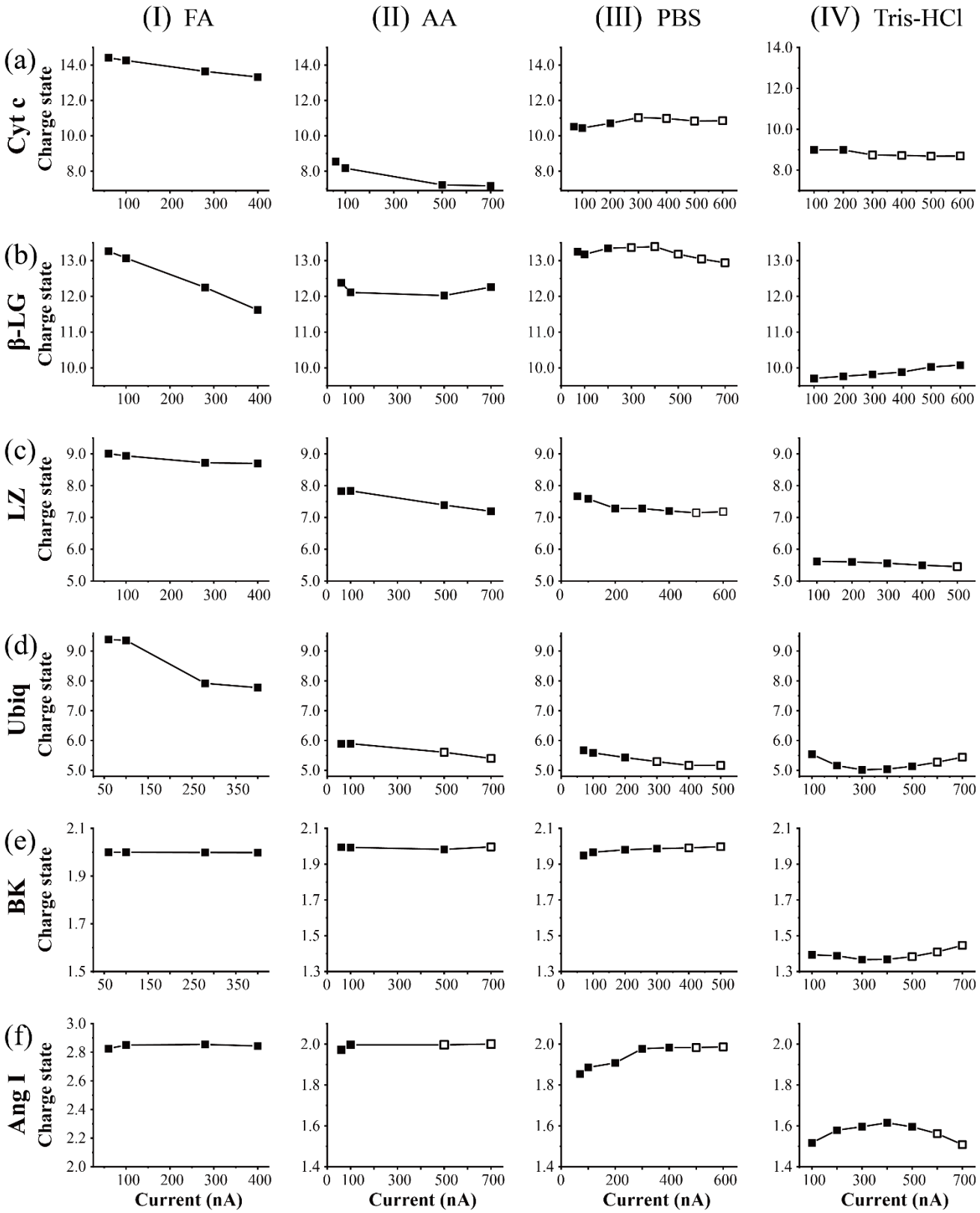

Figure 2.19. Average charge state of cytochrome c (a), β-lactoglobulin (b), lysozyme (c), ubiquitin (d), bradykinin (e), and angiotensin I (f) in 1% formic acid (I), 100mM ammonium acetate (II), PBS (III) and 1M Tris-HCl (IV) aqueous solution acquired at different spray currents. Open squares indicate a weak ion signal.

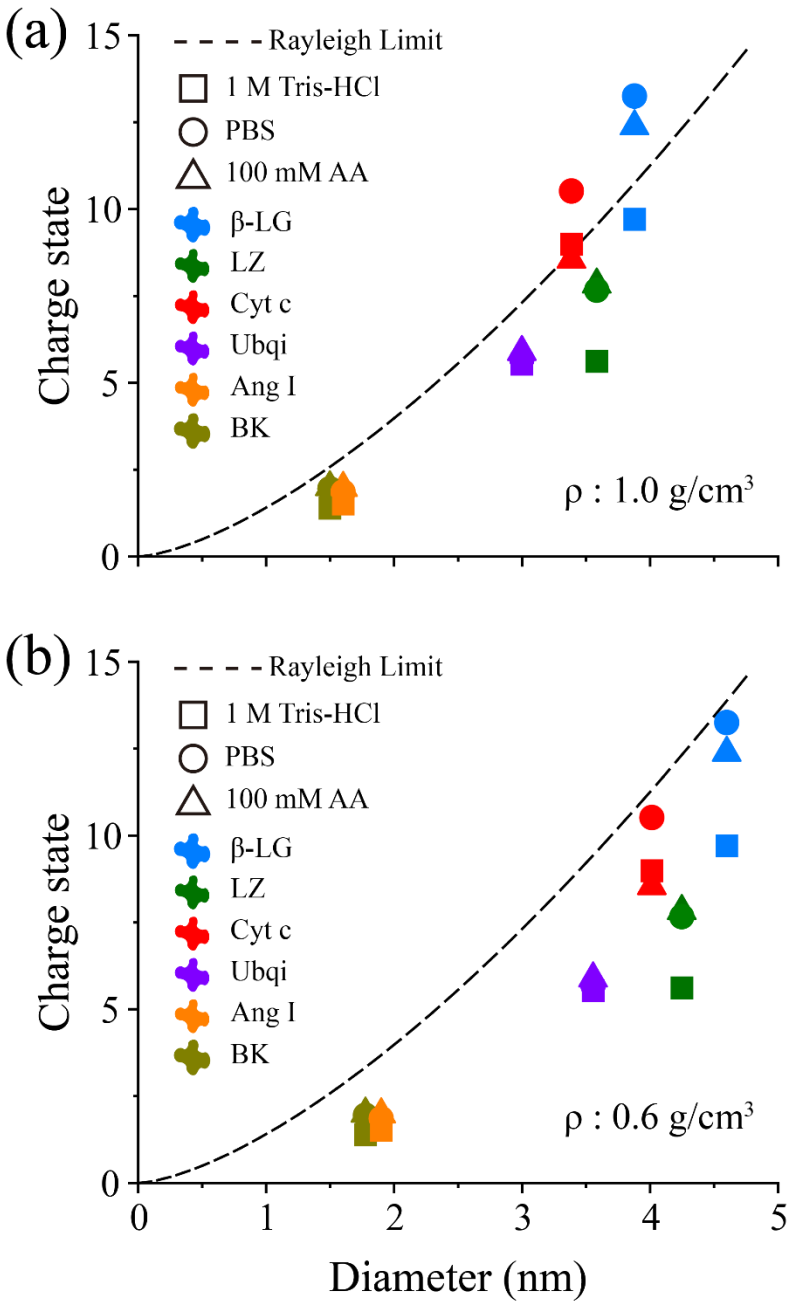

Figure 2.20. Plot of average charged state versus protein diameter. The protein diameter is calculated using a) protein density ρ = 1.0 g/cm^3, and b) density ρ = 0.6 g/cm^3.

Conclusions

In the Chapter 2, stable Taylor cones with a half apex angle close to the theoretical Taylor angle have been generated for highly conductive aqueous solutions by operating the electrospray at spray currents near the minimal levels under a high-pressure condition. The formation of the aqueous Taylor cone from a large emitter capillary (i.d. 0.4 mm) that was typically difficult under atmospheric pressure was made possible under a super-atmospheric pressure condition. The emitter capillary was operated “off-line”, i.e. it was not connected to liquid pumps to maintain a zero-pressure difference between its both ends. The physical and ionization characteristics of this electrospray have been evaluated by the measurements of spray current, cone geometry, liquid flow rate, and mass spectrometry. The scaling law for spray current and flow rate which was previously established using a liquid pump-based system was found to be valid for the off-line system down to the nL/min flow regime. The flow rate in the present system was solely controlled by the applied potential and the choice of electrolytes, and the spray current was a reliable indicator of instantaneous liquid flow rate. The solution flow rate was finely tuned over the range of <0.2 nL/min to 120 nL/min using applied potential alone without changing the size of the emitter capillary. The spray current was used as the real-time indicator for the instantaneous flow rate and initial droplet size. High-resolution flow rate scanning and simultaneous acquisition of spray current and MS can also be performed to correlate the ionization results with the physical variables such as flow rate and initial droplet size with higher precision. From the evidence of solution flow rate and mass spectrometric results, it was verified that the ultra-small size of the emitter is not an essential factor to produce the “true nanoelectrospray” equivalent ionization. Compared to the capillary-based methods, the present method allows the fine-tuning of flow rate and initial droplet size without changing the diameter of the emitter tip, which is beneficial for the fundamental study of the ionization mechanism. Artifacts originating from the surface interaction with the emitter can also be avoided when studying the physical chemistry of charged nanodroplets and liquid interface. The same working principle and the scaling law should also apply to smaller capillaries as long as the jet diameter is much smaller than the inner diameter.

Chapter 3: Novel characteristic of HP nano-ESI: nanoflow rate alters the ionization response

Summary

The small charged droplet generated from the nanoelectrospray ionization (nanoESI) at nL/min flow rate gives its unique feature of high-performance ionization. A continuous scan of the flow rate in this regime can trace the effect of droplet size in greater detail for a better understanding of the ionization process. To date, such practical implementation is hindered by the lack of a suitable liquid pump and the reproducibility of microcapillaries-based systems. Here, an offline nanoESI mass spectrometry with a continuously varying flow rate in a dynamic range of several hundred pL/min to ~100 nL/min was performed by precision scanning of the ESI high voltage (HV). The principle is based on the new paradigm of generating nanoelectrospray from a large Taylor cone with a known spray current-flow rate relationship. The instantaneous flow rate controlled by the HV modulation can be calculated by the simultaneous measurement of the spray current. The system is successfully applied to reveal the role of nanoflow rate on the average charge state of proteins, analysis of analyte mixture, and desalting effect. With the use of buffer solution with high electrical conductivity, a highly controllable oxidative modification was also observed by tuning the flow rate below a threshold at ~5 nL/min, a finding that has a potential application to on-demand oxygen labeling.

Introduction

In an unassisted electrospray, the liquid anchored to the emitter tip is charged to form a liquid cone (Taylor cone), and from its apex emits a fine jet that breaks into small charged droplets. A sequence of solvent evaporation and coulombic fission (also called Rayleigh fission) leads to the formation of last-stage droplets from which analyte gaseous ions are generated. The flow rate of electrospray is a key operating parameter that affects the size of the initial charged droplets, which in turn has a substantial effect on the detection sensitivity, tolerance to impurities, and quantitative performance of ESI.[43,44] While the high-flow ESI sources are used to accommodate the working flow

rate of LC, a low flow rate operation is known to give higher sensitivity and better sample utilization which is crucial for proteomics and native MS that required the ESI of analytes from a salt-rich physiological condition. The nanoESI with a flow rate range of 20~300 nL/min can be performed by using emitter capillaries with an inner diameter of several tens micrometers.[62] The ultra-low flow rate of < 20 nL/min usually requires an off-line capillary with i.d. of several micrometers.[26,41] There was also development on ESI with sub-micrometer capillaries.[45,46,63] The mechanism behind some unique features of a nanoESI was given by Karas et al,[43,44] and there are rich literature reports on the enhanced sensitivity for peptides and proteins by lowering the flow rate of nanoESI. But by using a nanospray emitter, an opposite result was also observed, i.e. higher flow rate generated higher ion signal intensity for relatively small compounds such as amphetamine, caffeine, and cocaine.[64] A recent report on the surface modification of nanoESI capillary also found that in their case, the improved sensitivity for the detection of protein was due to an increase in flow rate for modified capillaries rather than the reduction in nonspecific adsorption.[65] The rule of thumb that the smaller the flow rate the higher the ion signal for nanoESI may not always hold.

High-speed tuning of the nanoflow rate thus becomes necessary for the determination of optimum flow rate and to reveal the complete response of ESI over an appropriate flow rate window. As the flow rate reflects the average size of droplets, precision control of its instantaneous value can provide an in-depth understanding of the ESI process. For a microflow ESI, flow rate tuning from 0.1 μL/min to several tens μL/min can be performed using a programmable syringe pump. High flow rate scanning (40 ~ 800 μL/min) using a Peristaltic pump had also been reported,[66] but the large initial droplet with a wide distribution of size required pneumatic assistance, and the heated gas for desolvation. Flow rate regulation for online nanoESI was possible with a precision liquid pump,[67,68] but the response time for each adjustment was in the order of minutes and the applied potential might need to the readjusted. As for the offline microcapillary-based nanoESI, the dynamic range for a stable operation is quite narrow, and the flow rate is sensitive to the tip dimensions. The adjustment of the flow rate usually requires a change of capillaries of varying sizes. As such, a two-flow rate mode operation was previously possible using a hybrid emitter in which a finer emitter was incorporated into another nanoESI capillary for a rough step-wise flow rate switching.[69] Reproducibility due to the defects, the damage of the fragile orifices, and the clogging are also issues associated with the fine

nanoESI capillaries.

Previously we reported a new paradigm of generating nanoESI from large-bore capillaries with a well-controlled flow rate that is insensitive to the inner diameter of the capillary.[32,33] The concept is based on the well-established spray current-flow rate relationship for steady cone-jet mode under an electrical-discharge-free condition. The new ion source employed a high-pressure ESI technique which was developed previously in our laboratory to handle pure water,[23] superheated solutions for high-throughput proteomics,[53] and the direct hyphenation with high-temperature liquid chromatography.[54,55] Common micropipette tips could be conveniently employed as the emitter for the direct detection of proteins from the high-salt buffers without clogging and with minimal interaction with the capillary surface.[32] Based on this new technique, we report the implementation of a scanning voltage nanoESI with a continuously varying flow rate to reveal the ionization response to flow rate in the nL/min flow regime.

In this part, a disposable micropipette tip with a tip opening of 0.4 mm was used to perform nanoESI under a super-atmospheric condition (Figure 3.1a). Controlled by a master computer that synchronizes the electrospray operation and the MS acquisition, the nanoflow rate was scanned solely by ramping down the high voltage (Figure 3.1b). The spray current I was measured simultaneously to give the value of the instantaneous flow rate Q. In the absence of discharge, the flow rate from a steady liquid cone (Taylor cone, inset in Figure 3.1a) is given by the well-known scaling law as[24]

$$I = f\left(\frac{\gamma K Q}{\epsilon_r}\right)^{1/2} \quad (1)$$

, where ϵ_r is relativity permittivity, γ is surface tension, K is the electrical conductivity of the liquid, and $f = 18$ for aqueous solutions. The validity of the scaling law in the nanoflow regime was verified in our previous publications (see combined dataset in Figure 2.9).[32,33] The radius of the initial droplet R_o is related to the flow rate by[24]

$$R_o \sim \left(\frac{\epsilon_o \epsilon_r Q}{K}\right)^{1/3} \quad (2)$$

It is noted that Eq 1 and Eq 2 assume a much smaller jet diameter relative to the nozzle diameter, thus it may not apply to the fine capillary-based nanoESI.

Experimental section

Ion source and instrument

Figure 3.1 shows the schematic of the high-pressure ion source and the block diagram for the control of flow rate. Polypropylene micropipette tips with a tip opening inner diameter of 0.4 mm (Eppendorf, Hamburg, Germany) were used as the electrospray emitters. A platinum wire (dia: 0.2 mm) was inserted into the pipette tip to make electrical contact with the loaded liquid. The ion source consisted of an aluminum chamber and an insulating flange made of polyetheretherketone (PEEK). The ion source was pressurized with dry air (humidity < 10%) from an air compressor at room temperature to a gauge pressure of 5 bar. MS measurements were performed using a benchtop Orbitrap mass spectrometer (Thermo Fisher Scientific, Bremen, Germany). The ion source was coupled directly to the mass spectrometer using a custom-made ion transmission tube with 0.25 mm i.d. to match the acceptable gas throughput of the vacuum pump. When the ion source was pressurized, the pressure in the fore vacuum was ~1 mbar, approximately the same as the original reading of the mass spectrometer under standard working conditions.

Sample preparation

The ramping of high voltage and the simultaneous acquisition of spray current and mass spectra were controlled by a PC via a custom program written in C#. The spray current was measured by sensing the voltage drop across a 1 MΩ resistor. The signal for the spray current and HV were read and recorded by multimeters controlled by the PC. The potential applied to the liquid was ramped up and down by sending the control signal from the PC via the programmable DC supply to the HV module (Bellnix, Saitama, Japan). The ramping down of HV was performed at 1V/step. The precision of the flow rate control was in the order of 0.05 nL/min per step. The default value for HV ramping speed was approximately 3 V/s. The conventional nanoESI-MS was performed using capillaries with a tip i.d. of 1 μm (New Objective, Littleton, MA) under atmospheric pressure with the standard ion inlet tube (0.55 mm i.d.).

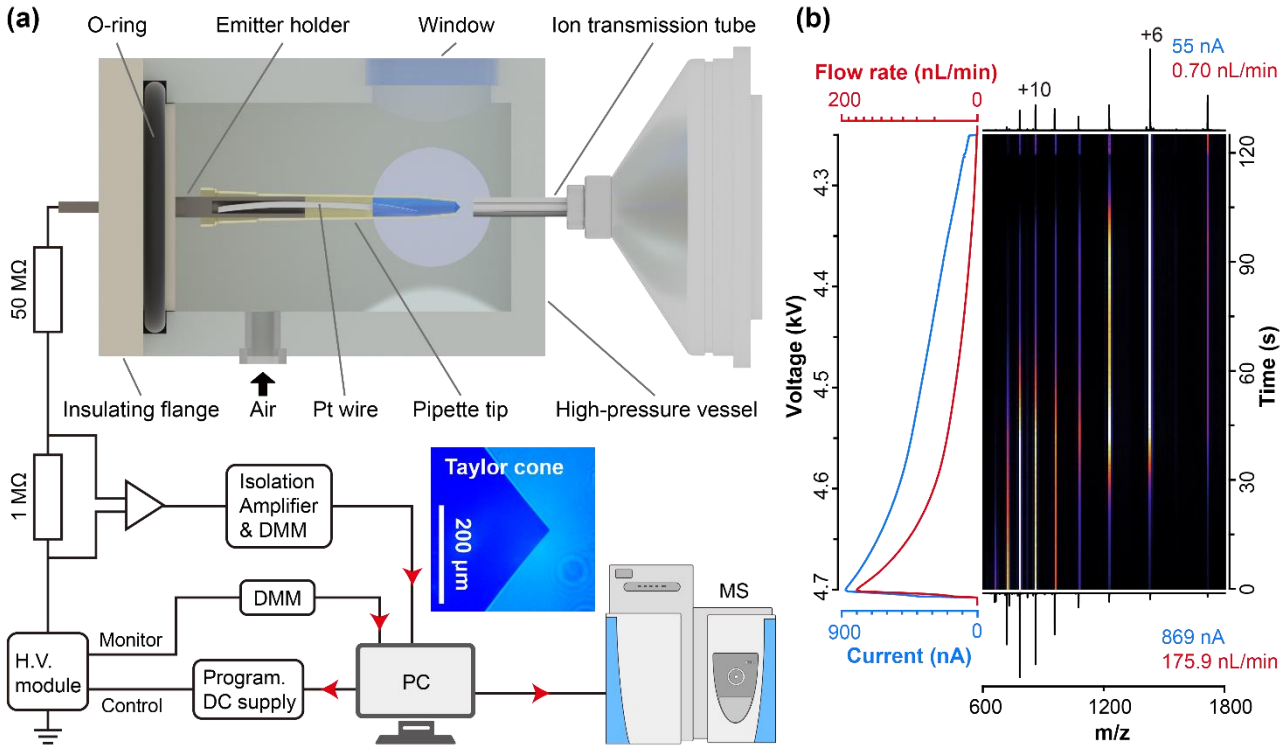

Figure 3.1. a) Schematic of the high-pressure nanoESI ion source and the block diagram for flow rate tuning. A micropipette tip is used as the emitter. A master PC sends the control signal to the HV supply, reads HV and spray current signal, and triggers the acquisition of MS. **b)** Scanning of ESI HV. The HV is rapidly ramped up to initiate the Taylor cone and gradually ramped down until the collapse of the Taylor cone. The heatmap showing the normalized intensity is constructed from the mass spectra taken at different spray currents and flow rates. The sample is ubiquitin in 100 mM ammonium bicarbonate.

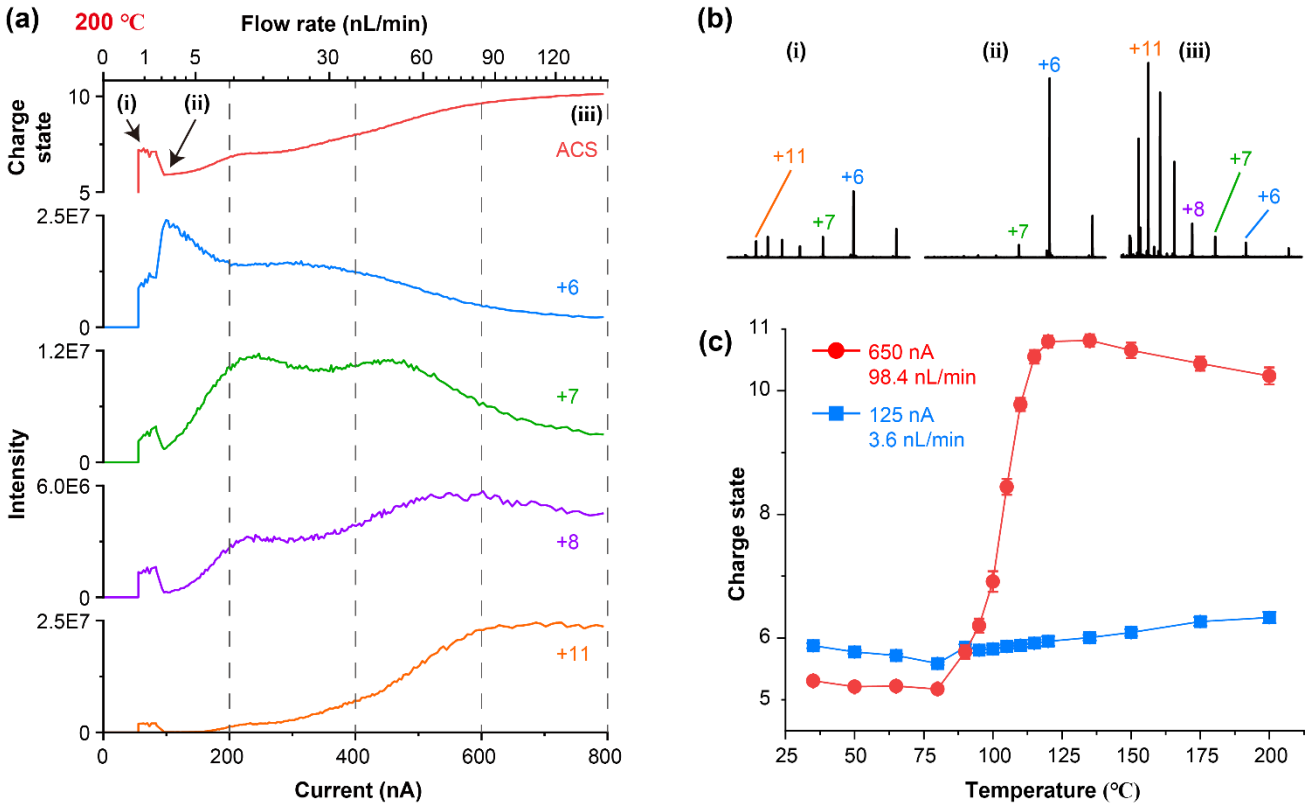

Figure 3.2. Detection of ubiquitin in 100 mM ammonium bicarbonate. **a)** Average charge state and the ion intensities of selected charge states versus flow rate acquired at 200 °C ion inlet temperature. **b)** Corresponding mass spectra at flow rates indicated by (i)-(iii). **c)** Average charge states versus ion inlet temperature obtained at different flow rates.

Results and Discussion

Ammonium bicarbonate

The present method was first applied to evaluate the flow rate dependence on the charge state distribution (CSD) of proteins in ammonium bicarbonate (AB) and ammonium acetate (AA). Despite being a stronger pH stabilizer than the ESI-friendly AA, AB was known to produce highly charged protein, a phenomenon coined as "electrothermal supercharging" by Williams et al as the degree of unfolding was found to increase with the interface temperature and applied HV.[70] The measurement results of ubiquitin in 100 mM AB are shown in Figures 3.1b and 3.2. The mass spectra taken at different flow rates and the recorded spray current were used to construct the heatmap as shown in Figure 3.1b. The trace of the selected ion signal, the average charge state (Figure 3.2a), and the selected mass spectra (Figure 3.2b) clearly show a higher charge state at a larger flow rate when operated under a standard operation at 200 °C ion inlet temperature. A reduced denaturation effect was observed when the flow rate was decreased to ~3 nL/min (ii in Figure 3.2a). An explanation for such observation is that the droplet generated at a lower flow rate is smaller and dissolve faster before they entered the heated inlet tube. In another word, the "denaturation" only became efficient by heating the large AB-containing droplet. The effect of heating on the change of charge state was further evaluated by operating the nanoESI at two flow rates at different inlet tube temperatures (see average charge state in Figure 3.2 and mass spectra in Figure 3.3). Figure 3.4 shows the reduced unfolding effect observed at a much lower inlet temperature of 35 °C, supporting the hypothesis that the shift of CSD was due to the heating of the AB droplet. A similar result was also obtained using cytochrome c (Figure 3.5).

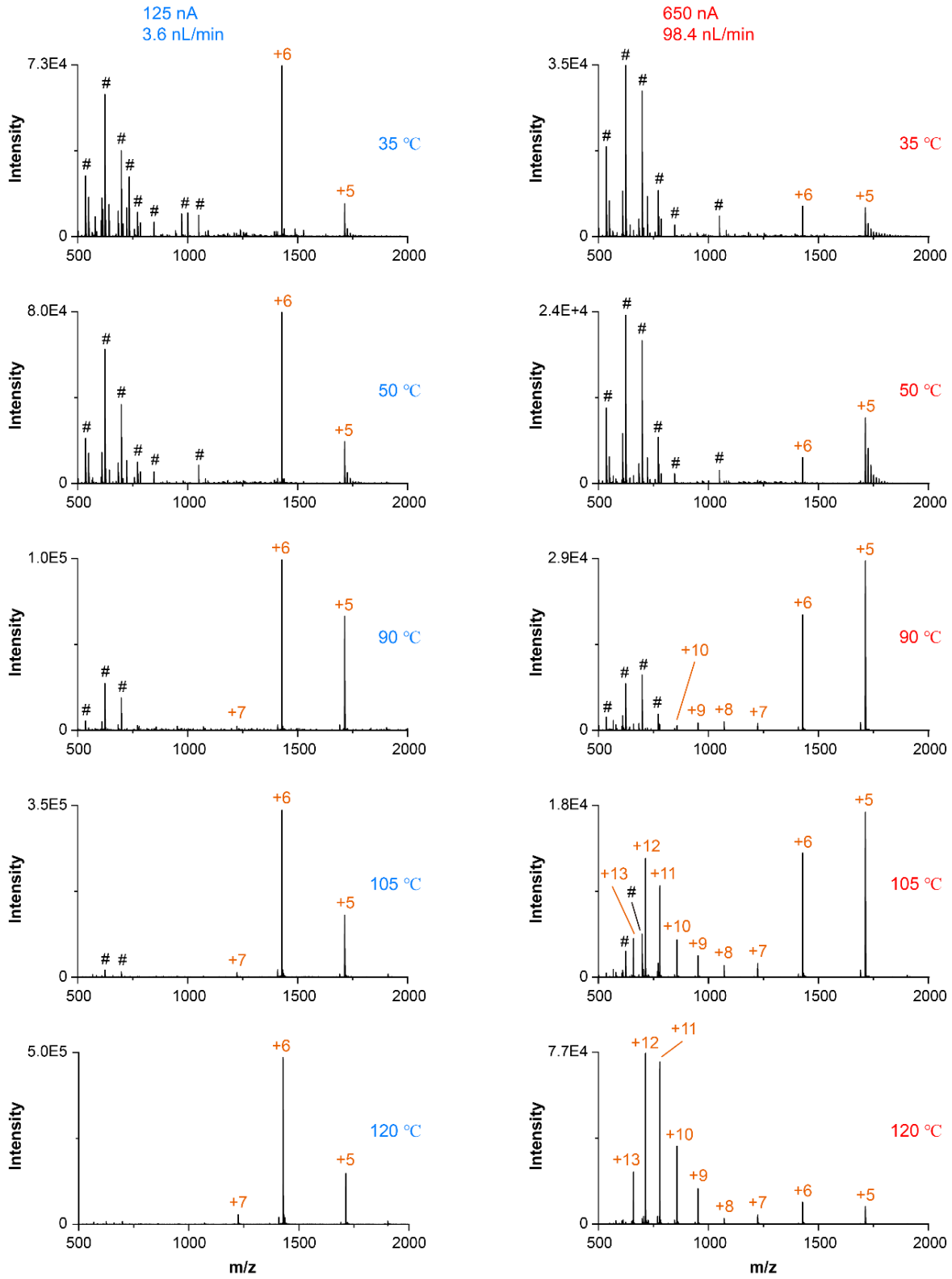

Figure 3.3. Mass spectra of ubiquitin in 100 mM ammonium bicarbonate acquired at different temperatures (35 °C ~ 120 °C) and different spray currents and flow rates. Left column: 125 nA, 3.6 nL/min. Right column: 650 nA, 98.4 nL/min. # denotes the background peak.

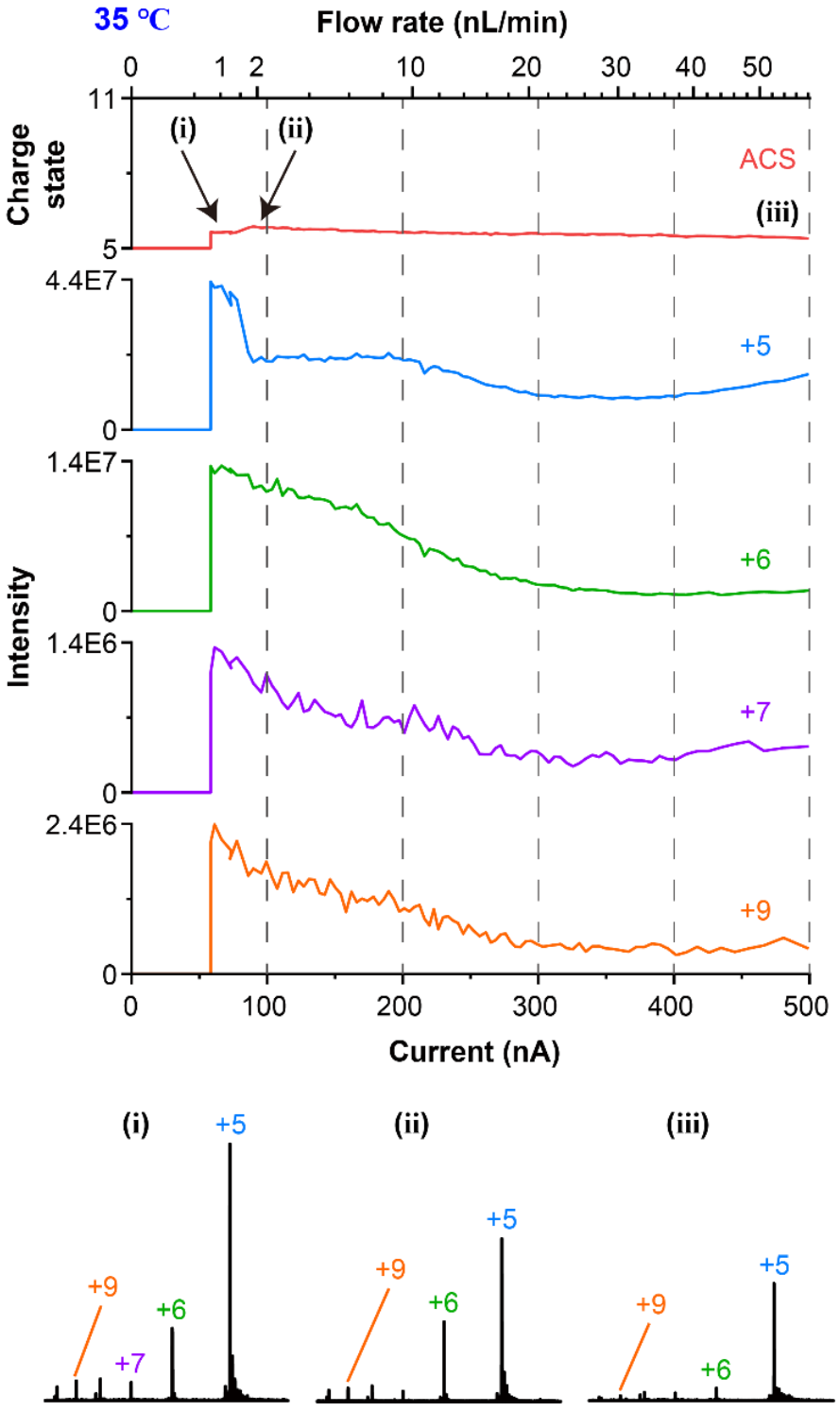

Figure 3.4. The charge state and ion signal response of ubiquitin in 100 mM ammonium bicarbonate to the flow rate acquired at 35 °C ion inlet temperature.

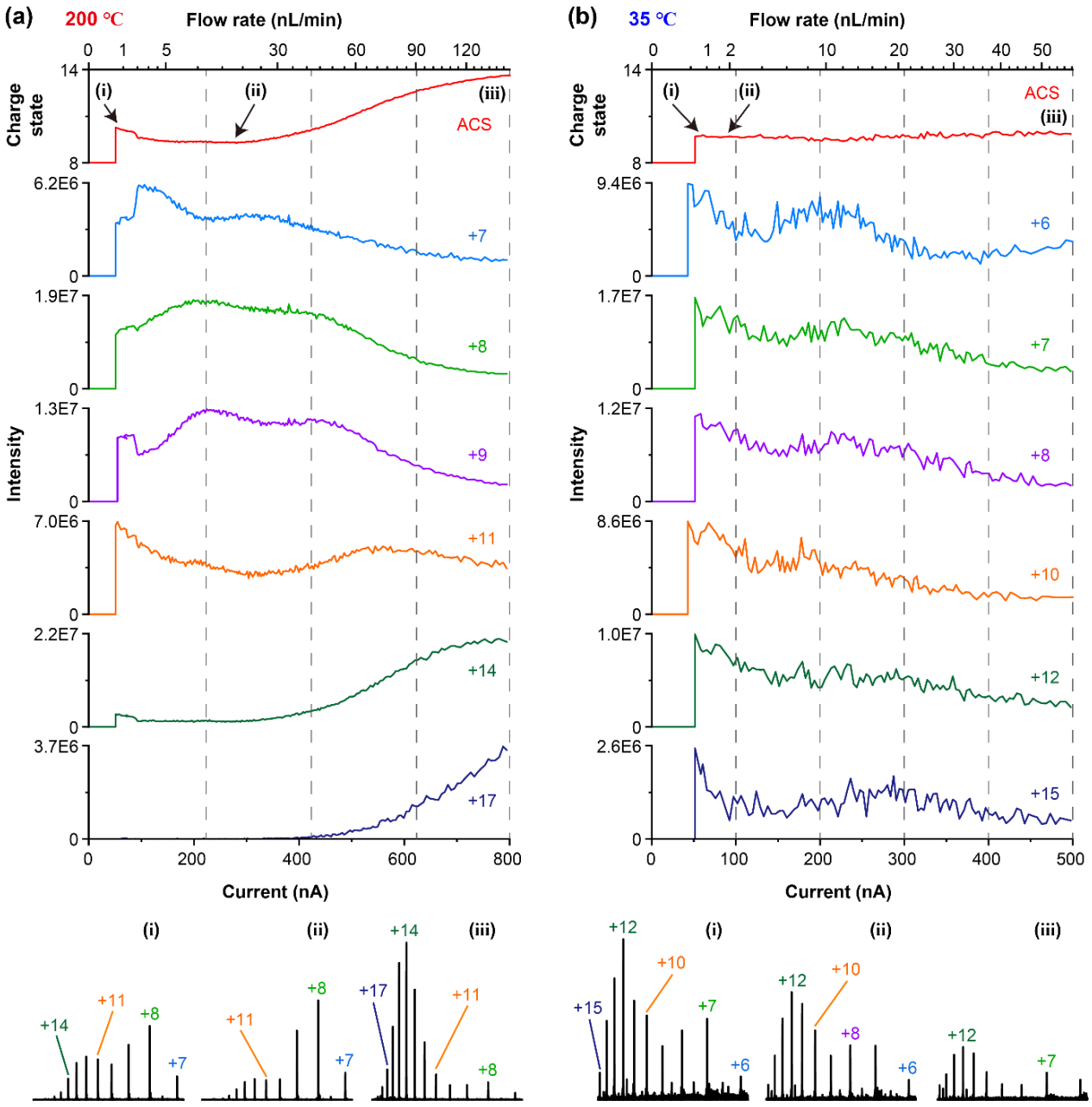

Figure 3.5. The flow rate response for the detection of cytochrome c in 100 mM ammonium bicarbonate.
a) Average charge state (ACS) and the ion intensities for selected charge states versus spray current and flow rate acquired at 200 °C ion inlet temperature. (i)-(iii) show the respective mass spectra taken at different flow rates. At the high inlet temperature, the ACS shows an uptrend for flow rate greater than ~30 nL/min, generating highly charged species due to the heating of AB-containing droplets.
b) Same measurement for ion inlet temperature of 35 °C. Unlike ubiquitin, the highly charged species still appear in the mass spectra. The ACS is relatively constant with the change in flow rate.
(i)-(iii) show the mass spectra acquired at different flow rates.

At a high flow rate of ~98 nL/min, a drastic increase of charge states (i.e. folding condition) took place at 100~120 °C. As expected, the heating effect was less pronounced when operated at a low flow rate operation of 3.6 nL/min. This observation was consistent with another report that found a reduced unfolding effect when using a submicron nanoESI capillary.[71] However, here, the key parameter was not the i.d. but the flow rate of the nanospray. Our result suggested that the role of applied voltage in the "electrothermal supercharging" with AB solution was on the instantaneous flow rate and the size of the initial charged droplet. Unlike AB, the evaluation of ubiquitin and cytochrome c in ammonium acetate solution shows a much smaller dependency on flow rate at 200 °C ion inlet tube temperature (Figure 3.6).

The bicarbonate anion was thought to have a destabilizing effect that enhanced the denaturation induced by the rapid heating.[70] Recently, the bubble formation in AB solution when heated was also proposed as a possible cause for the protein unfolding.[72] Further work will be performed to evaluate these two hypotheses. Although the reduced denaturation at a low flow rate was expected, a fine scan of the flow rate also revealed a sudden jump in ion signal (for +7 and +8 in Figure 3.5 and +5 in Figure 3.4) and the average charge state at the extremely low flow rate before the collapse of the Taylor cone. The phenomenon was not fully understood yet, but it was reproducibly observed by finely reducing the flow rate. In that flow rate range, the Taylor cone was the sharpest, i.e. the electrical field and the spray current density at its tip were the greatest. A local heating effect might be triggered at the tip of the Taylor cone which increases the average charge state and the ion intensity.

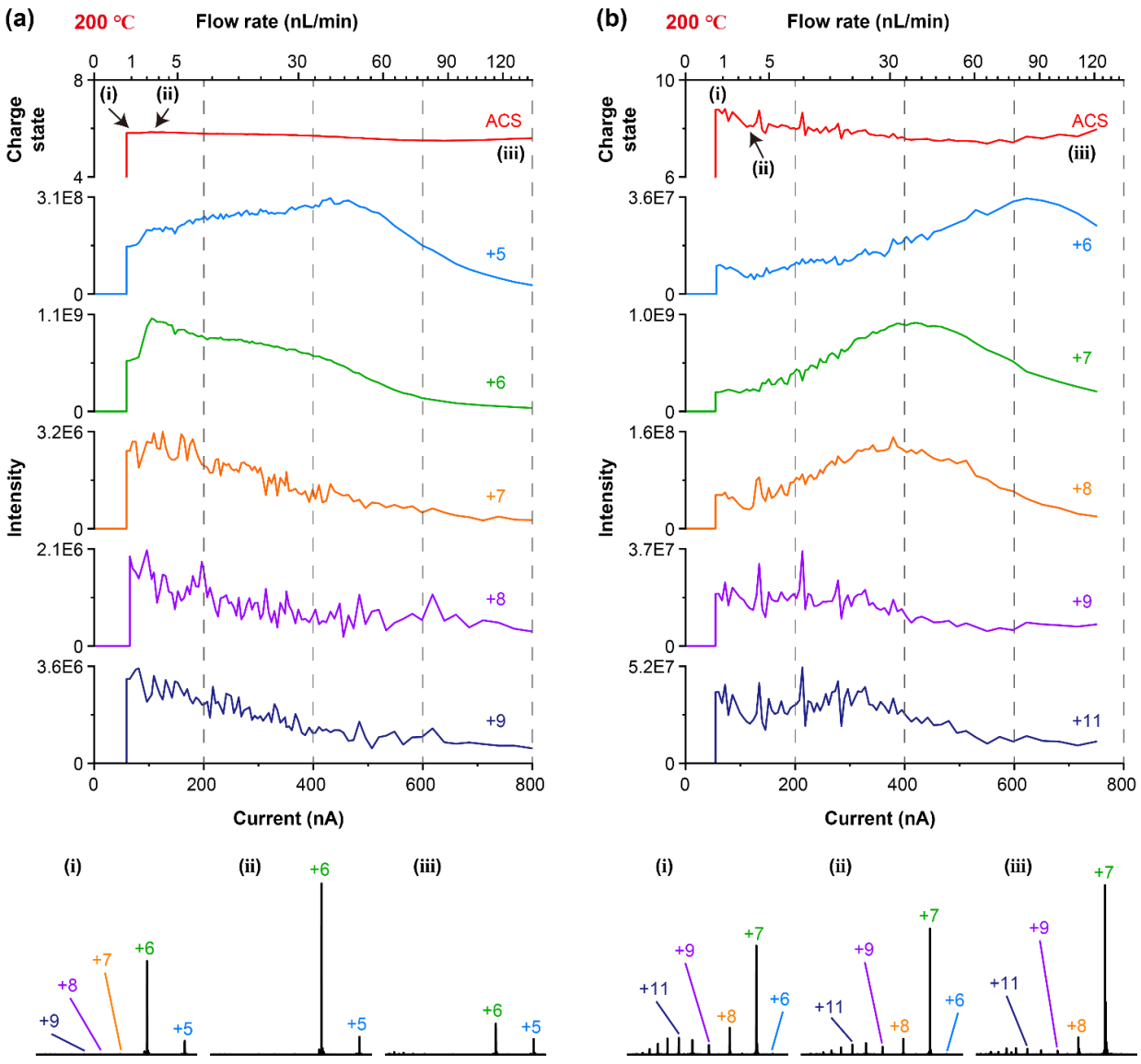

Figure 3.6. The detection of ubiquitin (a) and cytochrome *c* (b) in 100 mM ammonium acetate. Graphs show the changes in average charge states (ACS) and the ion intensities for selected charge states with the flow rate. (i) – (iii) show the respective mass spectra taken at the different flow rates.

Analyte mixture

Ion suppression affects the quantitative performance of ESI for analyte mixture, and one of the causes is the partition of analytes based on their relative surface activities.[73] For example, in Figure 3.7, the preferential ionization of the relatively surface-active peptide (gramicidin S) suppressed the detection of other hydrophilic peptides (bradykinin and angiotensin I) in the mixture during the high-flow operation in the pulsation mode. The ion suppression was nearly absent when the nanoflow was established in the cone-jet mode, but their ion intensity signals still exhibit a flow rate dependency.

For example, in Figure 3.7, the preferential ionization of the relatively surface-active peptide (gramicidin S) suppressed the detection of other hydrophilic peptides (bradykinin and angiotensin I) in the mixture during the high-flow operation in the pulsation mode. The ion suppression was nearly absent when the nanoflow was established in the cone-jet mode, but their ion intensity signals still exhibit a flow rate dependency.

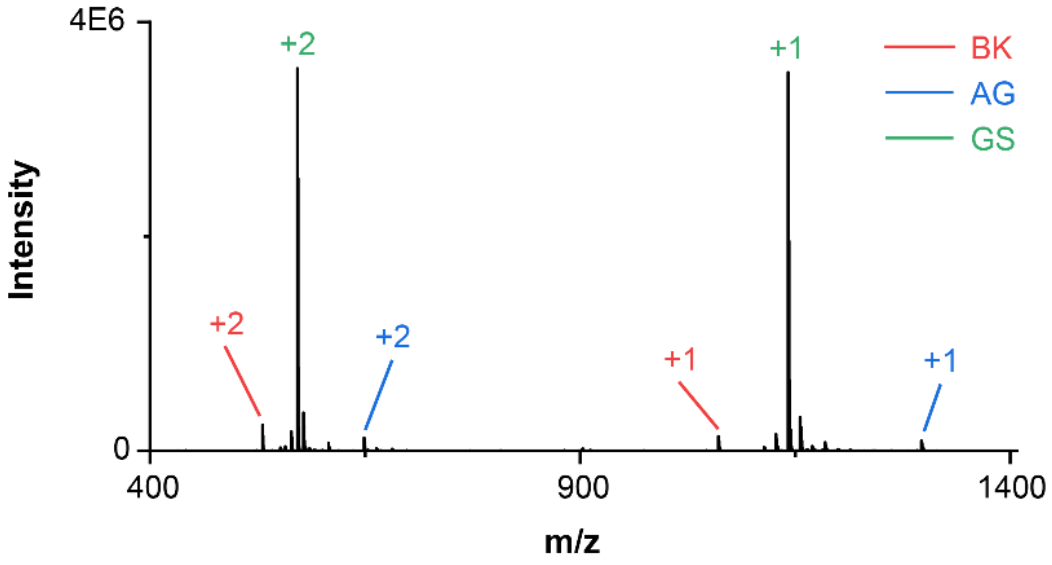

Figure 3.7. The ESI-MS for an equimolar mixture of bradykinin (BK), Angiotensin I (AG), and Gramicidin S (GS), each of 5 μM in 100 mM ammonium acetate acquired at a high-flow rate operation in the pulsation mode of the electrospray. The flow rate here is greater than 200 nL/min. The preferential ionization of the relatively surface-active cyclic peptide (gramicidin S) suppresses the detection of BK and AG. A similar ion suppression result was also obtained using standard micro-flow electrospray.

Figure 3.8a shows that the highest ion intensity for each analyte did not coincide at the same flow rate. A continuous flow rate scan located a flow rate at ~7 nL/min that yields approximately equal ion intensities for all analytes in the quantitative analysis of the equimolar peptide mixture. The measurement of cytochrome c, ubiquitin, and bradykinin mixture in Figure 3.8b also shows that each analyte exhibited its own ion signal responses and the maxima were located at different nanoflow rates. Nevertheless, the ionization efficiency, if defined as ion signal divided by flow rate was still the highest at the lowest possible flow rate (Figure 3.9). It is also intriguing to note that the trends for each analyte in the mixture closely resembled the trend when the analytes were measured individually (compare the cytochrome c, ubiquitin, and bradykinin in the equimolar mixture shown in Figure 3.8b with their individual measurement in Figure 3.9). The finding points to the possibility of using nanoflow rate as an axis for the multidimensional analysis of analyte mixture.

Here, the arbitrary flow rate of the same emitter could be tuned instantly within ~0.5~100 nL/min window. One full scan of flow rate from 0~100 nL/min usually took less than one minute to complete, consuming less than 50 nL per scan. Thus, a quick flow rate scan before the routine measurement was feasible even for samples with limited volume. As for the micropipette tip used in this study, the typical loading volume was 1~3 μL, but by adjusting the position of the Pt electrode, the nanoESI could be performed with sample amounts down to 200 nL. For even smaller volumes or pro-long measurements, narrower tips such as those of 20~100 μm i.d. could be used to prevent solvent evaporation. The same working principle and the scaling law for spray current should apply to those capillaries as long as the electrospray's jet diameter is much smaller than the inner diameter.

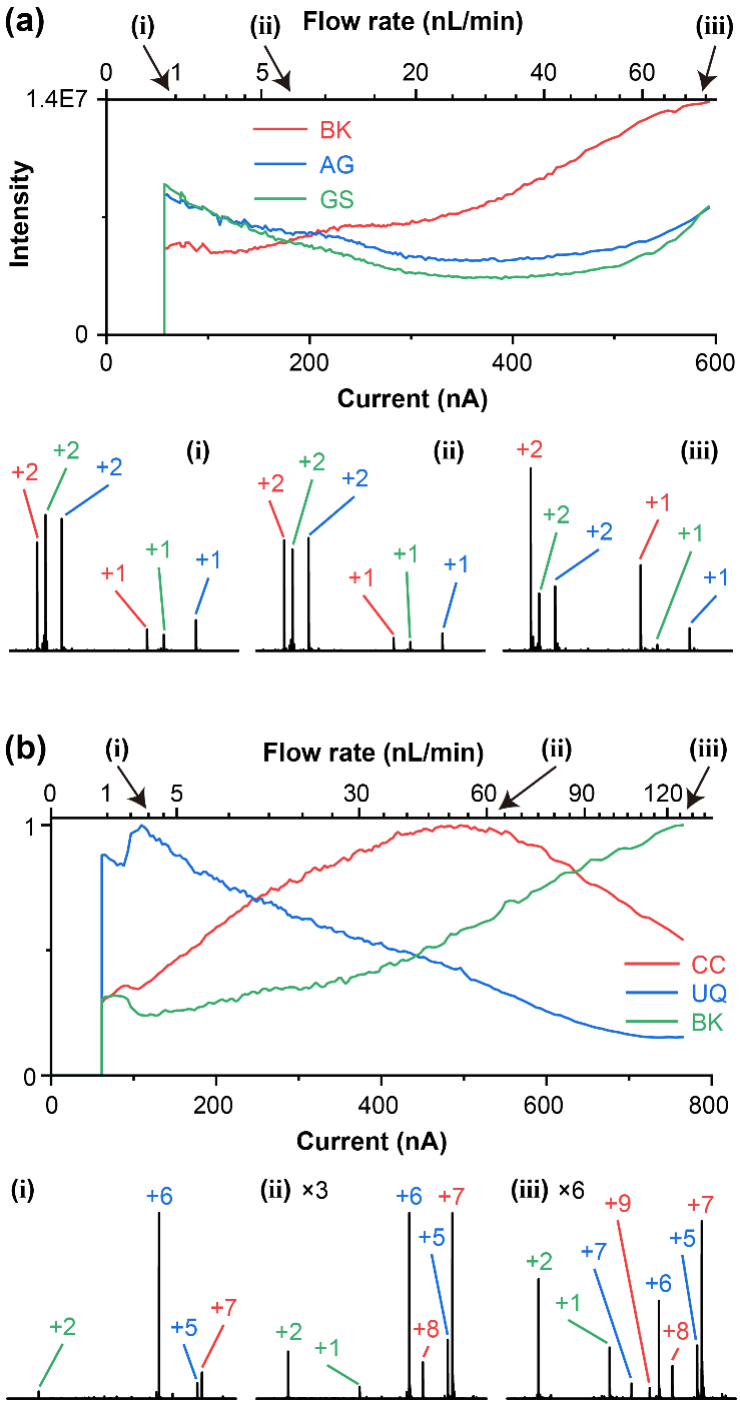

Figure 3.8. Detection of analyte mixtures. **a)** Ion signals versus flow rate for an equimolar mixture of bradykinin (BK), angiotensin I (AG), and gramicidin S (GS), each of 5 μM in 100 mM ammonium acetate aqueous solution. (i)-(iii) are the mass spectra acquired at different flow rates. A flow rate at ~7 nL/min (ii) produces approximately the same ion intensity for all peptides. **b)** Ion signals versus flow rate for the equimolar mixture of proteins and a peptide in 100 mM AA, each of 5 μM. CC: cytochrome *c*, UQ: ubiquitin, BK: bradykinin. (i)-(iii) are the mass spectra acquired at different flow rates. The peak height in (ii) & (iii) are magnified 3× and 6× for comparison with (i).

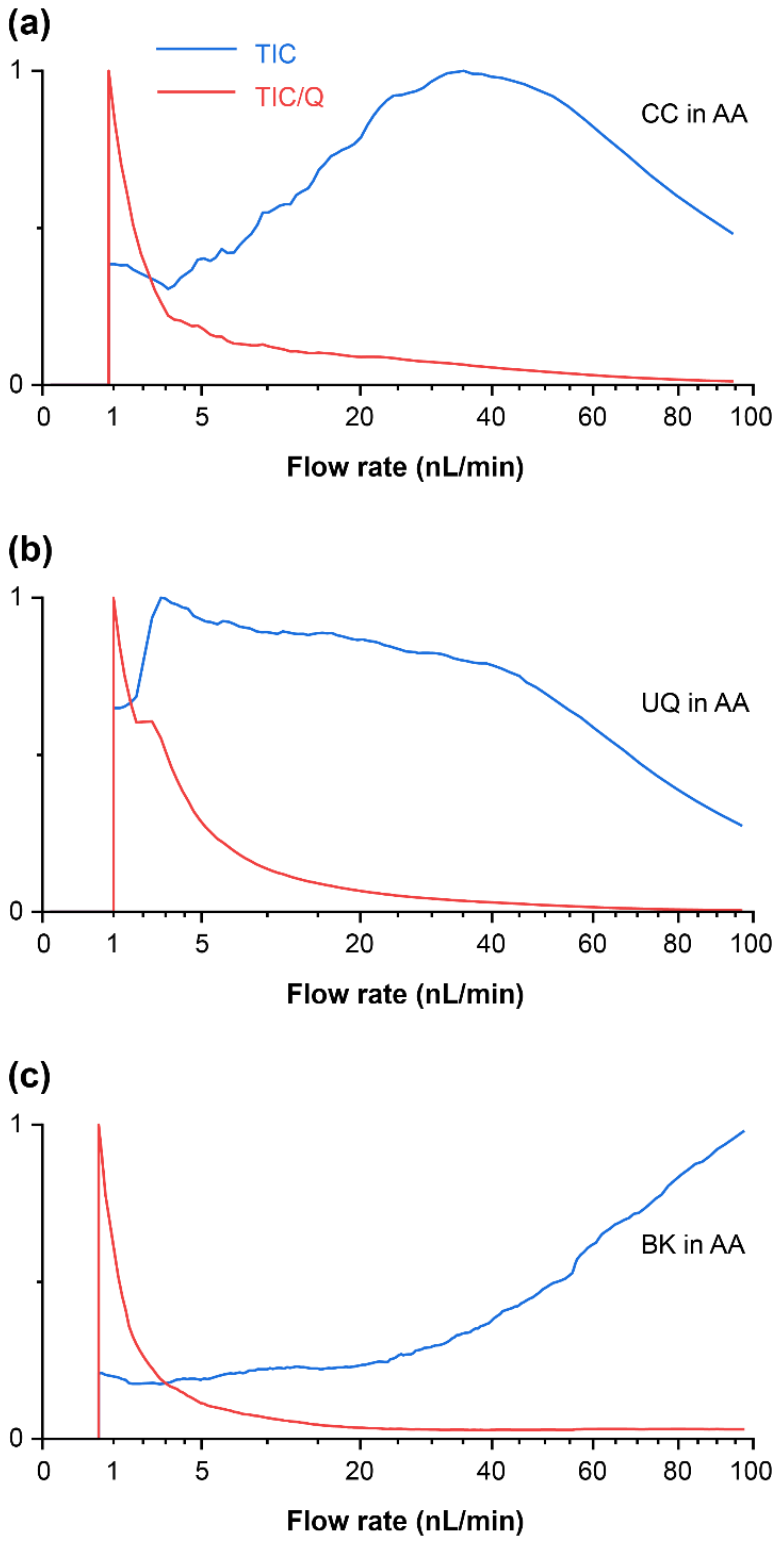

Figure 3.9. Total ion count (TIC, blue line) originated from the analytes for three separate measurements for cytochrome *c* (a), ubiquitin (b), and bradykinin (c) in 100 mM ammonium acetate under different flow rates. Red line shows the normalized value for TIC/*Q*. *Q*: flow rate.

Nonvolatile salts

The presence of nonvolatile salts in the electrospray solution causes the adduction of salt-related ions or neutral to the analyte which results in the spreading of ion peak and reduction in peak height. Such an effect was more pronounced in the microflow regime due to large initial droplets. Even in the nanoflow regime, the degree of peak spreading was also found to be flow rate dependent. Figure 3.10 shows the effect of adding 1 mM NaCl to the 100 mM ammonium acetate solution for the detection of cytochrome *c*.

As a comparison of droplet size, at the low flow rate of 2 nL/min at 100 nA, the radius calculated using Eq 2 is 30 nm. At the high flow rate of 35 nL/min at 400 nA, it is 76 nm. The peak spreading for the charge state +7 was due to the incorporation of Na and NaCl which increased with the flow rate, hence the size of the initial droplet. Interestingly, the addition of NaCl also caused the appearance of higher charge state species (e.g. +11) which were relatively free of salt adducts. Some degree of denaturation should have taken place during the ionization process. For the lower charge state species, they were generally thought to be formed via the charge residue model. In a recently proposed chain ejection model, proteins were found to snake out from the droplet in the simulation.[74] That may provide an ionization route to the highly charged species from the pH-neutral droplet. Further work is still needed for verification.

A low flow rate operation was found to be crucial for the detection of proteins directly from the biological buffer such as undiluted phosphate-buffered saline (PBS). PBS contains a high concentration of nonvolatile salt (136.9 mM NaCl, 8.1 mM Na_2HPO_4, 2.7 mM KCl, and 1.5 mM KH_2PO_4), and is known to be an unfriendly buffer even to nanoESI. The scanning of HV and spray current in Figure 3.11 shows an optimum flow rate at ~1 nL/min for the detection of ubiquitin from PBS. A comparison using a commercial nanoESI capillary with an inner diameter of 1 μm under atmospheric pressure is shown in Figure 3.12.

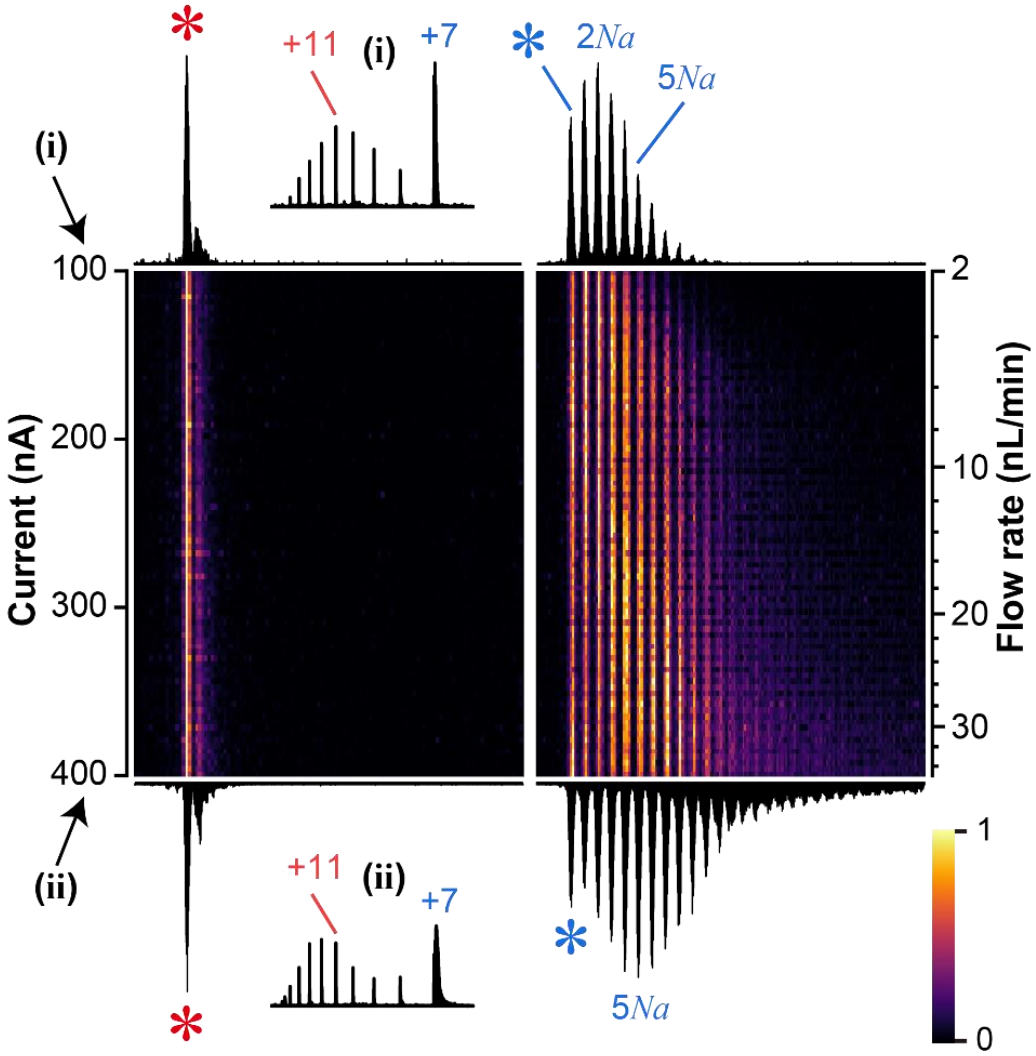

Figure 3.10. Effect of flow rate for the detection of cytochrome *c* in 100 mM ammonium acetate containing 1 mM NaCl. Heatmaps indicate the normalized intensities acquired at each spray current (or flow rate) for two mass ranges (horizontal axis, left: *m/z* 1105-1165, right: *m/z* 1740-1830). (i)&(ii) are the mass spectra taken at 35 and 2 nL/min. The asterisks depict the protonated peaks for charge states +11 and +7.

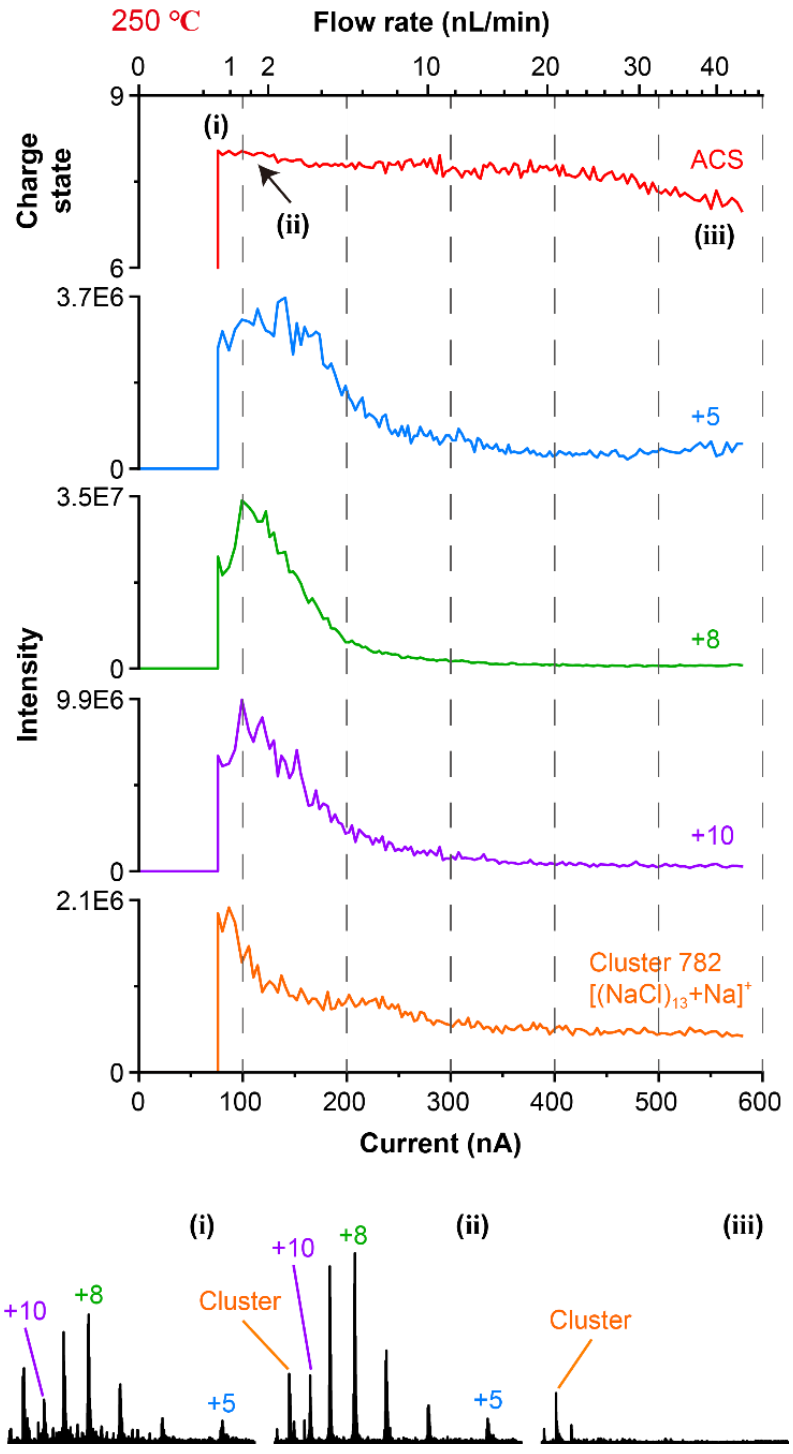

Figure 3.11. The detection of ubiquitin from undiluted Phosphate buffered saline (PBS). Graphs show the changes in the average charge state and the ion intensities of the selected charge with flow rate. The mass spectra taken at different flow rates are depicted by (i)-(iii). A clean mass spectrum is acquired at an optimum flow rate of ~1 nL/min. The composition of PBS is 136.9 mM NaCl, 8.1 mM Na_2HPO_4, 2.7 mM KCl and 1.5 mM KH_2PO_4.

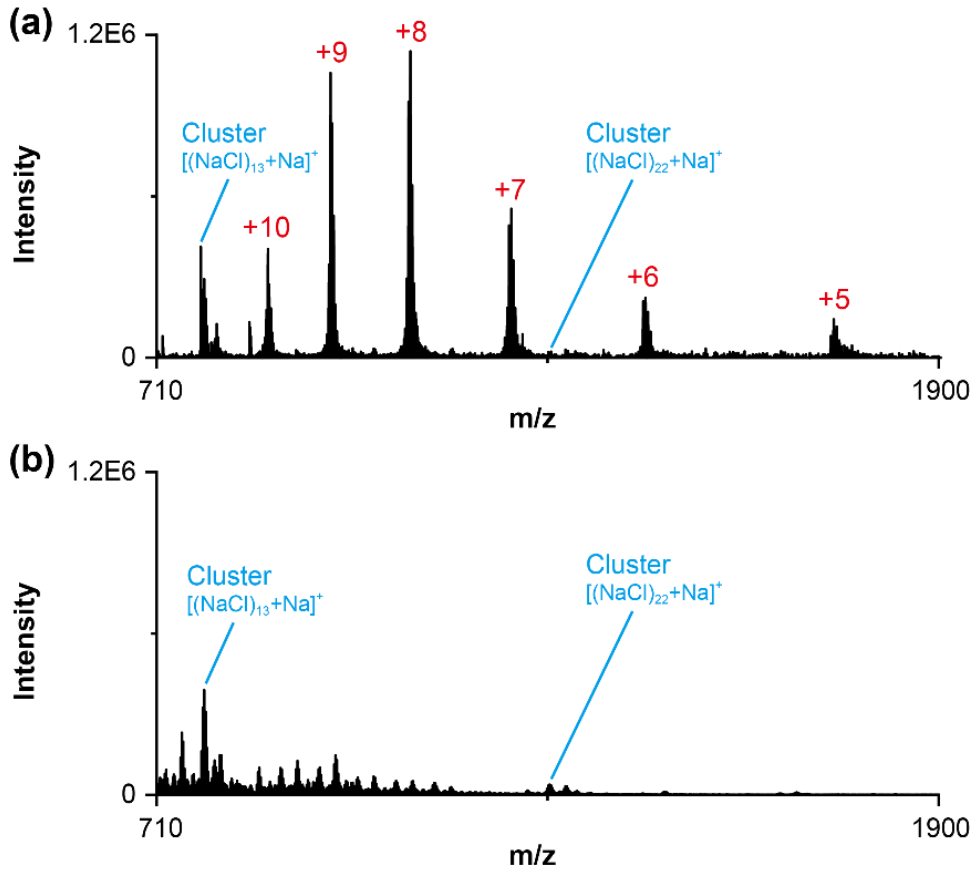

Figure 3.12. Detection of 1×10^{-5} M ubiquitin from undiluted phosphate-buffered saline (PBS). **a)** Mass spectrum obtained by the present high-pressure nanoESI from micropipette tip at flow rate 1.2 nL/min **b)** Mass spectrum obtained by a commercial capillary nanoESI (tip i.d.; 1 μm) under atmospheric pressure.

Ion signals from NaCl cluster $[(NaCl)_n+Na]^+$ with a magic number $n = 13$ were present in the mass spectra acquired by the commercial nanoESI and the present method. However, the detection of protein ions was difficult from the commercial nanoESI. Possible causes may be the difficulty to sustain a stable cone-jet mode under atmospheric pressure and the adsorption of the analyte on the inner surface of the glass capillary. The measurement of ubiquitin in 1 M Tris-HCl (Figure 3.13) also shows an optimum point at ~1 nL/min.

The large i.d. of the emitter used in this study enabled the direct ionization of the "dirty sample" without the clogging problem. Figure 3.14 shows the direct measurement of bradykinin in the undiluted human urine. The electrical conductivity of the urine was ~1.3 S/m. The optimum flow rate for bradykinin was in the range of 4~6 nL/min. The intensity of creatinine, (one of the major contents in urine) at that point was lower as compared to the higher flow rate region but was not at the minimum. The plot of bradykinin intensity acquired at 6 nL/min versus its concentration shows good linearity for a concentration range of 5×10^{-8} to 5×10^{-5} M without the use of internal standards. When the bradykinin was dissolved in the clean aqueous solution containing only ammonium acetate or acetic acid, the sensitivity of detection was approximately 10 times higher.

As a comparison, Figure 3.15 shows the selected mass spectrum for 5×10^{-5} M acquired using a commercial nanoESI (tip i.d. 1 μm). It is noted that the clogging took place during several unsuccessful trials with the fine capillary nanoESI but was complete absence with the micropipette tip emitter. The bradykinin was detected from the raw urine samples using both methods but the intensity ratio of peptide to creatine was higher for the present method. The overall ion intensity for the commercial nanoESI was higher as it was taken using the standard ion inlet tube of 0.55 mm i.d., whereas for high-pressure nanoESI in this study, a custom inlet tube of 0.25 mm i.d was used and a higher ion transmission loss was anticipated. Future improvement in the ion transmission was possible by using a funnel-type interface,[55] or by increasing the gas throughput of the MS instrument with an external booster pump.[75]

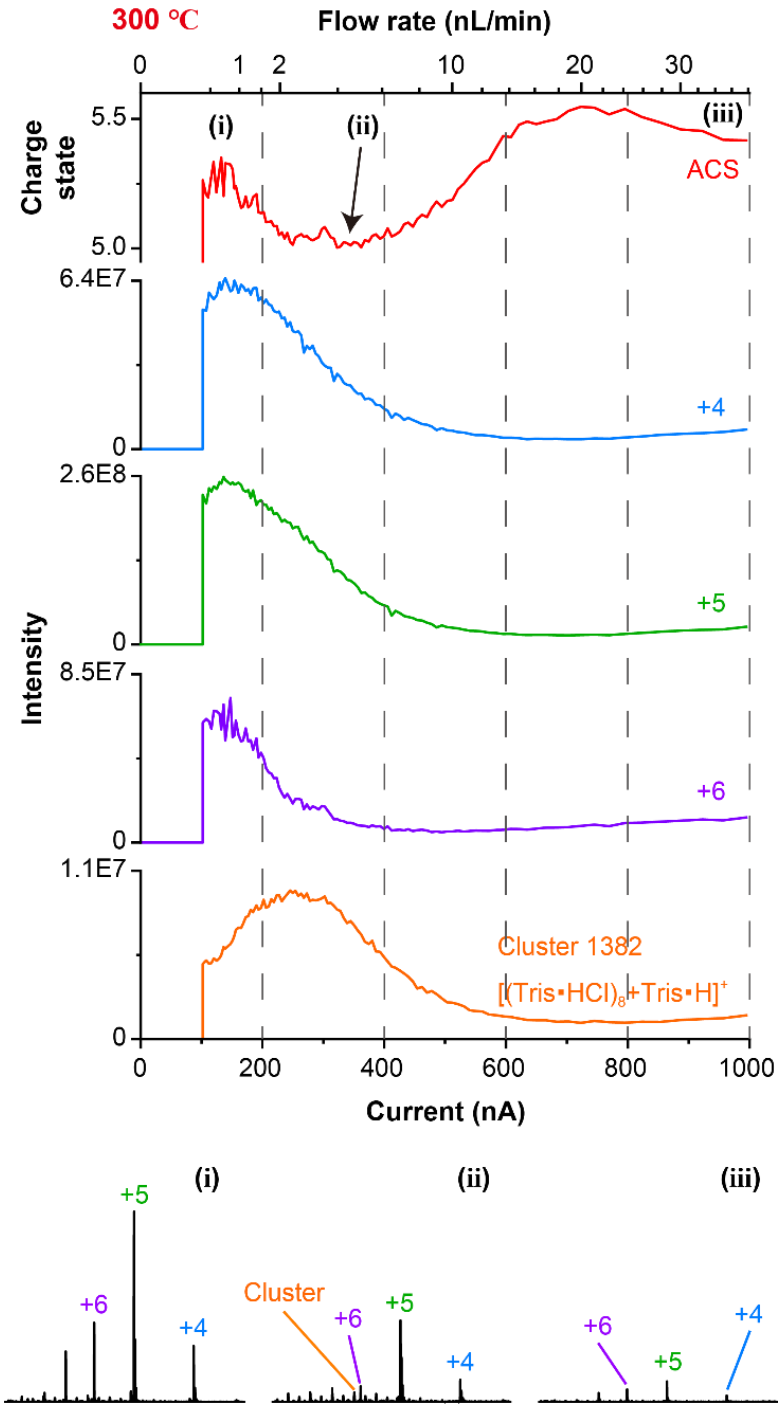

Figure 3.13. The detection of ubiquitin from 1 M Tris-HCl buffer. Graphs show the changes in the average charge state and the ion intensities of the selected charge with flow rate. (i)-(iii) are the mass spectra taken at different flow rates.

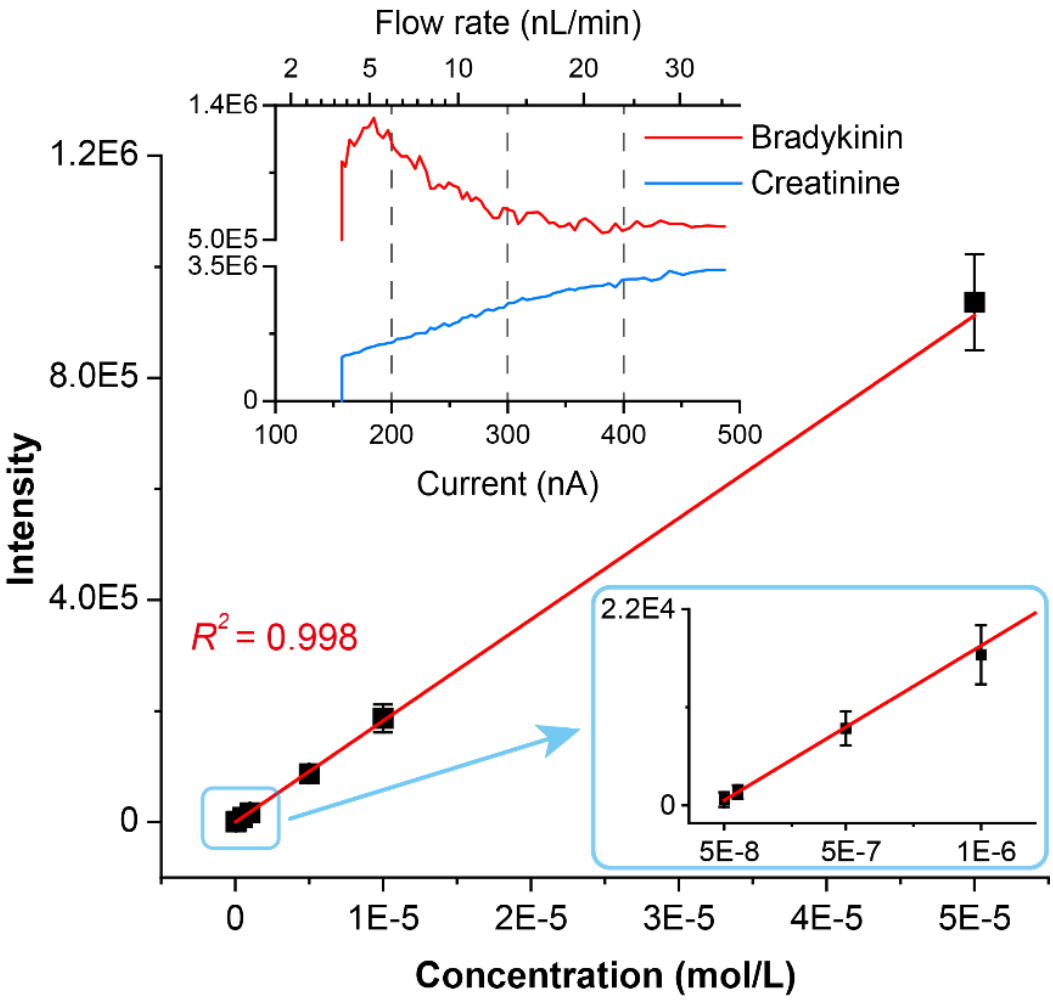

Figure 3.14. Detection of bradykinin of varying concentrations from the undiluted human urine (electrical conductivity ~ 1.3 S/m). The upper inset shows the change of ion signal of bradykinin (sum of all species of charge state 2+) and the protonated creatinine with the flow rate.

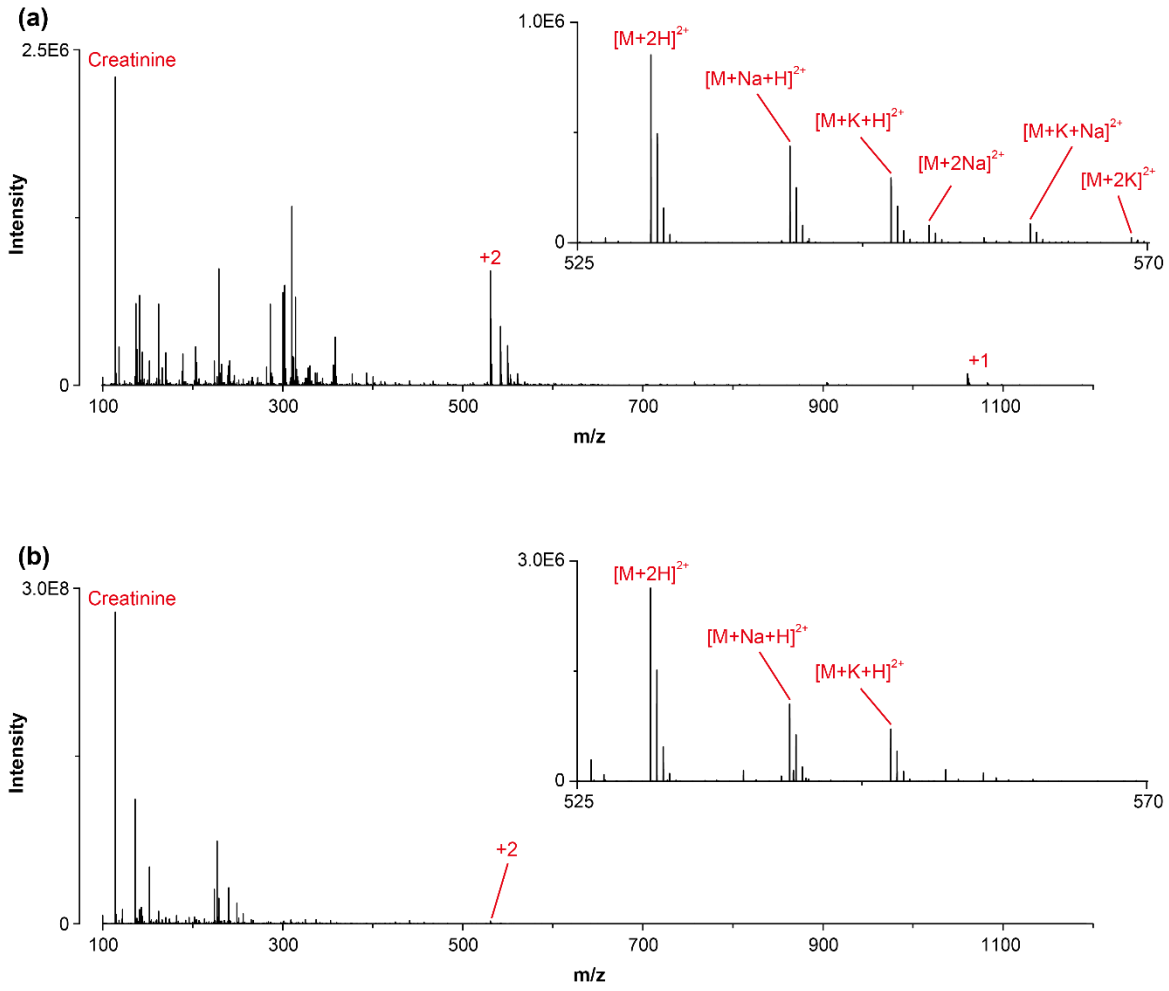

Figure 3.15. Detection of bradykinin (5×10^{-5} M) in undiluted human urine using **a)** present high-pressure nanoESI at 5 nL/min, and **b)** commercial capillary nanoESI (tip i.d.; 1 μm). Insets show the magnified mass spectra. The overall ion intensity for commercial nanoESI was higher as it was taken using the standard ion inlet tube of 0.55 mm i.d. whereas, for high-pressure nanoESI in this study, a custom-made ion inlet tube of 0.25 mm i.d. is used.

Controlled Oxidation

Protein oxidation can be induced by an electrochemical reaction and the corona discharge that is initiated when operating ESI at elevated voltage.[76,77] By using a visible corona discharge and oxygen as the reactive gas, radical-induced oxidative modification of proteins has also been exploited for protein structural analysis.[78] Controlled oxidation using UV lasers to produce hydroxyl radicals from the solution containing protein and hydrogen peroxide also existed.[79,80] Here, we found that by using a highly conductive solution such as 1 M ammonium formate (K = 8.7 S/m), oxidative modification of the analyte could be selectively initiated at a low flow rate of < 5 nL/min. The degree of oxygen incorporation was adjustable by controlling the nanoflow rate (see Figures 3.16a for cytochrome *c* and Figures 3.17 for ubiquitin). Another measurement in Figure 3.16b shows the controlled oxidation of phosphatidylcholine (PC 18:1/18:1).

Two major oxidative species were detected, and the in-source CID revealed that oxygen was incorporated into the location of the carbon-carbon double bonds (Figure 3.18). This result was similar to an earlier report by Yan *et al*. on the epoxidation of PC by ESI using a high concentration of hydrochloric acid in acetonitrile solutions.[81] In their case, the H^+ and Cl^- ions were found to be crucial for the *in-situ* formation of the reactive hypochlorite anion. In our case, the low flow rate and the high electrical conductivity appeared to be the key factors. Besides ammonium formate, the same phenomenon was also observed using ammonium acetate solution.

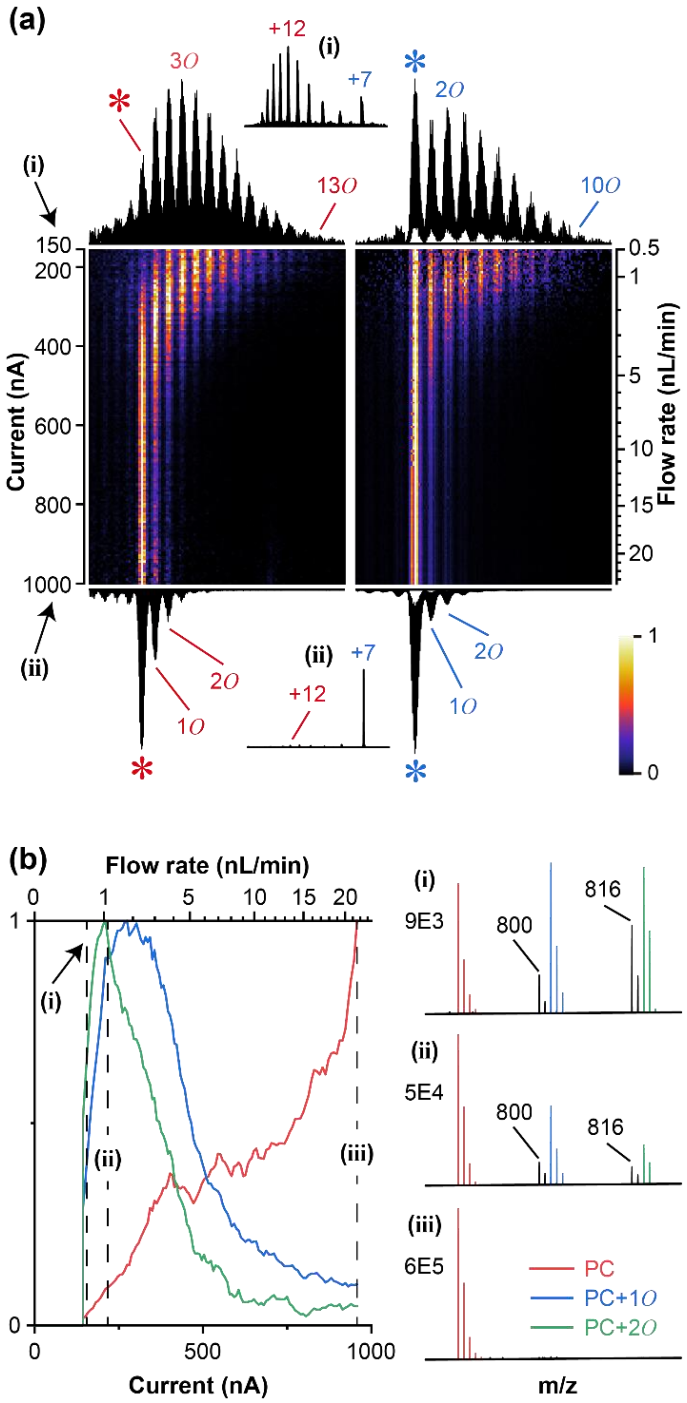

Figure 3.16 a) Flow rate-dependent oxidative modification of cytochrome *c* in 1 M ammonium formate solution (AF). Heatmaps show the normalized intensities at each flow rate for two mass ranges (horizontal axis, left: *m/z* 1015-1040, right: *m/z* 1740-1775). Asterisks depict the protonated peak without oxidation. The number of incorporated oxygen atoms is labeled as *nO*. **b)** The ion intensities of the oxidatively modified ions and the unmodified ion versus flow rate for 1 µM L-phosphatidylcholine, dioleoyl (PC 18:1/18:1) in AF. (i)-(iii) show the mass spectra acquired at the respective flow rates.

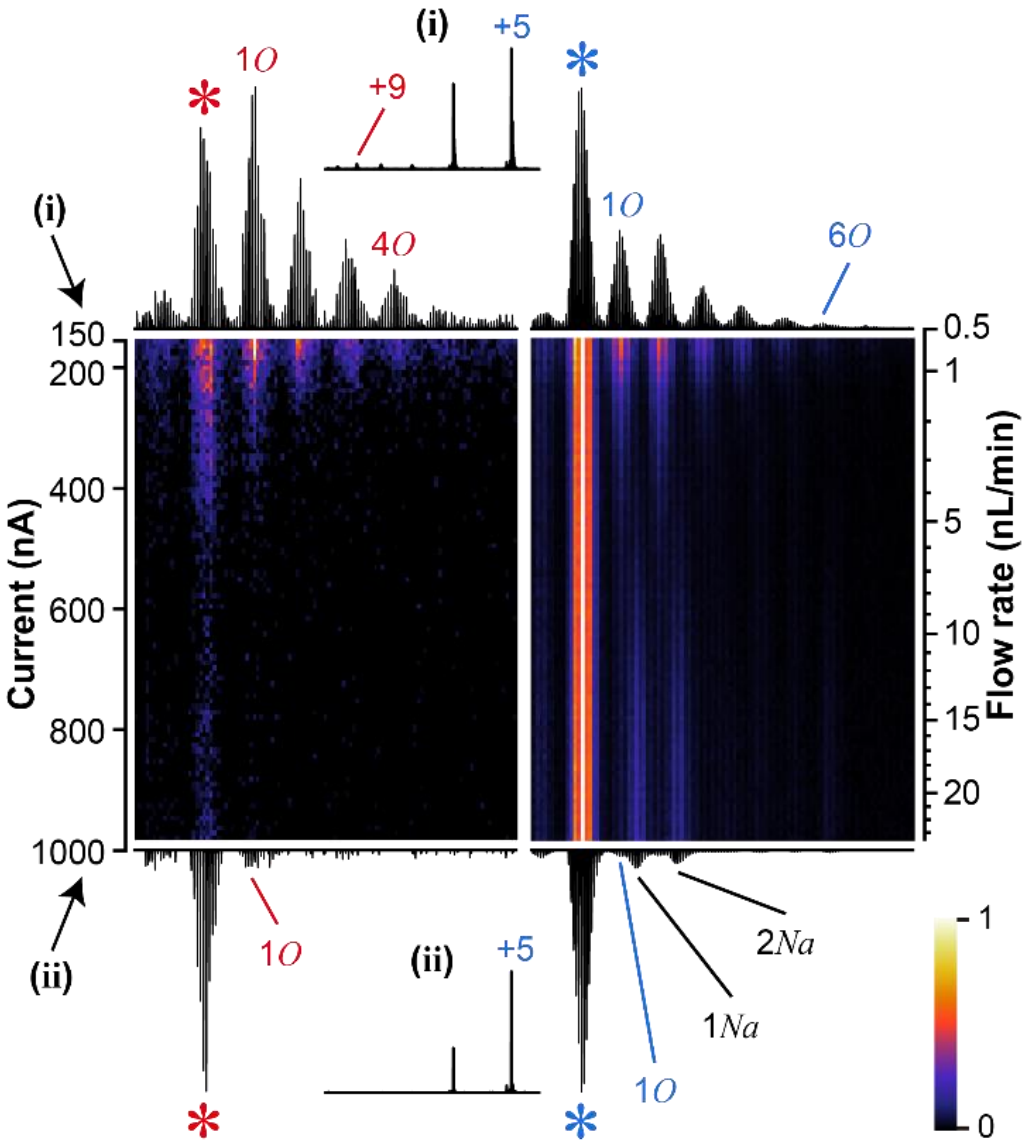

Figure 3.17. Flow rate dependent oxidative modification of ubiquitin in 1M ammonium formate. The heatmap shows the normalized intensities at each flow rate for the mass ranges (m/z 946-950 and m/z 1710-1740). Asterisks depict the protonated peak without oxidation. The number of incorporated oxygen atoms is labeled as *nO*.

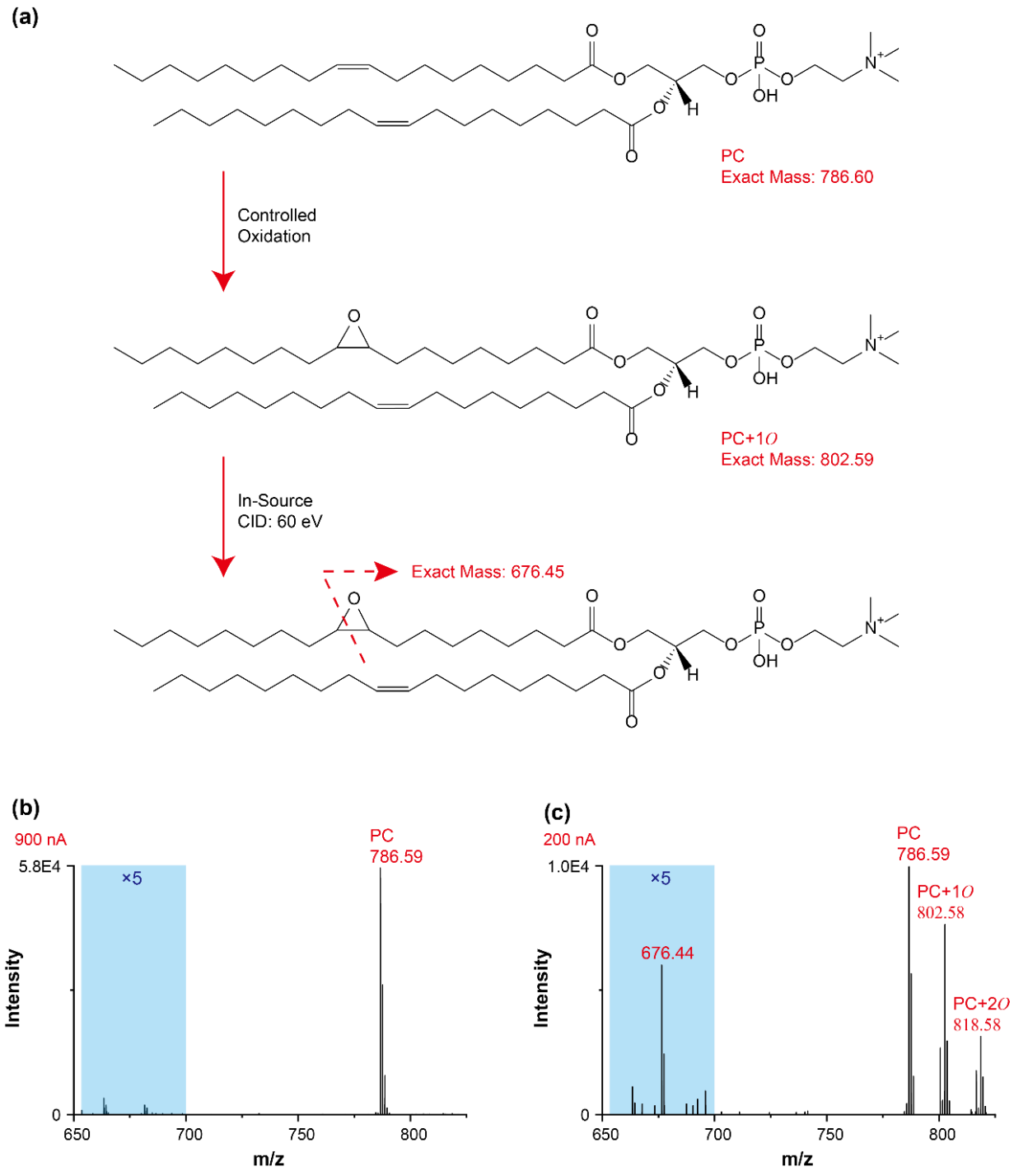

Figure 3.18. a) Controlled oxidative modification and the in-source CID of L-phosphatidylcholine, dioleoyl (PC 18:1/18:1). **b)** Mass spectrum of PC without oxidative modification (spray current: 900 nA). **c)** Mass spectrum of PC with oxidative modification (spray current: 200 nA).

The ion signal of the oxidation species responds instantaneously to the change in flow rate, i.e. the oxidation could be turned on and off in less than a second when the flow rate was switched from ~1 nL/min to ~10 nL/min. The electrode in this measurement was placed approximately 5 mm away from the emitter tip. The instant response of the oxidation ruled out the cause by the electrochemical reaction at the electrode/liquid interface because, at an nL/min flow rate, it would take several tens minutes to transport the oxidation products to the Taylor cone when turning ON and to deplete them when turned OFF. As for the possibility of corona discharge, we had not detected any glow and anomalies in the spray current associated with the partial breakdown of the operating gas. Changing the operating gas from air to SF_6 (a stronger insulating gas to prevent electrical discharge) and to pure nitrogen also showed the same oxidation effect (Figure 3.19).

It is also noted that the oxidation species were at their highest abundance at the lowest HV, thus, the commonly encountered corona discharge in the atmospheric pressure ESI was unlikely to be the cause. Nevertheless, electrical field-induced processes such as those in the early stage of plasma formation cannot be ruled out. At the lowest flow rate, the Taylor cone approached its ideal theoretical shape (Figure 3.20), and the electrical field at its apex was the highest. In the study of ion evaporation kinetics of Taylor cone, Gamero-Castaño and Fernández de la Mora used

$$E = \gamma^{1/2} K^{1/6} / (\varepsilon_o^{2/3} Q^{1/6}) \tag{4}$$

to estimate the largest electrical field on the Taylor cone.[40] Applying their equation to our experimental condition gives $E \approx$ 1.4 V/nm, a field that was large enough to induce ion evaporation. We hypothesized that the analytes at the sharpest end of the Taylor cone were subject to oxidation by the reactive oxygen species formed in the presence of strong electrical fields. One candidate for the reactive species was hydroxy radicals, a highly reactive oxidant that is known to exist in the atmospheric pressure plasma.[82] Identifying the reactive species and their formation mechanism is worth further investigation. In sum, the controlled oxidation phenomenon can be exploited for the on-demand oxidative labeling for analyte characterization. Since the aqueous buffer solution used here was compatible with the native ESI-MS, the oxidative labeling can be performed in line with the native protein analysis from the same emitter without the use of oxidative reagents such as H_2O_2 and UV activation.

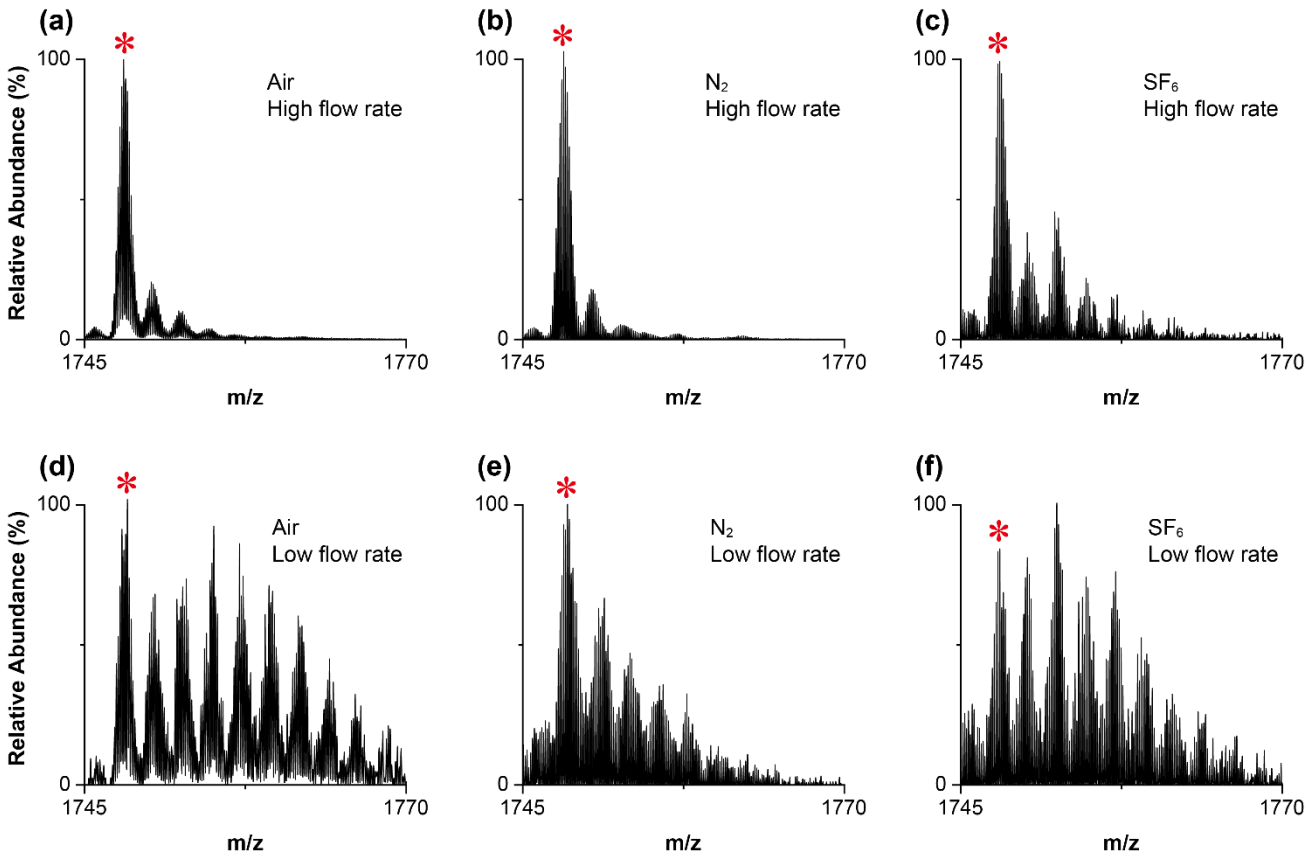

Figure 3.19. The magnified mass spectra for the charge state +7 of cytochrome *c* in 1 M ammonium formate solution acquired using different operating gases for the high-pressure nanoESI source.
Upper row: Acquired at a high solution flow rate of ~20 nL/min.
Lower row: Acquired at a low solution flow rate of ~1 nL/min

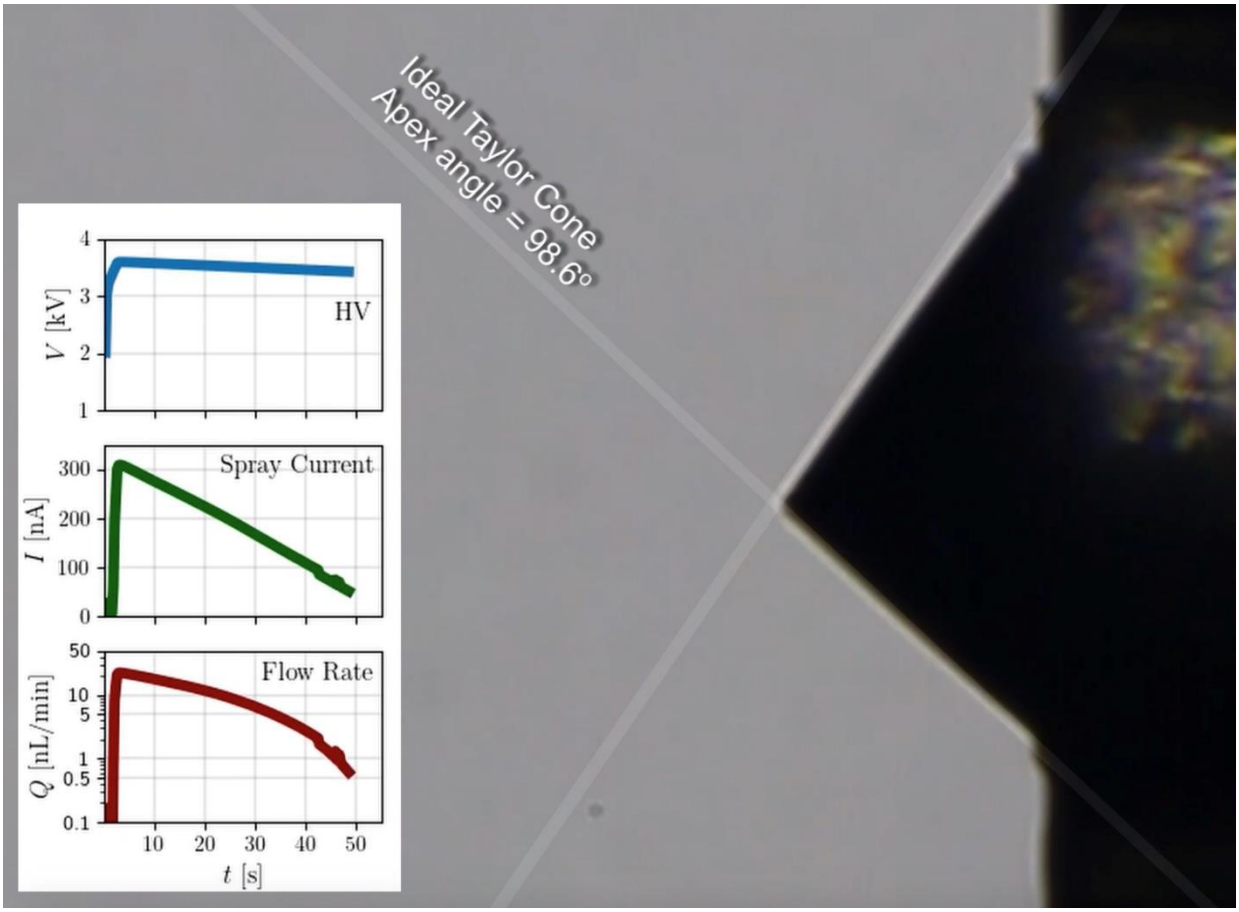

Figure 3.20. Photograph of the Taylor cone formed at the opening of the micropipette tip. The inner diameter of the micropipette tip is 0.4 mm. The graphs show simultaneous measurements of high voltage applied to the liquid (*V*), spray current (*I*) and the flow rate (*Q*) calculated using the scaling law. The image here depicts the condition near the minimum flow rate and the apex angle is close to the theoretical value of 98.6° for a static Taylor cone. The solution is 100 mM ammonium bicarbonate in water.

Implication for the ion response models

Here we discuss the ionization response with reference to the models developed by Tang & Kerbarle,[83]

and the Enke model.[84] For a two-electrolyte system consisting of analyte A and electrolyte B with concentrations C_{A} and C_{B}, the analyte current i_{A} in the Tang & Kerbarle's model is given as[83]

$$i_{\mathrm{A}} \propto \frac{k_{\mathrm{A}} C_{\mathrm{A}}}{(k_{\mathrm{A}} C_{\mathrm{A}} + k_{\mathrm{B}} C_{\mathrm{B}})} i_s \qquad (5)$$

, where k_{A} and k_{B} are the respective ion evaporation coefficients (also called sensitivity coefficients in later literature) and i_s is the spray current. Enke's model shares a similar form but it uses the equilibrium constants K_{A} and K_{B}, for the ion's preference for the surface or the interior phases. Only ions in the surface phase are eventually released into the gas phase and the ion signal s_A is assumed to be proportional to the "concentration of excess charge" $[q]$ as[84]

$$s_{\mathrm{A}} \propto \frac{K_{\mathrm{A}} C_{\mathrm{A}}}{(K_{\mathrm{A}} C_{\mathrm{A}} + K_{\mathrm{B}} C_{\mathrm{B}})} [q] \qquad (6)$$

The $[q]$ is proportional to the spray current divided by flow rate, i.e. $[q] \propto i_s/Q$. Both models correctly described the dependence of the analyte ion signal on its concentration and the ion suppression effects when there is a presence of surface-active compounds in the solution. But as the size of the initial droplet gets much smaller than 1 μm, which is the condition of nanoESI with flow rate <100 nL/min, the equilibrium partitioning based on surface activity may become less relevant. This can be seen from the reversal of ionization preference for the surface-active gramicidin S from microflow (Figure 3.7) to nanoflow (Figure 3.8a). The relatively hydrophilic peptides were detected with higher ion intensity, indicating that the source of selectivity had shifted from the surface activity to other parameters.

As for the relationship with flow rate, if we include the scaling law $i_s \propto \sqrt{Q}$ to Eq 5 and Eq 6, Tang & Kerbarle's model yields an ion response of $s_A \propto \sqrt{Q}$, i.e. ion signal increase with the flow rate. For Enke model, it is $s_A \propto \sqrt{1/Q}$, which appears to agree with the nanoESI situation where the ion signal increase with a reduction in flow rate. However, the result of this study showed that the ion response is not as straightforward. For example, the ubiquitin and bradykinin in ammonium acetate

solution (Figure 3.8b) exhibit opposite trends with the flow rate within the range of 3 to 120 nL/min, while cytochrome *c* attained a maximum point at 50 nL/min. Overall, the presence of stationary points (local maximum and/or minimum) suggest that a general description perhaps should consist of multiple terms of flow rates of different orders. Finally, the ion transmission and desolvation factors in their models may also be a function of flow rate because the size of the initial droplets should have a substantial influence on the desolvation efficiency and the transmission of ions to the MS vacuum.

Conclusions

In summary, an offline electrospray with a continuously varying flow rate in the nL/min regime had been developed to provide a more quantitative assessment of the nanoflow rate effect on the ionization response. The working principle based on the scaling law of spray current and flow rate is straightforward, and the technical requisites for scaling law to be valid: a large dimension ratio of emitter opening to the jet, operation in the cone-jet mode, and the absence of electrical discharge were met by operating the ion source in high-pressure. The dependence on flow rate for ion intensity, charge state distribution, peak spreading and oxidative modification shows that there is no universal optimum flow rate for all analytical purposes. A high throughput flow rate tuning within a flow rate window of several hundred pL/min to ~100 nL/min can thus be used to provide a full ionization response for the handling of analyte mixture, automatic searching for the flow rate best suited for each application, on-demand switching of flow regime, and the direct detection of protein from the high-salt buffer for native spectrometry. The present method also provides a platform to study electrospray-related phenomena taking place under a high electrical field at an extremely small flow rate.

Chapter 4: Novel application of HP nano-ESI: oxidative modification by strong electrical field

Summary

Oxidative modification is usually used in mass spectrometry (MS) for labeling and structural analysis. In Chapter 4, we report a highly tunable oxidation that can be performed in line with the nanoESI-MS analysis at the same ESI emitter without the use of oxidative reagents such as ozone, H_2O_2, and UV activation. The method is based on the high-pressure nanoESI of a highly conductive (conductivity >3.8 S/m) aqueous solution near the minimum flow rate. The ion source is operated under super-atmospheric pressure (0.5 MPa gauge pressure) to avoid the contribution of electrical discharge. The analyte at the tip of the Taylor cone or in the emitter droplet can be locally oxidized in an on-demand manner by varying the nanoflow rate. With an offline nanoESI, the degree of oxidation, i.e. the average number of the incorporated oxygen atoms can be finely tuned by voltage modulation using spray current as the feedback signal. Oxidations of easily oxidized residues present in peptides/proteins and the double bonds of the unsaturated phosphatidylcholine occur at low flow rate operation (<5 nL/min) when the electrical field at the tip of the Taylor cone and the initially produced charged droplet reaches approximately 1.3 V/nm. The oxidized ion signal responds instantaneously to changes in flow rate, indicating that the oxidation is highly localized. Using isotope labeling, it was found that the incorporated oxygen primarily originates from the gas phase, suggesting a direct oxidation pathway for the analyte-enriched liquid surface by the reactive oxygen atoms formed by the strong electrical field.

Introduction

In ESI, the analyte-containing solution is dispersed electrically to produce charged micro/nanodroplets. The excess charges on the charged droplet are ultimately transferred to the solute, generating gaseous ions for mass spectrometry. Depending on the experimental condition, ions owing to the incorporation of the oxygen atom (such as $[M+nH + mO]^{n+}$) can appear along with their

protonated ion species[77]. Such oxidative modification to the analytes can be caused by i) electrochemical reactions involved in the electrospraying process, and ii) electrical discharge (such as corona discharge) when the HV applied to the emitter is raised to a much higher than normal value[76,85].

For a sustained electrospray, the continuous flow of spray current involves electrochemical reactions (ECR) at the liquid/electrode interface. Electrospray is thus regarded by some as a "*special kind of electrolytic cell,*"[17] The adverse effects of ECR include the corrosion of electrode, the change of pH, and oxidation of analyte that result in artifacts to the mass spectra[86–88]. The inert platinum electrodes are usually a preferred choice to avoid corrosion, and there are also ways to reduce the ECR effects by operating the ESI at a higher flow rate and the separation of ECR products from the ionization. The supposed "downside" of ESI oxidation had also been utilized for special-purpose analyses[76,81,89–92]. For example, Cheng *et al.* use a Pd electrode to release the Pd cation to catalyze the Suzuki coupling reaction at room temperature during mass spectrometry analysis[89]. Tang *et al*. identified the position of lipid C=C isomers and *sn*-isomers by combining two voltage-dependent electrochemical reactions, interfacial electro-epoxidation, and cobalt anodic corrosion in a single nano-ESI[81,92]. Double bonds are widely present in biomolecules, and it is a significant contributor to the spatial conformation of biomolecules. The efficient identification of the position and the number of double bonds in biomolecules is important in biochemistry as it helps reflect the misexpression of cells and other related information of metabolic diseases.

Electrical discharge (e.g. corona discharge) takes place when the potential at the ESI emitter or on the conductive liquid surface exceeds the threshold voltage for gaseous breakdown. The reactive oxygen species (ROS) generated by the discharge is known to cause the oxidation of analyte generated from ESI. Because the discharge could disrupt the stability of the electrospray and generate unwanted background ions, it usually needs to be avoided. A method like high-pressure ESI has been developed to prevent the discharge during the electrospraying of pure aqueous solution[23]. Nevertheless, the discharge has been generated alongside electrospray (with a higher HV) for the selective oxidation of the peptide, tagging the oxygen atom to the easily oxidized residue such as Met, Trp, and Tyr of peptide or protein[77]. The oxidation effect was further enhanced by using oxygen as the nebulizing gas for ESI to increase the abundance of ROS in the plasma[78]. The oxidation is also found to attack the C=C bond preferably, forming signature fragments when the oxidatively modified ion is subject to dissociative

activation. This enables the determination of double bond position for structural analysis of compounds[91]. Selective epoxidation with discharge in combination with ESI tandem mass spectrometry has also been performed using AC paper spray with co-induced mild discharge[90], field-induced droplet ionization (FIDI) technique with the dielectrical barrier discharge (DBD)[93], co-spraying the sample with radical water ions generated from corona-discharge[94], and nanoESI with sample pretreatment with low-temperature plasma (LTP) torch[95]. Recently, it is reported by Zare et al. that oxidation can take place even in the uncharged microdroplets, leading to the spontaneous generation of H_2O_2 from neutral spray[96], and condensation of water on a cooled substrate[97]. Although there is a possibility that air-borne ozone might contribute to H_2O_2 formation[98,99], Zare et al. managed to reproduce the results in the absence of ozone[100]. Simultaneous and spontaneous oxidation and reduction of phosphonates are also reported in microdroplets, and the active reagent is thought to be the free water radical cation and anion ($H_2O^{+\bullet}$ & $H_2O^{-\bullet}$)[101,102]. It is speculated that the high electrical fields at the air-water interface, which can reach as high as 1 V/nm on the surface of the neutral microdroplet, are responsible for that unusual chemical transformations[103]. This part reports the oxidative modification of peptide, protein, and lipid with unsaturated hydrocarbon chains that takes place when operating an offline high-pressure nanoESI of highly conductive aqueous solutions. This method is based on the precise nanoflow rate control of nanoESI using voltage modulation[104]. The nanoESI is performed using a micropipette tip with an inner diameter of 0.4 mm but the solution flow rate is sustained in the order of nL/min on par with those using fine glass-pulled capillary[33]. The high stability of the aqueous Taylor cone under a discharge-free condition is maintained by operating the ion source under a super-atmospheric pressure. The abundance of the oxygen-incorporated ion species can be tuned by the applied voltage. But in contrast to the case where apparent discharge is co-generated with ESI, the most prominent oxidation takes place when the applied voltage is reduced to a value near its lowest, i.e., the spray current, solution flow rate, and the size of the precursor droplet are near their lowest value. Similarly, the formed Taylor cone is at its sharpest with the highest electrical field. In this chapter, the description of this oxidation phenomenon is given with comparisons to the oxidation by corona discharge, dielectric barrier discharge, in-emitter electrochemical reaction, and the nanoESI under the presence of ozone.

Experimental section

Ion source and instrument

Figure 4.1 shows the schematic of the high-pressure nanoESI ion source. The ion source is filled with compressed air with an operating gauge pressure of 0.5 MPa and a humidity of < 10%. Polypropylene micropipette tips with a tip opening inner diameter of 0.4 mm (Eppendorf, Hamburg, Germany) were used as the ESI emitters. A platinum wire (dia: 0.2 mm) was used as the electrode to apply the high voltage (HV) to the solution. MS measurements were performed using a benchtop Orbitrap mass spectrometer (Thermo Fisher Scientific, Bremen, Germany). The ion source was coupled directly to the mass spectrometer using a custom-made ion transmission tube with 0.25 mm i.d. to match the acceptable gas throughput of the vacuum pump. The distance between the tip of the Taylor cone and the ion inlet was approximately 1 mm. When the ion source was pressurized, the pressure in the fore vacuum was ~1 mbar, approximately the same as the original reading of the mass spectrometer under standard working conditions. The spray current flowing through a 1 MΩ sensing resistor was measured using a high-impedance OpAmp and digital multimeter.

Sample preparation

Proteins, peptides, caffeine, and water-18O (97% atom) were purchased from Sigma Aldrich. Phosphatidylcholine was purchased from Fujifilm. 10-Acetyl-3,7-dihydroxyphenoxazine (ADHP) was purchased from Cayman Chemical. Hydrochloric acid, ammonium formate, ammonium acetate, and tetraethylammonium bicarbonate were from Kanto Chemical (Tokyo, Japan). All chemicals were used without further purification. The electrical conductivity of the solution was measured using a conductivity meter (Mettler Toledo). The 18O content for the isotope-labeled samples was greater than 87 % atom.

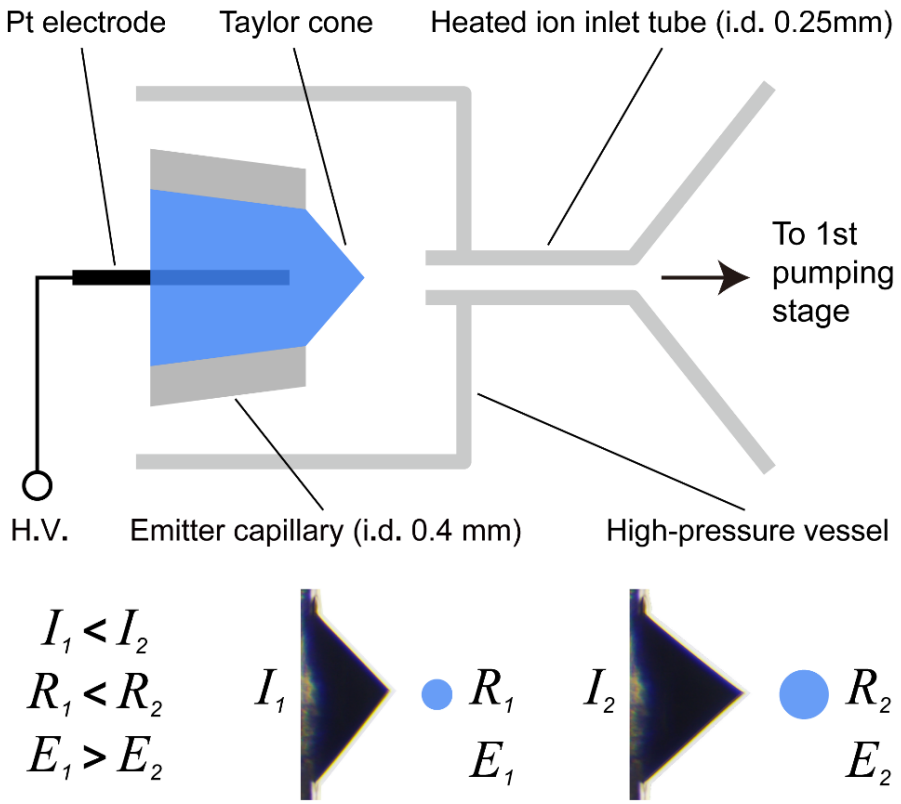

Figure 4.1. Schematic of the offline high-pressure nanoESI ion source. The emitter capillary is a micropipet tip with an i.d. of 0.4 mm. The solution flow rate is determined from the measured spray current I. Insets show the shape of the Taylor cones formed at different flow rates. A lower flow rate produces a charged droplet of a smaller radius R with a higher electrical field E.

Results and Discussion

Flow rate-dependent Oxidation

To enable a stable electrospray for highly conductive aqueous solutions without discharge, all measurements were performed under a super-atmospheric condition. The flow rate of the offline ESI emitter was controlled solely using the applied voltage. Under a steady cone-jet mode, the flow rate of the solution was estimated using the following equation[24].

$$I = f(\epsilon_r)\left(\frac{\gamma K Q}{\epsilon_r}\right)^{1/2} \quad (1)$$

, where ϵ_r is relativity permittivity, γ is surface tension, K is the electrical conductivity of the liquid, and $f = 18$ for aqueous solutions. When using typical buffered aqueous solutions with an electrical conductivity of ≤ 1.5 S/m, and a spray current of approximately 100 nA, the flow rate was in the order of several to several tens nL/min. Such condition was non-oxidizing and the typical mass spectra resemble those taken using standard nanoESI with fine capillary or pneumatically assisted ESI. For example, the mass spectra of cytochrome *c* and melittin with a low charged state distribution acquired from ammonium salt solutions commonly used in native MS are shown in Figure 4.2.

It was found that by increasing the conductivity of the solution to >3.8 S/m and by reducing the flow rate of the nanoESI near its minimum value, the ion of the analyte was modified with the incorporation of oxygen atoms. The amount of the incorporated oxygen, i.e. the degree of "oxidation" could be reproducibly adjusted by precision tuning of the applied voltage which in turn changes the spray current and the solution flow rate. Figure 4.3a shows the magnified mass spectra for the charge state +7 of cytochrome *c* (cyto *c*) acquired from 1 M ammonium formate solution under different measured spray currents. Figure 4.3b shows the variation of the average and the maximum number of oxygen atoms incorporated into cyto *c* for all charged states with the change of spray current. The average number of oxygen $\bar{m}$ is calculated by $\bar{m} = \sum_n \sum_m m I_{m,n} / \sum_n \sum_m I_{m,n}$, where m and n are the oxygen number and charge state and $I_{m,n}$ is the corresponding peak area. The secondary x-axis shows the flow rate calculated using Eq 1. Here, the naturally present oxidized cyto *c* has an average of 0.6 oxygen atoms. Under the strongest oxidizing condition at the lowest spray current, approximately 14 oxygen was found to attach to the cyto *c* (Figure 4.4). Figure 4.3c shows the ratio of

total oxidized ion species to the total ion signal originating from cyto *c*. The percentage of the oxidized species could reach up to ~90% of the TIC at the lowest spray current. The concentration of the cyto *c* here was 25 μM. From the average oxygen number and the fraction, the concentration of reactive oxygen species generated should be at least ~120 μM in terms of equivalent liquid phase concentration.

The oxidation was also accompanied by the denaturation of cyto *c* as indicated by the change of average charge state in Figure 4.3c and the plot of the heatmap in Figure 4.5a. A higher charge state typically has a higher number of incorporated oxygens. It was reasonable as the unfolding of protein exposed more oxidizable amino acid residues to the ROS. It is worth noting that the unfolding of cyto *c* preceded the oxidation. The unfolding may be due to the strong electrical field and/or the thermal effect caused by high spray current density at the tip of the Taylor cone.

The degree of oxidation also varied with the type of proteins. Compared to cyto *c*, the highest degree of oxidation of ubiquitin in Figure 4.6 was less pronounced. The average charge of ubiquitin also remained relatively constant at around 5.5, unaffected by the nanoflow rate (Figure 4.6c). These results suggest that the structure of ubiquitin is more rigid relative to cytochrome c. Table 1 shows the amino acid sequences of cytochrome *c* and ubiquitin. The amino acid residues of phenylalanine (F), tyrosine (Y), histidine (H), tryptophan (W), cysteine (C), and methionine (M) are generally considered to be susceptible to oxidation[105–109]. Cytochrome *c* contains 16 easily oxidized amino acid residues, while ubiquitin has only 5. These numbers agreed with the maximum number of attached oxygens observed in Figures 4.3 and 4.4.

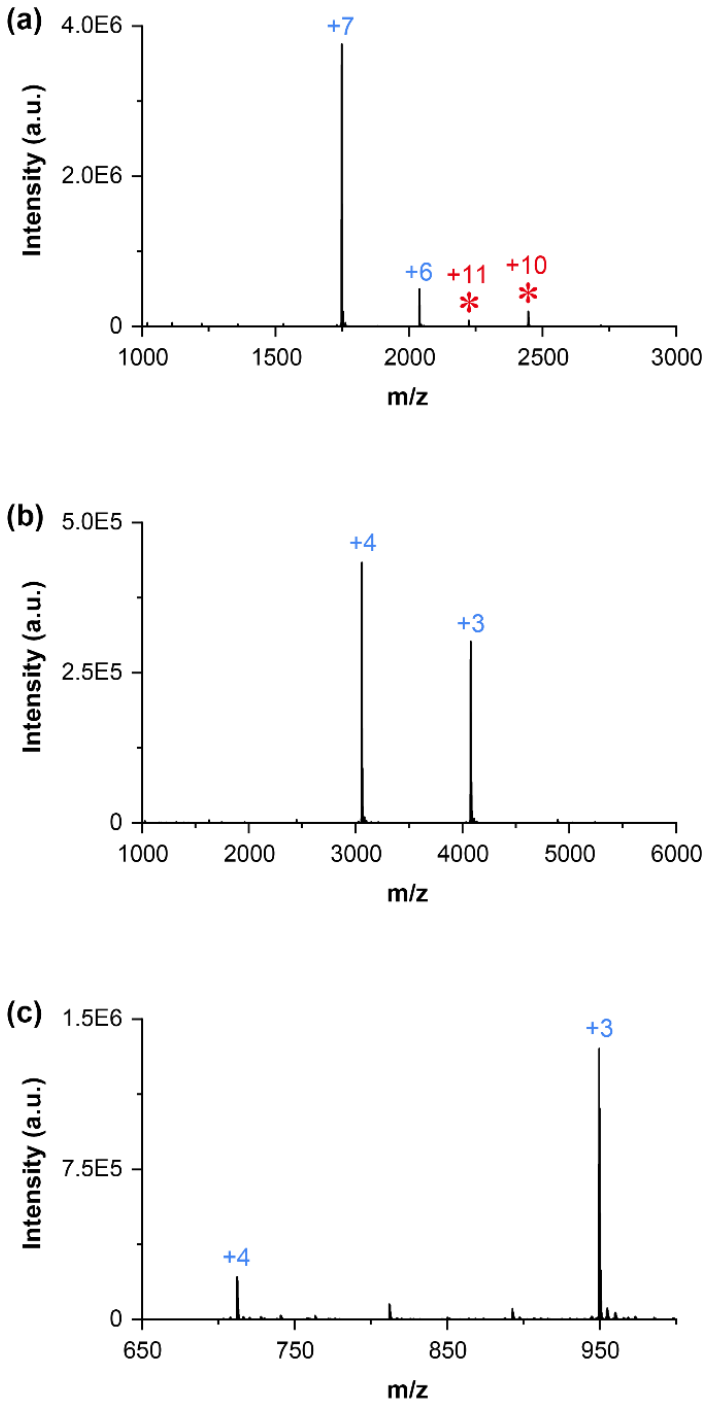

Figure 4.2. Typical high-pressure nanoESI mass spectra of protein and peptide acquired under nonoxidizing conditions. **a)** Cytochrome *c* (10 μM) in 100 mM ammonium formate. Asterisk * denotes the dimer. **b)** Cytochrome *c* in 100 mM tetraethylammonium bicarbonate. **c)** 10 μM melittin in 100 mM ammonium formate.

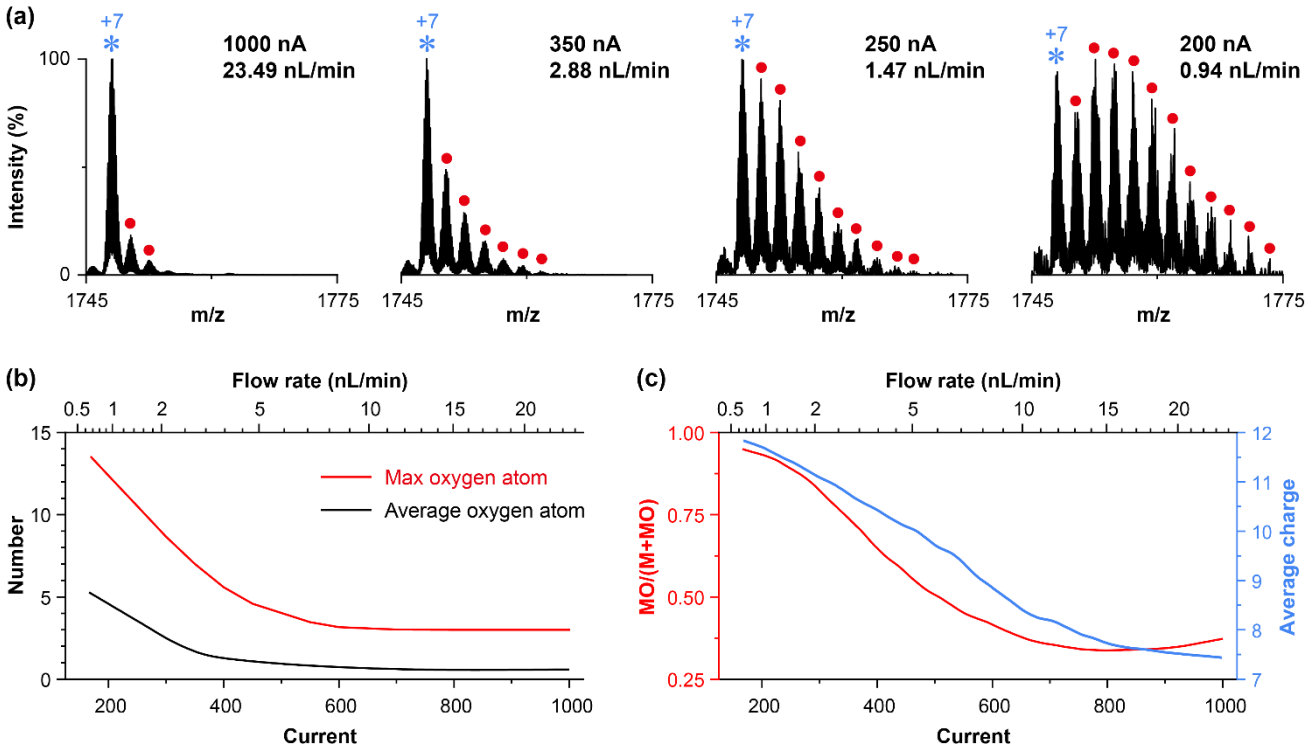

Figure 4.3. a) Mass spectra of cytochrome *c* (25 μM) in 1 M ammonium formate aqueous solution acquired at different spray currents. Red solid circle denotes the oxidized peak. Asterisk denotes the unoxidized peak. **b)** Maximum (red) and the average (solid) number of oxygen atoms versus spray current. **c)** Ratio of total oxidized ion species to the total ion signal (red) and the average charge state (blue) versus spray current.

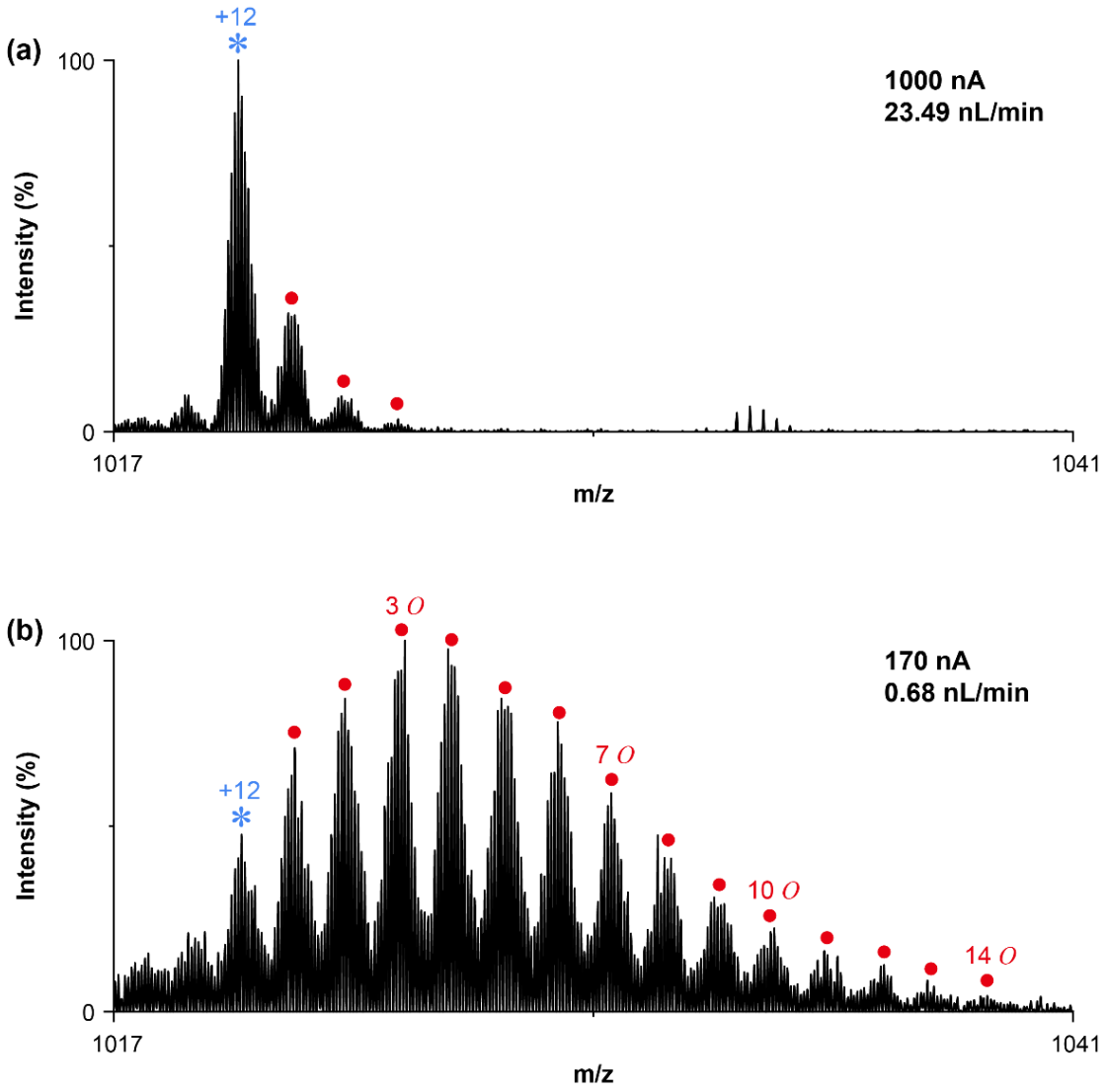

Figure 4.4. Mass spectra of cytochrome *c* in 1 M ammonium formate acquired at different spray currents and flow rates. **a)** Spray current: 1000 nA, flow rate: 23.5 nL/min. **b)** Spray current: 200 nA, flow rate: 0.9 nL/min. Red circle denotes the oxidized peak (M + n*O*). Asterisk denotes the unoxidized peak.

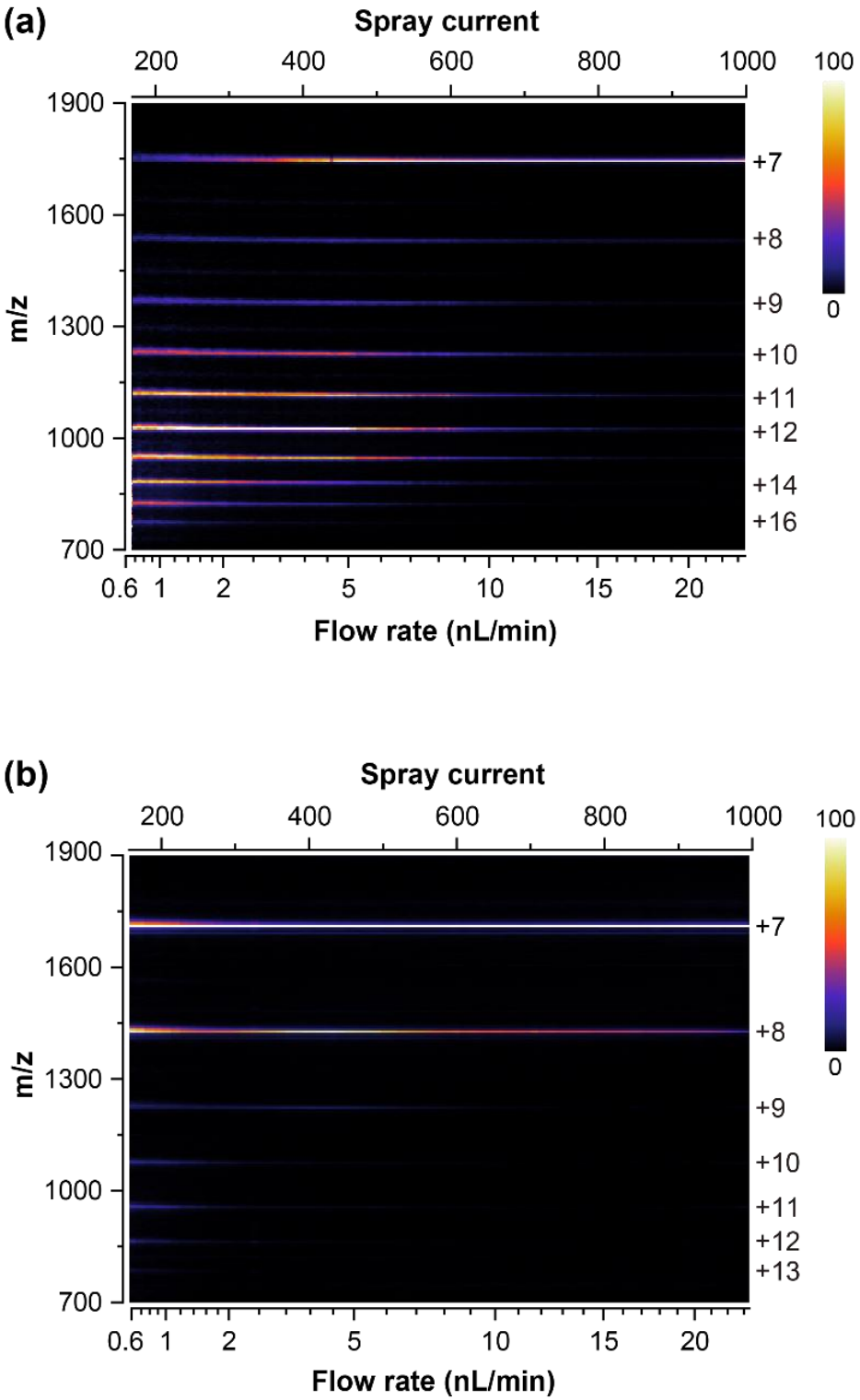

Figure 4.5. Heatmaps showing the effect of flow rate on the charged state of a) cytochrome *c* (25 μM) and b) ubiquitin (25 μM) in 1 M ammonium formate aqueous solution.

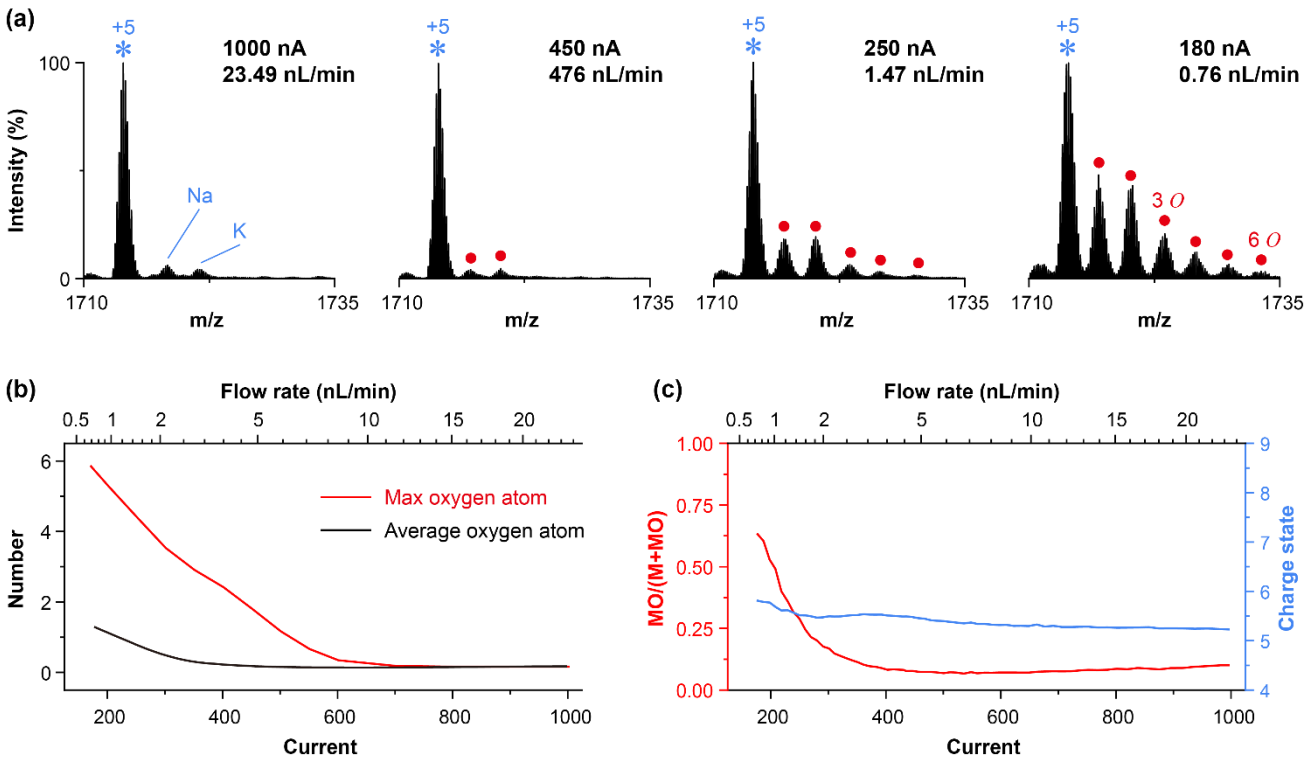

Figure 4.6. a) Mass spectra of ubiquitin (25 μM) in 1 M ammonium formate aqueous solution acquired at different spray currents. **b)** Maximum (red dashed) and the calculated average (solid black) number of oxygen atoms versus spray current. **c)** Ratio of total oxidized ion species to the total ion signal (red) and the average charge state (blue) versus spray current.

Apo-cytochrome *c* (CC) 11572.35

GDVEKGKKIFVQKCAQCHTVEKGGKHKTGPNLHGLFGRKTGQAPGFSYTDANKNKGITWGEETLMEYL
ENPKKYIPGTKMIFAGIKKKGEREDLIAYLKKATNE

Ubiquitin (UB) 8564.84

MQIFVKTLTGKTITLEVEPSDTIENVKAKIQDKEGIPPDQQRLIFAGKQLEDGRTLSDYNIQKESTLHLVLRL
RGG

Melittin (MLT) 2847.5

GIGAVLKVLTTGLPALISWIKRKRQQ

Angiotensin (AG) 1296.49

DRVYIHPFHL

	Cys (C)	Met (M)	Trp (W)	Tyr (Y)	His (H)	Phe (F)	Total
CC	2	2	1	4	3	4	16
UB	0	1	0	1	1	2	5
MLT	0	0	1	0	0	0	1
AG	0	0	0	1	2	1	4

Table 4.1. Amino acid sequences of apo-cytochrome c, ubiquitin, melittin, and angiotensin. The amino acids whose R group is easily oxidized are marked in red.

On-demand switching of oxidation

Figure 4.7 shows the switching between nonoxidizing and oxidizing conditions by modulating the HV applied to the emitter. Using spray current as the feedback signal, the HV was feedback controlled with a personal computer using a custom program written in C#. The spray current was step-modulated between 200 and 600 nA (Figure 4.7a). The ratio of the EIC of the oxidized peak to the EIC of the non-oxidized peak responded near-instantly (in less than 1 s) to the spray current (Figure 4.7b). This indicated that the oxidation was strongly dependent on the spray current, hence the flow rate. As the flow rate was switched to 8.4 nL/min from 0.9 nL/min, the oxidized species also depleted immediately back to the mass spectrum shown in Figure 4.7c (i) from 4.7c (ii).

It is well known that a sustained electrospray is associated with the inherent electrochemical reaction (ECR), thus one may wonder if the ECR was involved in the observed oxidation. Here, an inserted platinum wire was used as the charging electrode, and the distance between the distal end of the electrode to the tip of the ESI emitter was approximately 10 mm. Under the operating flow rate of several to several tens nL/min, it would take more than 10 ten minutes to transport the oxidation products generated by the ECR at the electrode to the Taylor cone. Likewise, it would take several minutes to consume the ECR product when the oxidation was turned OFF. The near instantaneous response of oxidation to the change in spray current provided clear evidence that the observed phenomenon was not relevant to ECR at the electrode. Instead, the oxidation was likely to take place at the tip of the Taylor cone, on/inside the charged droplets, or in the gas phase. It is noted that as the solutions used in this study were highly conductive, the spraying and the oxidation condition was not affected by the position of the platinum electrode.

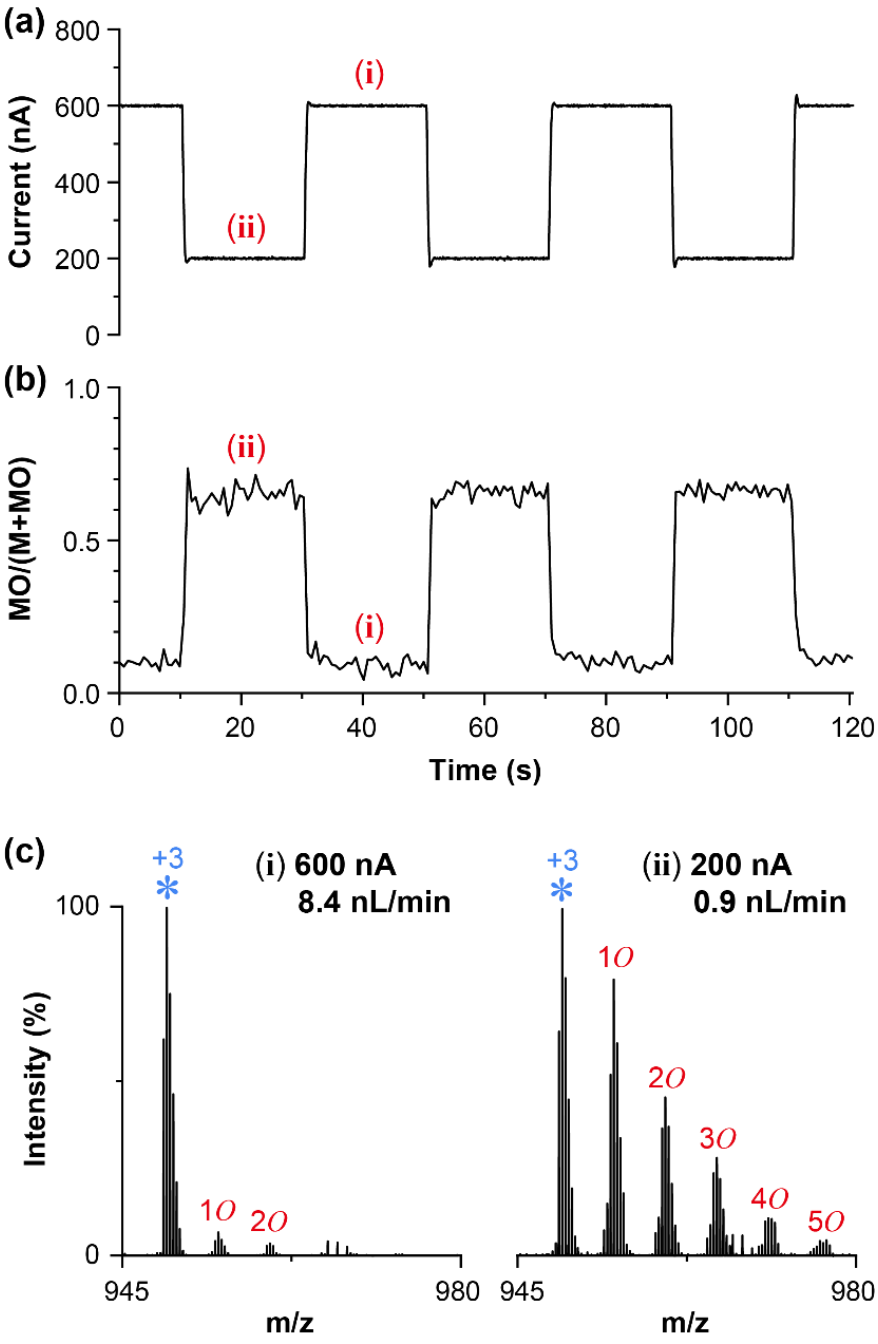

Figure 4.7. On-demand oxidation by step-modulation of spray current for 10 μM melittin in 1 M ammonium formate. **a)** Waveform of the measured spray current. The HV applied to the emitter is feedback-controlled using spray current as the feedback signal. The preset values for the spray current are 200 and 600 nA. **b)** The ratio of total oxidized ion species to the overall ion species. **c)** Mass spectra of melittin acquired at (i) high flow rate (600 nA) and (ii) low flow rate (200 nA). Asterisk denotes the unoxidized peak.

Dependence on electrical field

The oxidation was believed to involve the reactive oxygen species (ROS). The formation of ROS here was not spontaneous, i.e. it needed an external activation or energization. We hypothesize that the strong electrical field on the tip of the Taylor cone or the surface of the initially charged droplet was responsible for the observed oxidation phenomenon. Under the condition near the lowest flow rate and spray current, the formed Taylor cone was the sharpest, generating the finest charged droplet. Here the correlation between the electrical field and the threshold to induce oxidation was evaluated using cytochrome c in ammonium acetate and ammonium formate solutions of different electrical conductivities. The measurement began by operating the ESI in a nonoxidizing condition at a high current and high flow rate. The naturally occurring oxidized species detected at the high flow rate were defined as the baseline. The flow rate was gradually decreased by reducing the emitter voltage until the ion intensity of the total oxidized species account for 10 % of the TIC of cytochrome *c*. The measured spray current at that point was assigned as the threshold current for the estimation of the electrical field that trigger the oxidation. Following the scaling law[24], the radius of the initially produced charged droplet R_o can be approximated using[24]

$$R_o \sim \left(\frac{\epsilon_o \epsilon_r Q}{K}\right)^{1/3} \tag{2}$$

where ϵ_o is the vacuum permittivity. The flow rate Q can be readily calculated from the spray current following Eq 1. For an order of magnitude analysis, we assume the stress owing to the surface tension equals that of the electrostatic field (i.e. at Rayleigh limit). In that case, the electrical field strength on the initial droplet surface E_o is

$$E_o \sim 2\sqrt{\frac{\gamma}{\epsilon_o R_o}} \tag{7}$$

The value estimated using Eq 7 should reflect the order of magnitude of the electrical field on the droplet surface as well as on the tip of the Taylor cone when the droplet was generated. In terms of spray current, E_o is

$$E_o \sim 2\left(\frac{\gamma}{\epsilon_o}\right)^{2/3}\left(\frac{Kf(\epsilon_r)}{\epsilon_r I}\right)^{1/3} \tag{8}$$

Depending on the electrical conductivity, the spray currents (or the flow rates) to observe the oxidation were different. However, the plot of the radius R_o and electrical field E_o in Figure 4.8 shows an

interesting result that the initialization of oxidation takes place at an average R_o of ~ 19.2 nm and a E_o of 1.3 V/nm, independent of the conductivity and the choice of the buffer solution. This suggested that the turn-on of oxidation was strongly linked to the electrical field associated with the nanoESI.

One may argue that the phenomenon was identical to the commonly encountered corona discharge co-generated by the ESI at higher HV. An important discrepancy from the corona discharge-induced phenomenon was that the observed oxidation species were at their highest abundance at the lowest HV and spray current. Also, under the super-atmospheric pressure, an apparent corona discharge was absent as verified by microscopic inspection on the Taylor cone and the measurement of spray current. Still, the possibility of partial discharge could not be excluded because that current was at the same order of magnitude or lower than the electrospray current. We conjecture that despite the absence of apparent discharge, the local electrical field was strong enough the accelerate electron and ions in proximity to the liquid surface for the formation of reactive oxygen species. In the following sections, this oxidation taking place under a low flow rate is referred to as strong electrical field-induced oxidation (SEFO). It is noted that the flow rate in Eq 2 or the spray current in Eq 8 cannot be reduced to an arbitrarily small value because to sustain a steady cone-jet mode, there exists a minimum flow rate $Q_{\min}$ which is given as[24]

$$Q_{\min} \sim \frac{\epsilon_o \epsilon_r \gamma}{\rho K} \tag{3}$$

, where ρ is the density of the liquid[24]. This minimum flow rate limits the highest possible electrical field $E_{\max}$ that could be achieved for a given solution to

$$E_{\max} \sim 2 \left(\frac{\rho}{{\epsilon_o}^5}\right)^{1/6} \left(\frac{\gamma K}{\epsilon_r}\right)^{1/3} \tag{9}$$

Eq 9 implies that for an aqueous solution at room temperature where γ = 0.072 N/m, ρ = 997 kg/m^3, ϵ_r = 80, it requires a minimum electrical conductivity of 2.3 S/m to attain the threshold electrical field of 1.3 V/nm at the minimum flow rate. In practice, K needed to be greater than 3.8 S/m so that the operation above $Q_{\min}$ could still produce pronounced oxidation.

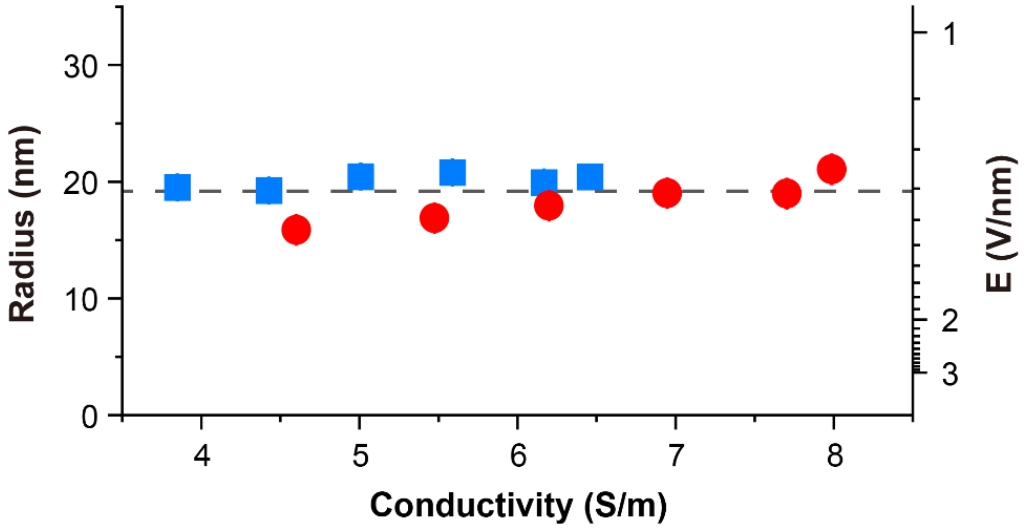

Figure 4.8. Radius and the electrical field of the initial droplet at the threshold for the detection of oxidized species. The sample is cytochrome *c* (25 μM) in different buffers solution of various electrical conductivities. Blue square: ammonium acetate. Red circle: ammonium formate. The average threshold radius and electrical field are ~19.2 nm and 1.3 V/nm.

Oxidation of molecular ion

The strong electrical field-induced oxidation of caffeine in Figure 4.9 shows some unusual results not found in typical ESI measurements. The solvent here was 200 mM HCl aqueous solution with an electrical conductivity of ~7 S/m. Using a highly conductive solution, the molecular ion of caffeine (M^+) was detected along with the protonated species ($[M+H]^+$) at a relatively higher flow rate (10 nL/min < Q < 30 nL/min). Although the detection of the molecular ion is common for electron ionization and field ionization, caffeine is usually detected almost solely as the protonated species using ESI or APCI. Due to the high electrical field, the presence of M^+ may indicate the presence of field ionization. Another possible ionization route is via charge transfer from the water radical cation which is reportedly present near/at the droplet-air interface under a strong electrical field[101]. The incorporation of oxygen into the molecular ion was also observed by decreasing the spray current to < 10 nL/min. The abundance of M^+ was found to decrease with the rise of $[M+O]^+$ at *m/z* 210, and $[M+HO_2]^+$ at *m/z* 227. The intensity ratios of $M^+/[M+H]^+$, $[M+O]^+/[M+H]+$, and $[M+HO_2]^+/[M+H]+$ are shown, respectively in the subplots of Figure 4.9.

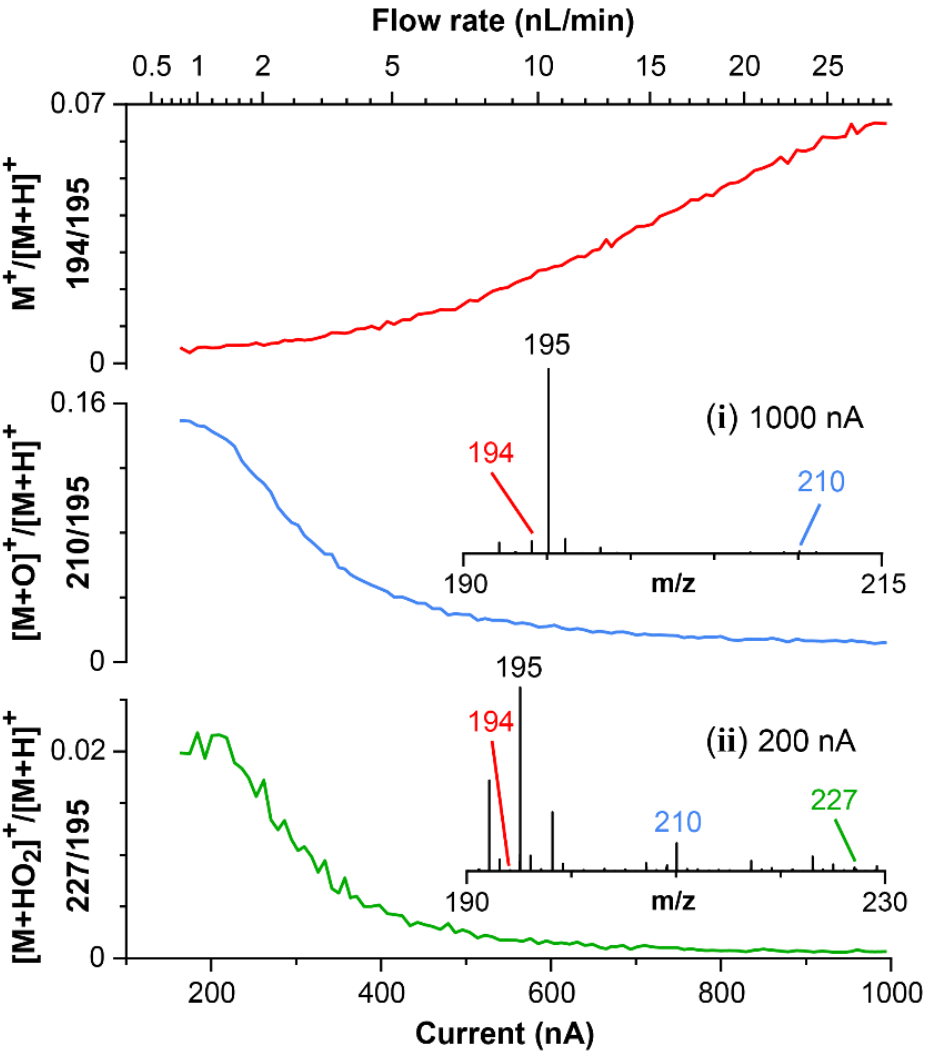

Figure 4.9. Detection of caffeine (25 μM) in 200 mM HCl under different spray currents. Red: Intensity ratio of $M^+/[M+H]^+$. Blue: $[M+O]^+/[M+H]^+$. Green: $[M+HO_2]^+/[M+H]^+$. Mass spectra in the inset are taken at 1000 and 200 nA.

Comparison with other oxidation methods

For comparison, the oxidation of cytochrome *c* was performed using various in-situ oxidation devices operated together with the same nanoESI source. Figure 4.10 shows the results of i) atmospheric pressure corona discharge (APCD), ii) in-emitter electrochemical (EC) reactor, iii) dielectric barrier discharge (DBD), and iv) ozone generated from DBD. Mass spectra in row (a) are taken when oxidation devices were in the initial OFF condition. Those in row (b) are taken after the oxidation devices were turned ON and sufficient time has passed for the ion signal to reach a steady state condition.

For APCD in column (i), the result was taken by placing a corona discharge needle in between the high-pressure ion source outlet and the MS ion inlet. This arrangement which separated the ESI source from the discharge source was chosen to preserve the stability of the electrospray. The discharge current was > 10 μA. Surprisingly, no obvious oxidation was observed. Possible explanations are a low concentration of ROS and a poor interaction between the charged droplets/ions and the ROS. The repulsive force may prevent the charged droplet from approaching the ROS-rich high electrical field region. Changing the polarity of the corona discharge shifted the charge state distribution to a low charge without any improvement in the oxidation performance. Figure 4.11 shows another APCD measurement in which the corona discharge was co-generated at the stainless-steel emitter of an atmospheric pressure ESI source. The HV was increased up to the level before the fluctuation of the spray but only a weak oxidation peak was detected.

Column (ii) shows the electrochemical oxidation performed inside the capillary of the emitter. In addition to the primary HV electrode for electrospray, another wire with insulator cladding was inserted into the ESI capillary as the second electrode. A ~3V potential difference was applied between those electrodes. The HV electrode was the cathode and the second electrode was the anode. The choice of the second electrode was important to prevent anodic oxidation and the formation of metal ions in abundance (Figure 4.12). Mass spectra in Figure 4.10 (ii) were taken using a platinum wire with Teflon cladding as the second electrode. After turning ON of the EC cell, the oxidation peak increased gradually and reached a steady state after 20 min. Only one oxygen attachment was observed.

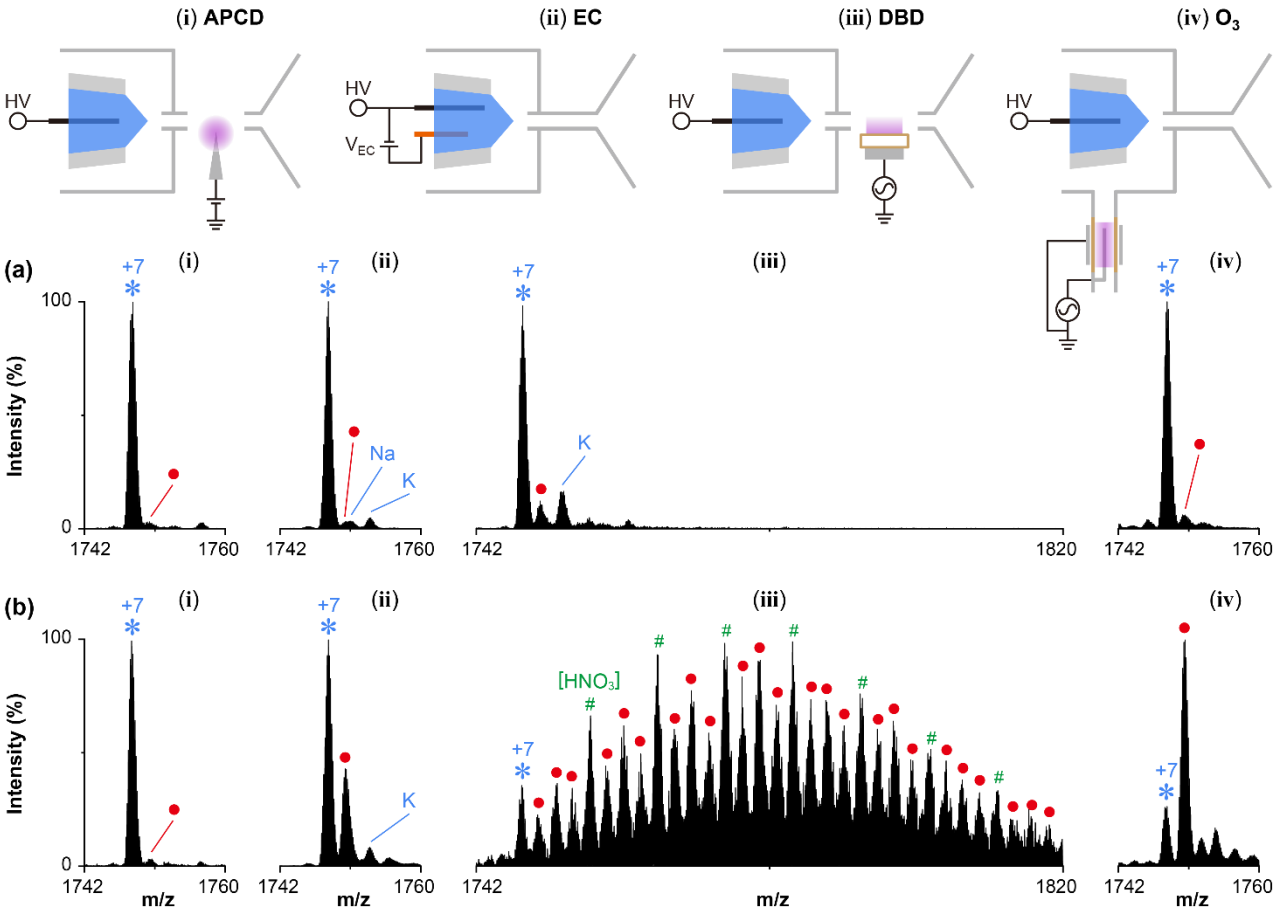

Figure 4.10. Oxidation of cytochrome *c* using i) atmospheric pressure corona discharge (APCD), ii) in-emitter electrochemical reactor (EC), iii) dielectrical barrier discharge (DBD), and iv) ozone generated from DBD. Red circle denotes the peak due to the incorporation of oxygen into the cytochrome *c*. Asterisk denotes the unoxidized peak. # sign denotes the peak due to the adduction of HNO_3. Sample: 10 μM cytochrome *c* in 100 mM ammonium formate.

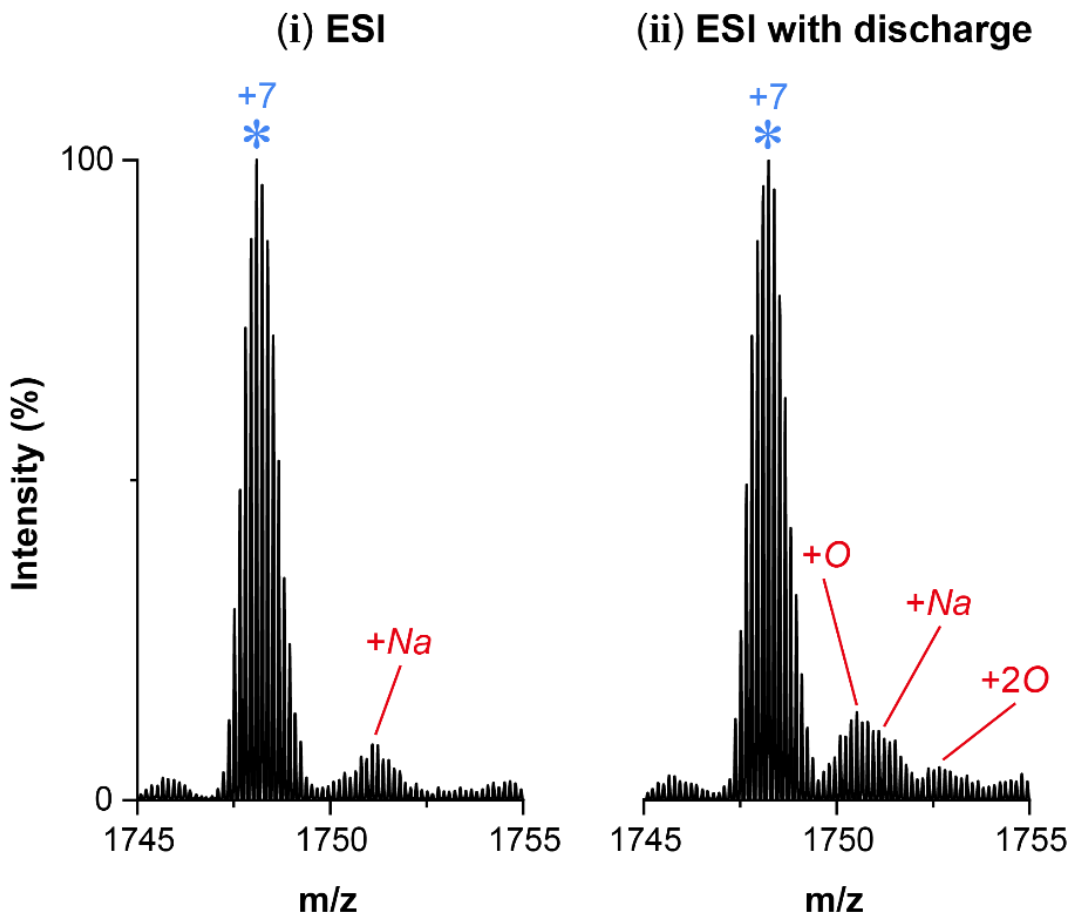

Figure 4.11. Mass spectra of cytochrome *c* (10 μM) in 100 mM ammonium formate in 50% ethanol. **(i)** Standard atmospheric pressure ESI. **(ii)** Atmospheric pressure ESI with a higher voltage to induce an electrical discharge with a current of 8 μA. The solution flow rate is 0.5 μL/min.

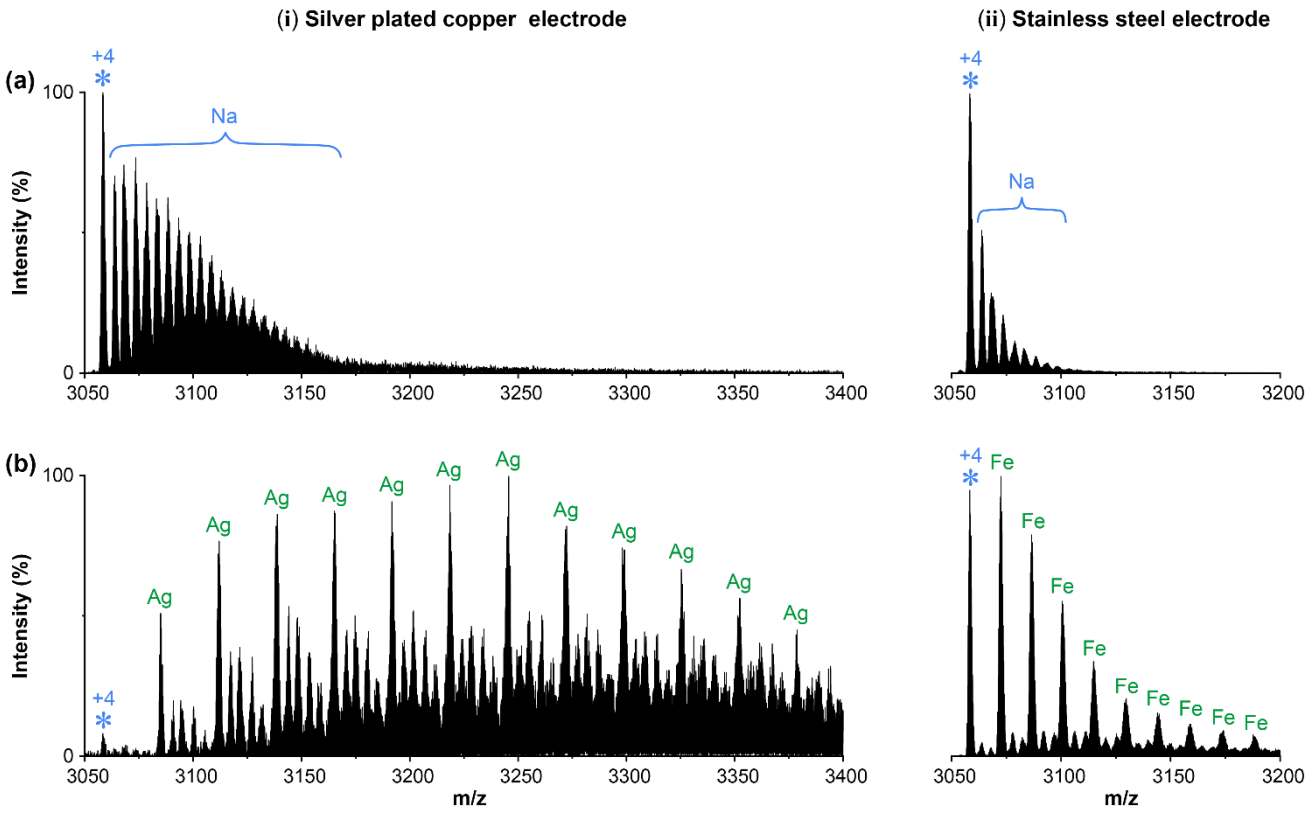

Figure 4.12. Mass spectra of cytochrome *c* in 100 mM tetraethylammonium bicarbonate acquired by nanoESI with an in-emitter electrochemical (EC) reactor. The oxidation electrodes are (i) Silver-plated copper and (ii) stainless steel. (a) and (b) are the mass spectra acquired at 0 min and 20 min after the turn ON of the EC reactor.

Dielectric barrier discharge was used in Figure 4.10 (iii) by placing the DBD source in between the ion source and the MS inlet. Glass was used as the barrier material. The discharge current for DBD was in the order of mA, significantly higher than the corona discharge source in (i), and the odor of ozone can be felt from 1 m away from the source. The degree of oxidation was much higher than corona discharge (i) and SEFO, well exceeding the number predicted by Table 4.1. However, the tunability for the degree of oxidation using this method was not easy and the mass spectrum was complicated by the presence of adduct species such as $n(HNO_3)$. Figure 4.10 (iv) shows the oxidation by ozone generated from the DBD. A cylindrical DBD source made of quartz tube was added in between the ion source and the gas supply line. The positive and negative ions from the DBD were annihilated by the metallic transfer tube and the inner wall of the ion source. This was verified by the observation that no background ion was detected when the DBD was turned ON, and ESI was turned OFF. By electrospraying the solution in the ozone-containing air, the oxidation peak gradually appeared and the intensity reached a plateau after ~ 5 min. The most dominant oxidation peak was the one with 1 oxygen atom. Even when the DBD was turned OFF, it took approximately 30 min for the mass spectrum to return to the oxidation-free condition, greatly exceeding the time needed to flush the ozone. This indicated that ozone has been dissolved into the solution phase via the Taylor cone.

Another comparison with ozone oxidation is shown in Figure 4.13 for peptides. The mass spectrum of the ozone-oxidized melittin in Figure 4.13a shows a dominant peak with the incorporation of three oxygen atoms. The finding by Richards et al also showed that the ozonated protein exhibits a predominant peak with three oxygens adduct[109]. The result by SEFO (Figure 4.7c (ii)) however shows a different oxygen distribution. The ion with the incorporation of one nitrogen was also detected which might be due to the interaction with other neutral species from DBD. The distribution of oxygen generated from ozone and SEFO were obviously quite different. Another measurement was performed using Angiotensin I which was reportedly not to be oxidized by ozone[109]. That same finding was reproduced in our experiment (Figure 4.13b) using ozone from DBD. Figure 4.13c shows the oxidation of angiotensin I was still possible by SEFO. In sum, the result in Figure 4.13 suggested that the main ROS involved in the SEFO was not ozone.

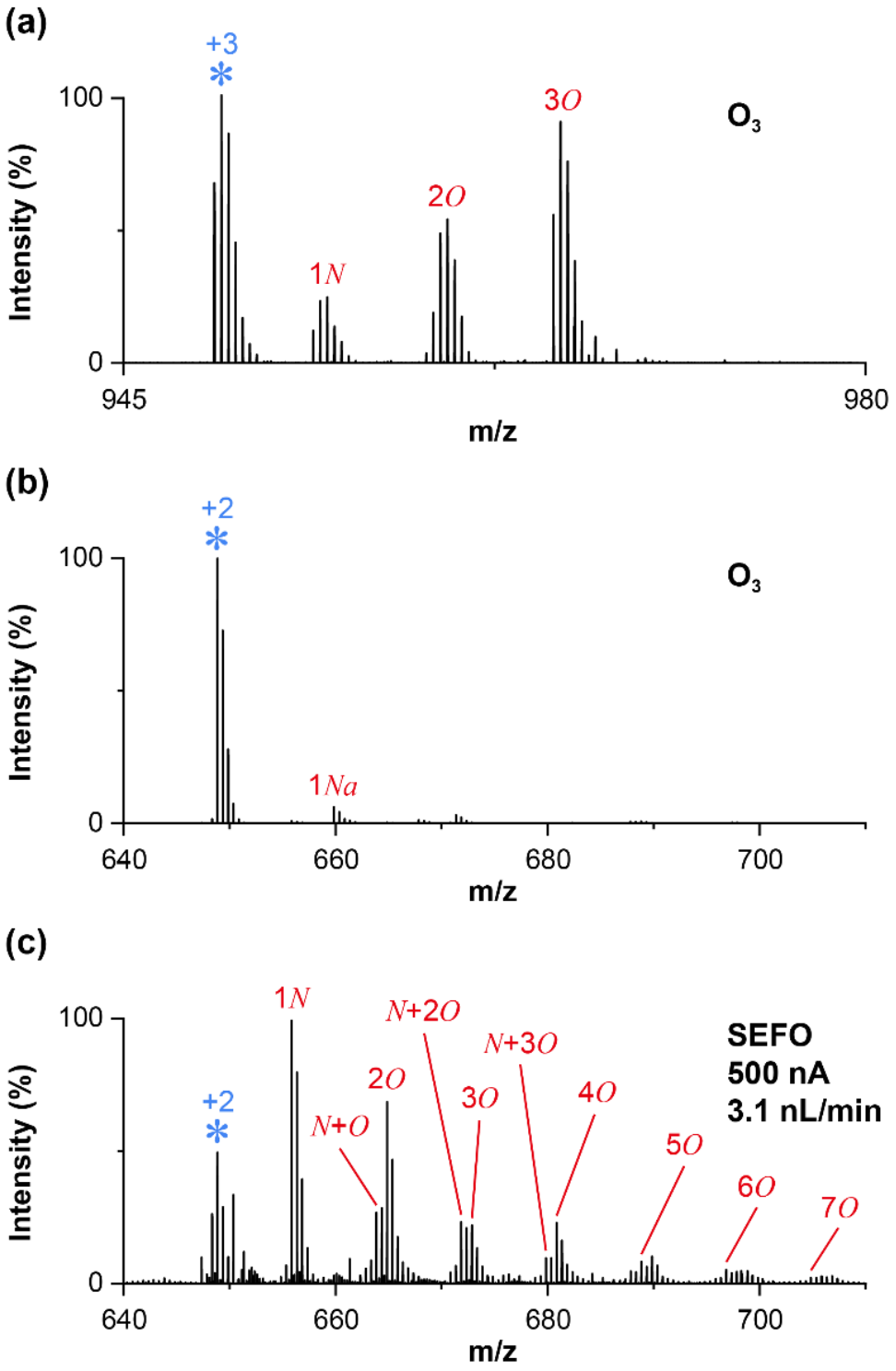

Figure 4.13. **a)** Oxidation of 10 μM melittin in 100 mM ammonium formate using ozone produced from DBD source. **b)** Oxidation of 20 μM angiotensin I in 50 mM HCl using ozone. **c)** Strong electrical field-induced oxidation of angiotensin I in 500 mM HCl. Asterisk denotes the unoxidized peak.

Source of oxygen atoms

The source of oxygen atoms attached to the analytes depends on the origin of ROS, and the subsequent interaction with the water and the analytes. If the phenomenon is discharge-like, the formation of ROS should take place in the gas phase. On the other hand, the strong electrical field established by the microdroplet electrical double layer (also reported to be in the order of 1 V/nm) was recently postulated by Zare and others to generate hydroxyl radicals in the liquid phase which contributed to the observed spontaneous formation hydrogen peroxide[103,110]. Isotope labeling method was used to determine the origin of the oxygen atom. The analyte was L-phosphatidylcholine (PC 18:1/18:1) with two double bonds (one at each fatty acid chain). Two sets of water solutions were used. One was prepared in normal pure water and another was prepared in $H_2{}^{18}O$ (97% atom). The measurement was performed using air and pure nitrogen as the operating gas for the ion source.

The mass spectra acquired using normal water solution and air are shown in Figures 4.14a (i) and 4.14b (i). Two dominant oxidation peaks were detected owing to the preferential attack of the double bond[104]. The result obtained using a water-^{18}O solution with air as operating gas is shown in Figures 4.14a (ii) and 4.14b (ii). The magnified mass spectrum in 8b shows that even with water-^{18}O, the dominant oxidation peaks were due to those of $[M+H+{}^{16}O]^+$, $[M+H+2{}^{16}O]^+$. Ion species of $[M+H+{}^{18}O]^+$, $[M+H+{}^{16}O+{}^{18}O]^+$, and $[M+H+2{}^{18}O]^+$ were detectable but with much weaker ion intensities (see intensity comparison in Figure 4.14c). Changing the operating gas to high-purity nitrogen (99.99995%) reduced the intensity of the oxidation peak as shown in Figures 4.14a (iii) and 4.14c. Even under that condition, the oxidation was still dominated by ^{16}O. A similar result was also observed for the melittin sample prepared in water-^{18}O (Figure 4.15).

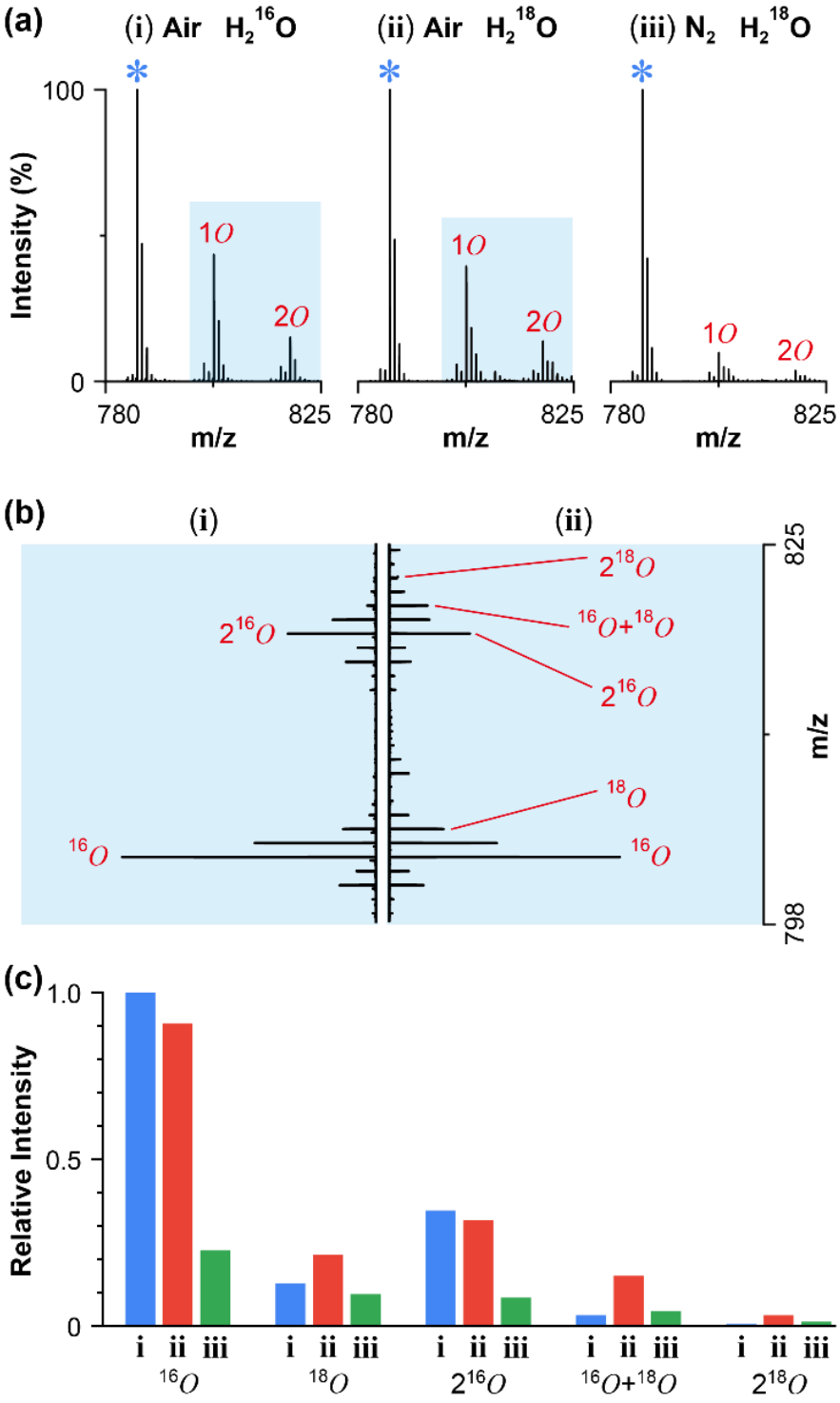

Figure 4.14. **a)** Mass spectra obtained under oxidized conditions for 5 μM L-phosphatidylcholine (PC 18:1/18:1) in 500 mM HCl prepared using normal water (i) and water-^{18}O (ii & iii). The operating gases are air (i & ii) and high-purity nitrogen (iii). Asterisk denotes the peak without oxidation. **b)** Enlarged view of (a)(i) and (a)(ii). **c)** Intensity comparison for different oxidation species.

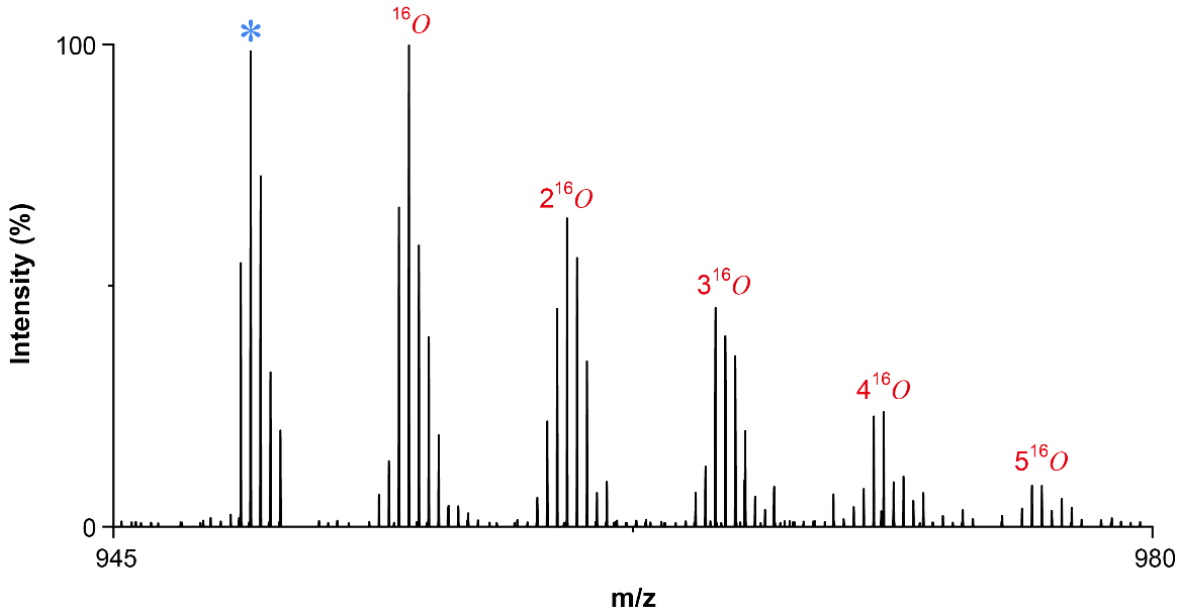

Figure 4.15. Mass spectrum of melittin oxidized by strong electrical field-induced oxidation. The sample solution is prepared using ammonium acetate (~1.5 M) in water-^{18}O.

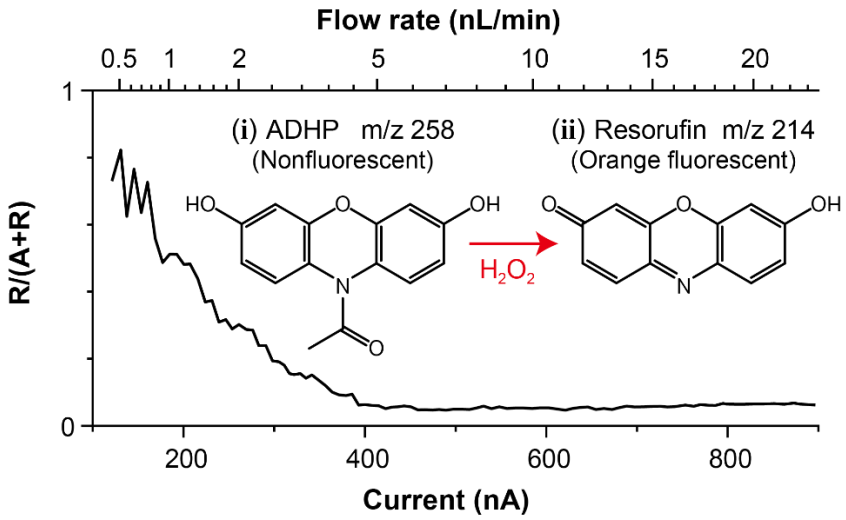

Figure 4.16. Detection of hydrogen peroxide H_2O_2 using ADHP.

The hydroxyl radical can form hydrogen peroxide H_2O_2 in solution. The detection of H_2O_2 in the solution is performed using 10-Acetyl-3,7-dihydroxyphenoxazine (ADHP, Amplex Red) which is a widely used fluorescent probe molecule for H_2O_2. ADHP converts to resorufin by H_2O_2. Because the electrical field-induced oxidation takes took place only within a small volume of the order of $(10\ nm)^3$, the direct fluorescent measurement at the Taylor cone tip is difficult. Nevertheless, resorufin and the ADHP are readily detected as protonated species by the present nanoESI-MS. Figure 4.16 shows the plot of the ratio of resorufin intensity to the intensity of (ADHP + resorufin) versus the spray current. The abundance of H_2O_2 is the highest at the strongest electrical field at the lowest spray current and flow rate.

With a sufficient acceleration of seed electrons near the charged liquid surface, the oxygen molecules in the proximity could be split into oxygen atoms which could eventually form ozone when combined with other oxygen molecules. Although the contribution by the ozone in SEFO could not be completely ruled out, the mass spectra obtained using external ozone (Figures 4.13a, 4.13b, and 4.12 iv) clearly showed that it was not the primary oxidation route. The ozone and/or the split oxygen atoms could react with the water to form hydroxyl radicals (•OH). The detection of ^{18}O-related peaks in the water-^{18}O sample supports the formation of ^{18}•OH. The detection of H_2O_2 (which can be formed by •OH) in Figure 4.16 also supports the formation of hydroxyl radicals. However, despite its presence, the low abundance of ^{18}O-related ions indicated that the hydroxyl radical oxidation was unlikely the main oxidation route in SEFO because the reaction of gas phase oxygen species with water-^{18}O should result in equal amounts of ^{18}•OH and ^{16}•OH. In sum, the primary source of oxygen in the SEFO was the gas phase $^{16}O_2$, suggesting a possibility of direct oxidation of analytes by the oxygen atoms generated by the strong electrical field. It is noted that oxidation by the atomic oxygen generated from the atmospheric plasma was also reported to be possible for the analyte in the solution[111].

Discussion

In summary, the initial size of the droplet, hence the strength of the electrical field were the key factors influencing the degree of oxidation. Following Eq 9, a solution needed to have sufficient electrical conductivity to attain a strong electrical field. The three aqueous solutions (ammonium acetate, ammonium formate, and HCl) tested in this study were highly conductive but still volatile and friendly to ESI without producing salt clusters. The highest electrical field was attained by the most conductive 500 mM HCl aqueous solution (K= 16.4 S/m). The jet and initial droplets generated from those solutions were smaller than the optical wavelength, therefore invisible under the optical microscope under all tested flow rates.

Regarding the accelerated redox reactions found to take place in the sprayed aqueous microdroplets, two types of water-originated reactants have been proposed. One is hydroxyl radicals generated from the hydroxide[112]. Another is the free water radical cations & radical anions generated from the dissociation of radical cation/anion pair[101,102]. Similar to the present study, the formation of those reactants was believed to require a strong electrical field at the aqueous microdroplet-air interface.

The oxidation by hydroxyl radical reported by Zare *et al*[112]. used a pneumatic sprayer with a broad distribution of droplet size in micrometers order. The redox by water radical ions reported by Cooks *et al*[101,102]. was performed by spraying acetonitrile solution with a trace amount of water using a nano ESI emitter with 5 μm i.d. Owing to the low electrical conductivity (K < 1mS/m) of acetonitrile, the initial droplet produced by the cone-jet mode should also be in the micrometer scale but not larger than 5 μm. Both studies by Zare and Cooks showed that the oxidation response increased with the emitter-ion inlet distance (or the droplet flight time). For the oxidation observed in this study, however, the generation of initial droplets of nanometer size was crucial. Due to the short lifetime of such droplets, increasing the emitter-inlet distance from the default 1 mm to >5 mm was not found to produce any effect on the degree of oxidation and the threshold E_o, except for causing a higher voltage to form Taylor cone and a drop in overall ion intensity. In sum, although the oxidation by the water-originated reactive species (such as hydroxyl radical and/or water radical cation) could not be excluded in our experiment, they were unlikely to be the main contributor as the majority of the incorporated oxygens were originated from the gas phase. By using 99.5% oxygen as the operating gas for the ion source, the average number of oxygens attached to the protein was also found to increase (Figure 4.17), supporting the contribution from the gas phase oxygen. The gas phase ROS could react directly with the analyte at the liquid-gas interface which was partially exposed to the gas phase.

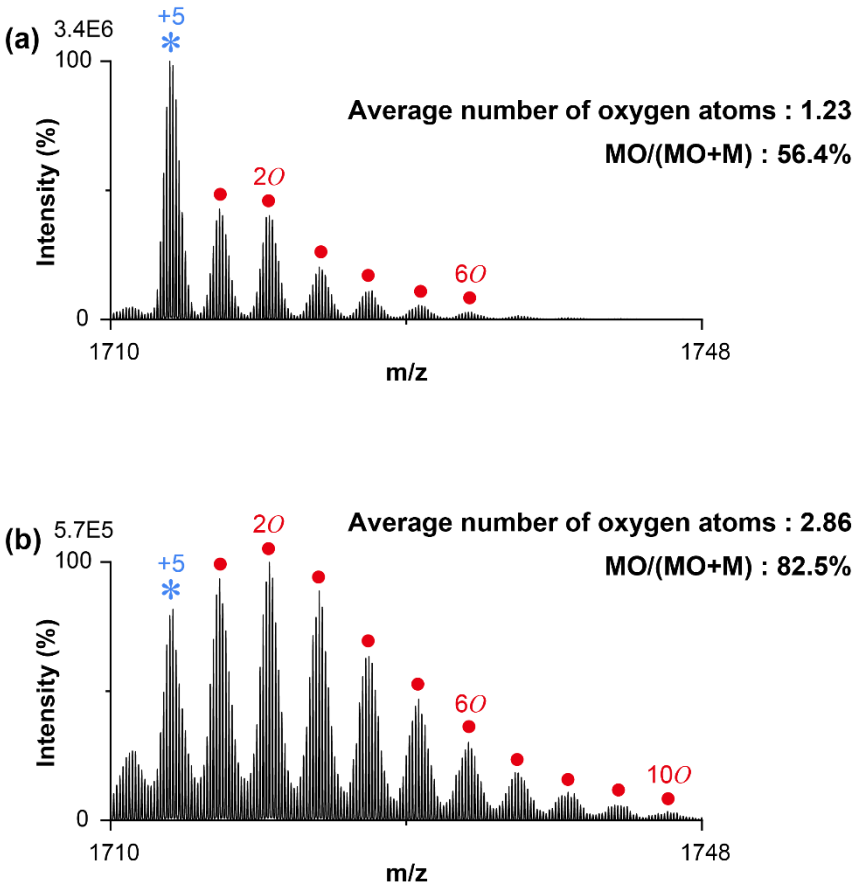

Figure 4.17: Oxidation of ubiquitin using air and oxygen as operating gases.
a) a) 0.5 MPa dry air (default in this study).
b) 99.5 % oxygen at 0.3 MPa.
The values show the average number of the incorporated oxygen atoms and the percentage of oxidation for charge state +5. The spray current is 200 nA. Ubiquitin concentration: 20 μM. The solvent is 1 M ammonium acetate aqueous solution.

Ozone is the common ROS formed by electrical discharge but the oxidation pattern and characteristics were different from that when ozone was intentionally introduced. We, therefore, propose the primary oxidant to be the oxygen atoms which are the precursor of ozone generated from the splitting of oxygen induced by the strong electrical field. While the average number of oxygen atoms incorporated into the analyte could be tuned by the emitter voltage, we have not attained 100 % oxidation. For example, the result of PC 18:1/18:1 in Figure 4.14a still shows a significant abundance of unoxidized PC. Replacing the air with 99.5% oxygen, and optimizing the ion source pressure to ~0.3 MPa shows an improvement in the percentage of oxidation from ~40 % to ~80 % (Figure 4.18). There was a drop in ion intensity due to a lower gas intake as the ion transmission tube in this work was optimized for 0.5 MPa. Nevertheless, it was an indication that further improvement in oxidation efficiency was still possible.

The present method also shared a similarity with the electro-epoxidation with nanoESI (EEnanoESI) by Yan *et al* in a way that the oxidation is controlled by the emitter potential[81]. While their process involved electrochemical reactions (ECR), the ECR was not relevant to our study. The oxidation effect was also observed using an ECR-free all-insulator bipolar ESI emitter[113]. Regarding the spraying mode, their microscopic image indicated that the liquid meniscus was in a high-frequency oscillation and the flow rate was approximately 100 nL/min. In our case, typical flow rates were below 5 nL/min, and it was under the well-characterized steady cone-jet mode. Interestingly, EEnanoESI required a capillary with a large i.d (75 μm) for the electro-epoxidation to occur. Coincidentally, this study also used an emitter with a large i.d. (0.4 mm) by default, but that was adopted for convenience and reproducibility. Measurements using smaller emitter capillaries with i.d. of 20 and 5 μm exhibited the same oxidation phenomena, and for a given solution, the thresholds of oxidation were observed at approximately the same spray current, regardless of the emitter size. The result obtained by the 5 μm capillary (purchased from Humanix, Hiroshima, Japan) is shown in the Figure 4.19. It is noted that for fine capillaries, it is necessary to avoid the high-frequency pulsation mode because Equations 1-3, 8, 9 are valid only for the steady cone-jet mode.

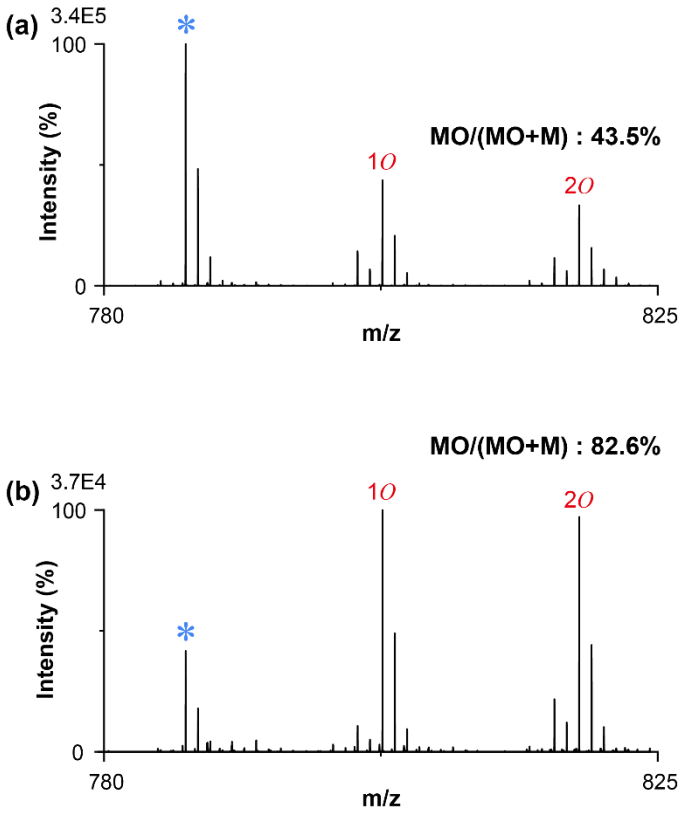

Figure 4.18. Oxidation of PC 18:1/18:1 using air and oxygen as operating gases.
a) 0.5 MPa dry air (default in this study). Percentage of oxidation = 43.5 %
b) 99.5 % oxygen at 0.3 MPa. Percentage of oxidation = 82.6 %
The spray current is ~250 nA in both cases. PC concentration: 5 μM. The solvent is 500 mM HCl in water:acetonitrile 9:1. K = 14.7 S/m.

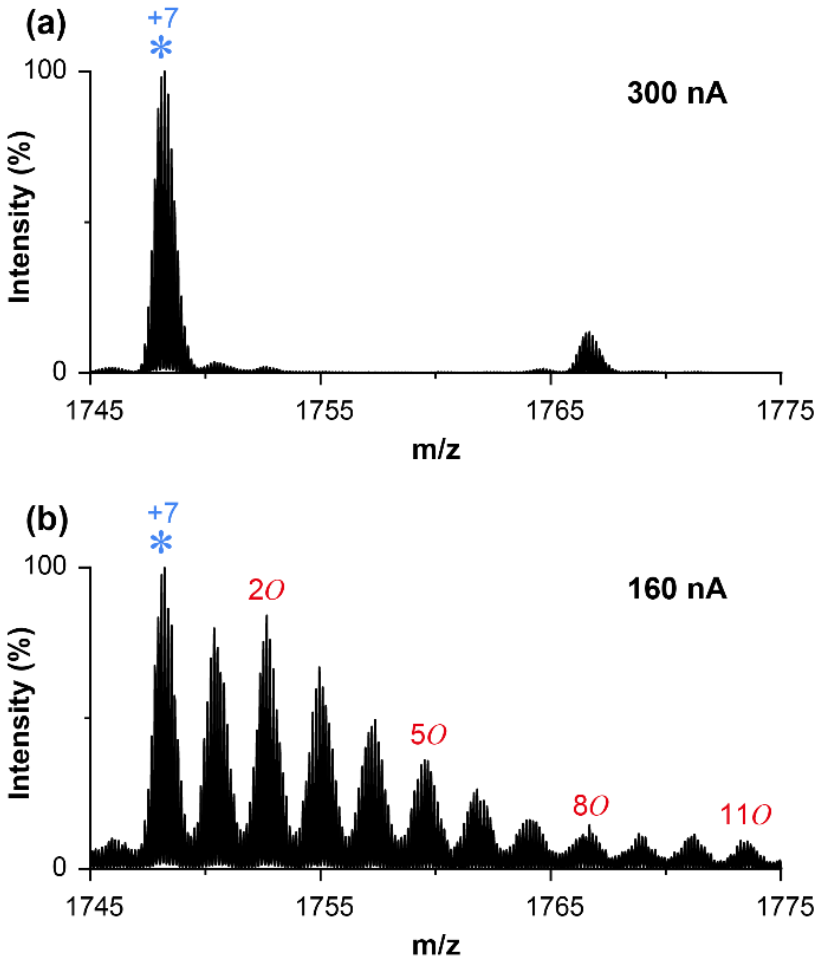

Figure 4.19. Oxidation of cytochrome c using fine glass capillary with i.d. of 5 μm.
a) Mass spectrum acquired at 300 nA spray current.
b) Mass spectrum acquired at 160 nA.
Sample: 20 μM cytochrome c in 1 M ammonium formate aqueous solution.
Operating gas: air at 0.5 MPa.

Conclusions

We have demonstrated an efficient oxidation method that relies on the strong electrical field on the surface of a charged droplet or at the tip of a Taylor cone. The degree of oxidation was highly tunable by varying the flow rate of the electrospray, hence changing the size of the initial charge droplet and the radius of curvature at the tip of the Taylor cone. On-demand oxidation had been performed by precision tuning of the nano-flow rate using HV modulation with spray current as the feedback signal. The response of oxidation to the measured spray current was almost instantaneous. Using the scaling laws for electrospray, the threshold electrical field to induce the oxidation was found to be in the order of 1 V/nm. The isotope labeling showed that the oxygen atoms originated from the gas phase. Ozone is commonly produced in electrical discharge but it was found not to be the final reactive oxygen species that reacted with the analytes. We postulate that the split oxygen atoms generated by electron activation under the strong electrical field reacted directly with the analytes to form the observed dominant oxidation species. The oxygen atom and the cogenerated ozone also reacted with water to form hydroxy radicals. The controlled oxidation can find application in the labeling of the analyte and the selective fragmentation that targets the oxygen-labeled location for structural analysis. As the present method only requires high electrical conductivity, the buffer solutions commonly used in the native electrospray to maintain a near physiological pH can be employed directly to perform native ESI-MS and oxidation analysis on the same sample in a single emitter. The use of electrical field strength, which can be estimated from the spray current, as the universal control parameter also improves the reproducibility across different emitters and solvent systems.

Chapter 5: Novel application of HP nano-ESI: Probing acid-induced compaction of denatured proteins

Summary

A further increase in acidity in the most denaturing acidic solution is known to induce compaction of the fully unfolded protein into a molten globule with a compact conformation. The phenomenon of "*acid-induced folding of proteins*" takes place at ~pH 1 in strong acid-aqueous solutions with high electrical conductivity and surface tension, a condition that is difficult to handle using conventional electrospray ionization methods for mass spectrometry. Here, the high-pressure electrospray (HP-ESI) is used to produce well-resolved mass spectra for proteins in strong acids with a pH as low as 1. The compaction of protein conformation is indicated by a large shift in the charge state from high charges to native-like low charges. The addition of salt to the protein in the most denaturing condition also reproduces the compaction effect, thereby supporting the role of anions in this phenomenon. Similar compaction of protein is also observed in organic solvent/acid mixtures. The charge state of the compacted protein depends on the type of anions that formed ion pairs with the positive charge on the protein. The dissociation of ion pairs during the ionization process forms neutral acids that can be observed by HP-ESI using a soft ion introduction configuration.

Introduction

A correctly folded protein in its native state has a tight three-dimensional conformation that is biologically active. As the higher-order structure of a native protein is maintained by the non-covalent interactions, it can be disrupted by denaturants such as harsh pH, high temperature, and organic solvent, resulting in the unfolding of the polypeptide chain.[114–116] Lowering the pH of protein solution by adding acid to around pH 2 is known to induce a fully unfolded conformation for proteins such as cytochrome c and apomyoglobin.[117] However, further increasing the acid concentration would induce a refolding of these proteins at ~ pH 1 into an "acid denatured" but compact molten globule state.[117] The "acid-induced folding of proteins" was first reported by Fink and coworkers using circular

dichroism spectroscopy.[117–119] The compaction of the denatured protein was attributed to the binding of anions that minimizes the effect of intramolecular charge repulsion that is responsible for protein unfolding. [117–119] The ionization state of the protein is unaffected as it is already maximally protonated at pH 2.

Mass spectrometry on the other hand is an indispensable analytical method for proteomics that provides a wealth of information for accurate molecular weight, structural elucidation, and isotopic distribution. Electrospray ionization (ESI) is a "soft" ionization method for mass spectrometry to generate intact protein ions with little or no fragmentation.[9,120] The gentle release of protein into the gas phase can even preserve the non-covalent bonding and the solution structure of proteins to a certain extent.[121] The charge state distribution (CSD) for the protein ions is influenced by the ionization route and the protein conformation at the last stage of desolvation. A compact molecule is expected to have a smaller effective area to accommodate the excess charges at the final stage of the desolvation process.[122] If the ionization route is via the charge residue model, the Rayleigh limit, i.e. the largest attainable charge for the last-stage droplet is correlated to the protein hydrodynamic radius.[60] Other ionization routes such as ion evaporation, chain, and bead ejections[13,16,123] are also expected to affect the CSD. Although the research on further understating those details is still ongoing, it is known that the charge state distribution (CSD) of protein ions generated by positive-mode ESI reflects the protein conformation in the solution.[114,124,125] For example, denatured proteins are manifested in the mass spectrum by a wide CSD with higher charge states (lower m/z), and more tightly folded proteins tend to exhibit a narrow CSD with lower charge states (higher m/z).

Here we perform the acid-induced compaction of the denatured cytochrome c, apomyoglobin, and ubiquitin in aqueous hydrochloric acid (HCl) and trifluoroacetic acid (TFA) at pH 1 and investigate the effect of salt and organic solvent using high-pressure electrospray mass spectrometry (HP-ESI-MS). The possible effect of acid-induced folding of protein on ESI mass spectra at low pH was first mentioned by Konermann & Douglas.[126] Low charge state peaks attributed to the acid-induced folded protein were observed by McLuckey and colleagues using standard nanoESI,[127,128] but the ion signal was weak and the peaks were not well resolved. Under ordinary atmospheric pressure conditions, the large surface tension and high electrical conductivity of the highly acidic aqueous solutions make the sprayer prone to electric discharge, which in turn affects the stability of the

electrospray, the efficiency of ionization, and the quality of the mass spectrum. The discharge issue is overcome by generating the electrospray inside a high-pressure gas environment, a technique that has been developed in our laboratory.[33,104,129] The reduced mean free path for gas molecules and electron under high pressure increase the gaseous breakdown voltage for discharge. For a special case of a homogeneous electric field, the relationship between the pressure and gaseous breakdown voltage is given by Paschen's law. Since the onset voltage for electrospray is unaffected by the gas pressure,[23] a high-pressure environment enables the formation of a highly stable Taylor cone even for pure water with large surface tension. Recently, HP-nanoESI of the highly conductive aqueous solution has also been performed using commercial pipet tips as the emitter,[33] eliminating the problems of clogging, interaction with the emitter inner surface, and the tip-to-tip reproducibility faced by the conventional pulled-glass capillary emitters. In the absence of discharge, the droplet size and the flow rate of a voltage-controlled ESI can also be accurately tuned using spray current as the monitor to manipulate the ionization species.[130]

Experimental section

Electrospray ion source

The schematic of the HP-ESI source is shown in Figure 5.1. The emitter was a micropipette tip with a 0.37 mm inner diameter (Eppendorf). A platinum wire (dia: 0.2 mm, Nilaco) was used as the electrode to make contact with the liquid inside the emitter. The whole emitter tip was placed inside a high-pressure vessel which consisted of an aluminum chamber and an insulating flange made of Polyetheretherketone (PEEK). The ion source was pressurized to 0.5 MPa gauge pressure using dry air from an air compressor (Anest Iwata). The pressure was monitored using a digital pressure gauge (SMC) and the gas flow rate was measured using a mass flow meter (Azbil). The spray current was obtained by measuring the voltage drop across a 1 MΩ resistor connected in series with the emitter using a custom-made isolation amplifier (ISO 121BG, Texas Instrument). The amplified signal was coupled to the multimeter (Agilent 34461A). The flow rate of the solution was tuned by adjusting the emitter voltage. For the electrospray in the steady cone-jet mode, the flow rate Q was estimated from

the spray current I using the equation $I = f(\varepsilon_r)\left(\frac{\gamma KQ}{\varepsilon_r}\right)^{\frac{1}{2}}$ developed by Fernández de la Mora & Loscertales,[24] where ε_r is relativity permittivity, γ is surface tension, K is the electric conductivity of the liquid, and $f(\varepsilon_r)$ = 18 for aqueous solutions. The radius of the initial droplet R_o was estimated by $R_o \sim (\varepsilon_o \varepsilon_r Q/K)^{1/3}$, where ε_o is the vacuum permittivity.[24] The fine capillary-based nanoESI-MS was performed using commercial pulled-glass capillaries with i.d. of 5 μm (Humanix, Hiroshima) and 1 μm (New Objective, MA).

Mass spectrometer

The ion source was connected directly to a benchtop Orbitrap mass spectrometer (Exactive, Thermo Fisher Scientific, Bremen, Germany) using a custom-made ion transmission tube (i.d.: 0.25 mm, length: 20 cm). Unless otherwise specified, mass spectra were acquired using the high-pressure ESI source. The default instrumental settings for the mass spectrometer were as follows: the temperature for the ion transport tube: 300 C, capillary and tube-lens voltage: 120 V. The maximum ion injection time was 50 ms. The pressure in the fore vacuum was ~1 mbar.

Sample preparation

Ubiquitin, bovine cytochrome c, myoglobin, and acetonitrile were from Sigma Aldrich (St. Louis, US). Formic acid (FA), trifluoroacetic acid (TFA), hydrochloric acid (HCl), ethanol, and ammonium chloride were from Kanto Chemical (Tokyo, Japan). Pure water was prepared using Simplicity UV (Millipore, Bedford, MA). All the chemicals were used without further purification. The electric conductivity and pH of the solution were measured using a conductivity and pH meter (Mettler Toledo SevenExcellence). The pH of solutions was adjusted by the slow addition of a small amount of concentrated HCl to the sample initially prepared in pure water. The sample was vigorously stirred with a magnetic stirrer with its pH measured using the preparation process.

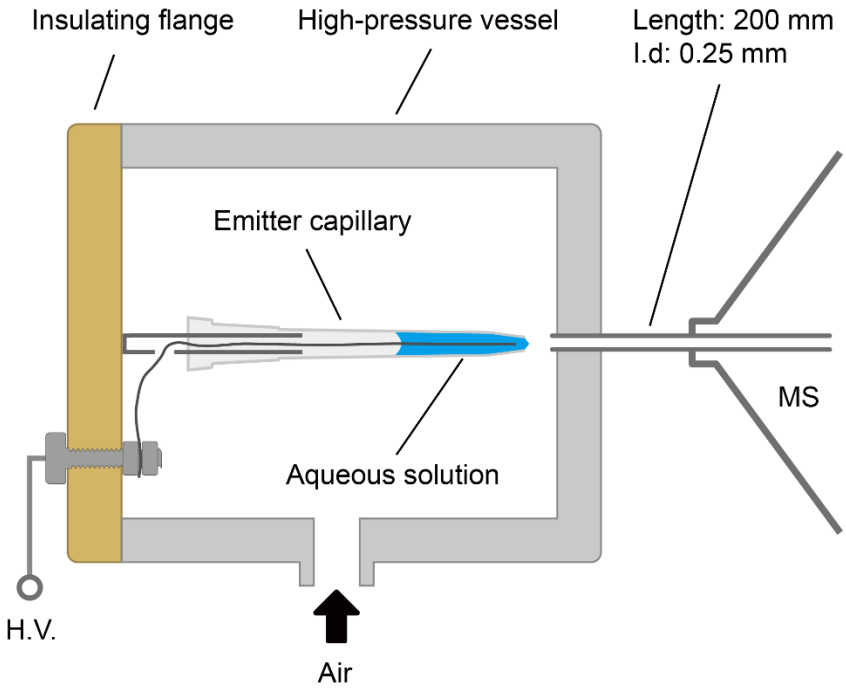

Figure 5.1. Schematic of the high-pressure nanoESI ion source. A micropipette tip was used as the emitter. A platinum wire was used as the electrode. The high-pressure ion source was connected directly to the mass spectrometer using an ion transmission tube with an inner diameter of 0.25mm.

Results and Discussion

High-pressure ESI mass spectrometry

The effect of pH on proteins was first evaluated by acquiring the HP-ESI mass spectra of cytochrome c in HCl solutions titrated to different pH (Figure 5.2). At pH 5, the low charge states of the protonated cytochrome c with +7 as the dominant peak indicated a still tightly folded structure (Figure 5.2a). CSD at pH 3 was bimodal due to the presence of highly unfolded and partially folded proteins (Figure 5.2b). The highly charged distribution was obtained at pH 2 (Figure 5.2c), in agreement with the observation by far-UV circular dichroism that the cytochrome c was fully unfolded under that condition.6 A further increase in acidity to pH 1 changed the CSD abruptly to lower charges centering at +6 (Figure 5.2d), a clear indication of cytochrome c assuming a compact conformation. When the same measurement was performed using the standard atmospheric pressure nanoESI using a pulled-glass capillary (i.d.: 5 μm), similar results were reproduced only for pH 5, 3, and 2 (Figures 5.3a-5.3c). At pH 1, the mass spectrum for cytochrome c was not well-resolved, although the low S/N peaks indicated the occurrence of protein compaction (Figure 5.3d). When the same nanoESI emitter was operated under high pressure, strong peaks, and a clean mass spectrum were obtained (Figure 5.4). A similar trend was also observed using nanoESI capillary with 1 μm i.d. (Figure 5.5) These findings highlight the distinct advantage of the high-pressure electrospray ion source over the conventional atmospheric pressure source for highly acidic solutions.

Figure 5.6 shows the decreasing pH effect on myoglobin in TFA. At pH 4, myoglobin was only partially unfolded and all detected ions were due to those of holomyoblobin with heme remaining intact (5.6a). This mass spectrum is similar to the typical “native mass spectrum” obtained using ammonium acetate as a "buffer",[131] although the role of ammonium salts in maintaining the native state of proteins is still controversial.[132–134] The abundance of the highly charged apomyoglobin (without heme) started to increase at pH 3.5 (5.6b) and reached its maximum at ~ pH 3 (5.6c). Further decreasing the pH to 1 significantly raised the intensity for charge states +7 and +6 for the compacted apomyoglobin (5.6d). Holomyoglobin (with heme) was not detected at that low pH. This result verified that the compacted molten globule state of apomyoglobin was significantly different from the native

state of myoglobin.

The HP-ESI-MS of proteins in acidic aqueous solutions was performed using a high-pressure ESI ion pressurized to 0.5 MPa gauge pressure with compressed air (Figure 5.1). The emitter was a micropipette tip with a 0.37 mm inner diameter that is placed inside a hermetically sealed high-pressure chamber. The ion source was connected directly to a commercial mass spectrometer using a custom-made ion transmission tube (i.d.: 0.25 mm, length: 20 cm). The flow rate was tuned by adjusting the emitter voltage and the measured spray current was used to estimate the solution flow rate according to established scaling laws for electrospray.[33,104] See supporting info for the experimental details. Unless otherwise specified, mass spectra were acquired using high-pressure ESI with a micropipette tip as the emitter.

The effect of pH on proteins was first evaluated by acquiring the HP-ESI mass spectra of cytochrome c in HCl solutions titrated to different pH (Figure 5.2). At pH 5, the low charge states of the protonated cytochrome c with +7 as the dominant peak indicated a still tightly folded structure (Figure 5.2a). CSD at pH 3 was bimodal due to the presence of highly unfolded and partially folded proteins (Figure 5.2b). The highly charged distribution was obtained at pH 2 (Figure 5.2c), in agreement with the observation by optical spectroscopy that the cytochrome c was fully unfolded under that condition. A further increase in acidity to pH 1 changed the CSD abruptly to lower charges centering at +6 (Figure 5.2d), a clear indication of refolding for cytochrome c. When the same measurement was performed using the standard atmospheric pressure nanoESI using a pulled-glass capillary, similar results were reproduced only for pH 5, 3, and 2 (Figures 5.3a-5.3c). At pH 1, the mass spectrum for cytochrome c was not well-resolved, there was a sign of protein refolding (Figure 5.3d). When the same nanoESI emitter was operated under high-pressure, strong peaks and a clean mass spectrum were obtained (Figure 5.4). These findings highlight the distinct advantage of the high-pressure electrospray ion source over the conventional atmospheric pressure source for highly acidic solutions.

Figure 5.5 shows the decreasing pH effect on myoglobin in TFA. At pH 4, myoglobin was only partially unfolded and all detected ions were due to those of holomyoblobin with heme remaining intact (2a). This mass spectrum is similar to the typical “native mass spectrum” obtained using

ammonium acetate as a "buffer",[131] although the role of ammonium salts in maintaining the native state of proteins is still controversial.[132–134] The abundance of the highly charged apomyoglobin (without heme) started to increase at pH 3.5 (2b) and reached its maximum at ~ pH 3 (2c). Further decreasing the pH to 1 significantly raised the intensity for charge states +7 and +6 for the refolded apomyoglobin. Holomyoglobin (with heme) was not detected at that low pH. This result verified that the refolded molten globule state of myoglobin was significantly different from its native state.

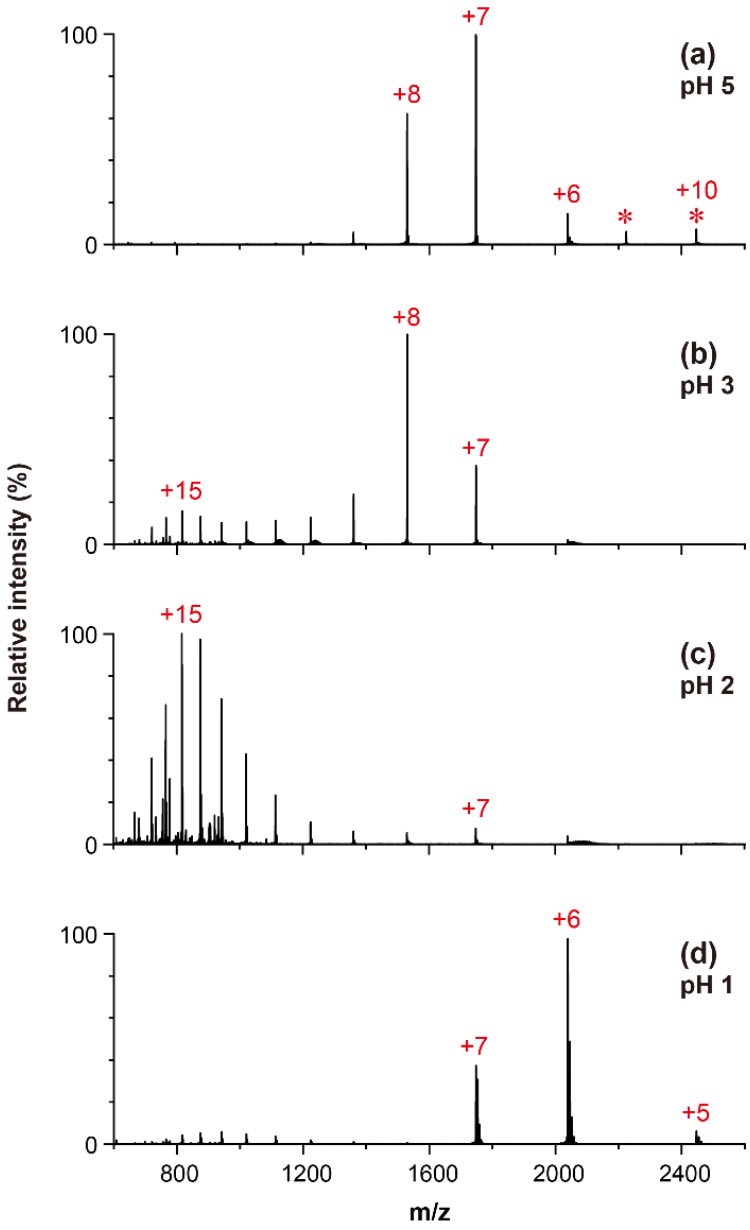

Figure 5.2. HP-ESI mass spectra of 10 μM cytochrome c in HCl aqueous solutions with different pH. The asterisk in (a) denotes the peak for the dimer.

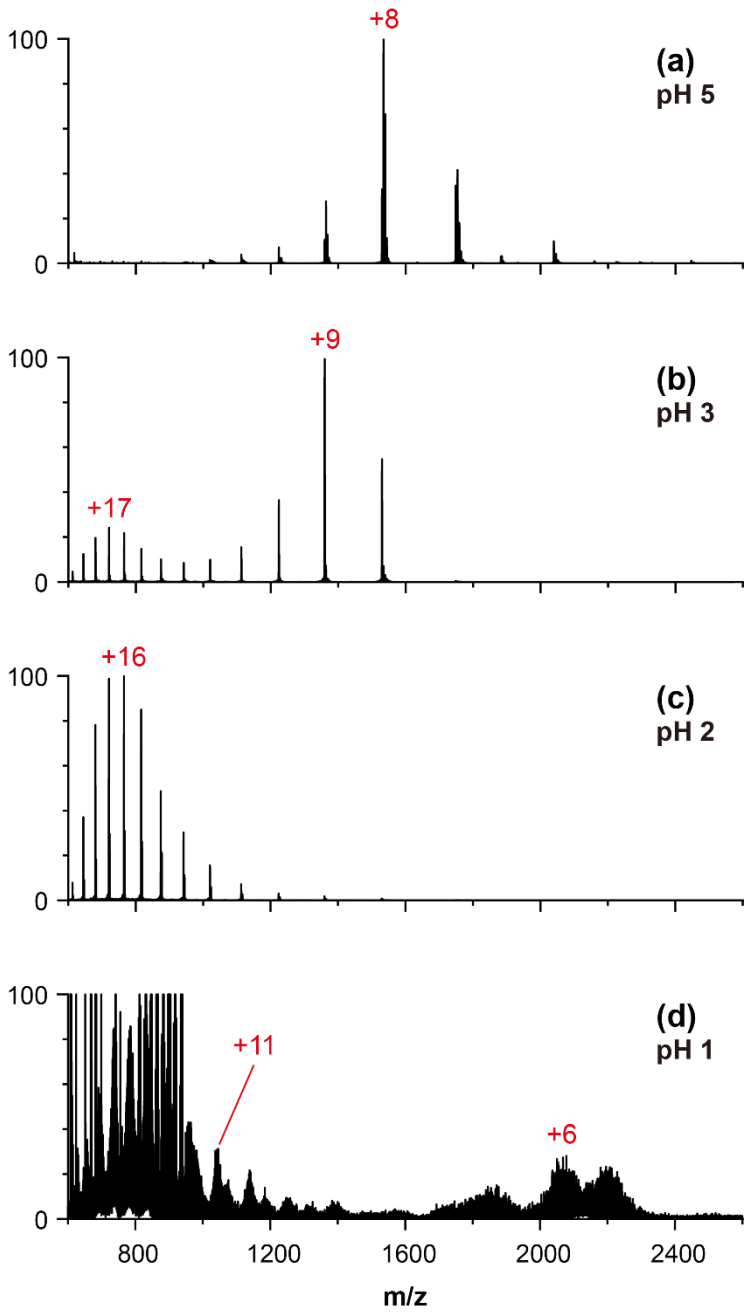

Figure 5.3. Atmospheric pressure nanoESI mass spectra of 10 μM cytochrome c in hydrochloric acid aqueous solutions of different pH obtained using standard pulled glass capillaries (tip i.d. = 5 μm).

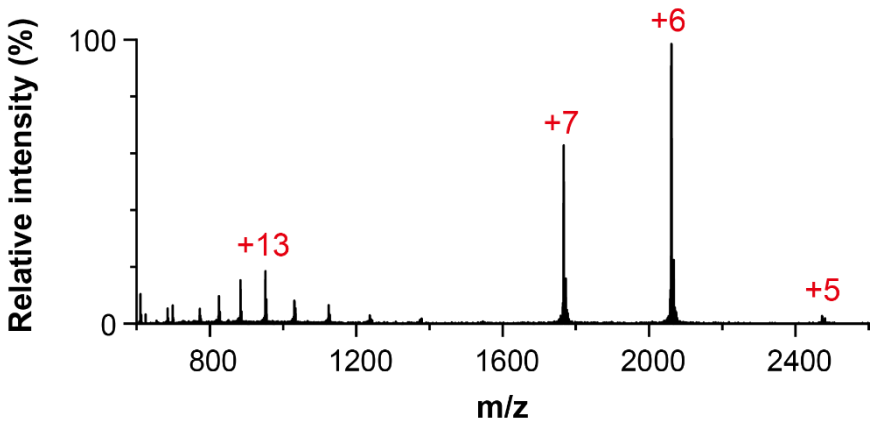

Figure 5.4. High-pressure mass spectra of 10 μM cytochrome c at pH 1 obtained from pulled glass capillary emitter (i.d. 5 μm) placed in a high-pressure ion source. Cytochrome c is prepared in hydrochloric acid aqueous solution.

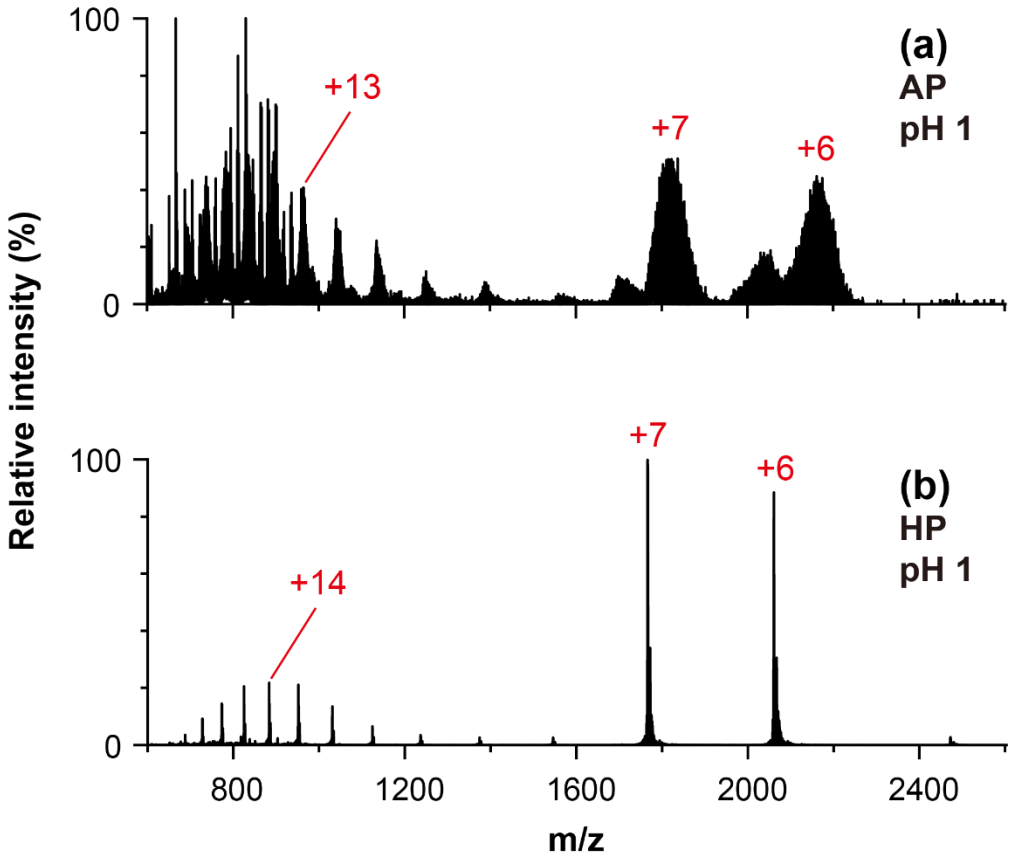

Figure 5.5. Atmospheric pressure (a) and high pressure (b) nanoESI mass spectra of 10 μM cytochrome c in hydrochloric acid aqueous solution of pH 1 obtained using commercial pulled glass capillaries (tip i.d. = 1 μm).

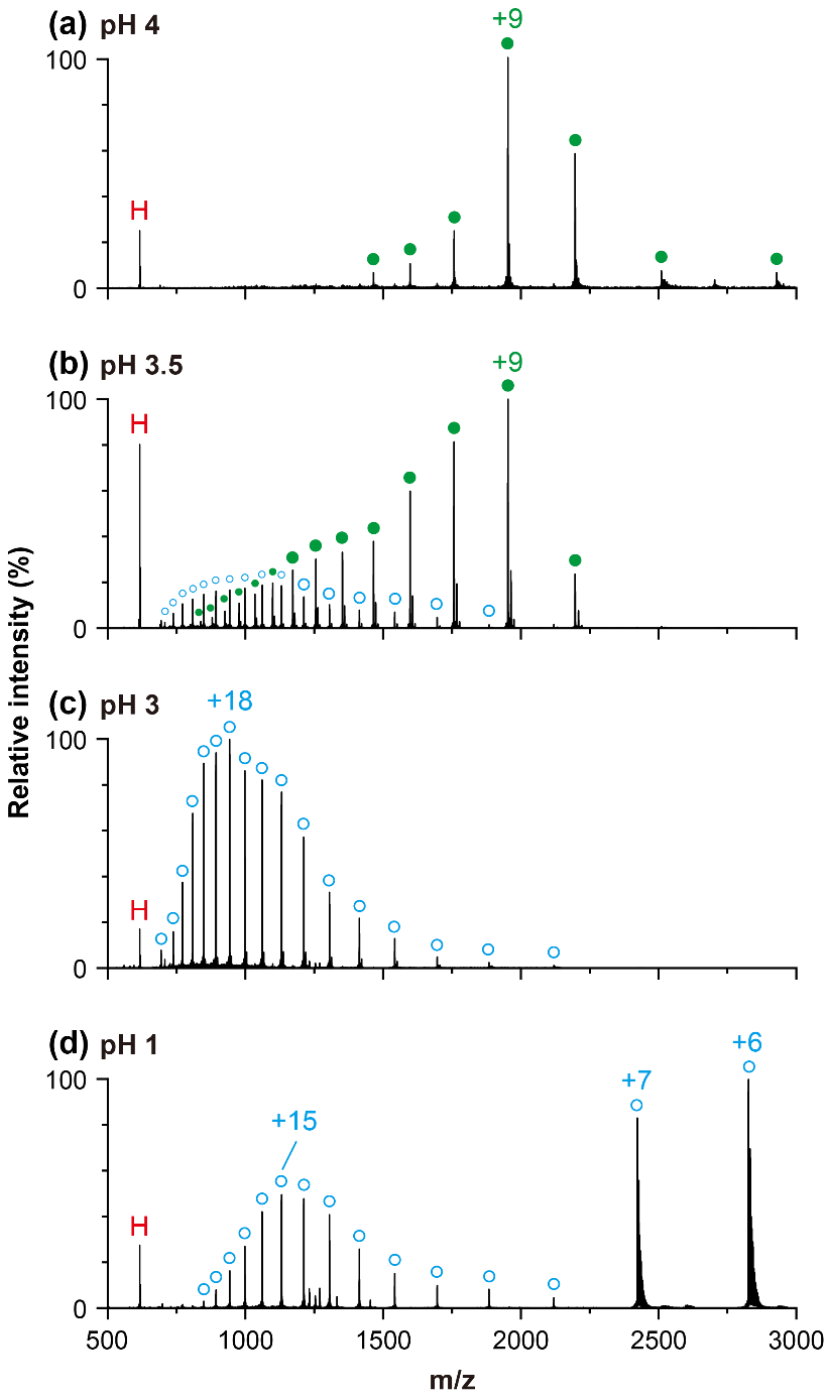

Figure 5.6. HP-ESI mass spectra of 10 μM myoglobin in trifluoroacetic acid (TFA) aqueous solutions with different pH. H denotes heme, the solid green circle denotes holo, and the open blue circle denotes apo myoglobin.

Average charge state

Figure 5.7 summarizes the effect of pH on the average charge states q_{av} for cytochrome c (CC), myoglobin (MB), and ubiquitin (UB) prepared in HCl and TFA aqueous solutions. The average charge state is calculated by $q_{av} = \sum n\, I_n / \sum I_n$, where n is the charge state, and I_n is the respective ion intensity. The corresponding mass spectra are shown in Figures 5.8-5.13. Both acids produced a closely resembling trend for each protein, indicating that the $q_{av}(p\mathrm{H})$ was dependent on the intrinsic properties of the proteins. The highest average charge state for CC was located at pH 2 which is consistent with the full unfolding observed using circular dichroism.[119] As for myoglobin, the q_{av} peaked at pH 3 (Figure 5.7b. The change of average charge state was not as abrupt because the highly charge species (unfolded species) were still present in high abundance at pH 1 (Figures 5.6, 5.10-5.11). The similar unfolding and refolding effect was also observed for ubiquitin (Figures 5.7c, 5.12, 5.13) in constract to a earlier result that UB assumed native-like spectroscopic spectra down to ≤ 1.[119] The acid-induced compaction effect was also observed using formic acid (Figures 5.14-5.15). Different from the cases of HCl and TFA, the dominant charge state for the compacted species was 1~2 higher. The small variation in charge state is believed to be related to another phenomenon: gas phase charge reduction that involves the ion pairing and the gas phase ion chemistry.[135,136] That anion-dependent effect will be further discussed in the latter section. It is further noted that due to a lower pKa, the concentration of formic acid needed to attain pH 1 was much higher (~55 % v/v), resulting in a fluidic condition that was quite different from TFA and HCl.

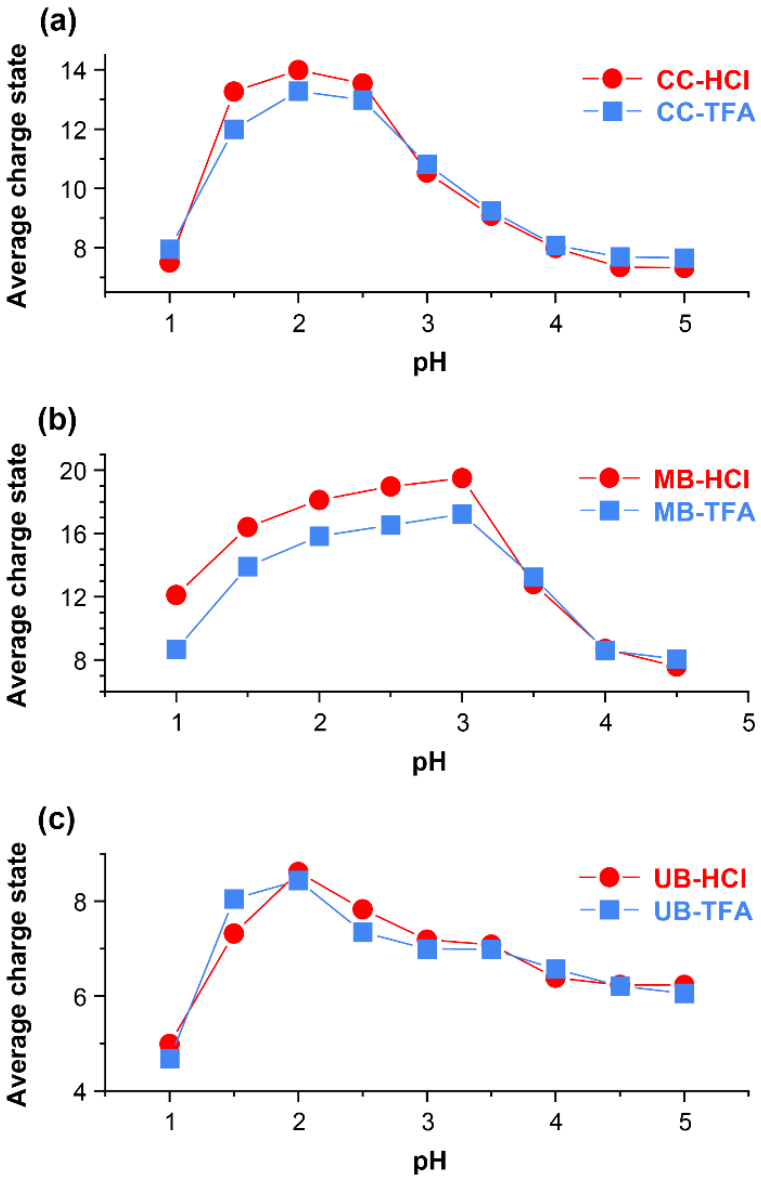

Figure 5.7. Average charge states of a) cytochrome c, b) myoglobin, and c) ubiquitin versus pH obtained in HCl (red circle) and TFA (blue square) aqueous solutions. Protein concentration: 10 μM.

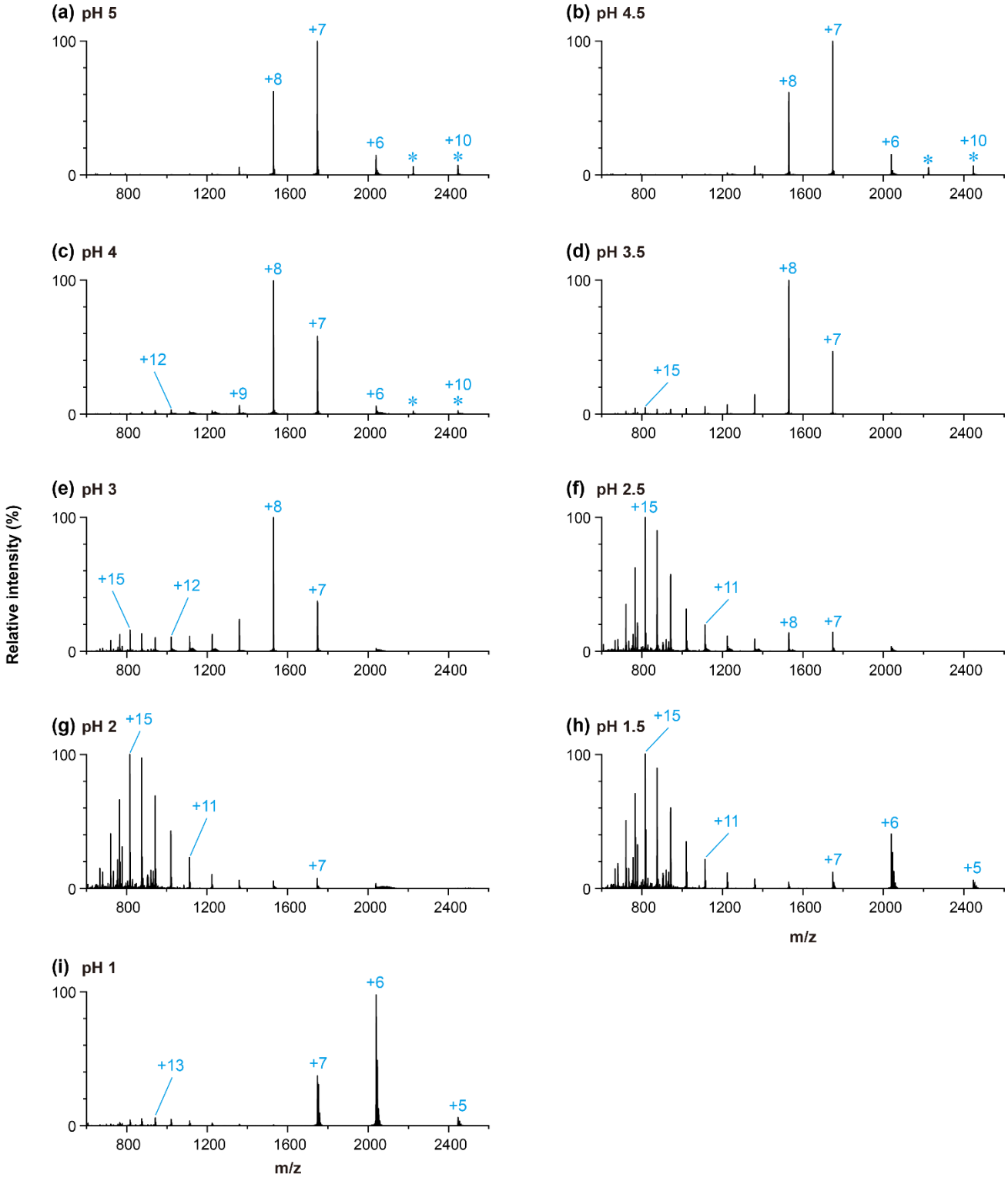

Figure 5.8. High-pressure ESI mass spectra of 10 μM cytochrome c in hydrochloric acid aqueous solutions with different pH.

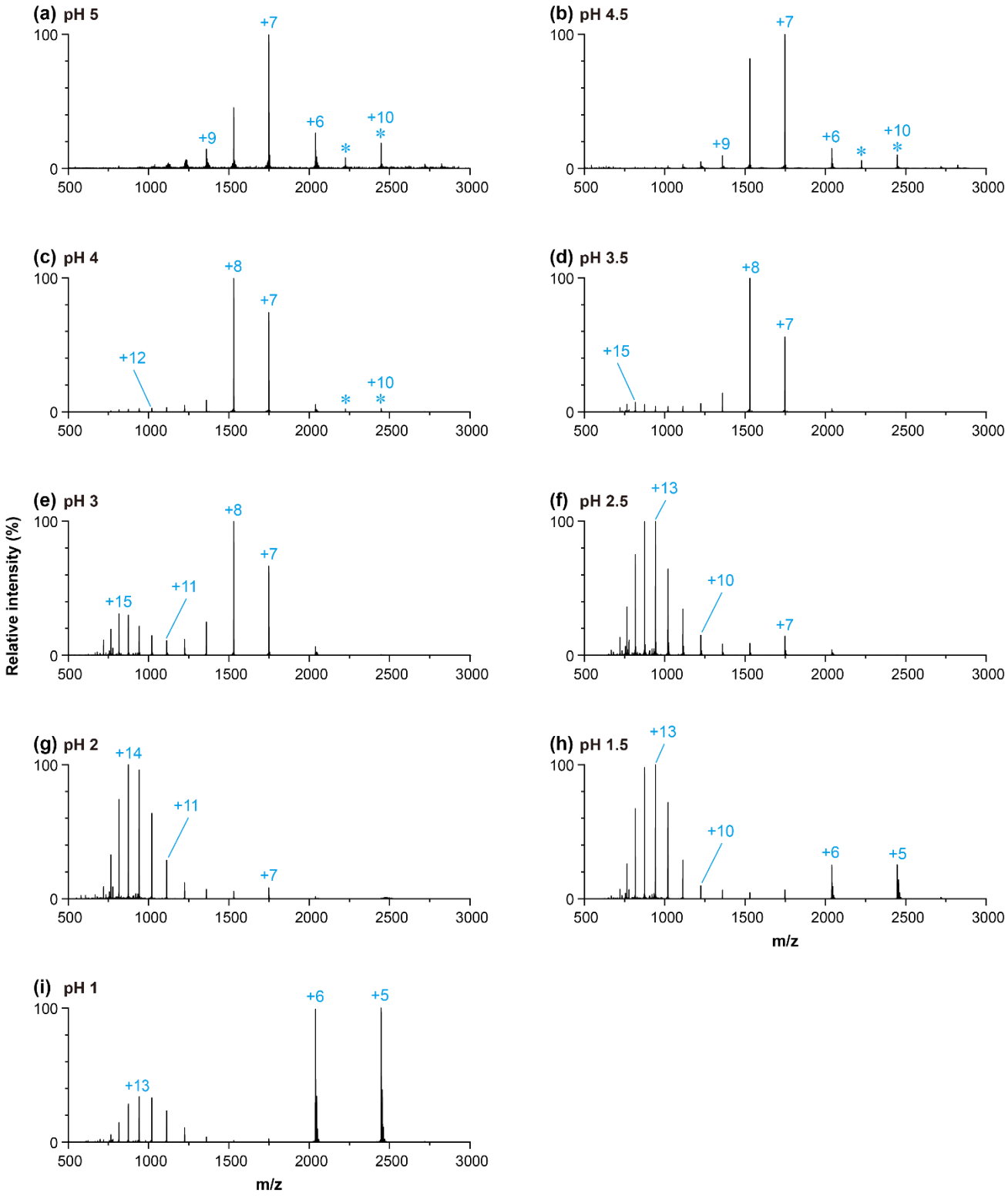

Figure 5.9. High-pressure ESI mass spectra of 10 μM cytochrome *c* in trifluoroacetic acid aqueous solution with different pH.

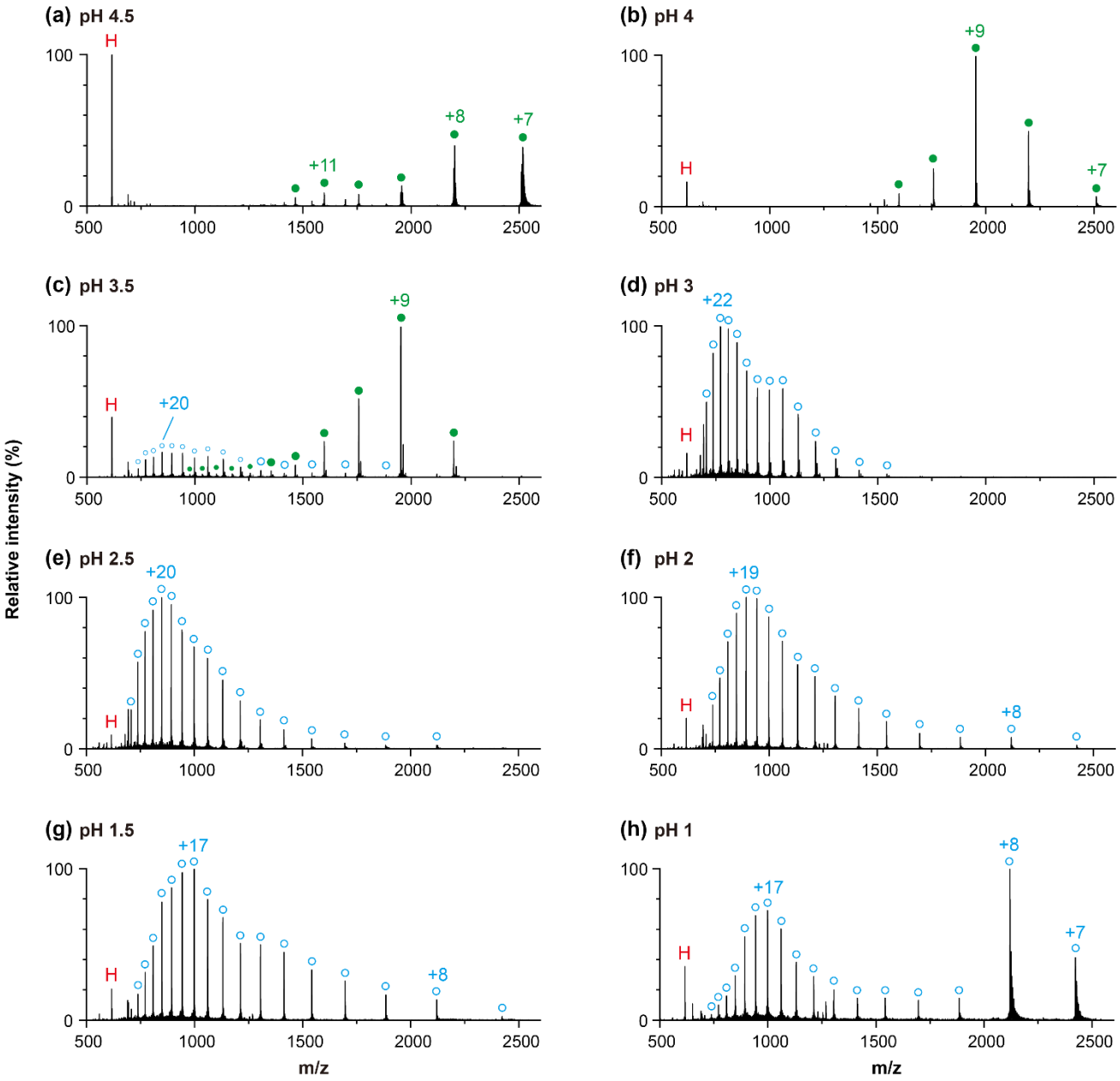

Figure 5.10. High-pressure ESI mass spectra of 10 μM myoglobin in hydrochloric acid aqueous solutions with different pH. H denotes heme, the solid green circle denotes holo, and the open blue circle denotes apo myoglobin.

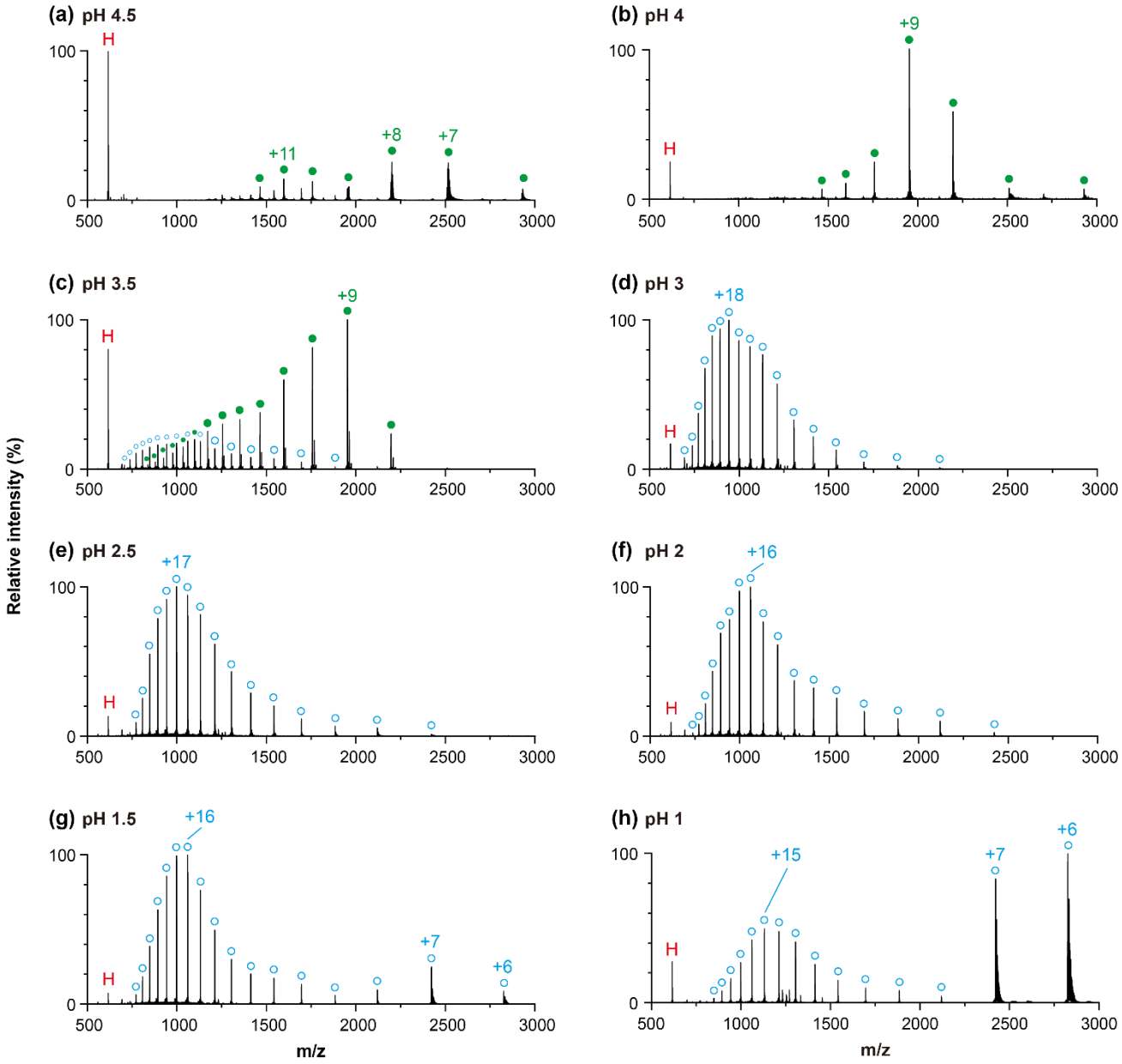

Figure 5.11. High-pressure ESI mass spectra of 10 μM myoglobin in trifluoroacetic acid aqueous solution of different pH. H denotes heme, the solid green circle denotes holo, and the open blue circle denotes apo myoglobin.

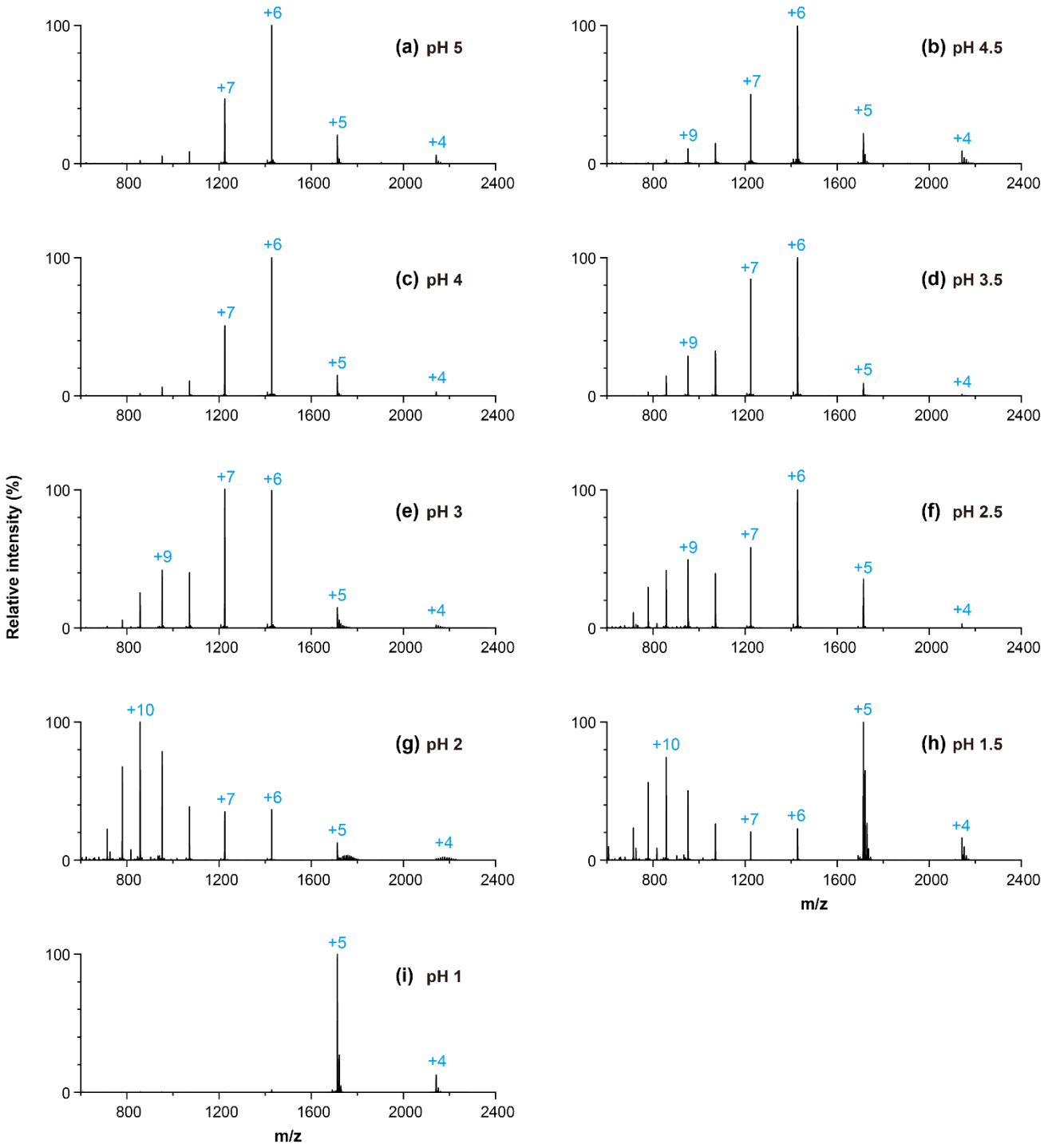

Figure 5.12. High-pressure ESI mass spectra of 10 μM ubiquitin in hydrochloric acid aqueous solution with different pH.

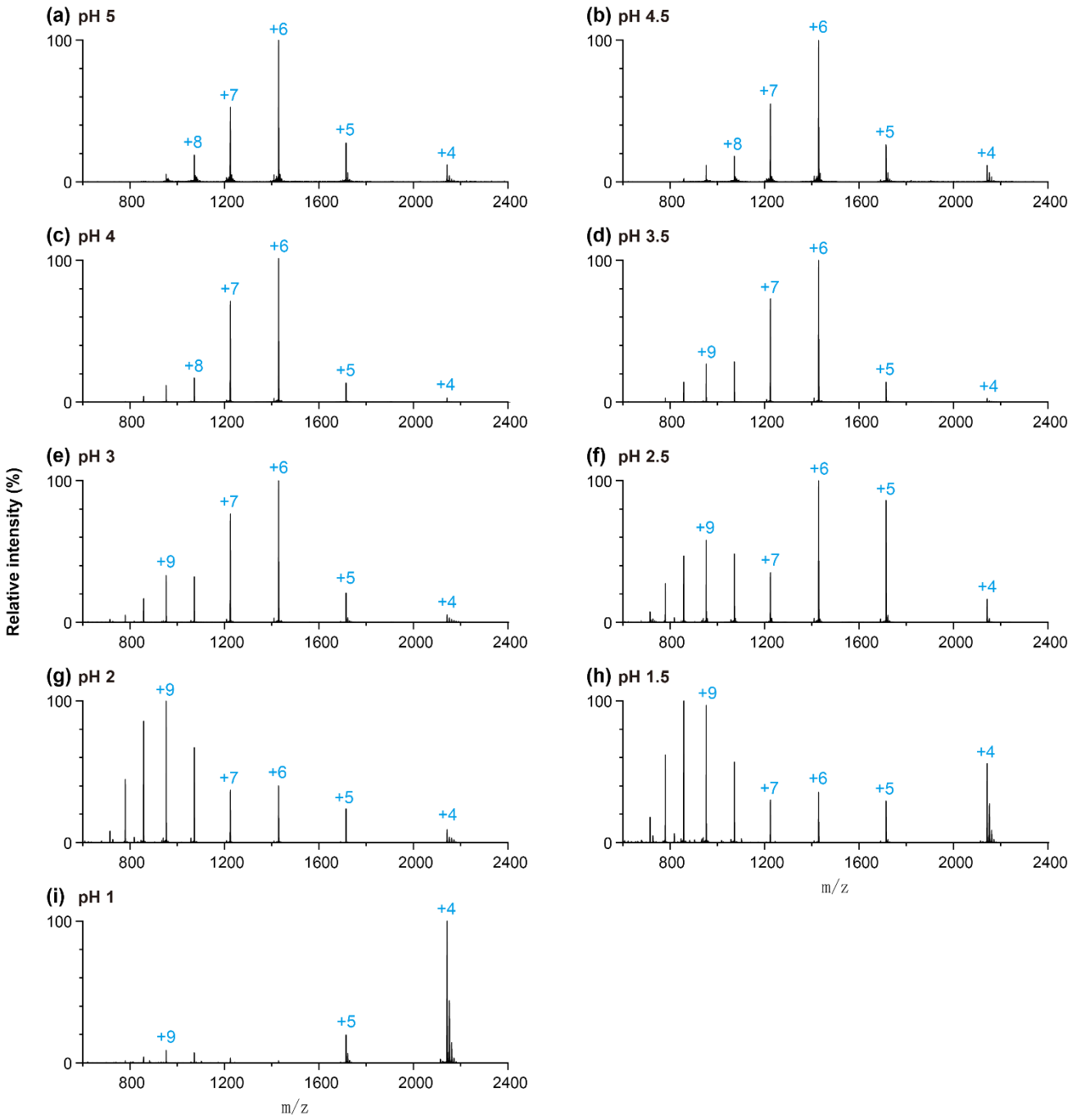

Figure 5.13. High-pressure ESI mass spectra of 10 μM ubiquitin in hydrochloric acid aqueous solution with different pH.

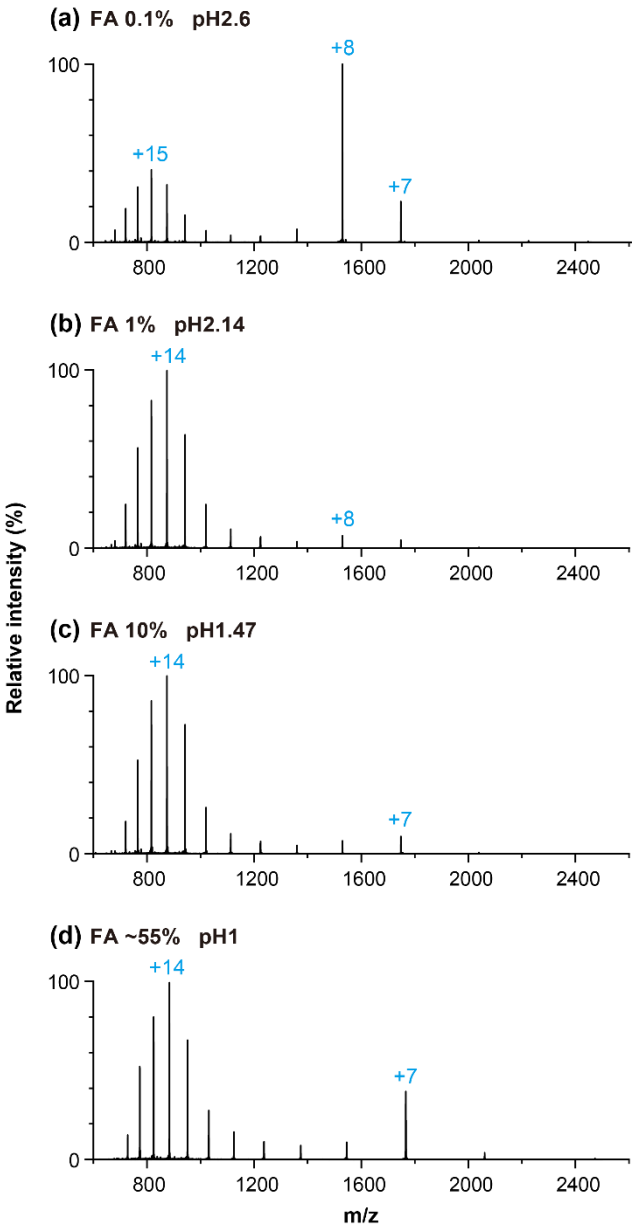

Figure 5.14. High-pressure ESI mass spectra of 10 μM cytochrome c in formic acid aqueous solution with different pH. For (d), the solution is titrated to pH 1. The concentration is ~55%.

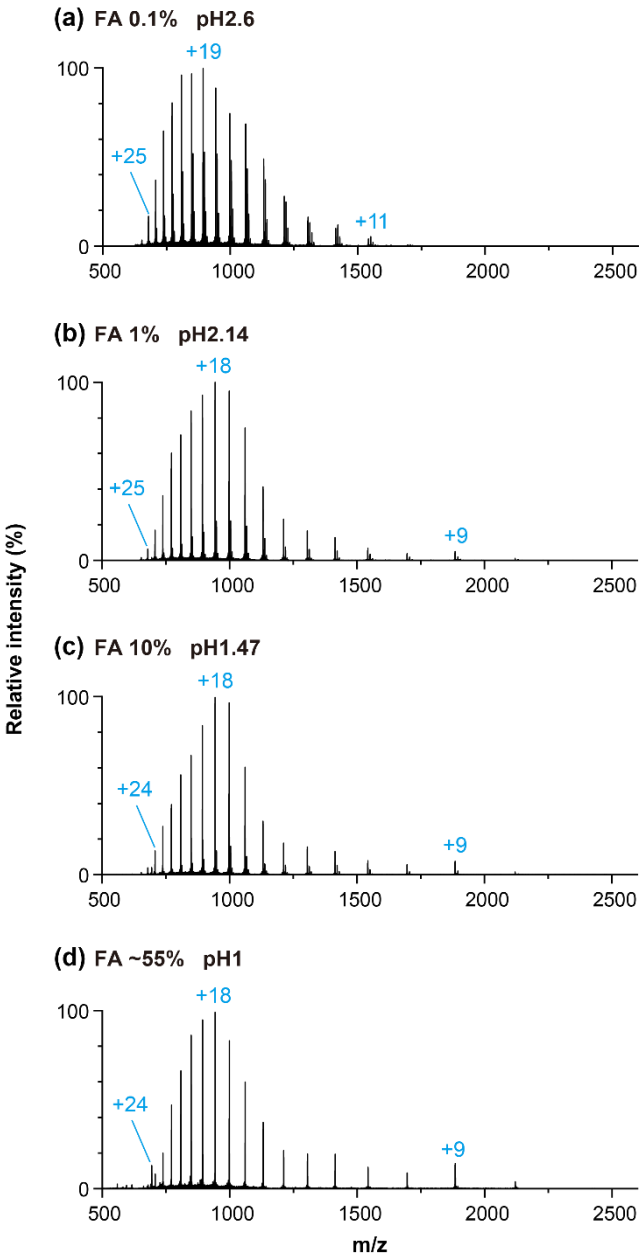

Figure 5.15. High-pressure ESI mass spectra of 10 μM myoglobin in formic acid aqueous solution with different pH. For (d), the solution is titrated to pH 1. The concentration is ~55%.

Effect of salt addition

Anion was previously believed to be the main factor for protein refolding.[117–119] Here, the effect of anion concentrations was examined by adding ammonium chloride to the cytochrome c solution with the most denaturing pH. NH4Cl was chosen because the formation of salt clusters and the adduction to the protein was less compared to other common chloride salts such as NaCl, KCl, and LiCl. Our previous results also showed that a high concentration of NaCl produced a high abundance of highly charged species for proteins even at pH 7.[32,33] The mechanism was yet not understood but that phenomenon hinders the use of NaCl in the present study. Figure 5.16a shows the decrease of the average charge state of cytochrome c with the concentration of NH4Cl in an HCl solution with pH 2 (see Figure 5.17 for mass spectra). At the lowest concentration of 1 mM, the q_{av} was 14, almost equal to that without anion addition, though a low abundance of charge state +6 was also observed (Figure 5.16b). The mass spectra became bimodal with the increase of low-charge state species (Figures 5.16c & 5.16d). This result indicates the compaction was taking place when extra anion was added to the protein that was already maximally protonated. A difference with the result obtained from the pure HCl solution with pH 1 was that the dominant low charge state species was +7 rather than +6.

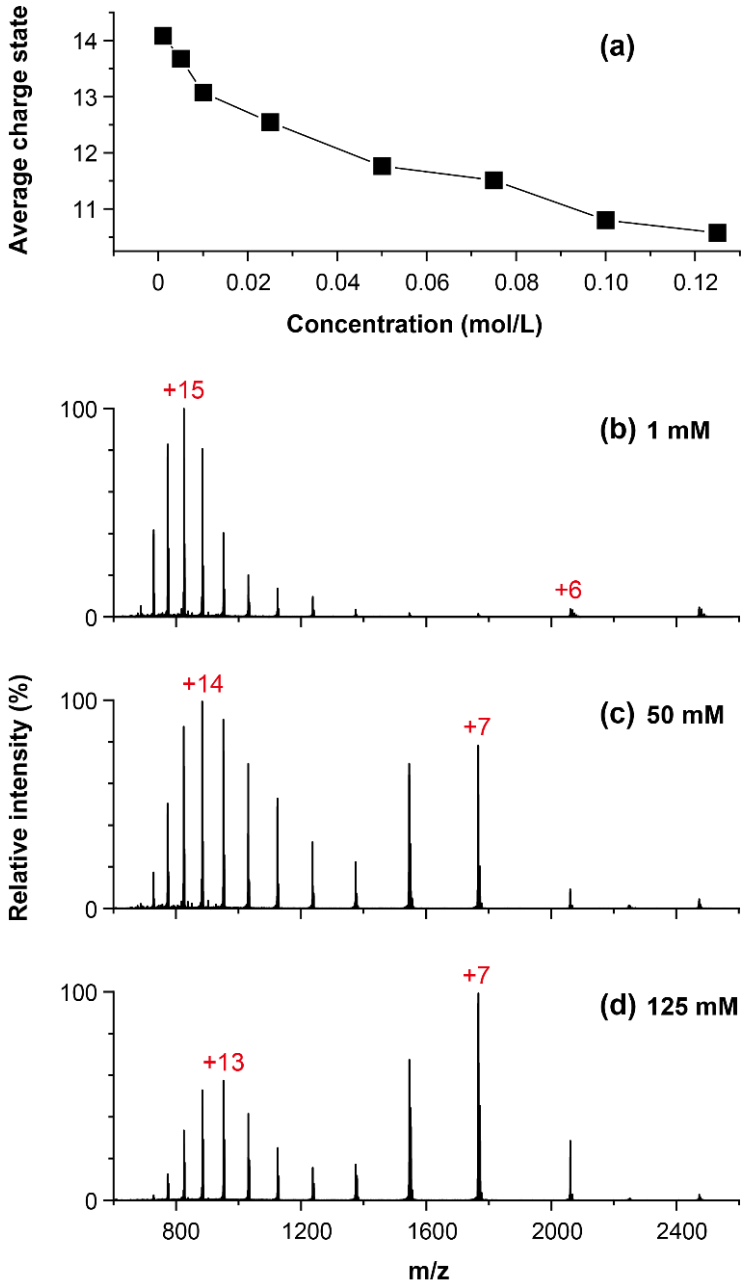

Figure 5.16. a) Average charge states of 10 μM cytochrome c versus concentration of ammonium chloride obtained in HCl (pH2) aqueous solution. (b)-(d) Mass spectra of cytochrome c with ammonium chloride concentrations of 1 mM (b), 50 mM (c), and 125 mM (d).

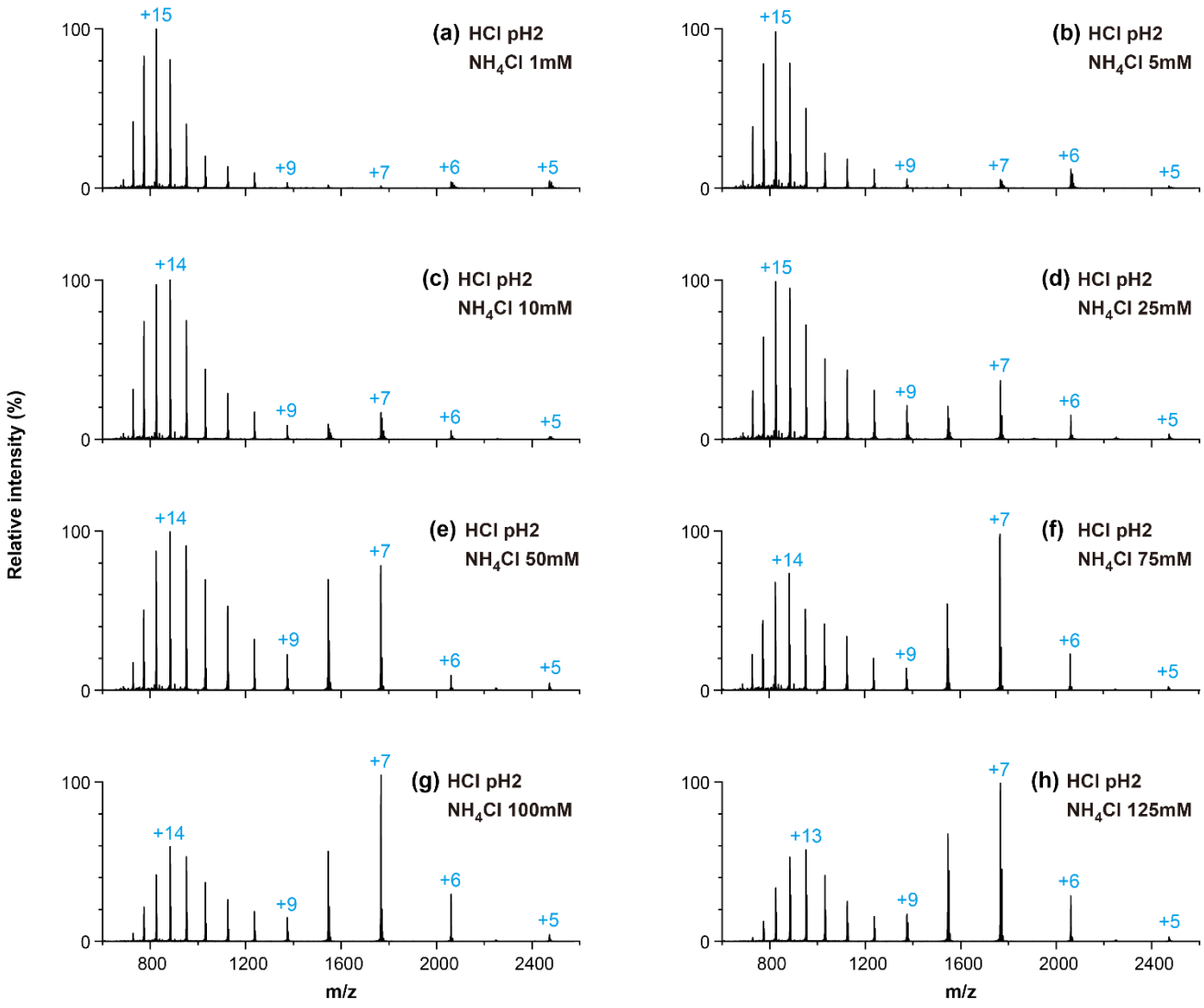

Figure 5.17. High-pressure ESI mass spectra of cytochrome c at pH 2 in hydrochloric acid solution with different concentrations of ammonium chloride concentrations.

Effect of organic solvents

Acidic organic solvent mixtures were also found to exhibit a similar acid-induced refolding trend observed in the aqueous solutions. The measurement was performed using cytochrome c in 50 % v/v ethanol/water and acetonitrile/water with different pH (Figures 5.18, 5.19, and 5.20). The major difference from the aqueous solution was that the highest charge state (fully unfolding state) took place at a lower acidity of pH 3, as the organic solvent disrupts the hydrophobic interactions of the native protein. As organic solvent mixtures were commonly used in the ESI-MS, the same measurement was repeated using the standard atmospheric pressure nanoESI with microcapillary (i.d. 5 μm). The result showed a similar trend of protein unfolding with the decreasing of pH from 5 to 2 (Figures 5.21 a-c). However, similar to the aqueous solution, the mass spectrum for protein at pH 1 was not well resolved (Figure 5.21 d). Interestingly, performing the nanoESI using the same capillary emitter under high pressure resolved the peak of the low charge state (Figure 5.22). This demonstrated that the high insulation of the working gas and the improved ion desolvation provided by the HP-ESI were important for the ionization of protein from highly conductive solutions.

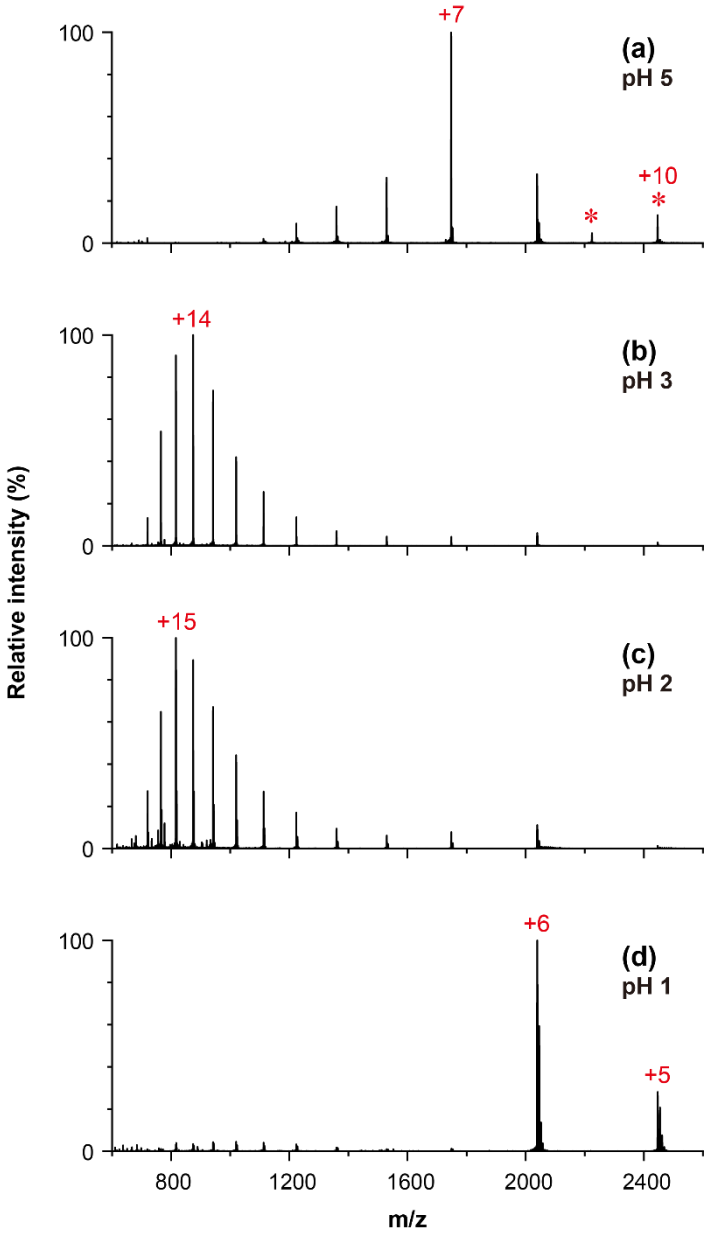

Figure 5.18. Mass spectra of 10 μM cytochrome c in 50 % v/v ethanol in hydrochloric acid with different pH. Asterisk denotes the peak for the dimer.

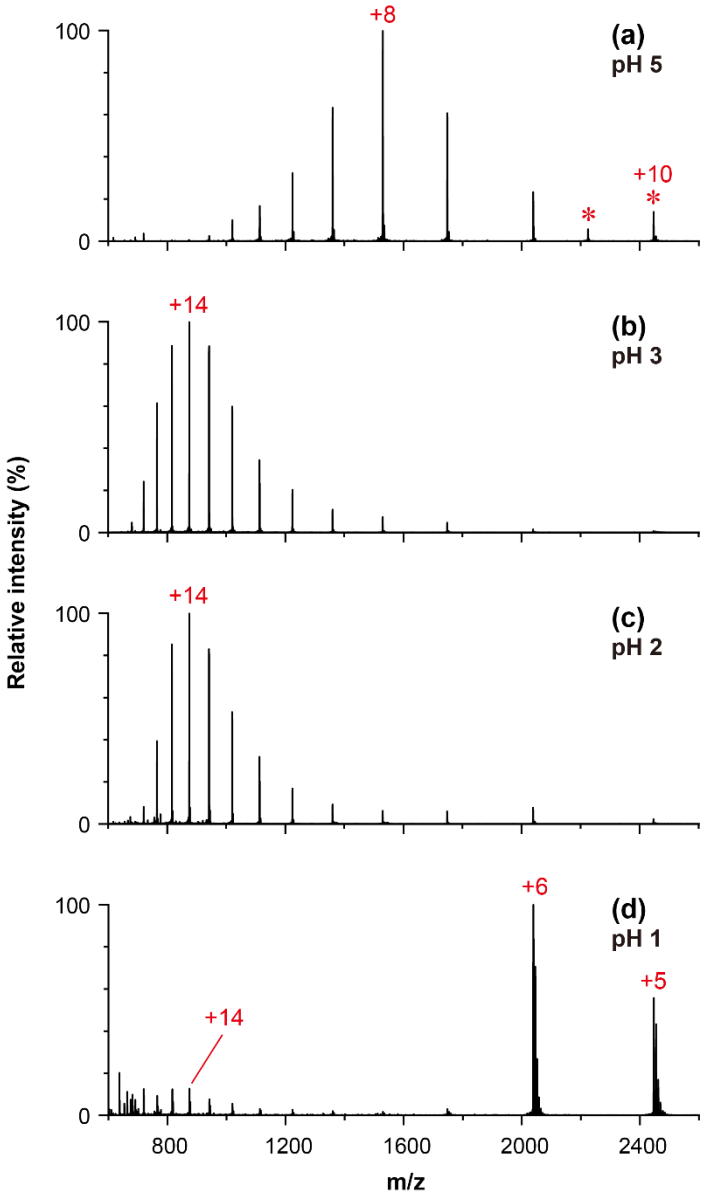

Figure 5.19. Mass spectra of 10 μM cytochrome c in 50 % v/v acetonitrile in hydrochloric acid with different pH. Asterisk denotes the peak for the dimer.

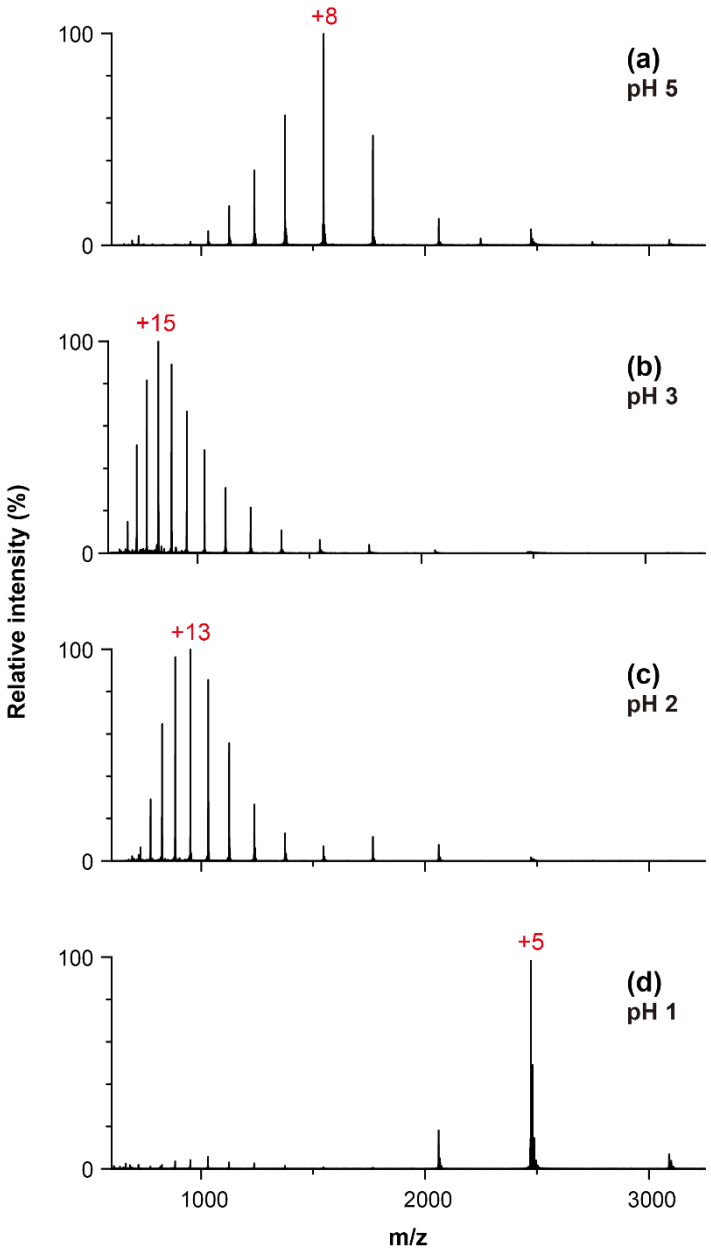

Figure 5.20. Mass spectra of 10 μM cytochrome *c* in 50 % v/v acetonitrile in TFA with different pH.

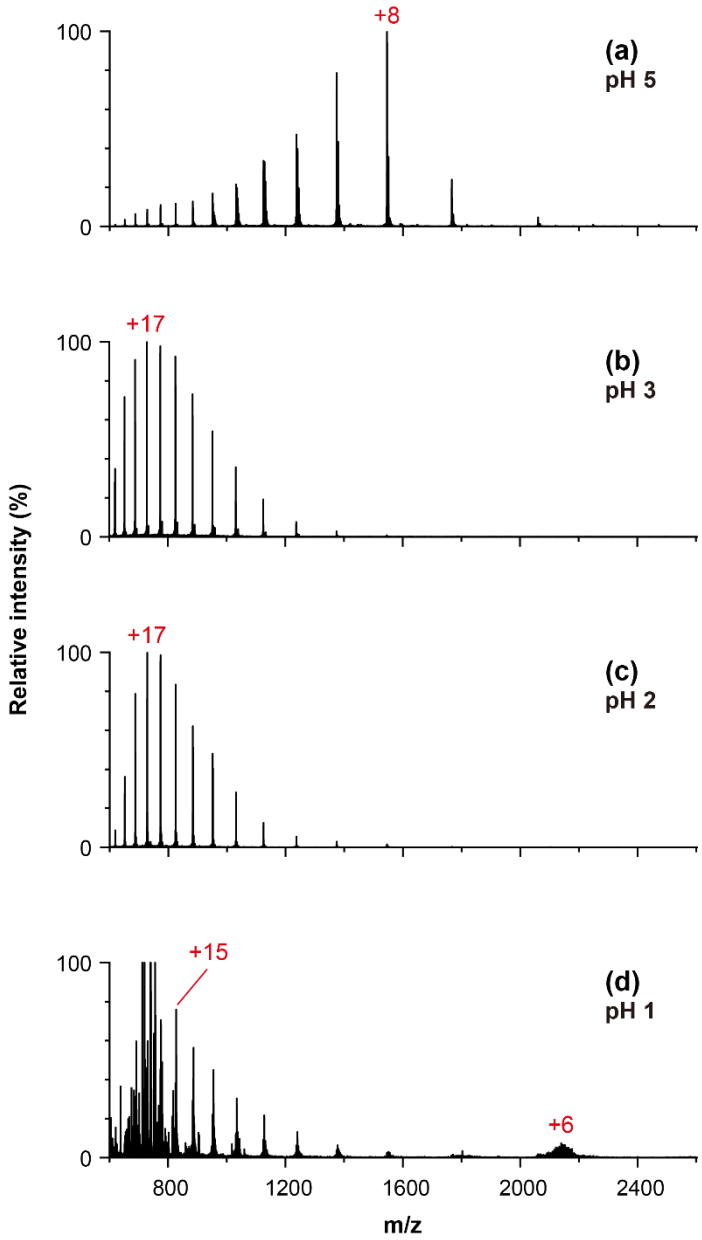

Figure 5.21. Standard AP µcapillary nanoESI mass spectra of 10 µM cytochrome c in 50 % v/v acetonitrile in hydrochloric acid with different pH. The emitter is pulled glass capillary with an inner diameter of 5 µm performed under atmospheric pressure.

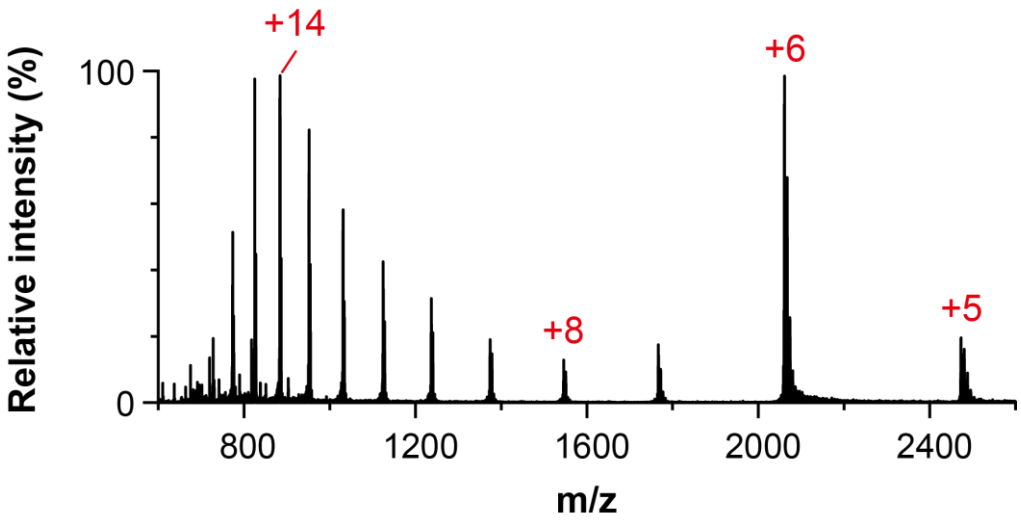

Figure 5.22. High-pressure nanoESI mass spectra of 10 μM cytochrome *c* at pH 1 acquired from pulled glass capillary emitter (i.d. 5 μm) placed under high pressure (0.5 MPa). Cytochrome *c* is prepared in 50 % v/v acetonitrile in hydrochloric acid with pH 1.

Flow rate effect

It is noted that for highly conductive solutions, the ion signal and CSD showed an anomalous response at an ultra-low flow rate when the size of the initial charge droplet was in the order of <30 nm.[104,130] For example, highly charged species of protein could be produced from the ~pH 7 solution when the flow rate was tuned to near its minimum value.[130] Possible reasons include the heating effect at high spray current density and the strong electric field effect. The flow rate effect on the average charge state for pH 2 and pH 1 solutions is shown in Figure 5.23. At pH 2, the average charge state was insensitive to the flow rate. As for proteins at pH 1, the high charge state rose drastically when the flow rate was decreased to < 10 nL/min. This trend was also found in the measurement of cytochrome c in 1 M ammonium formate at a low spray current.[104] We conjectured that the ion species generated at that ultra-low flow rate was not reflecting the condition in the solution phase, and the artifact was avoided by operating the flow rate at > 20 nL/min for acquiring the mass spectra for this study. Above that flow rate threshold, the average charge state was found to be insensitive to the flow rate with a small deviation of 0.5 charges.

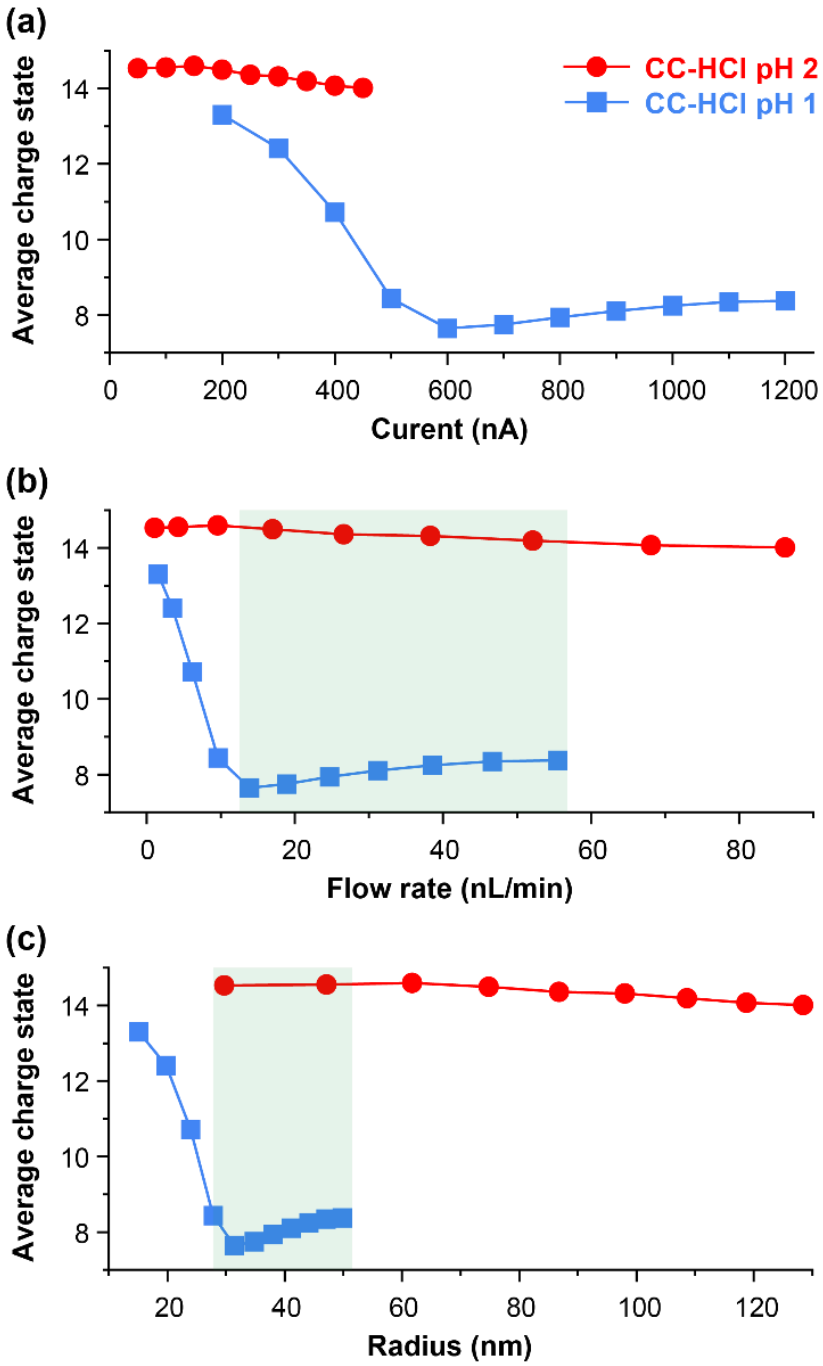

Figure 5.23. Average charge states of 10 μM cytochrome *c* versus a) spray current, b) flow rate, and c) radius of initial droplets obtained in hydrochloric acid aqueous solution with pH 1 or 2. The conductivity of hydrochloric acid aqueous solution at pH 1 and pH 2 are 5.2 S/m and 0.5 S/m.

Release of molten globule to the gas phase

The acid-induced molten globule should be maximally protonated in the solution,[117–119] however, in the gas phase, the number of excess charges carried by the "molten globule ions" was much smaller, approximately the same value observed for native protein. It is conceivable because, in the solution, some of the protonated basic groups on the protein were paired with anions. The dissociation of the ion pairs during the ion desolvation or in the gas phase process neutralized the protonated groups and produced neutral acid molecules (Figure 5.24). Those weakly bound neutral molecules were usually removed from the protein in the design of modern mass spectrometers but could be preserved by reducing the energy involved in the ion desolvation and transmission processes.[137] To detect those neutral, the softness of the present HP-ESI source was increased by changing the default ion transport configuration in Figure 5.1 to an indirect one shown in Figure 5.25. The ions/nano droplets generated inside the high-pressure chamber were first released to the atmospheric pressure to reduce their temperature by adiabatic cooling before the heated ion inlet of MS. With the soft HP-ESI-MS, the attachment of TFA (up to 11 molecules) to the compacted species of charge state +5 and +6 of cytochrome c (Figure 5.26) was observed.

The observed low charge states corresponding to the gas phase molten globule ions have the following features: i) the distribution was narrow, indicating that conformation was homogeneous, ii) the average value was approximately equal to but slightly lower than the typical "native charge state", iii) the average charge state in the low charge region obtained from different acids has the following order: Formic acid > HCl > TFA. For native proteins, it is generally believed that the ionization route follows the charge residue model, and the maximum charge for a globular protein is limited by its hydrodynamic radius.[60] We believe that is also true for acid-induced molten globule, that is the excess charge available to the molten globule should depend on its size. Molten globules were larger than native proteins,[119,138] therefore, the lower-than-native charge state observed in this study indicated the occurrence of charge reduction during the ionization process. An anion-dependent charge reduction mechanism has been put forward by Chait et al that also involves the ion pairing and the gas phase dissociation process.[135] Another study by Gumerov, et al. also showed that even by maintaining the

conformation of the protein, the composition of buffer could still alter the CSD of the protein due to the formation of protein-base complexes in the solution and the subsequent dissociation in the gas phase.[136] The charge reduction effect is anion-dependent and that explains the discrepancy in the charge state of molten globules in different acids. Finally, it is noted that the effectiveness of protein compaction in the solution was also reported to be anion-dependent,[118] but it was assumed that the subtle difference in the compacted conformation would not cause as much variation in the CSD as the effect of gas phase chemistry. Further investigation is needed to understand the impact of a minor conformational change on CSD. There exists a strategy to study the effect of pH on protein conformation while minimizing the contribution of gas-phase ion chemistry on the CSD by using a suitable solvent system.[139] Such a methodology will be attempted in the future.

In summary, the HP-ESI-MS of proteins in low pH acid solutions has revealed the two effects of ion pairing of anion and protein. One is the collapse of the unfolded polypeptide chain to a compact conformation (as reflected by the drastic CSD shift), and another is the gas phase charge reduction (as depicted by the small CSD shift).

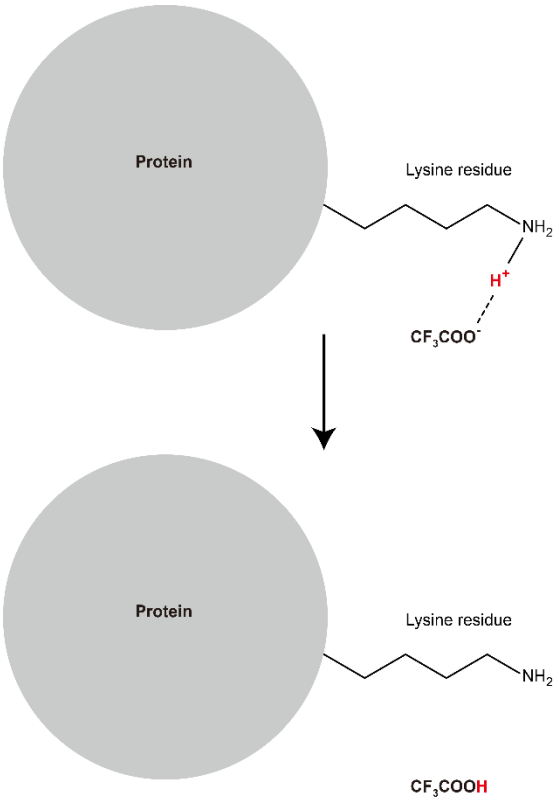

Figure 5.24. A simplified illustration of neutralization of the originally protonated basic group (Lysine for this example) by the dissociation of the ion pair ($CF3COO^-$ --- H^+) from the protein. The dissociation can take place during the ion desolvation or in the gas phase. The attachment of the electrically neutral TFA molecules (CF3COOH) can be detected by HP-ESI by lowering the energy deposited to the ion/charged droplets during the ionization and ion transmission processes.

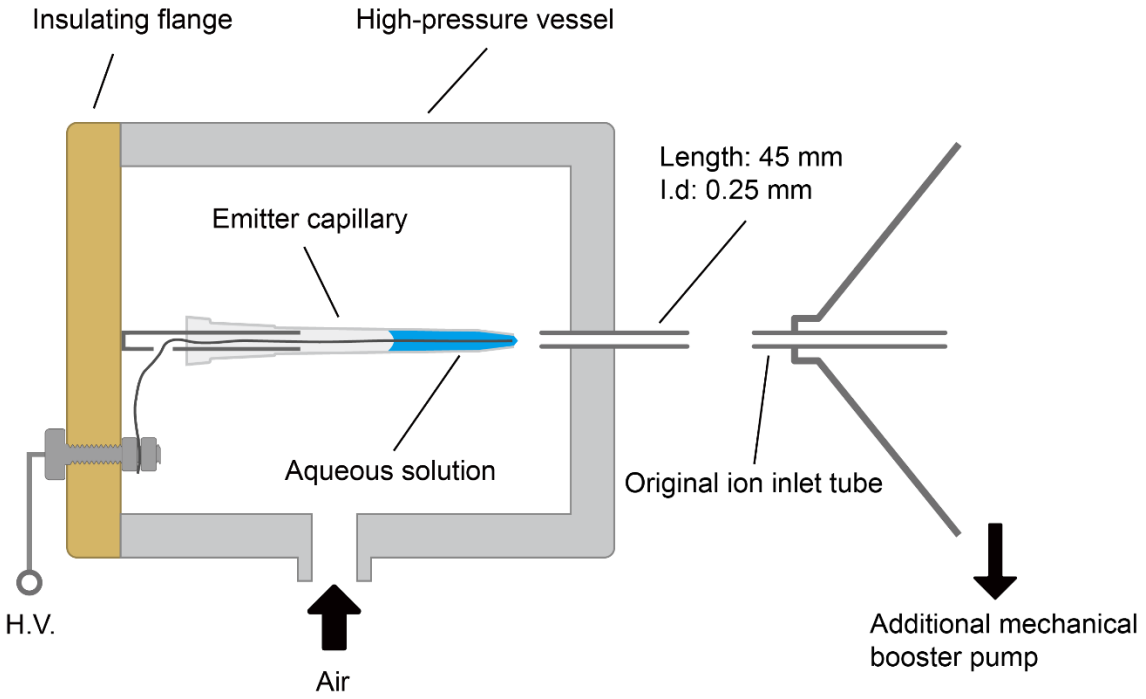

Figure 5.25. Arrangement of a soft high-pressure nanoESI ion source for the detection of neutral acid molecules weakly bound to the protein. Instead of connecting the ion source directly to the MS inlet, the ion/nanodroplets are first released to the atmospheric pressure to reduce their temperature via adiabatic cooling.

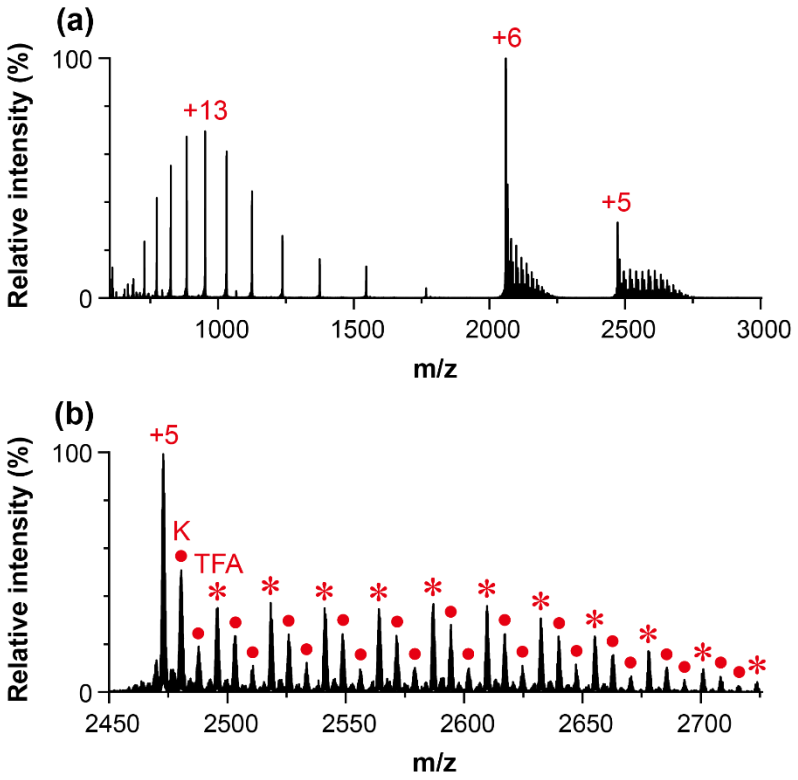

Figure 5.26. **a)** Soft HP-ESI Mass spectra of 10 μM cytochrome *c* in TFA aqueous solution of pH 1. **b)** Magnified mass spectrum for charge state +5. The solid circle denotes the adduction of potassium originated from the pH probe. The asterisk denotes the adduction of TFA.

Conclusion

The high stability and improved desolvation of HP-ESI have enabled a mass spectrometric study of acid-induced compaction of protein at pH 1, a condition that was difficult for conventional atmospheric electrospray and nanoESI. The conformational change of protein standards induced by pH was manifested by the drastic shift of the dominant charge state to low charge, producing mass spectra resembling the condition of a native protein. Each protein also has its unique charge state response to the pH. Increasing the concentration of anions at pH 2 using ammonium chloride replicated the compaction phenomenon, supporting the role of anions as the main factor for this phenomenon. The compaction of protein was also found to take place in acidic organic solvent mixtures containing 50 % ethanol or acetonitrile. The dominant and the average charge of the compacted protein show dependency on the type of acid that is related to the propensity for the anion to cause compaction and charge reduction effect. In sum, the HP-ESI-MS has been demonstrated to be a potential tool for probing the acid-induced compaction phenomenon which is critical for our understanding of the science behind protein folding.

Chapter 6: Fundamental study of AP ESI & the feedback control of ESI

Summary

The electrospray under the steady cone-jet mode is highly stable but the operation state can shift to other pulsation or multi-jet modes owing to the changes in flow rate, surface tension & and electrostatic variables. In Chapter 6, a simple feedback control system is developed using the spray current and the apex angle of the Taylor cone to determine the error signal for emitter voltage correction. The system is applied to lock the cone-jet mode operation against external perturbations for online and offline electrospray. For online electrospray under a regulated flow rate, the apex angle of the Taylor cone reduces with increasing voltage, but in contrast, the angle increases with the voltage for offline electrospray. A simple algorithm based on iterative learning control is formulated and implemented using a personal computer to automatically correct the emitter voltage in response to the error signal. For an offline ESI, the feedback control of spray current can also be used to regulate the flow rate to any arbitrary value or flow pattern. ESI-MS with feedback control is demonstrated to produce ion signal acquisition with long-term stability that is susceptible to emulated external disturbances.

Introduction

Electrospray ionization mass spectrometry (ESI-MS) is an indispensable tool for the analysis of a wide range of biomolecules such as peptides, proteins, and polymers. Upon the application of a high potential to the liquid at the ESI emitter, the strong electrical field cause the emission of charged droplets of the sample solution, and the desolvation of droplets generates the gaseous ions of the solute. For a given flow rate and HV, the electrospray condition can vary across different spraying regimes, i.e. dripping, pulsation/oscillation (in the kHz range), steady cone-jet, and multi-jet modes[25]. Among those regimes, the steady cone-jet mode is usually the preferred operating mode because it is highly stable as manifested by the stationary geometry of the liquid cone (Taylor cone) and a near-constant spray current. The apex angle of a static Taylor cone without pressure difference across the liquid-air interface is 98.6°[11]. In practice, the angle was usually smaller and the reasoning has been provided using treatment with[36], and without space charge effect[140]. The micro/nano droplets issued from the

steady Taylor cone are also monodispersed, i.e. it has a narrow distribution of initial droplet size. There also exist semi-empirical models for the cone-jet mode to describe the inter-relationship among the spray current, flow rates, droplet size, and other fluidic variables of the liquid[24,38]. Compared to the burst/dripping and the pulsation modes, the cone-jet mode also produces a higher ionization efficiency for ESI-MS[141].

The ESI can be operated in online and offline manners. The online operation employs a liquid pump such as a syringe pump or LC pump to deliver the solution to the sprayer, usually at a constant flow rate. Online operation is widely used in LC-MS and other routine analyses that require a constant supply of samples. The cone jet is stable if the supplied flow rate matches the natural volumetric emission rate of charged droplets. The stable operation of cone-jet mode depends on the applied HV, surface tension, and electrical conductivity. In the offline electrospray, the liquid loaded inside the capillary sprayer or liquid reservoir is drawn to the emitter by the electrospray. Unlike the online operation where the flow rate is regulated by the pump, the liquid flow rate is controlled solely by the high voltage. Offline electrospray has been performed using pulled-glass nanoESI capillary[26], wet metallic wire or solid needle emitter[27,28], solid substrate[29], paper[30], and pipet tip[31]. Recently we also reported an offline nanoESI using micropipette tips with large i.d. for highly conductive aqueous solutions[32,33].

The condition of electrospray will remain unchanged if the flow rate and other fluidic variables such as electrical conductivity, surface tension, and the electrostatic conditions, i.e. the electrical field on/around the liquid meniscus are constant. However, throughout ESI-MS analysis, perturbations such as variation in liquid properties, flow rate, liquid pressure, wetting condition, the built-up of charge on the oxide layer of the electrode surface, and the space charge effect can shift the operating condition of electrospray. In some cases, the perturbation is intentional. For example, the mixing ratio of aqueous/organic eluent is varied in the gradient elution LC-ESI-MS; the temperature gradient was employed in the high-temperature capillary ESI-MS[54]; a change in solution pH to trigger the protein denaturation during the time-resolved ESI-MS[142]; and the distance between the ESI emitter and MS inlet was varied to alter the flight time of microdroplets for reaction control[101].

This work is on the automatic correction of the electrospray operation to deal with those perturbations. The spray current is a key quality indicator and it is commonly used as the reference in

the feedback control of electrospray for the adjustment of emitter voltage. The closed-loop control of electrospray can be traced back to the stabilization of current emissions from liquid metal ion sources in the 1970s[143]. A constant spray current operation has been performed on nanoESI-MS analysis using PID control[144]. For gradient elution LC-MS, Smith's group proposed an automatic adjustment of voltage to the pre-determined optimal value based on the feedback from the spray current[145]. The prerequisite is that the spray current-optimal voltage (*I-V*) characteristic for the spraying solution is known in advance. Although the feedback control using spray current is simple to implement, it has the limitation of identifying the instantaneous operating state of electrospray in general. For example, in a flow rate-regulated electrospray, the spray current will reach a plateau in the *I-V* curve when reaching the steady cone-jet mode. As the current stays nearly constant right after the pulsation and before the initialization of multi-jet modes[37], it is difficult to derive the error signal to correct the course of operation from swaying away from the cone-jet mode.

Besides spray current, feedback control had also been performed using microscopic images of the liquid meniscus and/or the generated plume. It is quite common for the ESI practitioner to adjust a suitable voltage based on visual inspection of the electrospray. The automatic adjustment could be done with real-time image processing. For instance, an imaging system that combined a strobed and continuous illumination was employed to identify the spraying mode of nanoelectrospray[146]. A feedback control system based on the predetermined proper height of the Taylor cone was reported to improve the stability of the cone jet[147]. In another design to improve the constant current operation, an additional feedback loop for liquid meniscus control was added to the primary loop for spray current control[148].

Here, we develop a simple and robust feedback control system based on the spray current and the apex angle of the Taylor cone in order to correct the state of the electrospray while it is still in the cone-jet mode. Following the scaling law for the cone-jet mode, the relationship of spray current I, flow rate Q and other physical variables is in the form of[24,38]

$$I = f\left(\frac{\gamma K Q}{\epsilon_r}\right)^{1/2} \tag{1}$$

, where γ is surface tension, K is electrical conductivity, and ϵ_r is the relative permittivity of the liquid, and $f = 18$. Thus, for the electrospray system with an external flow rate regulation, we argue

that the spray current ought not to be kept constant by the feedback control as it need to vary with the supplied flow rate. The apex angle (β) is hypothesized to be an indicator of state to provide the error signal for voltage readjustment. For an offline operation, the liquid movement is driven electrostatically and the flow rate can be modulated by the emitter voltage. If other physical variables of the liquid remain relatively steady, the flow rate and the apex angle can be modulated and stabilized using spray current as the feedback signal. The benefits of feedback control for online and offline ESI-MS are evaluated under the perturbations of flow rate, surface tension, electrical conductivity, and electrode distance.

Experimental section

Online & offline ESI sprayer

The schematic of the ESI-MS system is shown in Figure 6.1. The emitter of the online sprayer was fabricated from a straight-cut stainless-steel capillary with 0.15 mm i.d and 0.3 mm o.d (Nilaco). A Tee-union was used for the experiment that involved the mixing of two liquids supplied from two separate syringe pumps (PHD and PHD ULTRA from Harvard). For a single solution operation, the unused port was closed using a PEEK plug. For the offline operation, a fused-silica capillary (i.d. 0.150, o.d. 0.375 mm) attached to a microcentrifuge tube was used by default. Offline nanoESI using pulled-glass capillary and micropipette tip (i.d. ~ 0.4 mm, Eppendorf) was also performed. A platinum or titanium wire was inserted into the emitter to make electrical contact with the liquid. The distance between the emitter and counter electrode was ~5 mm for the microliter/min flow regime and ~1 mm for the nanoliter/min operation. The HV for the emitter electrode was supplied by an HV power supply (Matsusada) in a remote-control mode.

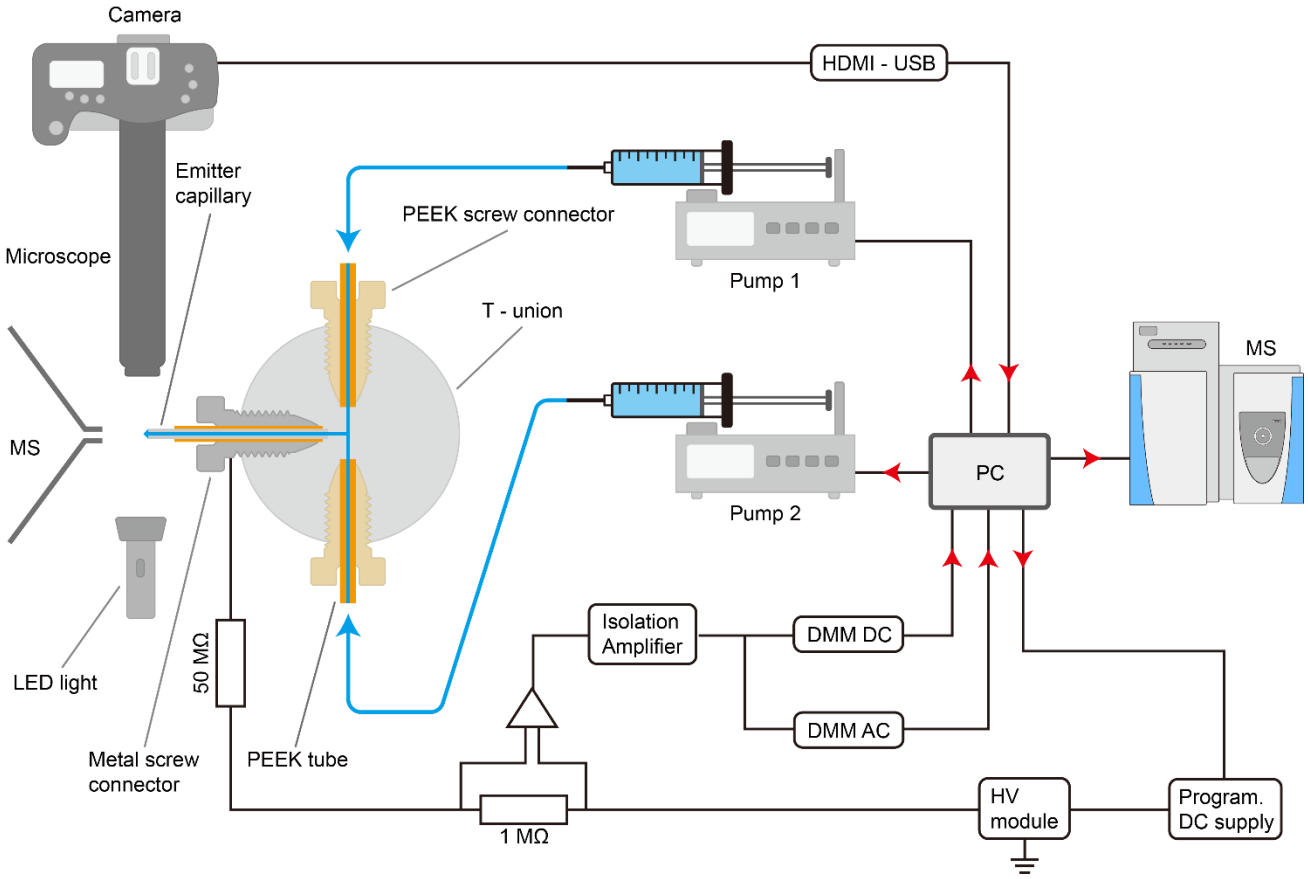

Figure 6.1. Schematic of the ESI-MS system with feedback control. An online electrospray is used for the illustration. A personal computer (PC) is used to receive readings of spray current from digital multimeters (DMM), acquire images from the camera via HDMI-USB converter, and send control commands to the programmable DC supply, syringe pumps & MS.

Measurement of spray current

The spray current was measured by sensing the voltage drop across a precision resistor (1.00 MΩ) on the high-voltage side. Another resistor (50 MΩ) was used to prevent short circuits and for user protection. The instantaneous current signal was amplified using a high-impedance instrumental amplifier (INA 116, Texas Instrument) and coupled to digital multimeters on the low-voltage side via an isolation amplifier (ISO 121, Texas Instrument). Two digital multimeters (Agilent and Keithley) were used. One was for the measurement of the average value (DC value), and another was for the root mean square value (AC value) of the spray current. The AC reading was not essential for the feedback control but was recorded to verify the stability of the spray current.

Acquisition of optical Image

The image of the liquid meniscus is acquired using a Zoom lens (Edmund Optics) connected to a single-lens reflex digital camera (Canon Kiss 10). The camera is connected to a personal computer using an HDMI-USB converter. The orientation of the optical axis is orthogonal to the sprayer-MS inlet axis. The image data is acquired and processed using the OpenCV library[149] to determine the spraying mode and to extract the edge coordinates of the Taylor cone for the computation of the apex angle. A back-light LED illumination was used to produce the shadowy image of the liquid meniscus.

Mass spectrometer

The MS experiment was conducted using a benchtop Orbitrap mass spectrometer (Exactive, Thermo Fisher Scientific). The instrumental settings for the mass spectrometer were as follows: the temperature for the ion transport tube was 300 °C, the voltages of the inlet capillary and the tube lens were 100~120 V, and the skimmer voltage was 20 V. The maximum ion injection time was 50 ms.

Sample preparation

The LC-grade ethanol was purchased from Kanto Chemical. Bovine heart cytochrome c was purchased from Wako Pure Chemical Industries. ubiquitin, bradykinin, ammonium acetate, ammonium

bicarbonate, D2O, and acetic acid were from Sigma Aldrich. Pure water was prepared using Simplicity UV (Millipore, Bedford, MA). All the chemicals were used without further purification.

Computerized control system

A simple control program was written in C#. The program performed the following functions: i) receive the DC and AC values of the spray current from the multimeters, ii) acquire the microscopic video images, iii) send controlling command to the programmable DC power supply for the remote control of the high voltage power supply, iv) send On/Off and flow rate control command to the syringe pumps, v) send Start signal to the mass spectrometer, and vi) execute the control algorithm based on the spray current and the optical image.

Results and Discussion

Online electrospray with regulated flow rates

The feedback strategy for an online electrospray was formulated based on the electrical and fluidic characteristics shown in Figure 6.2. The solution was water/ethanol 1/1 (v/v) with 0.1% acetic acid and the flow rate was 2 μL/min. To obtain the spray current-emitter voltage (I-V) curve (Figure 6.2a), the emitter voltage was gradually ramped up from 2200 to 4400 V and then ramped down to 2200 V with an increment and decrement of 2 V per step. The residence time for each step was approximately 0.2s. Here, the electrospray was scanned across three working modes: pulsation (oscillation in kHz frequency), steady cone-jet, and multi-jet, with each mode showing a distinct current level. The response of current over a large voltage window was stepwise, i.e. the current jumped from one level to another during the transition of mode. Within each mode, the current stayed nearly constant against the change in voltage. The hysteresis-like patterns also existed in the transition regions for pulsation ⇌ cone-jet and cone-jet ⇌ multi-jet. Within that "hysteresis" region, a given voltage could support two electrospray modes depending on the previous condition. Upon reaching the cone-jet mode, a change in emitter voltage within the widow of 3320 to 4160V induced only a mild change of spray current (110 to 120 nA). The apex angle, however, varied significantly with the emitter

voltage. The plots of cone-jet mode spray current (I) and the apex angle (β) versus emitter voltage under different solution flow rates are shown, respectively, in Figures 6.2b and 6.2c. If we assign an operating point as the middle point of the I-V curve (marked by vertical dashed lines), that operating point shifts with the change in flow rate. For this emitter, that operating point roughly stayed at the apex angle of 80° for all flow rates (horizontal dashed line in Figure 6.2c). Therefore, the shifting of the operating point caused by the perturbation of flow rate or other variables can be corrected by using the apex angle as the reference. With feedback, it was possible to lock the apex angle to an arbitrary value within 70~90° for μL/min operation. It should be noted that the feedback cannot extend the inherent stability island of the electrospray. Here, the highest flow rate that can sustain a steady cone jet was approximately 4μL/min.

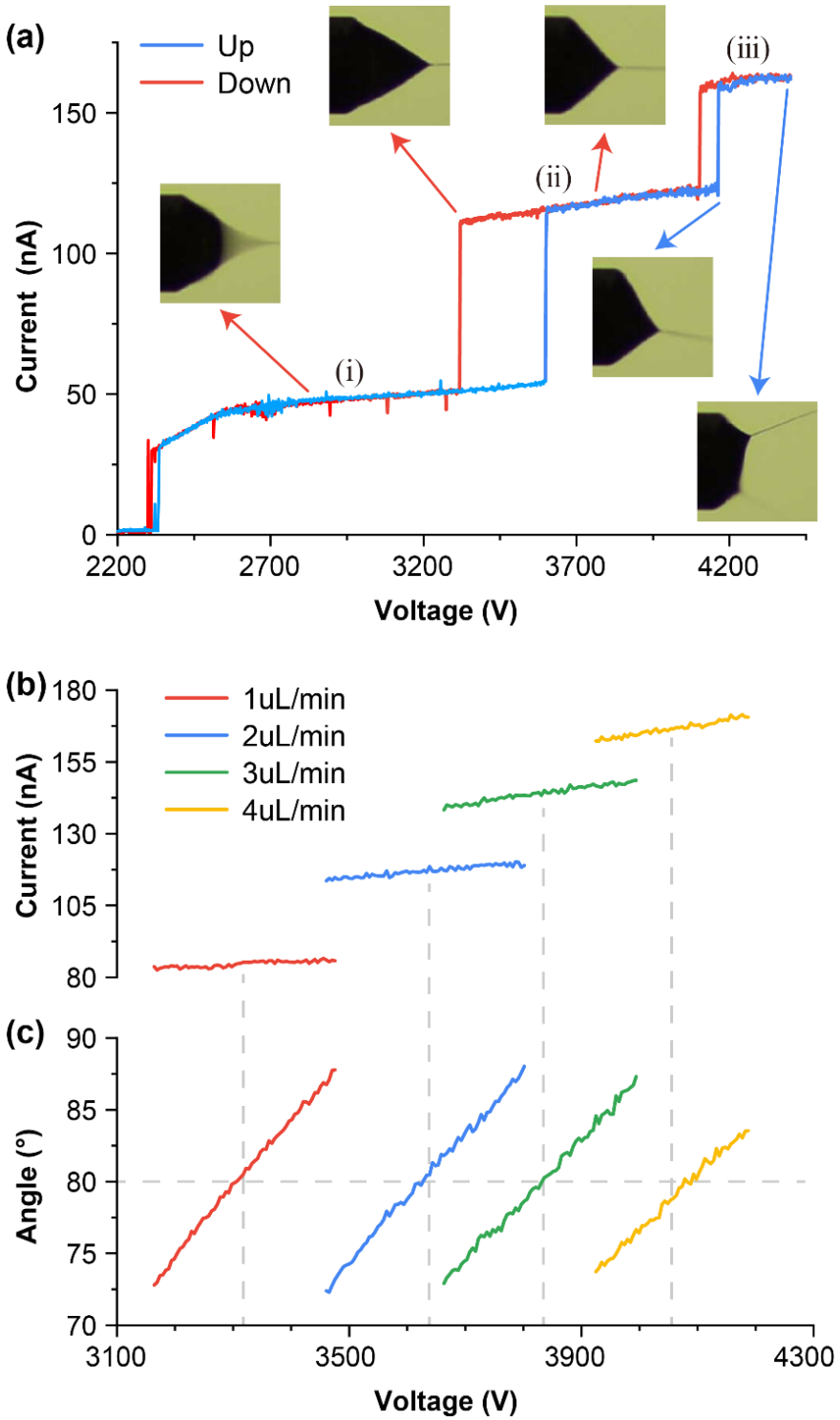

Figure 6.2. (a) Spray current versus emitter voltage relationship acquired by ramping the voltage up and down across pulsation, cone-jet, and multi-jet modes. Flow rate: 2 μL/min. (b)&(c) The plots of cone-jet mode spray current (b) and the apex angle of the liquid cone (c) versus emitter voltage under different flow rates. Solution for (a)-(c): water/ethanol 1/1 (v/v) with 0.1% acetic acid. (i) Pulsation, (ii) cone-jet, (iii) multi-jet modes.

Image processing and control algorithm

Feedback control based on apex angle was valid only when the electrospray was under cone-jet mode. Mode detection is needed to provide the correct control procedures for self-starting and self-recovery from other spraying modes. Figure 6.3 illustrates the scheme for mode detection and computation of the apex angle during the operation of the electrospray. Three scenarios: i) cone-jet, ii) pulsation, and iii) multi-jet modes are considered. In the pulsation mode, the liquid meniscus and the spray current was oscillating in a kHz frequency range. Using our camera with a 50 fps maximum frame rate, the liquid cone appeared to consist of a "blur" apex and a clear rounded base (Figure 6.3a ii). To identify the spraying mode, the original shadowy image (Figure 6.3a) was first converted to a gray-scale image which was then subjected to thresholding using two slightly different threshold values to construct two binary images (labeled as M_1 and M_2, respectively in 3b). The value of threshold 1 was so selected to produce a clear binary image (M_1) for cone-jet mode. As for threshold 2, it was selected so that the blur apex appeared clear in M_2. The edge image (labeled as Edge in 3c) was constructed by performing edge detection on M_1. Also shown in 3c is the resultant image of $M_1 - M_2$. A variable ξ was introduced to describe the difference between M_1 and M_2. It is defined as the sum of pixel values of $M_1 - M_2$. Finally, two straight linear regression lines were constructed using least-square fitting for the selected coordinates in the edge image (3d) and the apex angle β was calculated from their slopes. The coordinates were user-defined and should be selected to avoid the jet at the tip of the Taylor cone. The variable δ is the mean squared error (MSE) which is defined as $\delta = \frac{1}{N}\sum_{n=1}^{N}(y_n - \hat{y}_n)^2$, where N is the number of data points, y_n is the Y-axis coordinate, and $\hat{y}_n$ is the predicted value calculated from the least-square fitting. δ was small (usually < 1) if the liquid meniscus was close to a perfect cone. The spraying mode was determined by comparing the values of δ and ξ with user-defined $\delta_{\max}$ and $\xi_{\max}$. The image processing procedure here was minimalist and filtering can be added in the case of an optically noisy condition.

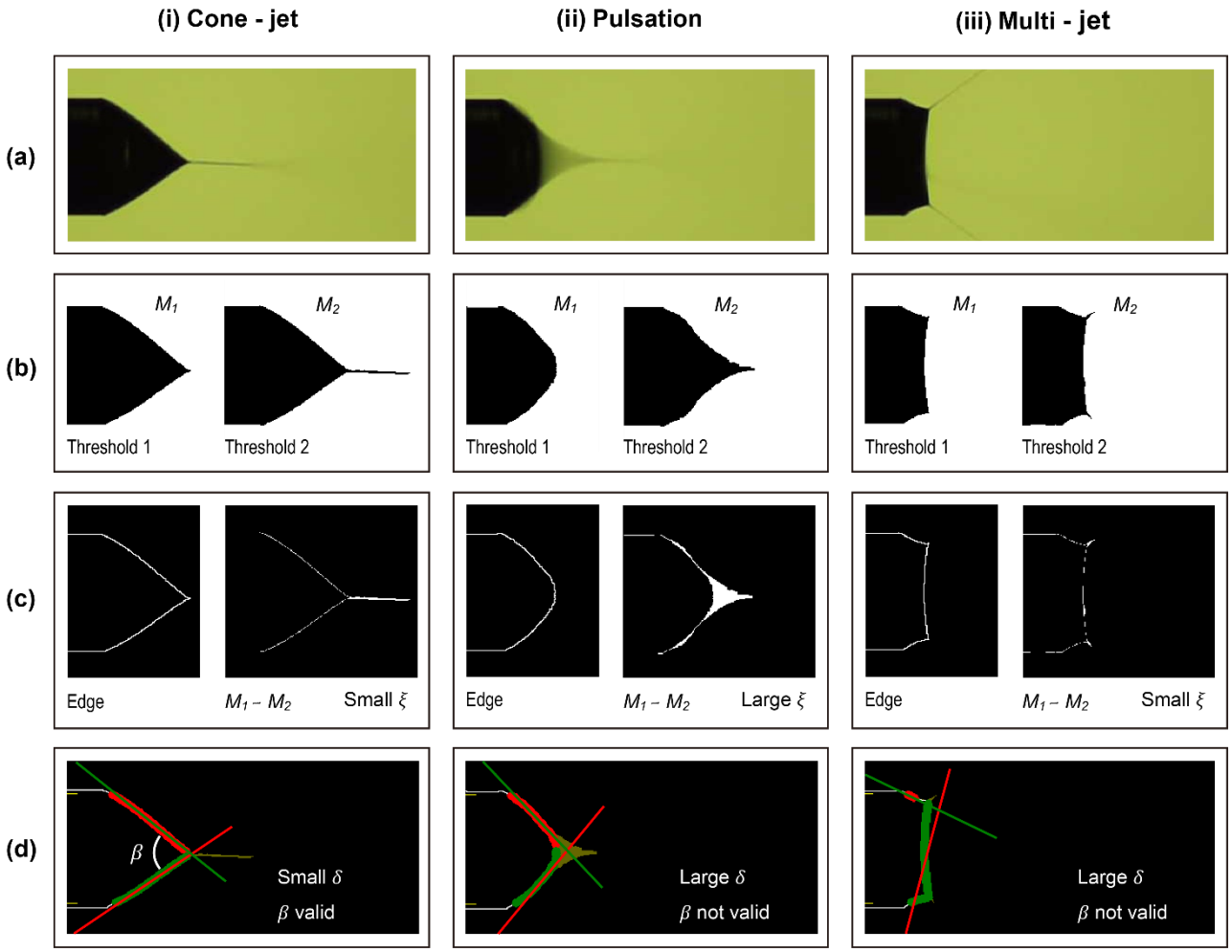

Figure 6.3. Illustration of the scheme to compute the apex angle and to detect the spraying modes (i-iii). **(a)** Acquisition of original image. **(b)** Construct images $M_1$and M_2 using binary thresholding using two slightly different threshold values. **(c)** Detect edge from M_1 and compute ξ which is the sum of pixel values of ($M_1 - M_2$). **(d)** Construct two linear regression lines from the selected coordinates of edges and compute apex angle β from the slopes and mean squared error δ of the regression analysis.

Since the AC reading of the spray current was also recorded in our system, one may wonder if the AC value could be used to detect the pulsation mode without image processing. The pulsation mode usually produced a high-frequency component in the spray current and the AC reading was adopted in the early development of this work. But occasionally, a highly stable spray current was detected without a significant AC component even though the electrospray was obviously in the pulsation mode as observed from the camera. The image processing method thus appeared to be more reliable for spraying mode detection.

Iterative learning control (ILC) method[150–152] was employed to lock the apex angle of the Taylor cone to a target value (β_{Target}), that is, the emitter high voltage was iteratively corrected by the following updating law.

$$V_{i+1} = V_i + \left(\beta_{\text{Target}} - \beta_i\right) G_\beta \qquad (10)$$

The magnitude of the control parameter G_β was 10 V/° in this study. The overall procedures for self-starting and the recovery of cone-jet from other modes are summarized in Algorithm 1. The process begins by assigning the emitter voltage (V_i) with an initial value V_{initial} (0 V or any adjusted value). The measurement of spray current and image acquisition was performed after a delay of ~50 ms. The spray was assumed to be established if the spray current (I_i) exceeded a minimum value I_{min} (10 nA in this study). If not, an increment of emitter voltage ΔV (set to 20 V) was executed until the spray was established. The apex angle β_i, and values of δ_i, and ξ_i were then computed. A condition of $\delta_i < \delta_{\text{max}}$ indicates a cone-jet mode operation, and the correction of emitter voltage was performed according to Eq 10. When the electrospray was strayed to the pulsation or multi-jet mode, δ_i became larger than δ_{max}. In that case, the condition of $\xi_i > \xi_{\text{max}}$ indicate a pulsation mode and the voltage was increased by a step of ΔV, otherwise, it was multi-jet and the voltage was reduced. To prevent a dangerous or out-of-bound value for the HV, a maximum value V_{max} was imposed on the emitter voltage. A finite time lag in obtaining the image and the calculation of the apex angle was ~ 100 ms.

Algorithm 1. Pseudocode for the Feedback control procedure

Algorithm 1. Feedback control procedure

$i \leftarrow 0$
$V_i \leftarrow V_{\text{initial}}$
while running **do**
    Set HV to V_i
    Delay t ms
    Acquire image and spray current I_i
    if $I_i < I_{\text{min}}$ **then**
        $V_{i+1} \leftarrow V_i + \Delta V$
        goto *finally*
    end if
    Compute β_i, δ_i, and ξ_i
    if $\delta_i < \delta_{max}$ **then**
        $V_{i+1} \leftarrow V_i + (\beta_{Target} - \beta_i) G_\beta$
        goto *finally*
    end if
    if $\xi_i > \xi_{\text{max}}$ **then**
        $V_{i+1} \leftarrow V_i + \Delta V$
    else
        $V_{i+1} \leftarrow V_i - \Delta V$
    end if
finally:
    if $V_{i+1} > V_{\text{max}}$ **then**
        $V_{i+1} \leftarrow V_{\text{max}}$
    end if
    $i \leftarrow i + 1$
end while

Flow rate perturbation

The feedback control of an online electrospray was first tested under a stepwise increment of flow rate (Figure 6.4a) and the emitter voltage was automatically adjusted to stabilize the apex angle to the preset 80°. The DC component (average value) of the spray current I_{DC} followed the flow rate pattern. The AC component of the spray current I_{AC} was an indicator for the stability of electrospray, it was usually under 1 nA under a steady cone-jet mode. Also shown is the MSE δ which indicates how the liquid meniscus deviates from the ideal cone. Without feedback control (Figure 6.4b), the apex angle reduced with the increment of flow rate until a point where the cone-jet turned into oscillation/pulsation mode as indicated by the surge of I_{AC} and MSE and a drop of I_{DC}. The calculated apex angle in the pulsation mode is not a valid value (NA).

Figure 6.5 shows the ESI-MS of ubiquitin with and without feedback control under a gradual increase in flow rate. The flow rate was programmed to start at a relatively low flow rate of 0.5 μL/min and increase to 3.4 μL/min (Figure 6.5a). Here the apex angle was locked to 80° while the spray current increased continuously with the flow rate. Without feedback (blue lines in Figure 6.5b), the transition from the cone-jet to pulsation mode took place at ~216 s. Before that transition, there was a fluctuation in apex angle indicating an astable state of cone-jet mode while but the spray current (DC) was still at the same level of cone-jet mode current. Right after the start of the measurement, the total ion intensity of ubiquitin increased slightly with the flow rate and remained relatively constant even with the further increase of flow rate. A higher spray current associated with a higher flow rate did not translate into a higher ion signal due to the lower ionization efficiency at a higher flow rate. The mass spectra in Figure 6.5c, further show that the charge state distribution shifted to a lower charge state at a higher flow rate for both feedback-controlled and uncontrolled conditions. For the case of uncontrolled electrospray (Blue), the total ion signal dropped when the pulsation mode was triggered.

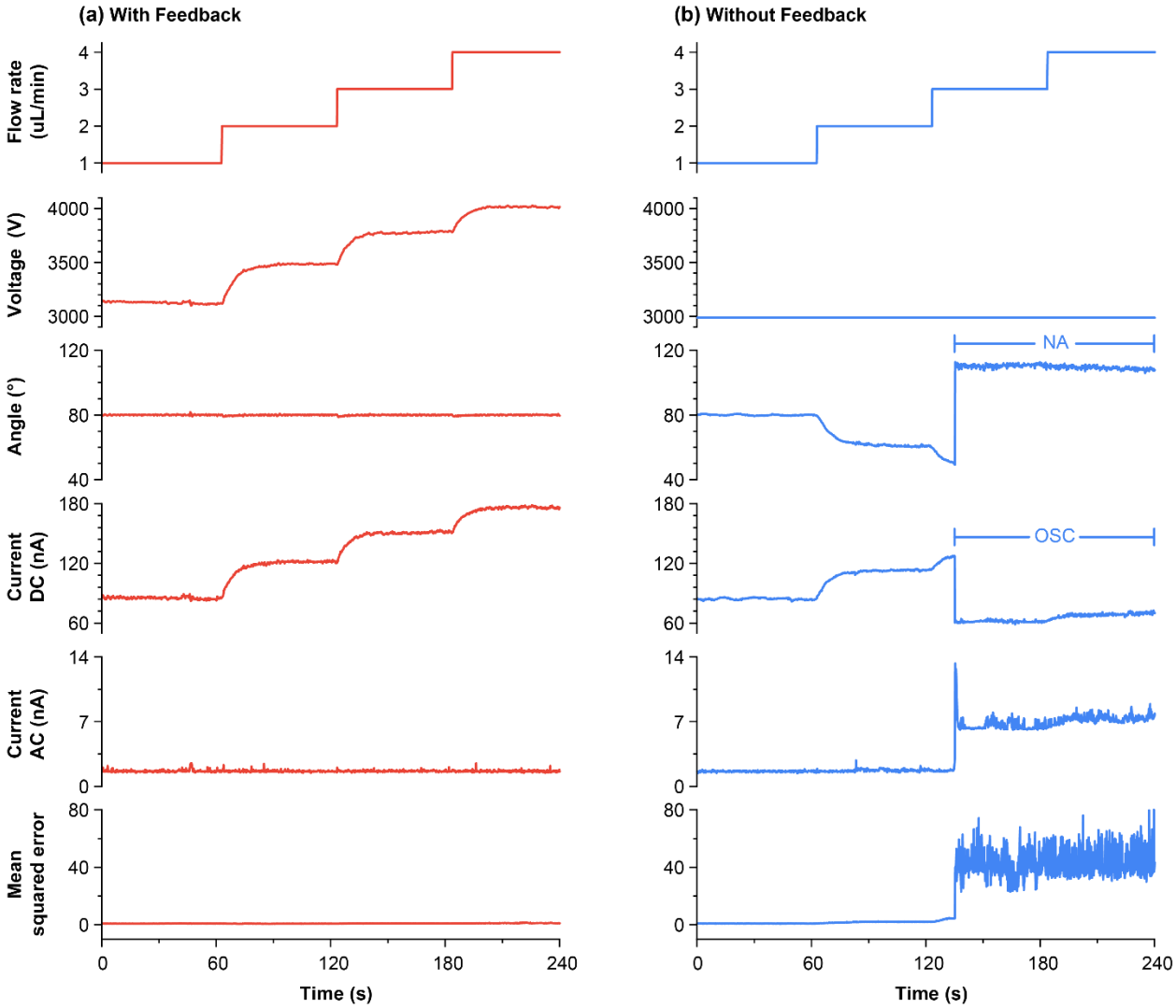

Figure 6.4. Feedback control for an online electrospray under the stepwise increment of the liquid flow rate. The Figure shows the flow rate, emitter voltage, apex angle, spray current (DC component), spray current (AC component), and the mean squared error in estimating the cone geometry. The apex angle is locked at 80°. (a) With feedback control. (b) Without feedback control (constant voltage). Solution: 0.1 % acetic acid in ethanol/water 1/1 v/v. OSC: Oscillation/pulsation mode.

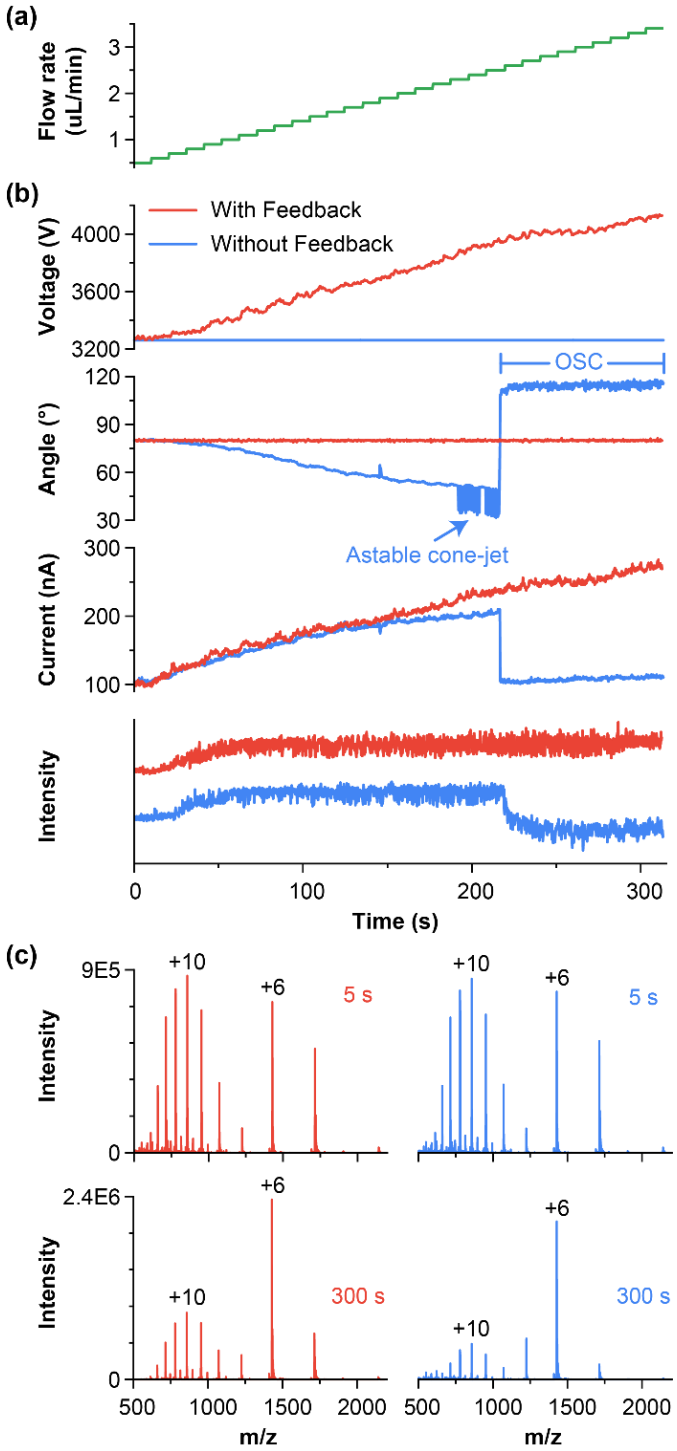

Figure 6.5. MS acquisition for ubiquitin (5 μM) with and without feedback control under the perturbation of flow rate. **(a)** Flow rate pattern fed to the syringe pump. **(b)** Emitter voltage, apex angle, spray current, and total ion intensity for ubiquitin. Red line: with feedback control. Blue line: without feedback control. **(c)** Mass spectra obtained at different times (5 and 300s). The red line (left): With feedback control. Blue (left): Without feedback control. Solvent: 25 % v/v ethanol in water containing 1 mM ammonium bicarbonate. The apex angle was locked at 80° in the feedback control. OSC indicates the kHz oscillation mode.

Figure 6.6 shows the H-D exchange measurement of bradykinin in which the ratio of D_2O and H_2O was adjusted using the flow rate. The bradykinin (10 μM) in H_2O/ethanol solution was delivered at a constant flow rate of 1.3 μL/min. The D_2O/ethanol solution was supplied at a varying flow rate from 0 to 3.4 μL/min. Here the measurement started at an apex angle of 75°. Without feedback control, the electrospray showed signs of instability after ~ 20 s of analysis. The fluctuations in apex angle and spray current indicated the repetitive transition between the cone-jet and pulsation modes. The total ion signal for bradykinin reduced with time due to the dilution of the analyte at a higher flow rate of D_2O/ethanol solution. Nevertheless, the overall ion signal for the electrospray with feedback control was stable. Without feedback, a strong ion signal could still be obtained when the electrospray was in the quasi-cone jet stage but the ion signal decayed at a higher rate compared to the feedback-stabilized ESI. The mass spectra acquired at different H_2O and D_2O mixing ratios at 5 and 90 s are shown in Figure 6.6c. The intermediate spectra are shown in Figure 6.7.

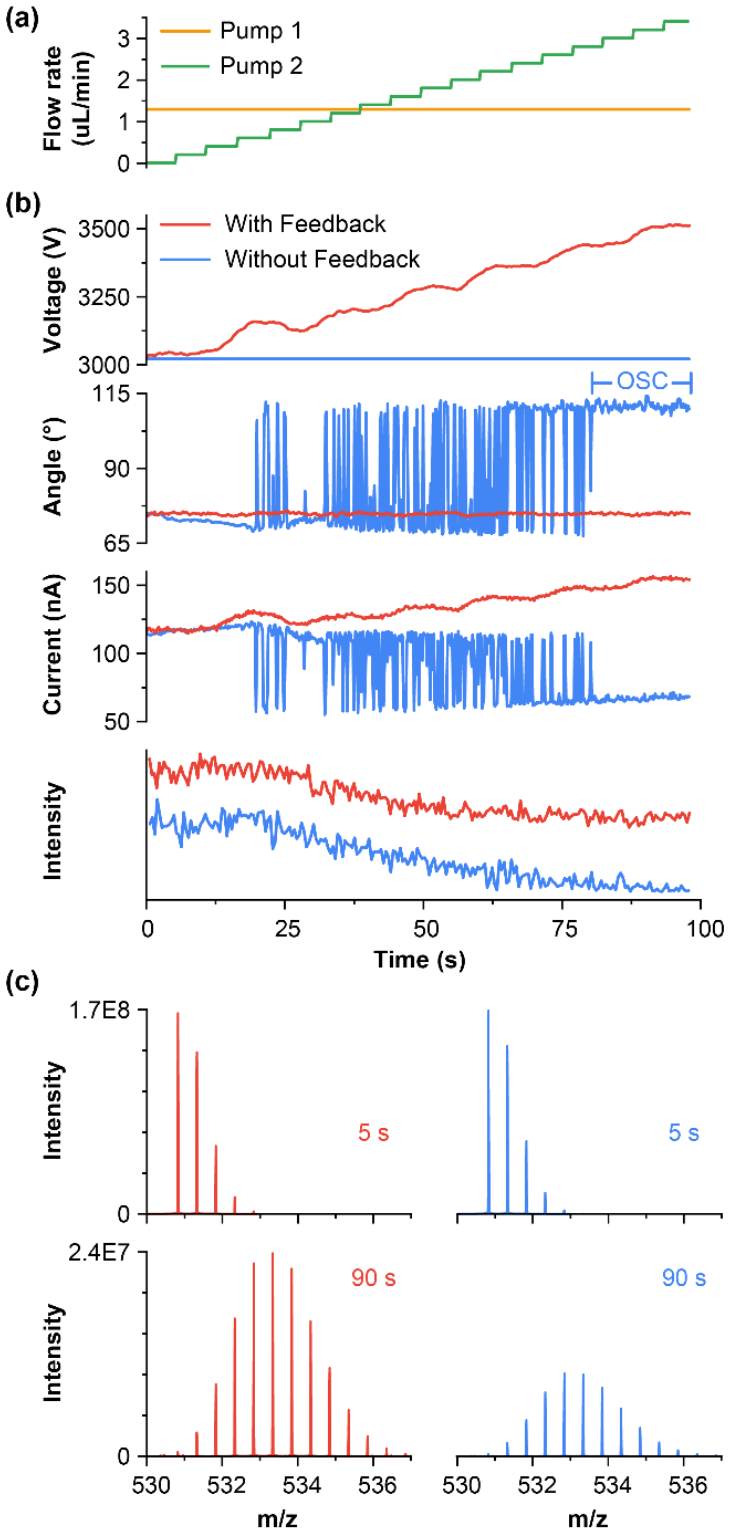

Figure 6.6. MS analysis of H-D exchange by mixing bradykinin in H_2O with D_2O solution. Pump 1: bradykinin in H_2O/ethanol 3/2. Pump 2: D_2O/ethanol 3/2. Both contain 0.05 % acetic acid. **(a)** Flow rates for Pump 1 (Orange) & pump 2 (Green). **(b)** Emitter voltage, apex angle, spray current and ion intensity vs time. Red line: with feedback control. Blue line: without feedback. **(c)** Mass spectra acquired at 5 and 90 s with feedback control (Red, left) and without (Blue, right) feedback control. OSC: kHz oscillation/pulsation mode. The target apex angle is 75°.

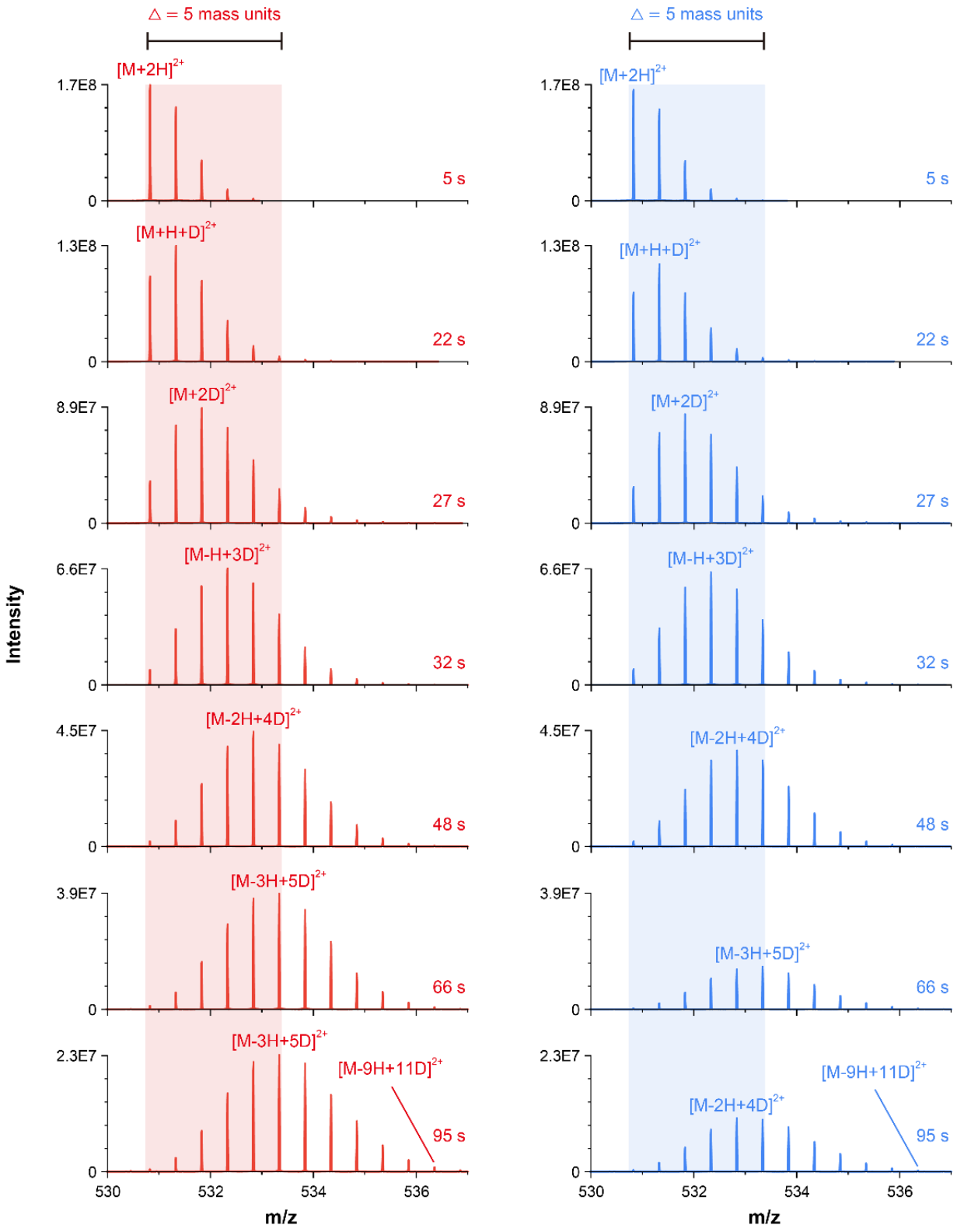

Figure 6.7. Time-resolved mass spectra for the H-D exchange measurement of bradykinin

Perturbation of surface tension

To attain the static condition under the Taylor cone assumption, the voltage V to produce electrostatic stress that matches the opposite surface tension at any point on the liquid surface is proportional to the root of surface tension γ,[11] i.e.

$$V \propto \sqrt{\gamma}. \qquad (11)$$

A perturbation of $\delta\gamma$ will destruct the stress balance and shift the cone-jet to the pulsation mode, or the multi-jet mode. Figure 6.8 shows the electrospray of solution with varying surface tension was performed by mixing two solutions of different ethanol concentrations at varying flow rates. One was 50 v/v % ethanol and another was 80 % v/v ethanol in water, each containing 5 μM ubiquitin, 0.05 % acetic acid, and 0.2 mM NaCl. The mixing following the flow rate pattern in Figure 6.8a resulted in a final solution with increasing surface tension. It was validated that by using the apex angle as the feedback signal, the emitter voltage could adjust itself with the change of surface tension (Figure 6.8b). The measurement of the spray current shows an increasing trend due to the increase of electrical conductivity and surface tension, agreeing with the established relationship of Eq 1. Without feedback control, the angle gradually reduced until ~ 66° before turning into pulsation mode. Compared to the cone-jet mode, the pulsation mode generated a larger initial charged droplet resulting in low ionization efficiency (see mass spectra in Figures 6.8c and 6.9). If the flow rate pattern is reversed to generate a decreasing surface tension, the emitter voltage with feedback control would reduce accordingly, and on the other hand, the spray without feedback could turn into a relatively unstable multi-jet mode.

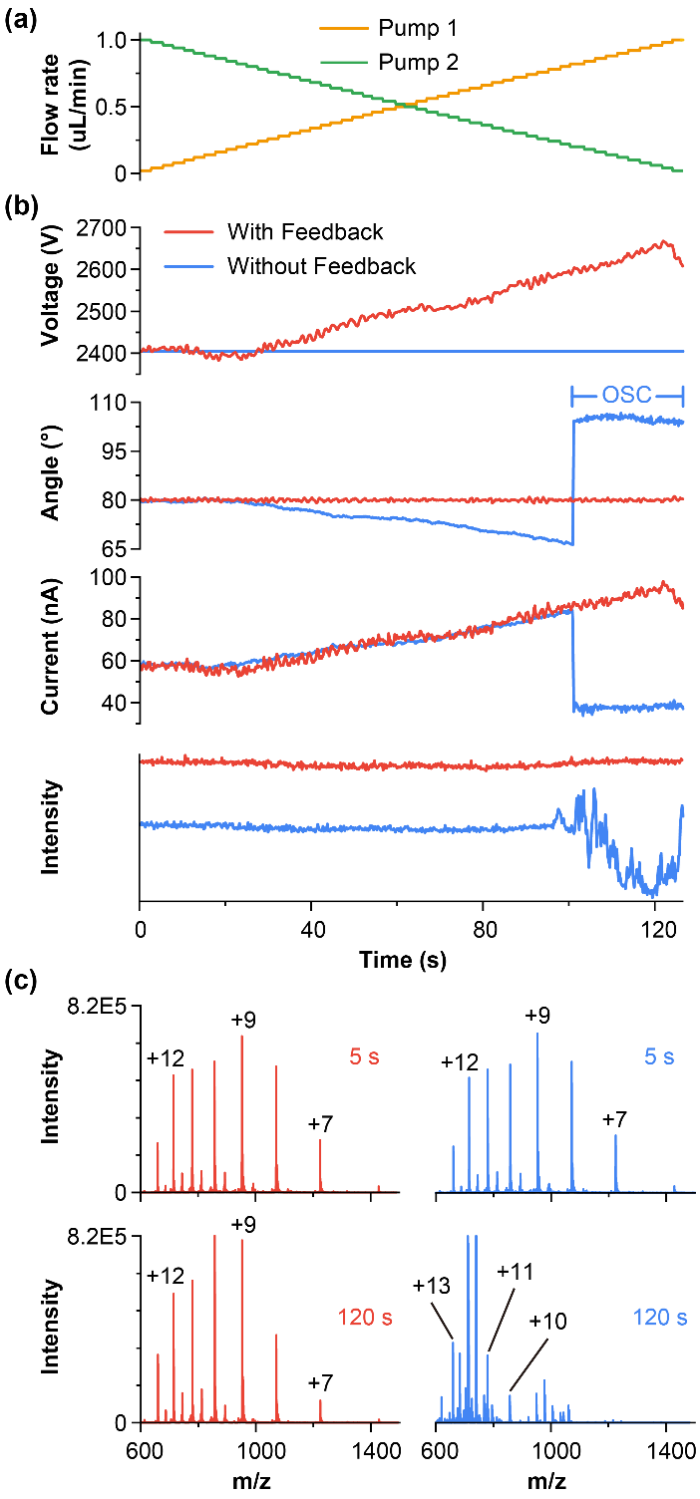

Figure 6.8. MS analysis of ubiquitin in a solution of changing surface tension. **(a)** The mixing of solvents from Pump 1 and Pump 2 delivers a total constant flow rate of 1 μL/min. Solvents in Pump 1 and Pump 2 are 50 % and 80 % ethanol solution, each containing 5 μM ubiquitin, 0.05 % acetic acid, and 0.2 mM NaCl. **(b)** Emitter voltage, spray current, apex angle, and ion intensity with and without feedback control. **(c)** Mass spectra obtained at different times. In the feedback-controlled ESI, the apex angle is locked at 80°. OSC: kHz oscillation/pulsation mode.

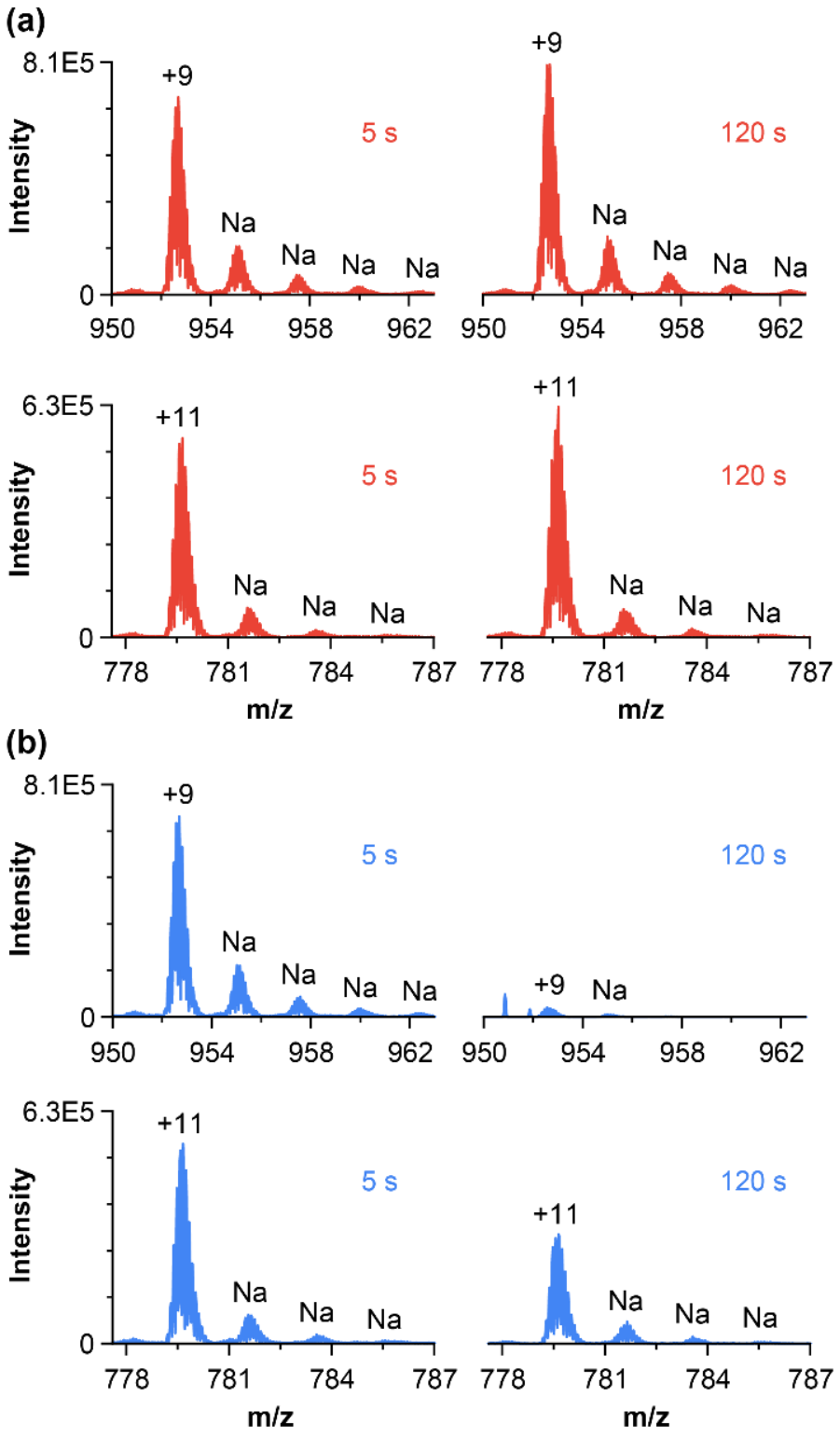

Figure 6.9. Magnified mass spectra for ubiquitin obtained at different times shown. (a) With feedback control. (b) Without feedback control. The MS is acquired under the perturbation of surface tension.

Characteristic of offline electrospray

The experimental condition of the offline ESI-MS was similar to the online version except for the replacement of the ESI sprayer with a custom-made offline sprayer (see schematic in Figure 6.10). The flow rate of the offline ESI was not fixed externally, thus its value varied with the emitter voltage. This resulted in a I-V curve (Figure 6.11a) which was quite different from the online counterpart. First, the distinct plateau for the cone-jet mode spray current was absent. A similar trend was also previously obtained for an offline bipolar electrospray[113], and nanoESI from micropipette tips[33]. In the case of online electrospray, the apex angle could increase from ~70 to ~90° by increasing the voltage under a given regulated flow rate. For the offline electrospray, however, the trend was in the exact opposite direction, that is the apex angle reduced with increasing spray current and voltage (Figure 6.11b). In response to this difference, the feedback control parameter G_β in Eq 10 needs to be a negative value. In this study, G_β was set to −10 V/° for offline, and 10 V/° for online electrospray.

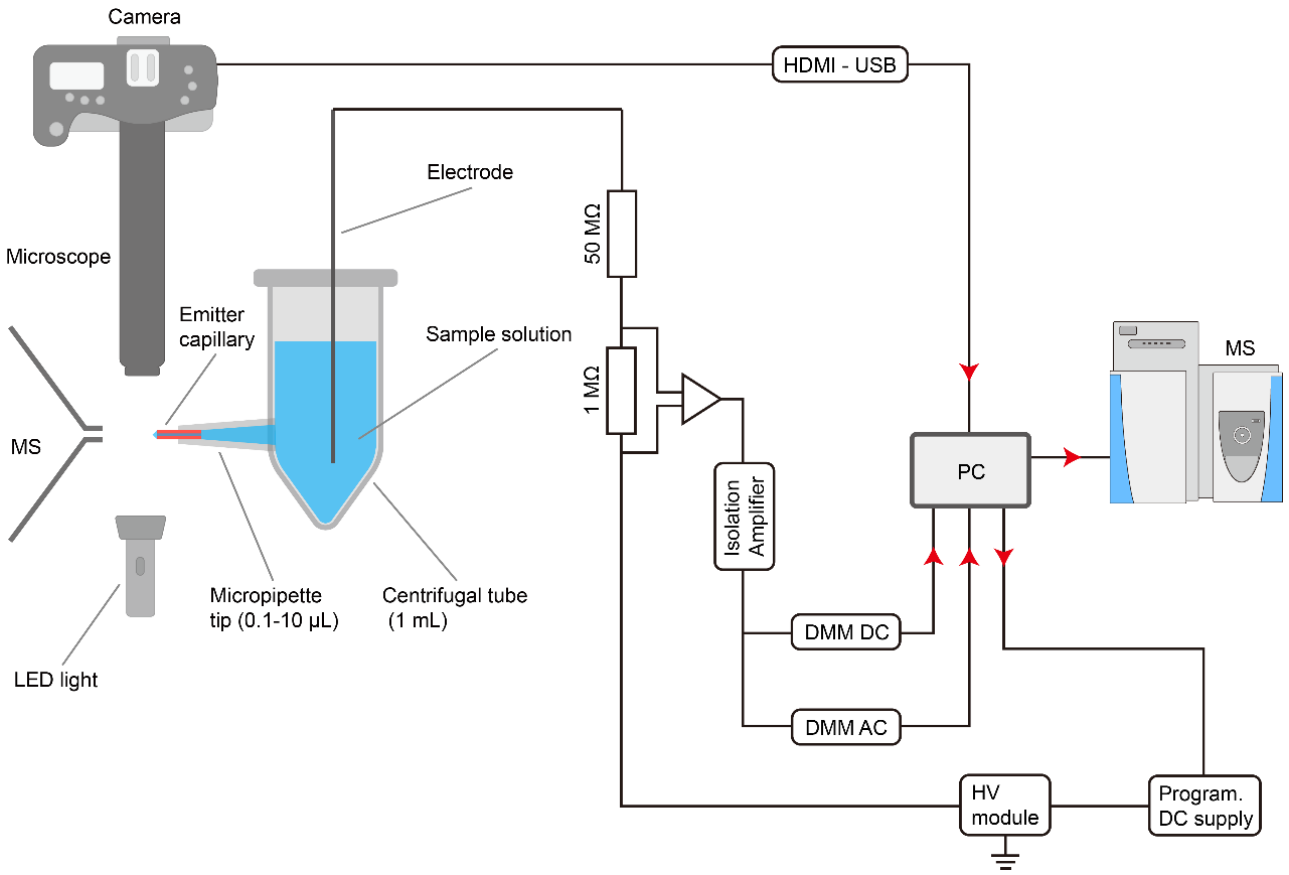

Figure 6.10. Schematic of the offline electrospray system. The experimental setup is similar to the online electrospray system except for the removal of syringe pumps and the replacement of the electrospray emitter.

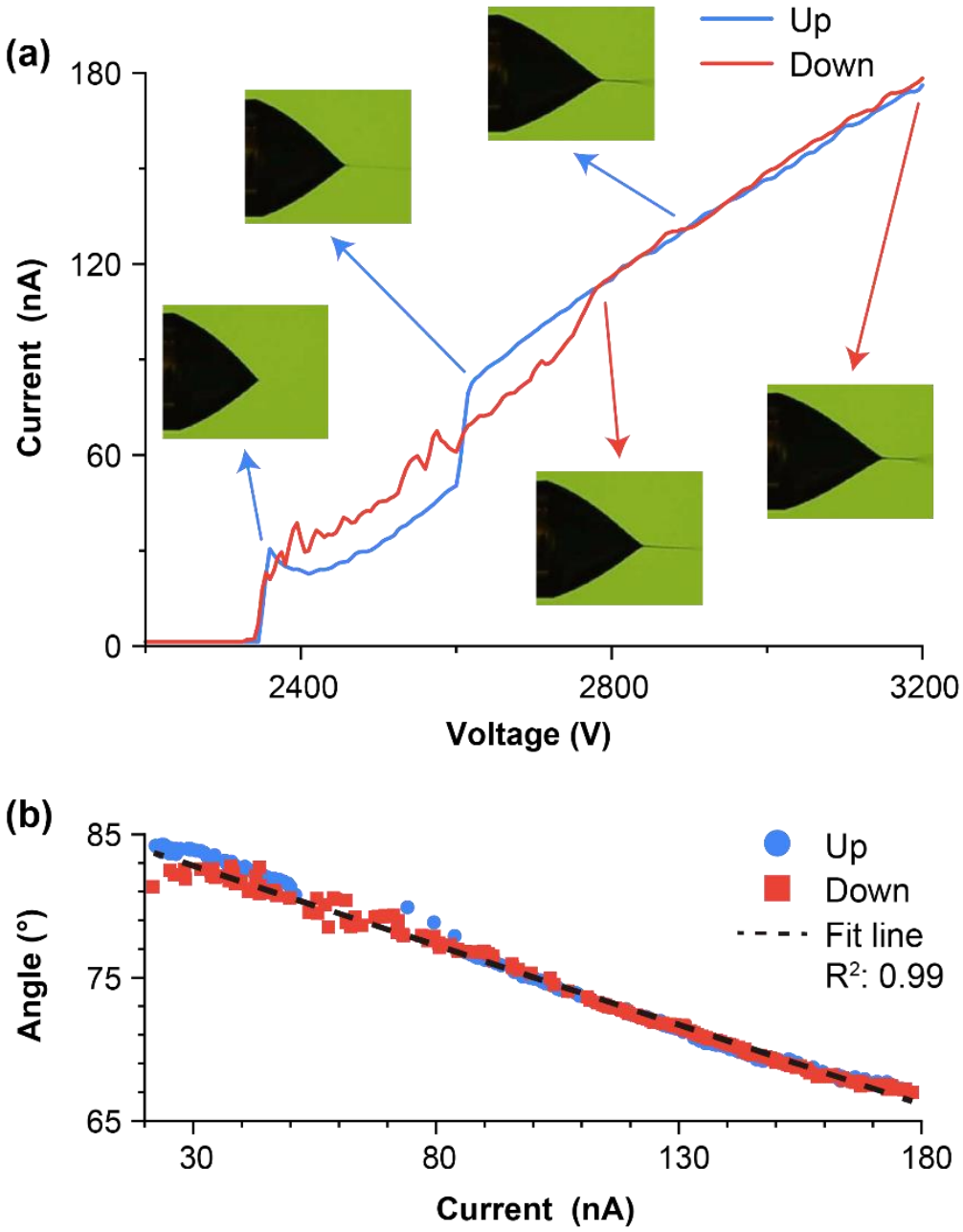

Figure 6.11. **(a)** Spray current versus emitter voltage relationship for an offline electrospray. Red line: increasing emitter voltage. Blue line: decreasing voltage. **(b)** The plots of apex cone vs spray current. In contrast to the online electrospray, the apex angle decreases with the spray current and emitter voltage. Solution: water/ethanol 1/1 (v/v) with 0.1 % acetic acid.

Electrostatic perturbation

The feedback control of the offline electrospray using the apex angle as the feedback signal is shown in Figure 6.12. To demonstrate the stabilization capability, an electrostatic perturbation was imposed on the electrospray system by changing the distance between the emitter and the counter electrode. Here, the angle was locked to 68°. Following the relationship observed in Figure 6.11b, the measured spray current was also stabilized to a constant DC level at 130 nA. Figure 6.13 shows that the reverse was also true, that is, when the spray current was locked to 120 nA, the apex angle was also stabilized to an average value of 72°. The locking of spray current was performed by replacing the updating Eq 10 with

$$V_{i+1} = V_i + \left(I_{\text{Target}} - I_i\right)G_I \qquad (12)$$

, where G_I is the control parameter (set to 1 V/nA in this study). In the demonstration shown in Figures 6.12 and 6.13, the measurements were started by optimizing the voltage at the position labeled as (i). The electrode distance was reduced by moving the effect towards the counter electrode to a position at (ii). Without feedback control, the spray current and the apex angle first increased, but the spray became unstable at ii which was approximately 2 mm from the original position.

In another measurement shown in Figure 6.14, the offline-ESI MS of ubiquitin started at position (i) which was ~5 mm from the MS inlet. The electrode distance was increased by moving the emitter further away from the MS inlet. The feedback control was performed solely by locking the spray current to 110 nA, and the resultant apex angle was naturally stabilized to ~73°. The ion signal was also well stabilized, producing near-equal total ion intensities at two different positions (Figure 6.14a). The charge state shifted slightly to a higher charge at a larger emitter-inlet distance (Figure 6.15). Without feedback, the spray stopped completely when the emitter was moved ~2 mm away from the original position (Figure 6.14b). Although the changing of the emitter position is usually unnecessary for typical MS applications, the feedback control system becomes beneficial for the search for the optimum position. The scanning of electrode distance has been employed for the evaluation of the flight time (or evaporation time) of droplets to study their effect on the ionization and in-droplet reaction process. Even for an application of fixed electrode distance, Figure 6.16 shows that the "long-term" ion signal stability was improved by imposing the feedback control (using spray current) to the

nanoESI source (homemade pulled-glass capillary).

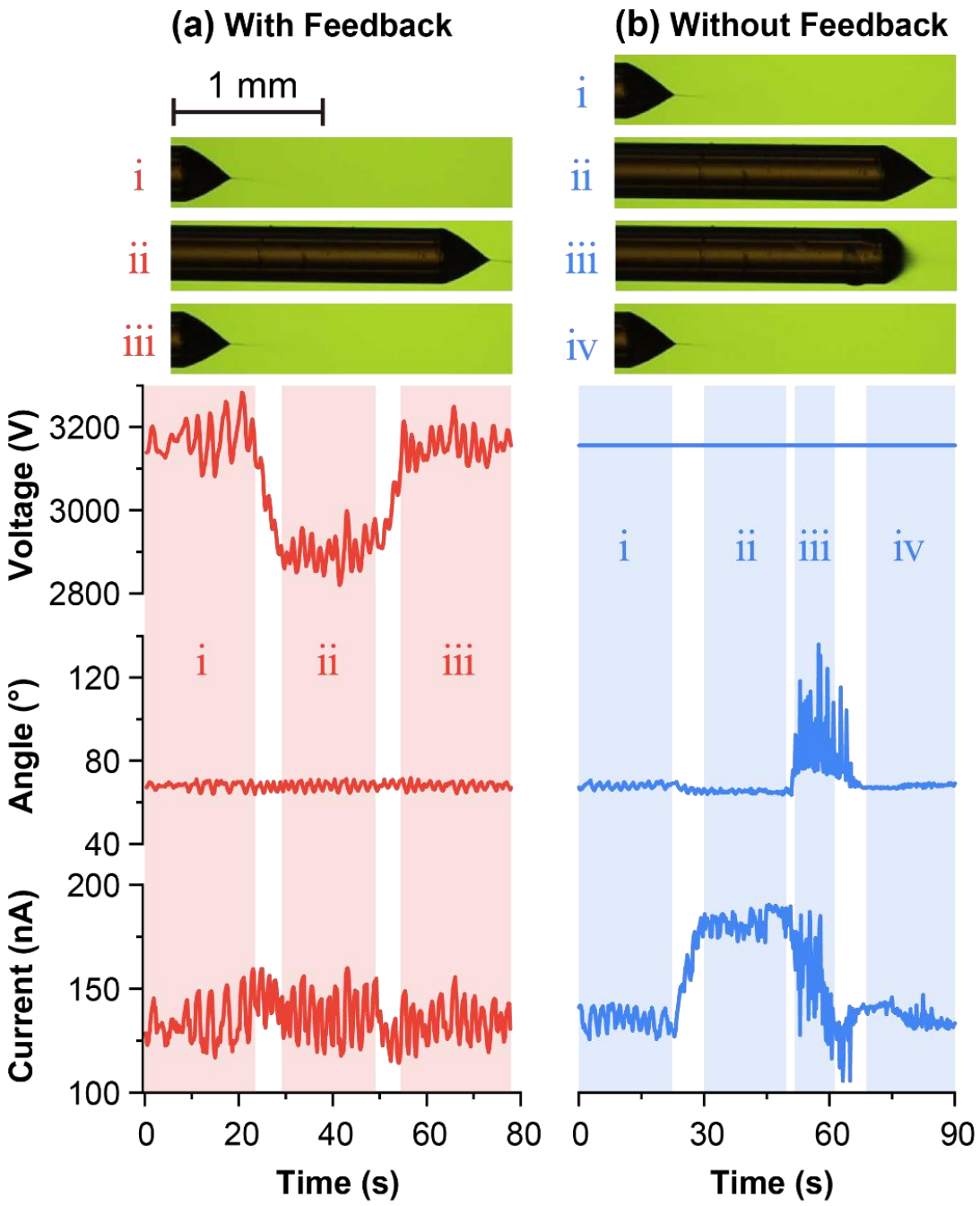

Figure 6.12. **a)** The feedback control of offline electrospray by locking the apex angle to 68° under the changing of electrode distance. **b)** Without feedback control. The figures show the relative emitter's positions, emitter voltage, apex angle and spray current. Solution: Water/ethanol 1/1 (v/v) with 0.1 % acetic acid.

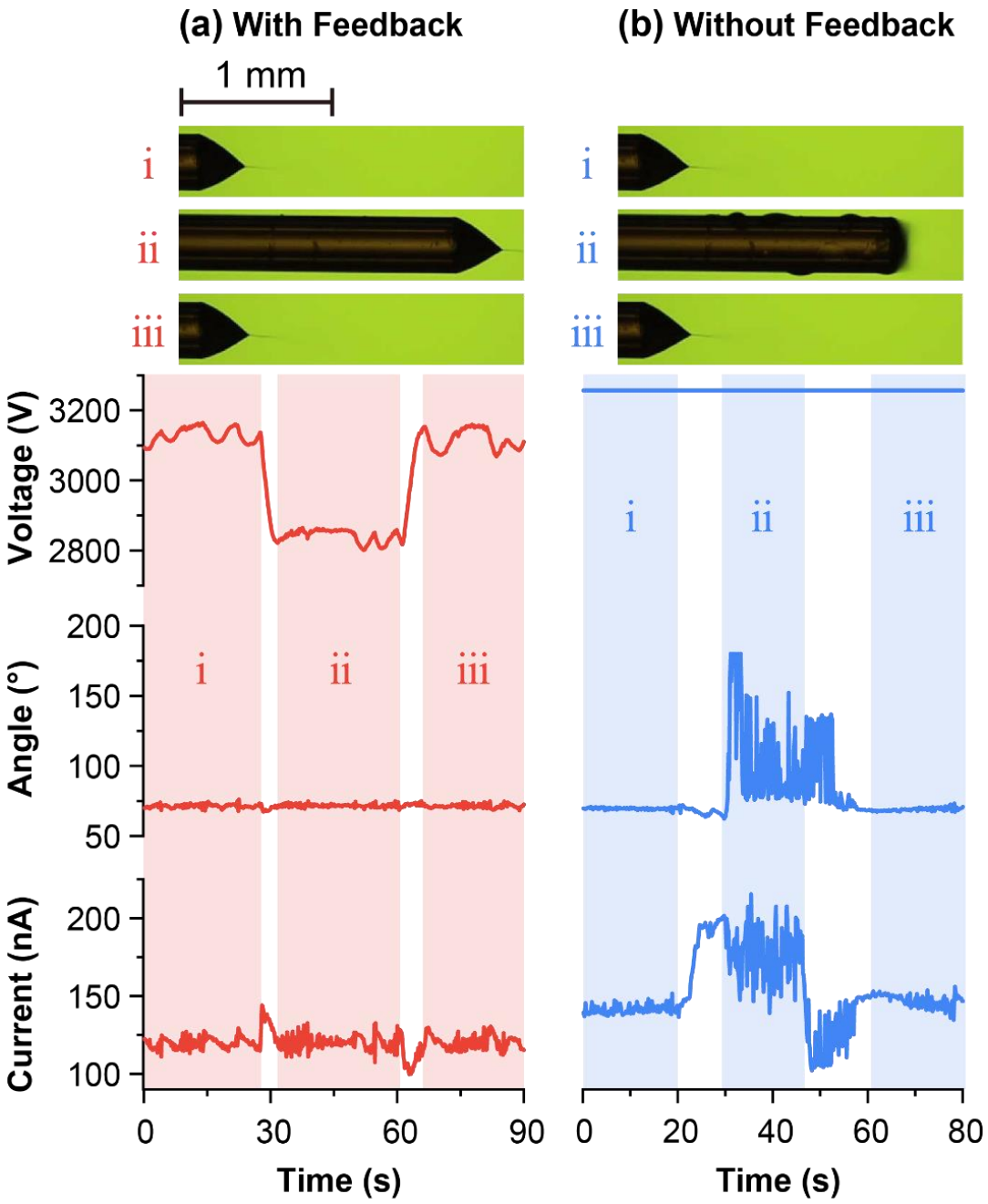

Figure 6.13. **a)** The feedback control of offline electrospray by locking the spray current to 120 nA. under the changing of electrode distance. **b)** Without feedback control. The figures show the relative emitter's positions, emitter voltage, apex angle and spray current. Solution: water/ethanol 1/1 (v/v) with 0.1 % acetic acid.

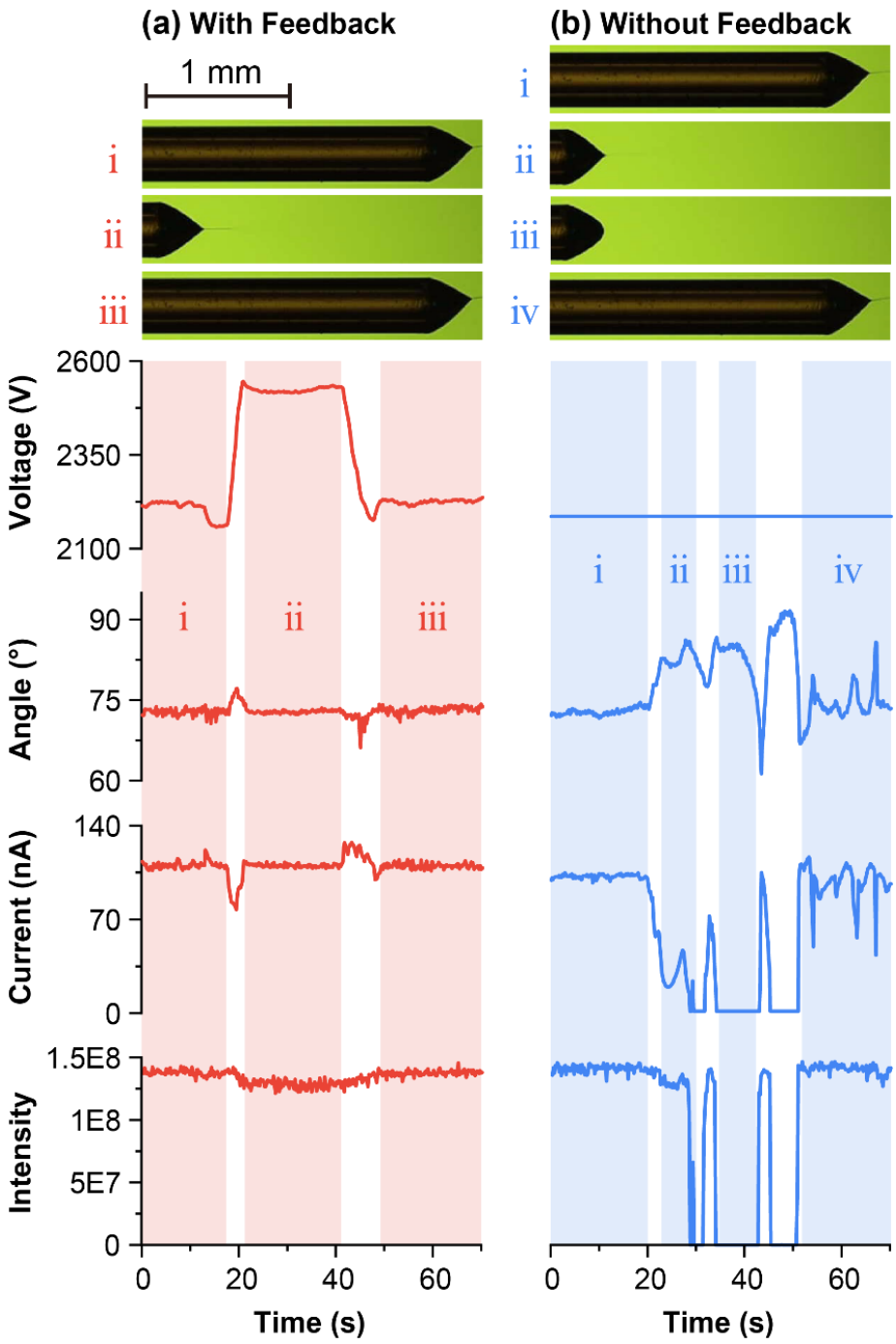

Figure 6.14. Emitter voltage, apex angle, spray current, and total ion intensity for MS of ubiquitin under varying emitter-to-inlet distance. **(a)** With feedback control. **(b)** Without feedback control. The distance is varied from 5 mm to 7 mm. Solvent: 50 % ethanol aqueous solution containing 1 mM ammonium bicarbonate. The spray current is locked at 110 nA (~ 73 ° apex angle) with feedback control.

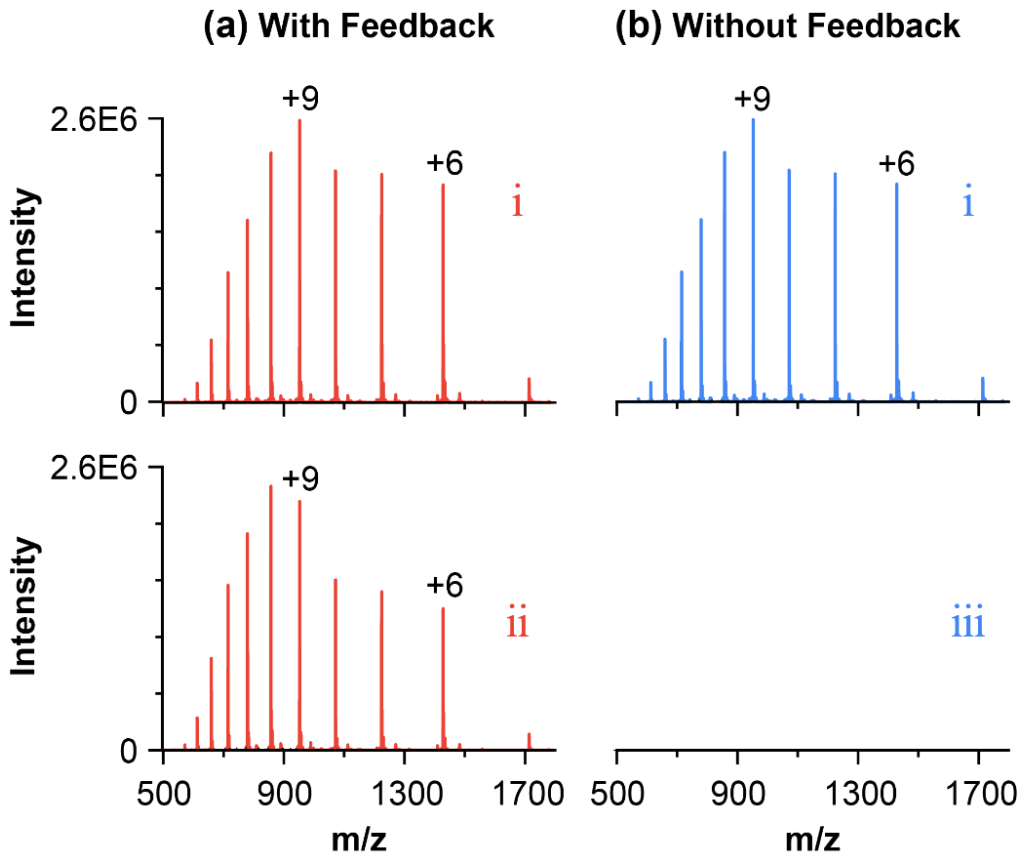

Figure 6.15. Mass spectra of ubiquitin acquired at different emitter positions with (a) and without (b) feedback control. The red i & ii in (a) and the blue i & iii are positions with the same labels.

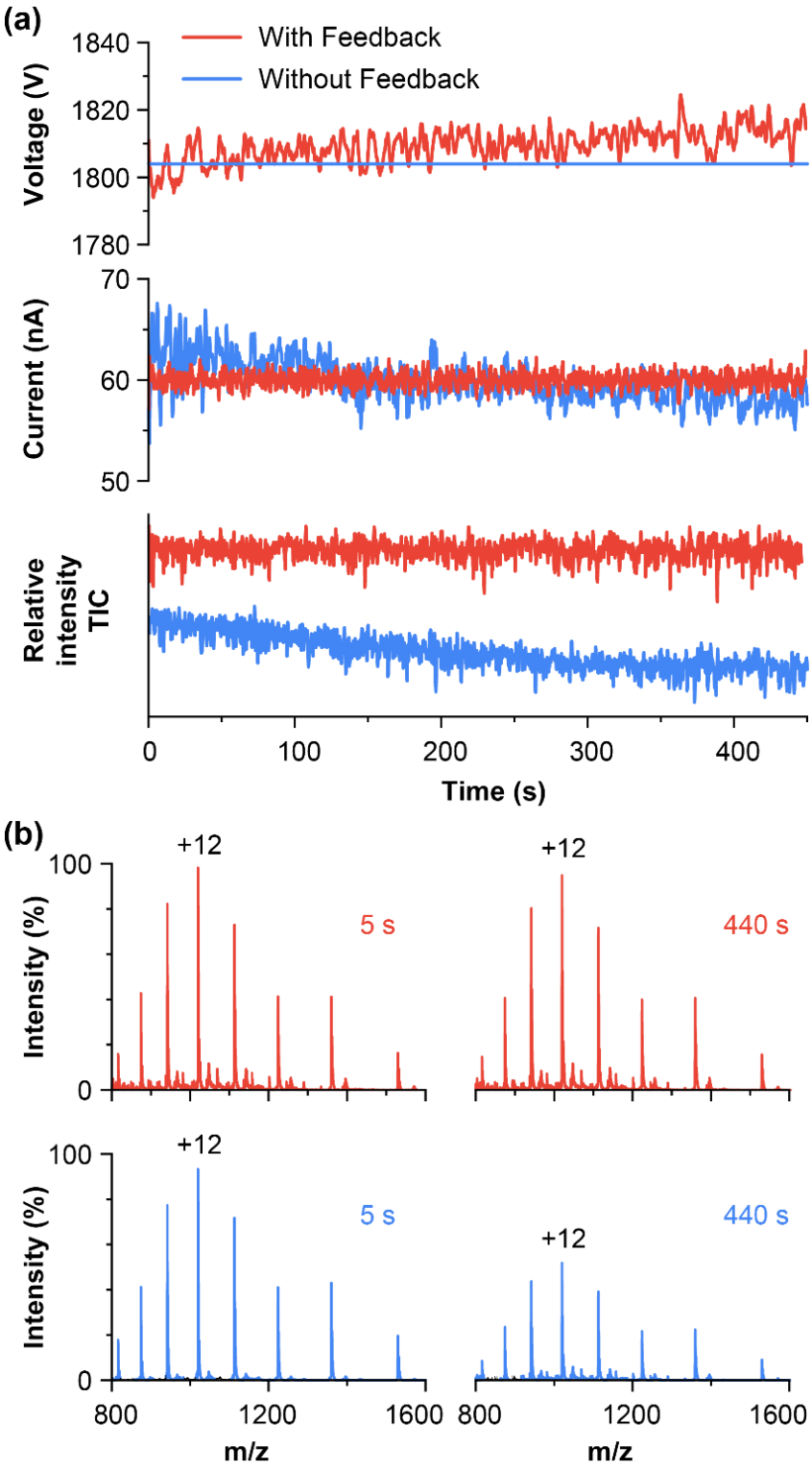

Figure 6.16. NanoESI-MS for cytochrome *c* with (Red) and without (Blue) feedback control. a) Emitter voltage & Spray current. b) Mass spectra acquired at different times. Ion source: homemade pulled glass capillary (o.d. ~ 20 μm, i.d. ~10 μm). Sample concentration: 5 μM in 50 % ethanol with 1 mM ammonium acetate)

Flow rate programming

An intriguing feature of offline electrospray is that if the electrical conductivity is constant and known in advance, the flow rate can be precisely controlled by the emitter voltage using the spray current as the flow rate indicator[32,33]. The scanning of voltage has been applied to acquire the response of ionization to nanoflow rate[104], and to trigger the oxidation caused by the strong electrical field around the Taylor cone at low flow rates[130]. With feedback control, the spray current and flow rate could be programmed to follow an arbitrary pattern. The measurement in Figure 6.17 was performed with spray currents locked to the user-defined staircase pattern (100 to 500 nA with a stepwise increment of 100 nA). The ionization was performed using a high-pressure nanoESI to handle the pure aqueous solution of cytochrome *c* and ammonium acetate. The electrical conductivity of the liquid was 0.5 S/m, and the flow rate estimated using the scaling law of electrospray (Eq 1) changed from 4 nL/min to 100 nL/min. Although nanoESI is well known to have high ionization efficiency, the ion intensity is not always higher at a lower flow rate. The total ion intensity originated from cytochrome *c* increased in the same flow rate pattern. This result agreed with our previous observation of cytochrome *c* using a continuous voltage ramping method. Here, a flat response of the ion signal at each flow rate indicated that the trend was reproducible and was not due to the transient effect.

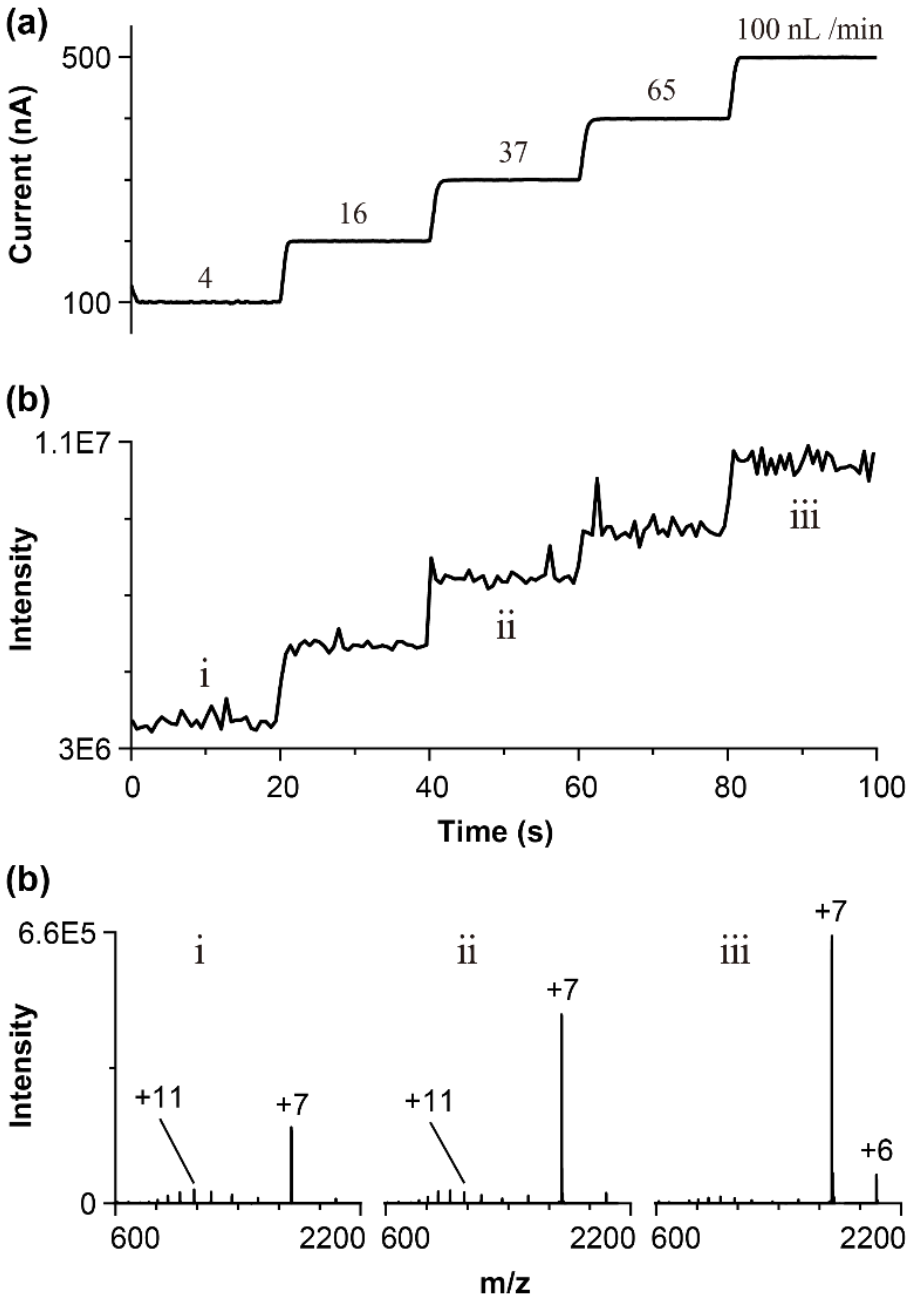

Figure 6.17. Offline high-pressure nanoESI-MS of cytochrome *c* in 50 mM ammonium acetate aqueous with spray currents that follow the user-defined pattern. **(a)** Programmed spray current. Labels show the calculated flow rates. **(b)** Total ion intensity of cytochrome *c*. **(c)** Mass spectra acquired at the time interval i-iii in (b).

Conclusions

A simple iterative learning feedback control system has been developed for ESI-MS which provided an automatic correction to the emitter voltage to ensure the cone-jet mode operation throughout the course of the analysis. Spray current and optical image were used to determine the spraying mode and for performing the closed-loop control using a simple updating rule to stabilize the apex angle or spray current to a user-defined value. The robustness of the feedback system was tested using emulated perturbation of flow rate, surface tension, and electrode distance. For an analysis involving changes in flow rate, and fluidic or electrostatic conditions, the locking of the Taylor cone ensured a steady cone-jet mode operation and overall ion signal stability. For an offline electrospray with constant fluidic variables, the locking of the spray current also stabilized the Taylor and the solution flow rate.

Chapter 7: New variation of AP or HP ESI: bipolar ESI

Summary

A bipolar ESI source is developed to generate a simultaneous emission of charged liquid jets of opposite polarity from an electrodeless sprayer. The sprayer consists of two emitters the electrosprays are initiated by applying a high potential difference (HV) across the counter electrodes facing each emitter. The sprayer and the liquid delivery system are made of all insulators without metal components, thus enabling the total elimination of electrochemical reactions taking place at the liquid-electrode interface in the typical electrosprayer. The bipolar electrospray has been implemented using an online configuration that uses a syringe pump for flow rate regulation and an offline configuration that relies on HV for adjusting the flow rate. The voltage-current and flow rate-current relationships of bipolar electrospray were found to be similar to the standard electrospray. The application of bipolar ESI to the mass spectrometry of protein, peptide, and metallocene without the electrochemically induced oxidation/reduction is demonstrated.

Introduction

Electrospray in general refers to the dispersion of liquid by an intense electrical field. In the unassisted electrospray, the conductive liquid anchored to the opening tip of an emitter is charged above a threshold potential that causes the liquid meniscus to deform and eject charged droplets. Depending on the charging potential, the meniscus can oscillate at a frequency related to the capillary wave, or attain a near-stationary conic shape with a fine jet emitted from the tip[141]. The latter is called steady cone jet mode. The jet breaks into isolated charged droplets and the shrinkage in droplet size due to solvent evaporation results in coulombic fission to generate even finer droplets. To operate an electrospray in a sustained manner, it needs to be powered by an external electromotive source, i.e applying a high voltage (HV) from a power supply to the metallic emitter. For a nonmetallic emitter such as a sharpened fused silica capillary, the electrical contact is on the inserted electrode or the metallic union. The flow of current in the electrospray of the solution involves ions, therefore the loop of the electrical circuit needs to be closed by electrochemical reactions at the electrode/solution

interface. Owing to this reason, Kerbale et al. viewed the ESI source as "*an electrolytic cell of a special kind*"[17]. Although the presence of electrochemical processes in the electrode interface of electrospray is indisputable, there are debates on its importance on ESI[18].

From an electrohydrodynamic point of view, the details of the involving electrochemistry are not essential in predicting the physical behavior of electrospray. The relationship between the flow rate and spray current and the size of the droplet it produces can be estimated using fundamental physical variables such as relative permittivity, density, viscosity, surface tension, and electrical conductivity of the liquids. But from a mass spectrometric point of view, the electrochemical reactions alter the composition of the electrospray solution and affect the MS results, therefore its effects can not be taken lightly. In the positive ion mode, the consequence of the electrochemistry are i) corrosion of the electrode that releases the metal ions to the solution, ii) the oxidation of solvent or analytes, and iii) the neutralization (oxidation) of the anion of the analyte or buffer salts. The corrosion of electrodes can be prevented by the use of inert materials such as platinum but that will instead give rise to other reactions such as the oxidations of solvent or analytes[19,20]. In the negative ion mode, the reduction can result in the deposition of metal ions on the electrode[21]. For an unbuffered solution, there could also be a change in pH caused by the inherent electrolytic process of the ESI source[19,20]. This intrinsic electrolytic effect of electrospray has also been exploited for analytical applications such as the detection of radical cations $M^{+\bullet}$ of porphyrins[22]. A combination of external electrochemical cells with the ESI source also exists[153].

For the typical ESI-MS however, the oxidation of analytes by the inherent ESI electrochemistry or the corona discharge is not desirable as it reduces the detection sensitivity and introduces artifacts such as a shift in m/z and the broadening of peaks distribution to the mass spectrum[76,78,88]. There are a few ESI source design which has been employed to avoid interference from the electrochemical reaction. One design separated the sample flow steam from the charging electrode using a microdialysis membrane tubing junction[154]. Another approach channeled the liquid into two flow streams: an analytical stream flowing to the emitter and a charging stream flowing to the waste. The HV electrode was placed at the charging channel and the electrochemical products were directed to the waste[155,156]. Electrically, electrochemical reactions were still involved in those sprayers, thus it is worthwhile to evaluate the stability and the performance of electrospray if the electrode

reactions are completely removed from the ESI emitter.

This chapter describes the operation of a bipolar ESI sprayer that is consisted of a pair of electrodeless emitters to discharge the positively and negatively charged droplets simultaneously. No electrochemical reaction is involved inside the emitter. The strong electrical field was provided by applying HV to the plane counter electrode placed at both ends of the emitter. The arrangement is electrically identical to the hypothetical bipolar electrospray device proposed by Manuel Martinez-Sanchez[18]. Although it is said that the *"idea has been around for a long time"* [18], the actual implementation of such ESI source and its physical and analytical properties has never been reported. Despite the difference in naming, the bipolar electrospray also shares a similarity with field-induced droplet ionization (FIDI) they both generate a pair of bipolar liquid jets[157,158]. In FIDI, an isolated liquid droplet that was dropped in between two plane electrodes was stretched to generate two liquid jets of opposing charge by a pulsed electrical field. Another version of FIDI had also been performed on the droplet emerging from the end of a stainless steel capillary[159]. Using a similar FIDI configuration, continuous bipolar jets had also been reported using a DC HV instead of a pulsed HV[160]. The size of the anchored droplet in those experiments was in the order of 1~2 mm. Due to the discharge problem, stable cone-jet mode operation was limited to the pure organic solution.

There is also a group of ESI variants in which the electrode is not in direct contact with the liquid. One example is the dielectric barrier electrospray that generates the dielectric polarization to initiate the electrospray[161]. Induced nanoESI by pulsed square wave without physical contact has also been used for multiplexed ESI array[162]. Instead of capillary, a solid ESI probe made of a glass-sealed stainless-steel electrode has also been demonstrated[163]. An electrically equivalent arrangement was performed by generating pulsed electrospray from the droplet deposited on an insulating plate backed with an electrode[164]. Similar to the dielectric discharge plasma device, those contactless ion sources required an AC or pulsed HV. The spray and the ion are not generated continuously and the polarity is in an alternative manner. Owing to the pulsing nature, the operation of non-continuous electrospray might be restricted to the pulsation mode, i.e. not being able to attain the steady cone-jet mode. Another related issue is the synchronization with the MS instrument. Nevertheless, the capacitively coupled ESI was reported to avoid the electrochemical oxidation of peptides and proteins in ESI[165]. Besides capacitive coupling, the charging of electrospray solution without "physical" contact had also been

demonstrated using electrical discharge[166], primary ions/charged droplets[167], and electrostatic induction[168]. The nanoESI powered by triboelectric nanogenerators also exists[169].

It is noted that the term "bipolar ESI" also refers to the one that uses two independent electrospray sources to mix the ions/charged droplets of opposite polarity for charge reduction[170,171]. Here, the bipolar electrospray originate from a single liquid supply. Continuous separation of anions and cations induced by the electrical field sustains a steady flow of spray current. Part of the experiment involving pure aqueous solution was performed under a high-pressure condition, i.e. the pressure of the gas/air that surround the emitters and their counter electrodes was higher than the atmospheric pressure. The concept of high-pressure ESI (HP-ESI) was previously developed in our laboratory to prevent the electrical discharge for the electrospray for high surface tension solutions[23,129], high-temperature ESI[53], and the generation of nanoESI from micropipette tip[32,33].

Experimental section

The online sprayer (Figure 7.1a) used a plastic syringe and a precision syringe pump (PHD ULTRA 4400, Harvard Apparatus, Holliston) to deliver the liquid at a constant flow rate. An insulating T-union made of polyether ether ketone (PEEK) was used to split the solution into two streams. The emitter capillaries, ~2 cm in length, were made from commercial PEEK tubing (i.d. 0.1 mm, o.d. 0.36 mm). No metal parts were present in the sprayer and the liquid supply line. A high voltage difference (HV) was applied between two counter electrodes to generate the bipolar electrospray. Two planar counter electrodes were used for the measurements of spray current-voltage and spray current-flow rate relationships. For the mass spectrometry (MS) measurement, only one planar electrode was used (Figure 7.1) and the ion inlet served as one of the counter electrodes. The planar electrode was applied with +HV for positive ion mode, and -HV for negative ion mode. The distance between the emitter and the MS inlet was 5 mm. The distance between another emitter capillary and the planar electrode was also 5 mm. The mass spectrometer was a benchtop Orbitrap (Exactive Plus) from Thermo Fisher Scientific, Bremen, Germany. The voltage of the MS inlet was provided by the internal power source board of the MS instrument. When put to run, the voltage was +24.5 V and -25.5 V in the positive and negative ion modes, respectively.

The offline sprayer (Figure 7.1b) was made by fusing two micropipette tips (10 μL max) into

another larger tip (200 μL max) that served as the liquid reservoir. The emitter capillaries were made by inserting the PEEK capillary into the 10 μL micropipette tips. The liquid flow rate for the offline sprayer was controlled by the potential difference applied between the counter electrodes. For pure aqueous solutions with large surface tension, the offline sprayer was operated under super-atmospheric pressure (~4 bar gauge pressure) using a sealed chamber to prevent electrical discharge. The photographs showing the constructed sprayer and the connection to the mass spectrometer are shown in Figure 7.2.

Bipolar electrospray emitters and MS

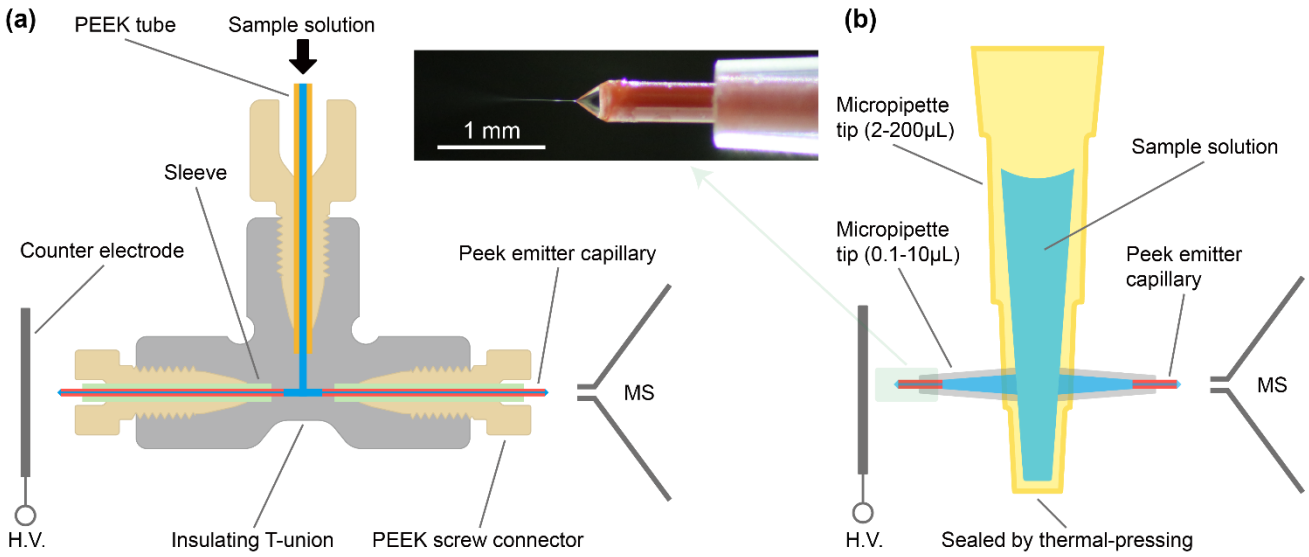

Figure 7.1. Schematics of the bipolar ESI source. (a) Online configuration. The sample solution is supplied from a plastic syringe. (b) Offline configuration. HV is applied to the planar counter electrode. In the positive ion mode, the voltage of the MS inlet is 24.5 V relative to the chassis ground.

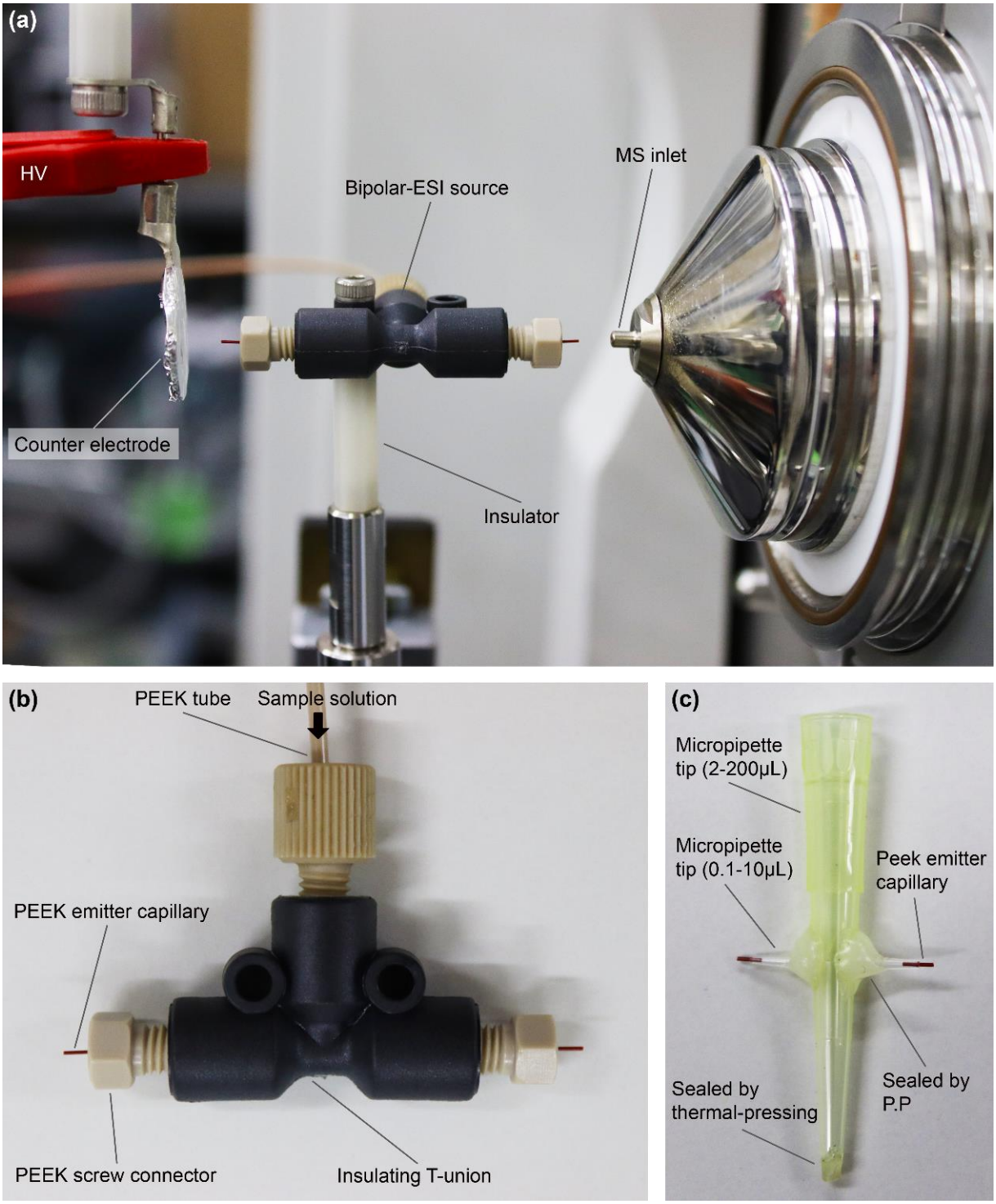

Figure 7.2. a) The connection of the bipolar ESI source to a commercial mass spectrometer. b) Online bipolar ESI source made of commercial PEEK T-union, and PEEK tubing. The sample solution is supplied from a plastic syringe. b) Offline bipolar ESI source made of micropipette and PEEK capillary. The offline bipolar ESI source can also be operated under high pressure for aqueous solutions.

Ramping of HV & regulation of spray current

The potential difference between the counter electrodes was ramped to evaluate the relationship between the spray current and voltage of the bipolar electrospray. The ramping of voltage from an HV power supply (Matsusada Precision, Tokyo, Japan) was remotely controlled using a PC via a programmable DC supply (Agilent). The voltage was ramped up from 5000 to 10000 V and then ramped down to 5000 V. The period for this tringle waveform was approximately 80 seconds. The ramping was performed at 5 V/step with a step interval of approximately 0.04 s. The spray current was measured by sensing the voltage drop across a 1 M resistor that was connected to the electrode of lower potential. The readings were read and recorded using a multimeter and PC. The flow rate for the offline sprayer at a constant spray current was measured by weighing the liquid in the sprayer while spraying using an electronic balance (Mettler Toledo).

Sample preparation

Cytochrome c (12.2 kDa), myoglobin (17.6 kDa), ubiquitin (8.6 kDa), melittin (2.8 kDa), and ferrocene (186 Da) were purchased from Sigma Aldrich. Formic acid, acetic acid, ammonium formate, and ammonium acetate were from Kanto Chemical (Tokyo, Japan). All chemicals were used without further purification. The electrical conductivity of the solution was measured using a conductivity meter (Mettler Toledo).

Results and Discussion

Optical inspection

Figure 7.3 shows the effect of increasing HV between the plane counter electrodes. The movies were taken by two long-working distance microscope cameras which were synchronized using a master PC. The liquid solution within the electrodeless emitter capillaries could be regarded as a conductor (though with relatively high resistance compared with metal). When the HV was applied, the electrical field between the plane electrode was not totally uniform, and a high field was concentrated at both distal ends of the capillaries. With a sufficient electrical field, two symmetric

Taylor cones formed and emitted charge droplets of opposite polarity similar to standard electrospray with a metallic emitter (Figure 7.3d). The electrochemical reactions were absent in the sprayer but took place at the two counter electrodes where the charged droplets are neutralized. Similar to the typical electrospray, the liquid meniscus underwent initial large droplet ejection, high-frequency pulsation, steady Taylor cone, and multi-jet formation with the increase of the electrical field. During the initial bursting and pulsation stage, the changing of meniscus shape and the emission of the bipolar jets were not always in sync. Out-of-phase jetting was also observed. The highly stable bipolar electrospray was achieved when steady cone-jet mode (stable Taylor cones) was attained at both emitters.

It is noted although a continuous bipolar electrospray could also be generated using an arrangement similar to FIDI, the Taylor cone formed was relatively large with a cone height of ~2 mm (Figure 7.4). Besides the reproducibility and the poor stability, the initialization of the Taylor cone was relatively difficult. A failed initialization caused the burst of the large meniscus, followed by a significant wetting on plane electrodes and arc discharge. Reducing the size of the liquid delivering capillary (e.g. to ~0.2 mm o.d.) was not helpful as it caused a sudden burst of large bipolar jets without the formation of stable Taylor cones.

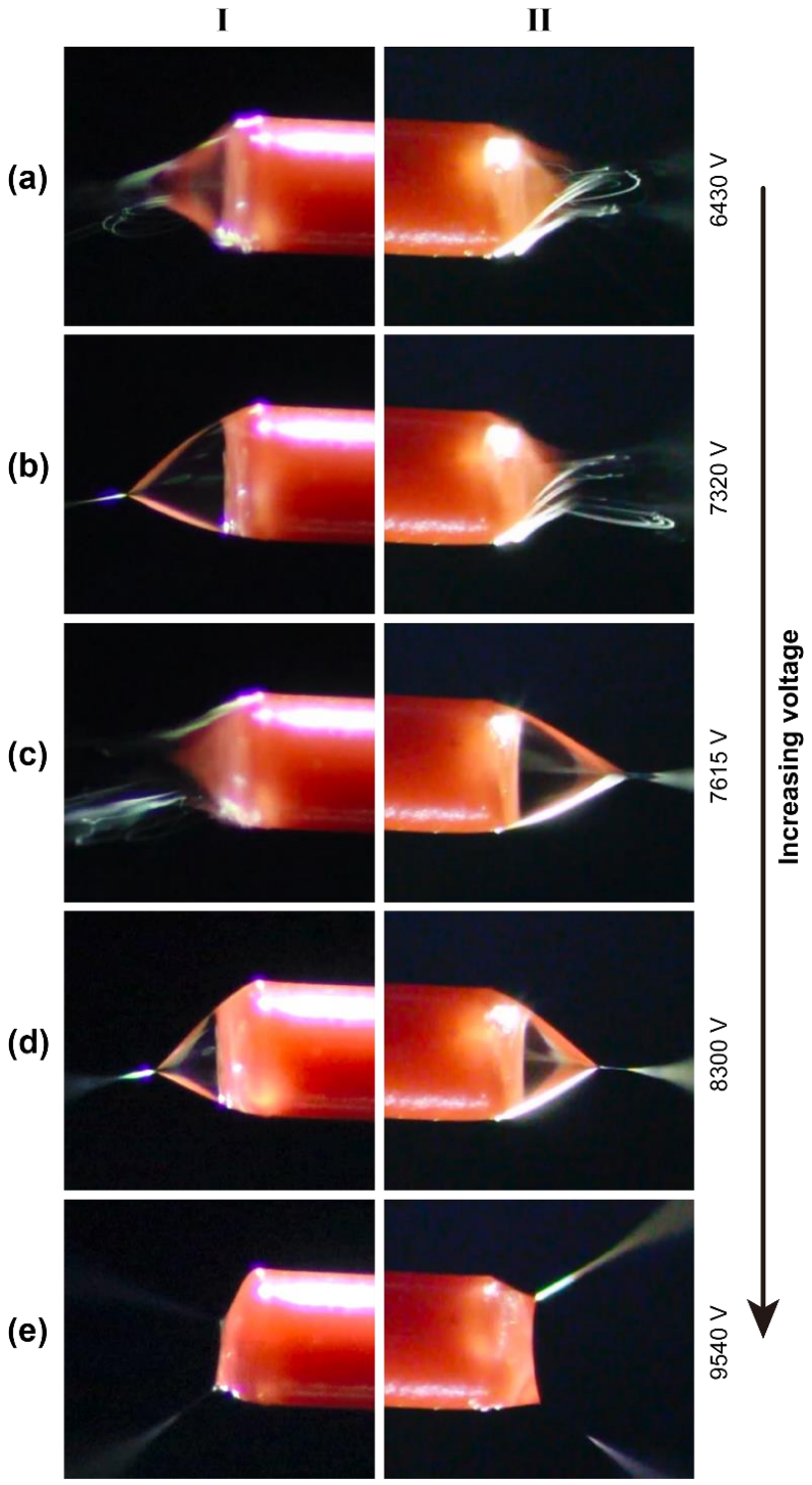

Figure 7.3. Initialization and the formation of bipolar electrospray. Column I: Negative ion mode. Column II: Positive ion mode. (a) Both are unstable, (b) & (c) Only one mode is stable. (d) Both are stable. (e) Both in two-jet mode. Images are extracted from the synchronized movies captured by two microscope cameras. The flow rate at each emitter is 2 μL/min.

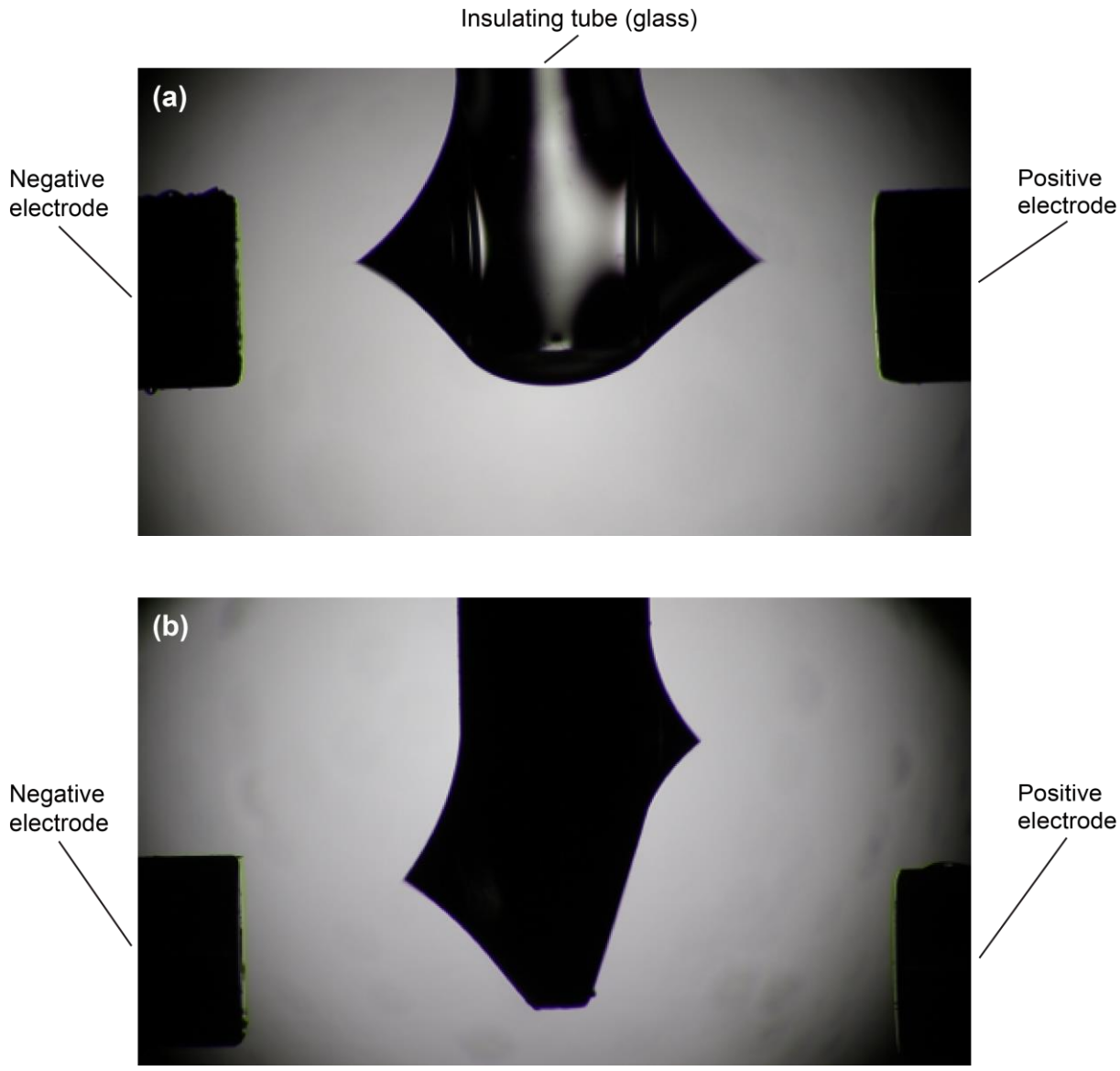

Figure 7.4. Generation of bipolar electrospray using the configuration similar to field-induced droplet ionization (FIDI) source. The liquid was supplied via the syringe pump. The solvent here is water containing formic acid. It is operated under high-pressure to prevent discharge.
a) Successful initialization of symmetric bipolar Taylor cone.
b) Asymmetric Taylor cone.

Spray current-voltage relationship

The spray current-voltage (I-V) relationship was first evaluated for an electrospray at a flow rate of 5 μL/min generated from a stainless-steel emitter capillary with approximately the same inner diameter as the PEEK emitter capillary (Figure 7.5a). To construct the I-V curve, the voltage applied to the capillary was first ramped up from 1.7 kV to 3.6 kV, and then reduced to 1.7 kV at the same increment/decrement rate. As is well known, the I-V curve of an un-assisted, flow rate-regulated electrospray exhibits a distinct step response when the electrospray turns from dripping/pulsation to a steady cone-jet mode. The value spray current in Figure 7.5 is the average value measured using a multimeter at an averaging time of 0.02 s. The high-frequency (kHz) current signal associated with the pulsation mode was monitored with an oscilloscope. Within the steady-cone jet mode, the spray current I and solution flow rate Q are related by the famous scaling law[24]

$$I = f(\epsilon_r)\left(\frac{\gamma K Q}{\epsilon_r}\right)^{1/2} \quad (1)$$

where γ is the surface tension, K is the electrical conductivity, ϵ_r is the relative permittivity of the liquid and $f(\epsilon_r)$ is a coefficient that depends on ϵ_r. Under a constant flow rate, the spray current stays nearly constant with the increment of high voltage until the emergence of two and multiple jets.

Figure 7.5b shows the I-V curve acquired for the online bipolar electrospray. The total flow rate supplied to the T-union was 10 μL/min. Before performing the electrospray, the following procedures were performed to ensure that the flow was equally split so that the flow rate for each emitter Q is half of the total supplied flow rate, i.e. 5 μL/min. First, the sprayer was flushed with a known amount of solvent with a flow rate greater than 100 μL/min, and the flushed solvent from each emitter was collected and weighed. Under the inspection of the microscope, the sprayer was supplied with the solution at a flow rate of ~4 μL/min for 30 s~1 min without the application of HV to compare the sizes of the liquid meniscus formed at each emitter. Electrically, both sprayers were connected in series, thus the same spray current flowed through both emitters. The voltage denotes the potential difference between the two counter-plane electrodes. The main finding here is that, despite using insulating emitters, the overall I-V trend is similar to the conventional electrospray. However, the bipolar electrospray needed to undergo a quasi-stable stage to fully complete the transition from the

pulsation to the steady cone-jet mode for both polarities. During the quasi-stable stage, the simultaneous formation of positive and negative Taylor cones was short-lived and one of the liquid menisci could turn to pulsation as shown in the drastic drop in the spray current and the optical observation in Figures 7.3b and 7.3c. The spray current became highly stable when the steady Taylor cones were formed at both emitters. The oscilloscope graphs corresponding to the stage of pulsation, quasi-stable, and cone-jet are shown in Figure 7.6. The I-V measurement for the offline bipolar electrospray shown in Figure 7.5c exhibited a different trend. Unlike the flow rate-regulated sprayer, there was no flow restriction thus the flow rate was free to adjust itself in response to the change in voltage. This contributed to the absence of a plateau in spray current, i.e. the spray current continued to rise with the increment of voltage even in the steady cone-jet mode. This trend was similar to our previous result for a high-pressure offline nanoESI with an inserted platinum electrode[33]. Another measurement using a different solvent (0.1% formic acid in 75% v/v ethanol) is shown in Figure 7.7.

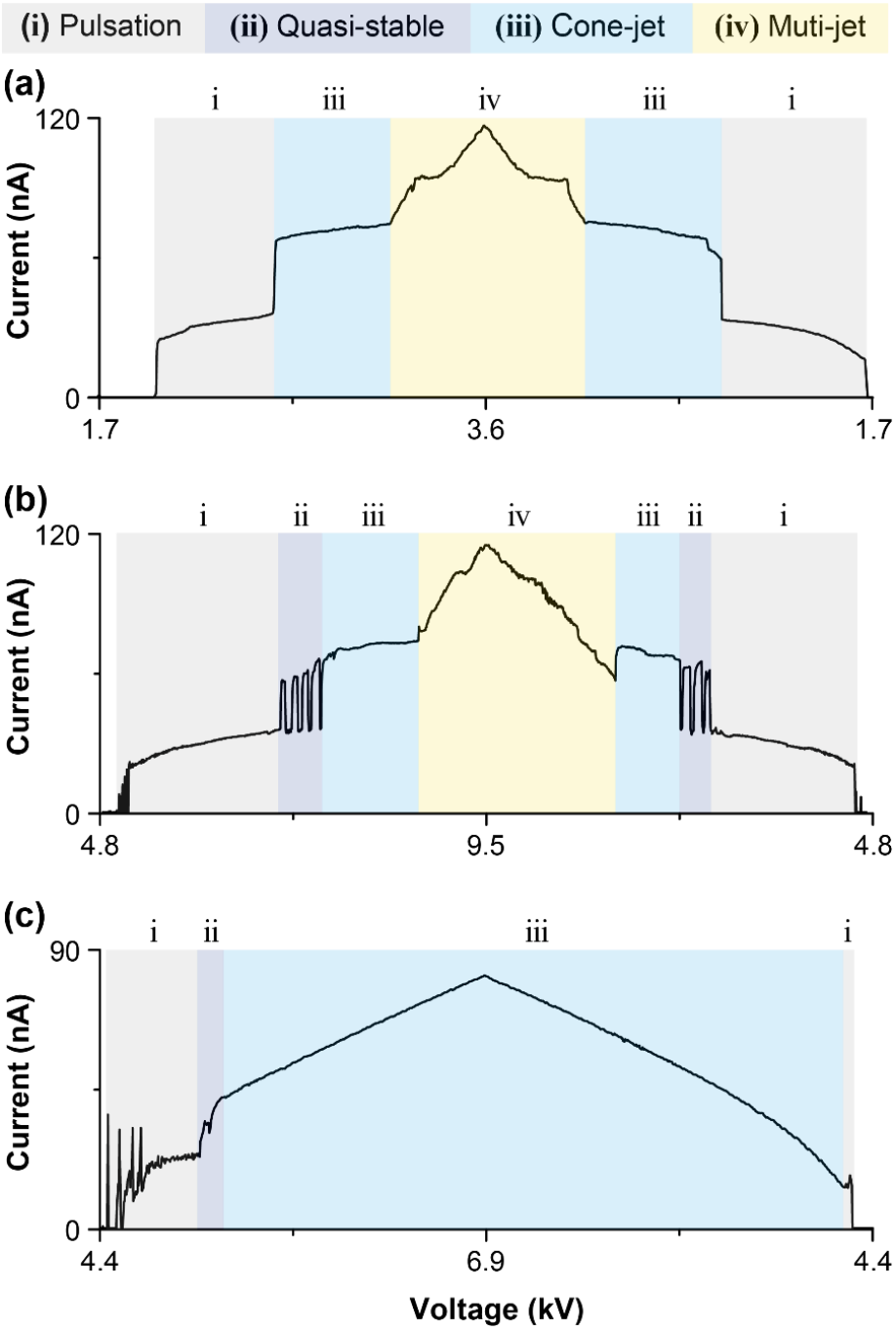

Figure 7.5. Measurement of spray currents versus voltage for 0.1% acetic acid in 75 v/v ethanol using different sprayers. (a) Standard electrospray with stainless steel capillary. (b) Online bipolar electrospray with PEEK capillary. (c) Offline bipolar electrospray PEEK capillary. For (a) & (b), the flow rate at each emitter is 5 μL/min. i) Dripping & pulsation, ii) quasi-stable, iii) steady cone-jet, iv) multi-jet.

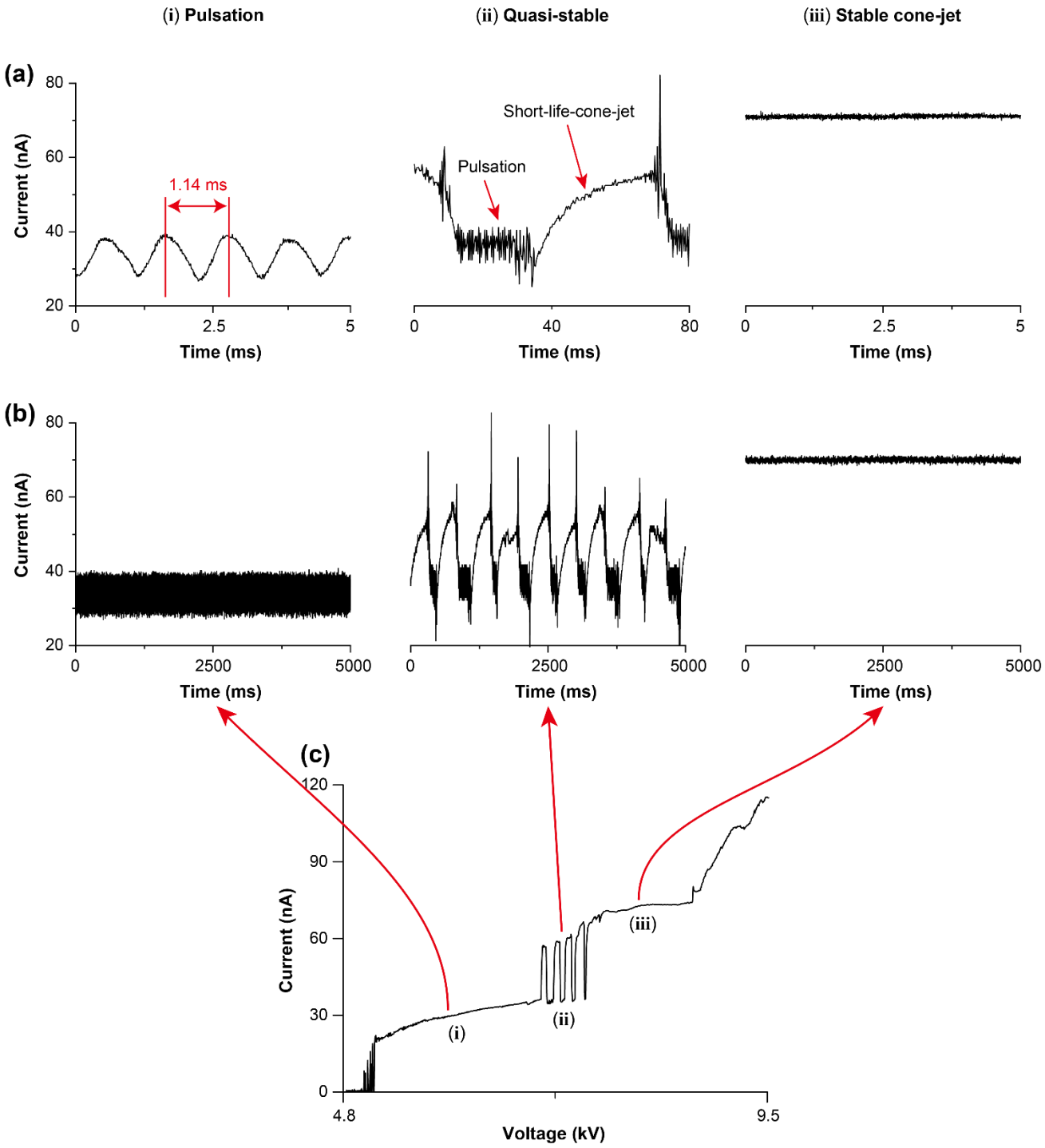

Figure 7.6. (a) & (b): Measurement of spray current of the bipolar electrospray in (i) pulsation, (ii) quasi-stable, and (iii) stable cone jet modes using an oscilloscope. (a) is the magnified waveform of (b). (c) Measurement using a multimeter (averaging time: 1/60 s). Solution: 0.1 % acetic acid in 75 % ethanol.

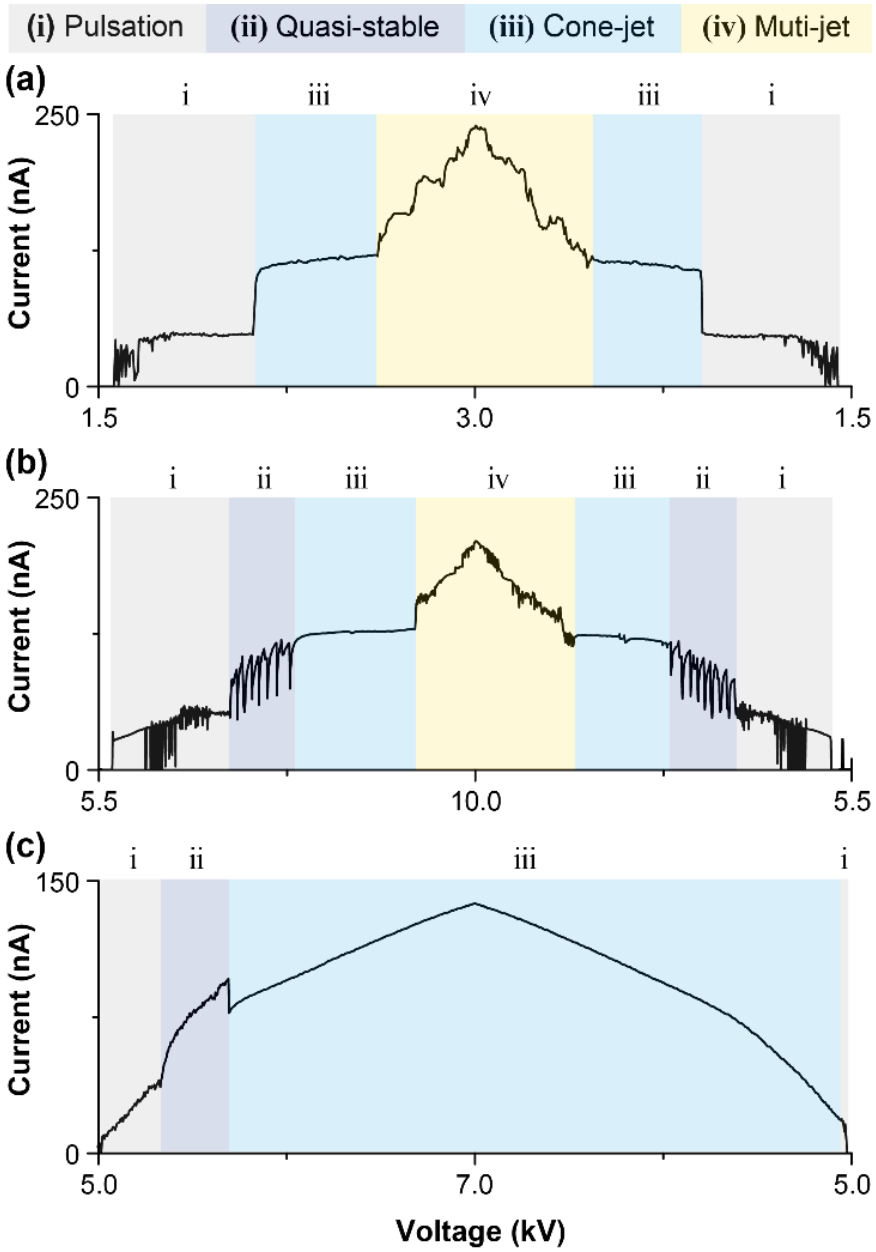

Figure 7.7: Measurement of spray currents versus voltage for 0.1% formic acid in 75% v/v ethanol using (a) standard electrospray with stainless steel capillary, (b) online bipolar electrospray with PEEK capillary (electrodeless), and (c) offline bipolar electrospray. For (a) and (b), the flow rate at each emitter is 2 μL/min. i) Dripping & pulsation, ii) quasi-stable, iii) steady cone-jet, iv) multi-jet.

Spray current-flowrate relationship

The spray current-flow rate (I-Q) relationship was evaluated to verify if the bipolar electrospray also followed the same scaling law (Eq 1). Figure 7.8 shows the plots of spray current and the solution flow rate for the standard unipolar electrospray using stainless steel capillary (red square), online bipolar electrospray (blue circle), and offline bipolar spray (green triangle). For the offline bipolar spray, the measurement of the flow rate was performed *in situ* by placing the sprayer on the electronic balance to sense the change in weight during the spraying process (Figure 7.9). Flow rate Q denotes the flow rate for each emitter, which is assumed to be half of the regulated or measured total flow rate. Three ethanoic solution samples of different surface tension and conductivities were used: i) 75 % v/v ethanol with 0.1 % acetic acid (Figure 7.8a), ii) 50 % v/v ethanol with 0.1 % v/v acetic acid (Figure 7.8b), and iii) 75 % v/v ethanol with 0.1 % formic acid (Figure 7.8c). Surface tension and relative permittivity were taken from the literature[172,173]. The plots of I versus $\sqrt{\gamma KQ/\epsilon_r}$ in the inset of each subplot show a good linearity between them. The gradient m of the solid line in the insets represent the coefficient $f(\epsilon_r)$ which is in the range of 12~13 in this experiment, and c is the *y*-intercept. The dashed lines were plotted using the values m and c. In sum, the electrical and hydrodynamic characteristics of the electrodeless bipolar electrospray follow that of the standard unipolar electrospray and were not affected by the absence of electrochemical processes in the emitter.

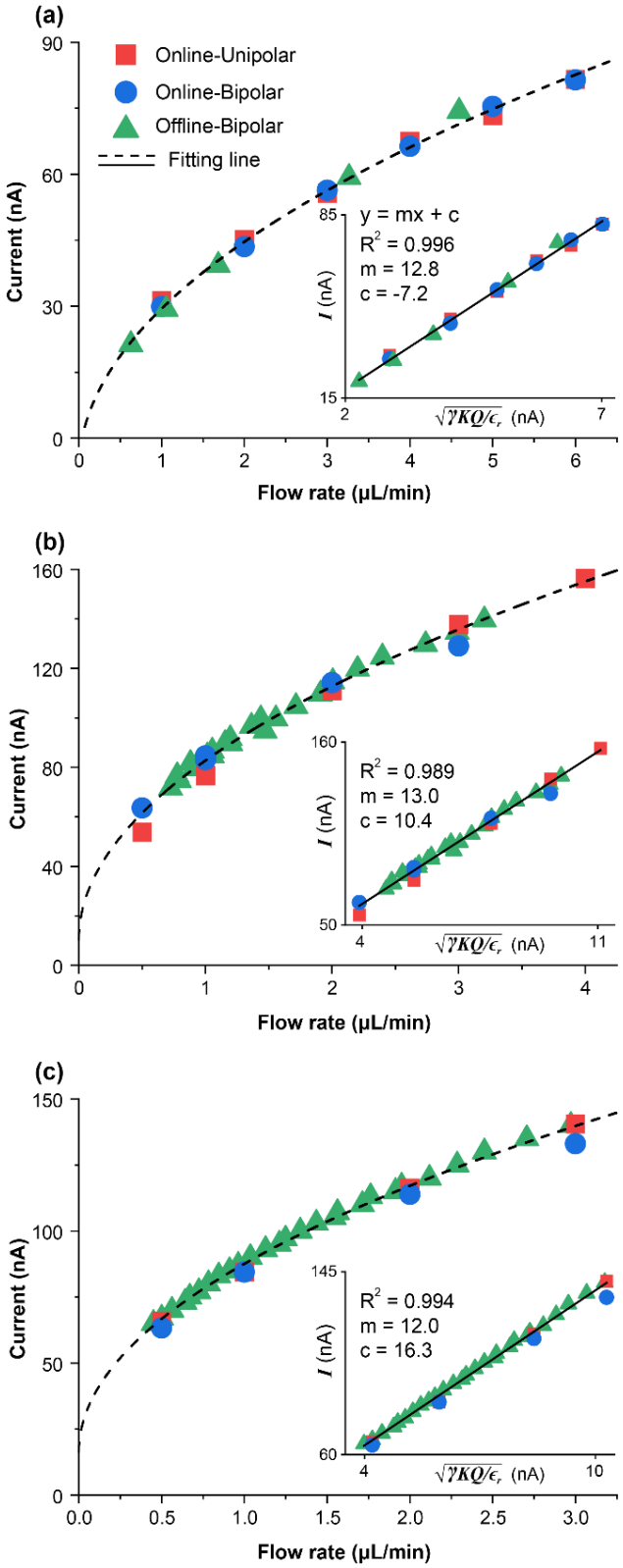

Figure 7.8. The relationship between spray current and flow rate for different solutions. (a) 75 % v/v ethanol with 0.1 % acetic acid (K = 0.78 mS/m, γ = 24.4 mN/m, ϵ_r = 38.74). (b) 50 % v/v ethanol with 0.1 % acetic acid (K = 3.32 mS/m, γ = 29.6 mN/m, ϵ_r = 53.4. (c) 75 % v/v ethanol with 0.1 % formic acid (K = 3.36 mS/m, γ = 24.4 mN/m, ϵ_r = 38.7). Flow rate Q is the flow rate at each emitter.

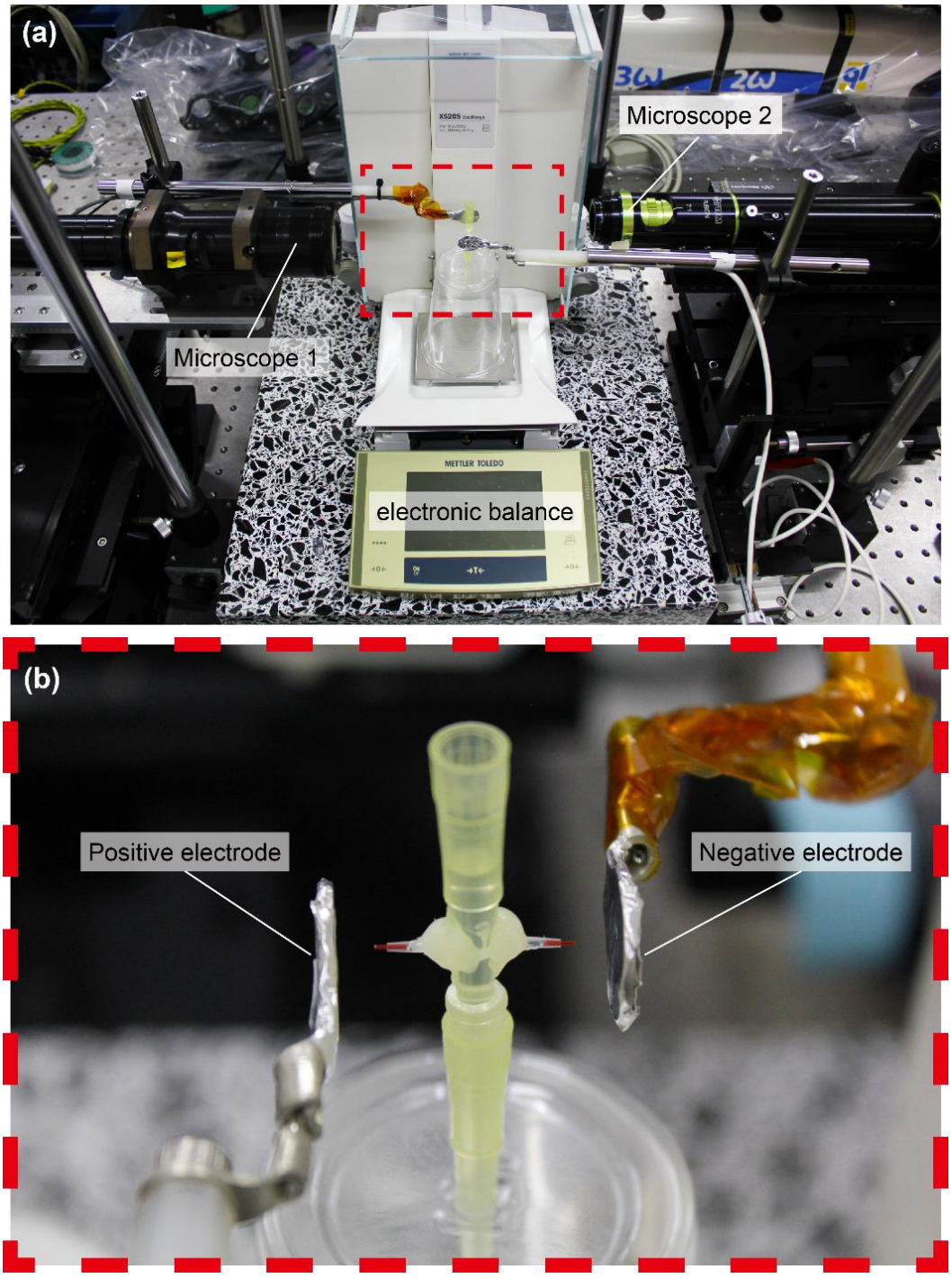

Figure 7.9. Measurement of flow rate for the offline bipolar electrospray using an electronic balance linked to a PC. Two microscopes were used to monitor the stability of the Taylor cone at both emitters. The recording of the weight of the liquid in the sprayer starts only when both positive and negative sprays are in the steady cone jet mode. The flow rate is calculated from the reduction rate of the liquid weight.

Protein standards

The performance of the bipolar electrospray ionization mass spectrometry was evaluated using three configurations: online configuration with flow rate controlled by a syringe pump which is the default configuration that could be readily constructed using commercial LC consumables and easily connected to the AP mass spectrometer (Figure 7.2). The comparison with the standard electrospray emitter with a stainless-steel capillary is shown in Figure 7.10. The inner diameter of the emitter capillary for both sprayers was the same (0.1 mm) and both were operated in the cone-jet mode. In the bipolar ESI, the continuous generation of excess charges onto the Taylor cone surface was purely due to the field-induced separation of anion and cation in the solution, while for the standard ESI, the emitted charge was replenished by electrochemical reactions. The ion intensities obtained from both ESI sources were of the same order of magnitude, indicating their ionization efficiency was approximately the same. The bipolar ESI mass spectra of various protein standards: cytochrome c, ubiquitin, and myoglobin are shown in Figures 7.11 and 7.12.

Figure 7.13 shows the measurement of cytochrome c in a pure aqueous solution of 100 mM ammonium formate using high-pressure offline bipolar ESI. The high-pressure operation was used for the prevention of corona discharge when dealing with a solution of high surface tension[23]. The hyphenation of the high-pressure source to the AP-MS followed the indirect coupling method described in our previous report[33]. In brief, the transmission of ions was via a transport tube of 0.5 mm i.d. The electrical conductivity here was ~ 1 S/m, and the electrospray current was ~200 nA. Under this condition, the flow rate at each emitter was estimated to be in the order of ~10 nL/min following Eq 1. In sum, the bipolar ESI-MS was found to exhibit typical electrospray ionization performance when operated in the steady cone-jet mode.

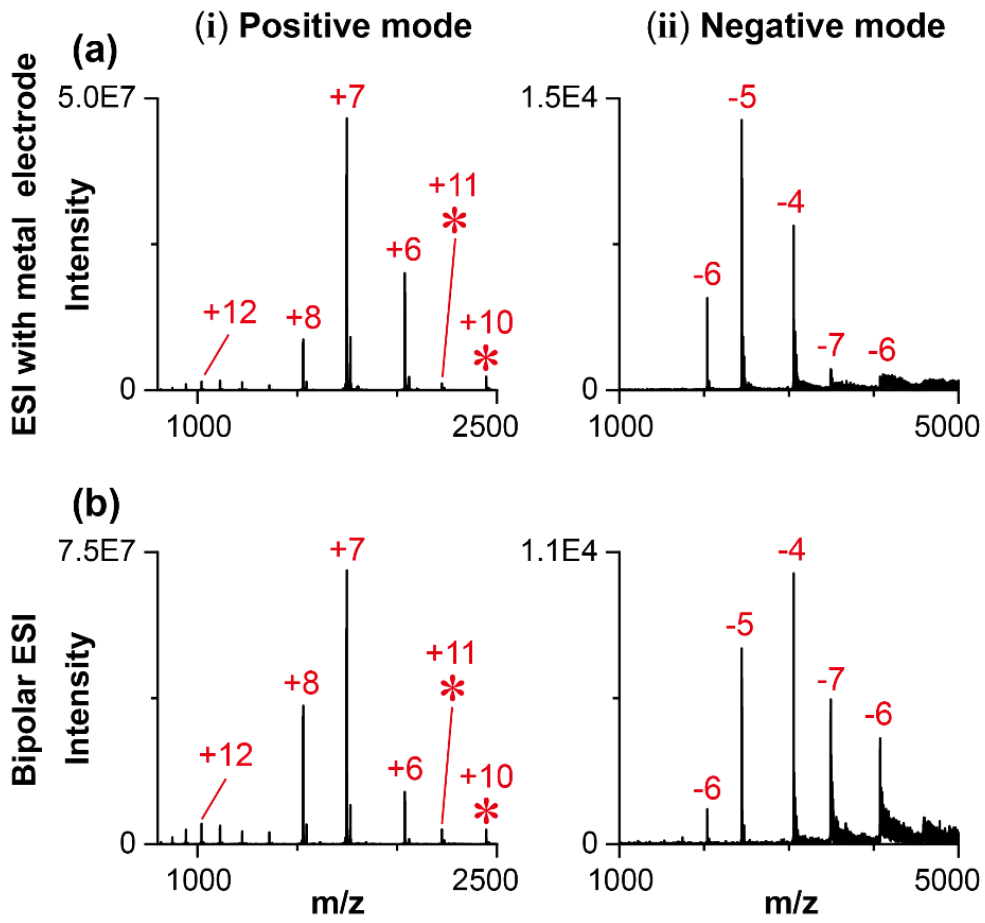

Figure 7.10. Mass spectra of 2 μM cytochrome *c* in 2.5 mM ammonium acetate in 1/1 v/v water/acetonitrile solution acquired using (a) ESI with stainless steel emitter capillary, and (b) bipolar ESI using electrodeless emitter. Flow rate is 1 μL/min. Asterisk denotes the peak for the dimer.

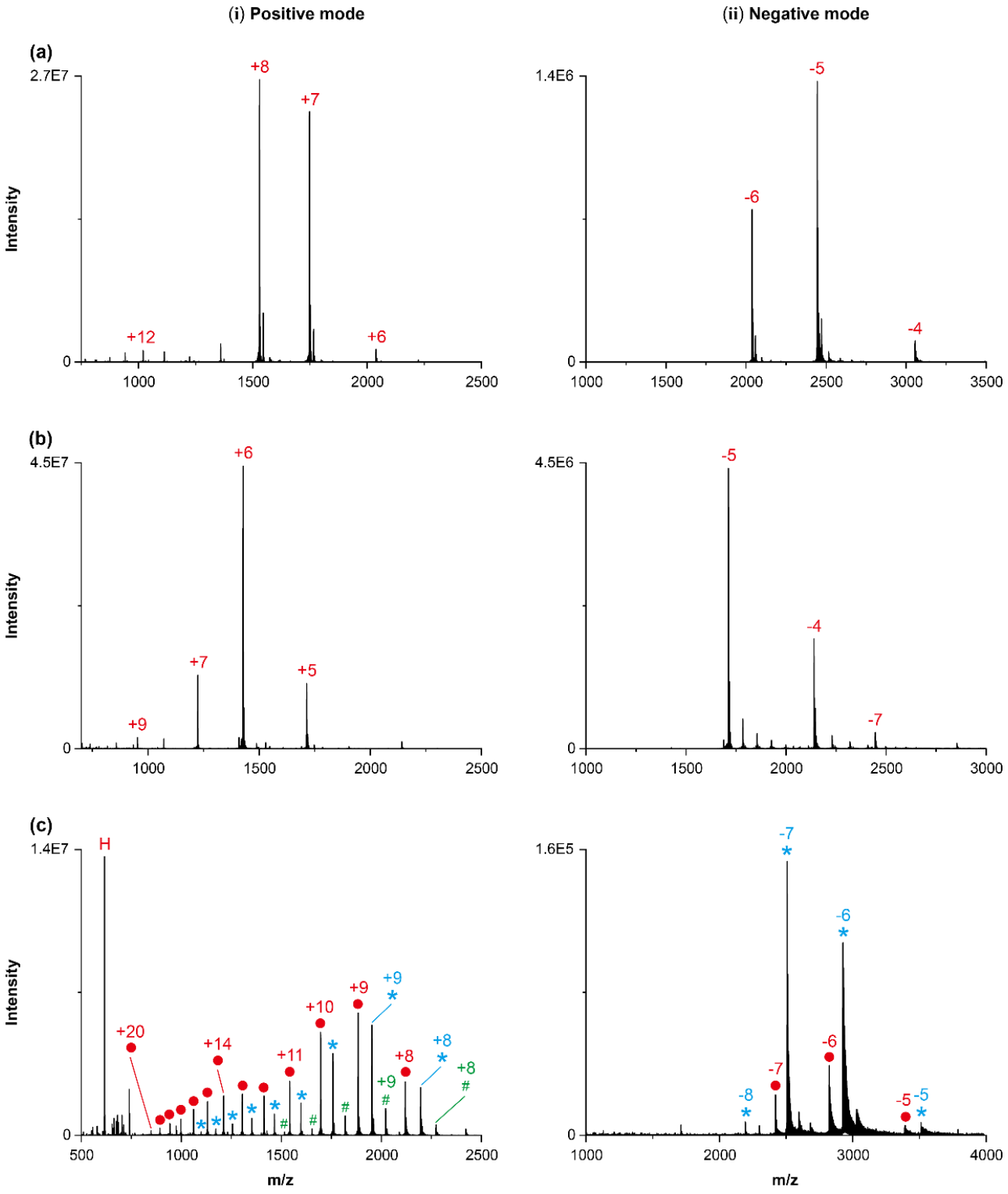

Figure 7.11. Positive and negative mass spectra acquired using online bipolar ESI for (a) cytochrome *c*, (b) ubiquitin, and (c) myoglobin. Solvent: 2.5 mM ammonium acetate in 1/1 v/v water/ethanol solution. Column (i) is for the positive and column (ii) is for the negative ion modes. Sample concentration: 2×10^{-6} M. For Myoblobin, H denotes heme, blue asterisk * denotes holo, red circle denotes apo myoglobin and # sign denotes peak due to the adduction of heme to the holomyoglobin. Flow rate for each emitter is 1 μL/min.

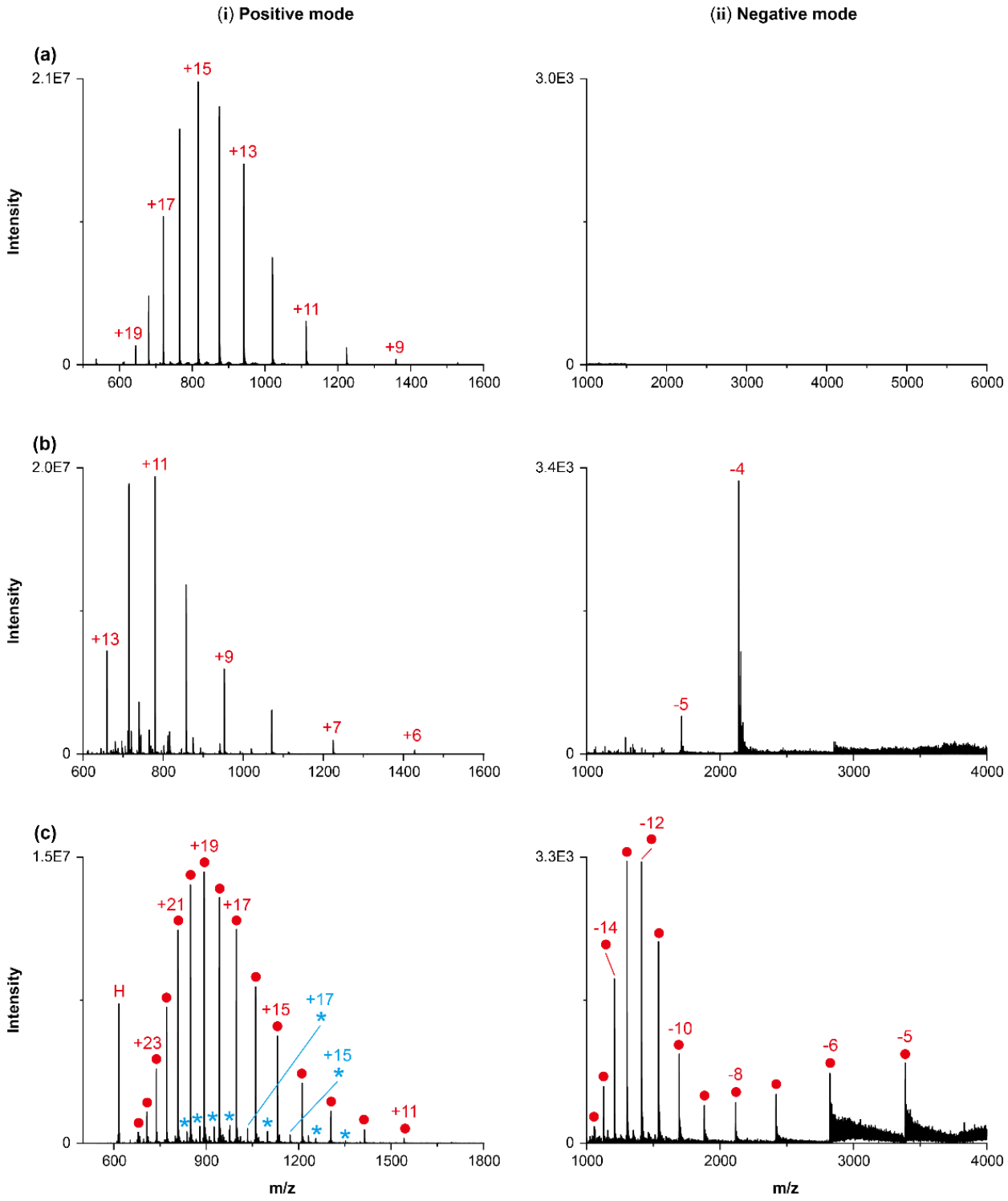

Figure 7.12. Positive and negative mass spectra acquired using online bipolar ESI for proteins in 0.1 % v/v formic acid in 1/1 v/v water/ethanol solution. (a) cytochrome *c*, (b) ubiquitin, and (c) myoglobin. Column (i) is for positive and column (ii) is for negative ion mass spectra.

Sample concentration: 2×10^{-6} M.

For Myoblobin, H denotes heme, blue asterisk * denotes holo, and red circle denotes apo myoglobin.

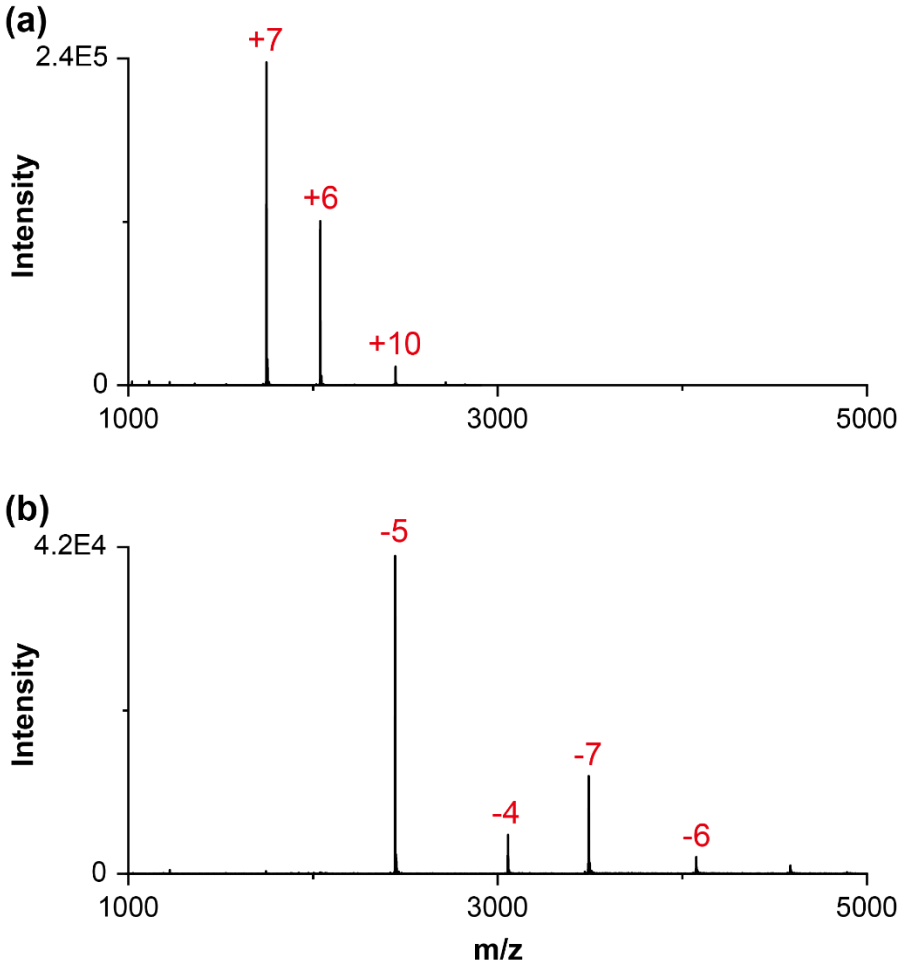

Figure 7.13. Mass spectra of cytochrome *c* (5 μM) in 100 mM ammonium formate aqueous solution (pH ~6.5). a) Positive ion mode. b) negative ion mode. The ion source is offline bipolar ESI operated under a high-pressure condition.

Melittin

Melittin, a peptide containing easily oxidizable amide acids such as tryptophan and leucine was previously reported to be sensitive to the oxidation caused by the electrochemical reaction taking place in the standard ESI[165]. Here, we adopted their approach of using melittin as the model compound. The sample was first tested using the standard ESI under the cone-jet mode with a stainless steel capillary (at 1 μL/min) 0.1 % formic acid in 50% ethanol solution. The ion peaks associated with oxidation ($[M+nH+mO]^{n+}$), although present, was not significantly stronger when compared to the bipolar ESI. The oxidation peak was observed only when the HV was drastically increased to generate electrical discharge with a current greater than 1μA. Although there was no obvious glowing at the tip of the metal capillary, the oxidation was believed to be due to the gaseous reaction with reactive products generated from the dark current discharge. The oxidation peaks dropped nearly instantly when the spray current was reduced to the normal value (Figure 7.14).

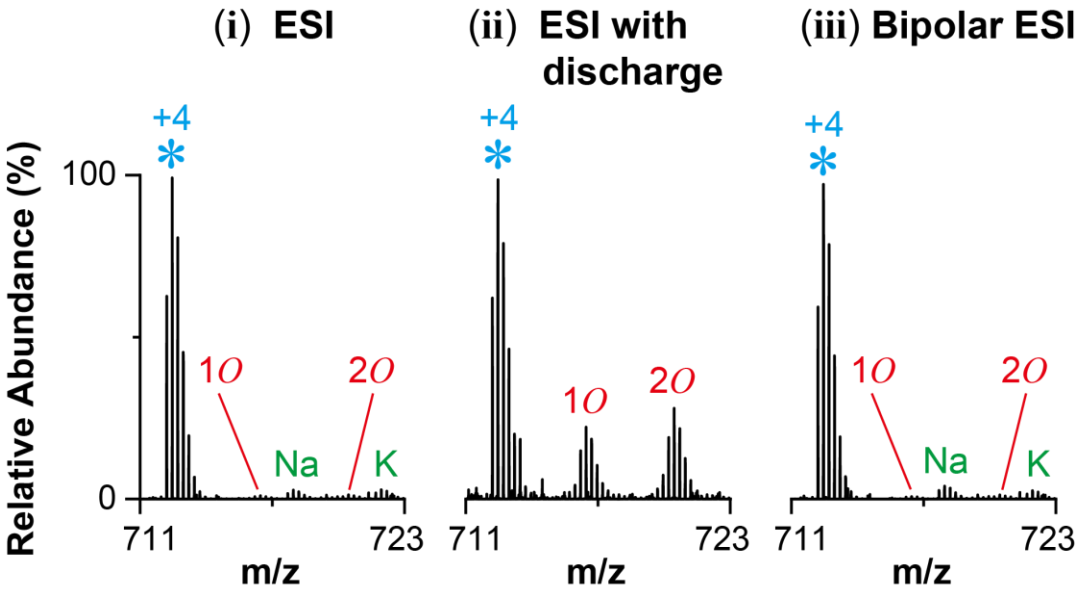

Figure 7.14. Mass spectra of melittin (2 μM) in 0.1 % formic acid in 50% ethanol. (i) Standard ESI with stainless steel capillary. (ii) Standard ESI with a much higher voltage to induce an electrical discharge with a current in the range of 1~4 μA. (iii) Bipolar ESI without electrode. Flow rate ~0.5~1 μL/min.

As the electrochemical reaction should be more pronounced for a more conductive solution under a lower flow rate, another evaluation was performed involving the ESI of melittin in 100 mM ammonium acetate aqueous solution under an nL/min flow regime. The measurement was performed under a high-pressure condition to avoid the effect of corona or dark current discharge. Figure 7.15a shows the result taken using an offline HP-ESI source with platinum wire as the charging electrode. A micropipette tip was used as the emitter and sample reservoir. The distance between the distal end of the inserted Pt wire to the end of the pipet tip was ~4 mm. The flow rate was in the order of 80 nL/min. The intensities of the oxidation species showed an increasing trend with the time reaching a plateau after ~20 min of measurement. In terms of the percentage of the oxidized species, it increased to 21 % from the initial 6 %. This increasing trend was due to the transport of the oxidation product from the electrode to the Taylor cone. The transport could be via a combination of the linear flow stream, diffusion, and the stirring effect caused by the circulating flow stream generated inside the Taylor cone. The measurement of the same sample taken using high-pressure bipolar ESI is shown in Figure 7.15b. The peak of the oxidized species was not completely absent but their low intensities remained constant with time. The percentages of the oxidized species were 6 % at the beginning and after 20 min of measurement. As the electrode was not present in the bipolar sprayer, the contribution from the electrochemistry at the liquid/electrode could be safely eliminated, therefore, the observed oxidized species in Figure 7.15b were originally present in the solution or were formed by other causes during the transfer of ion to the gas phase and the subsequent transmission to the MS vacuum.

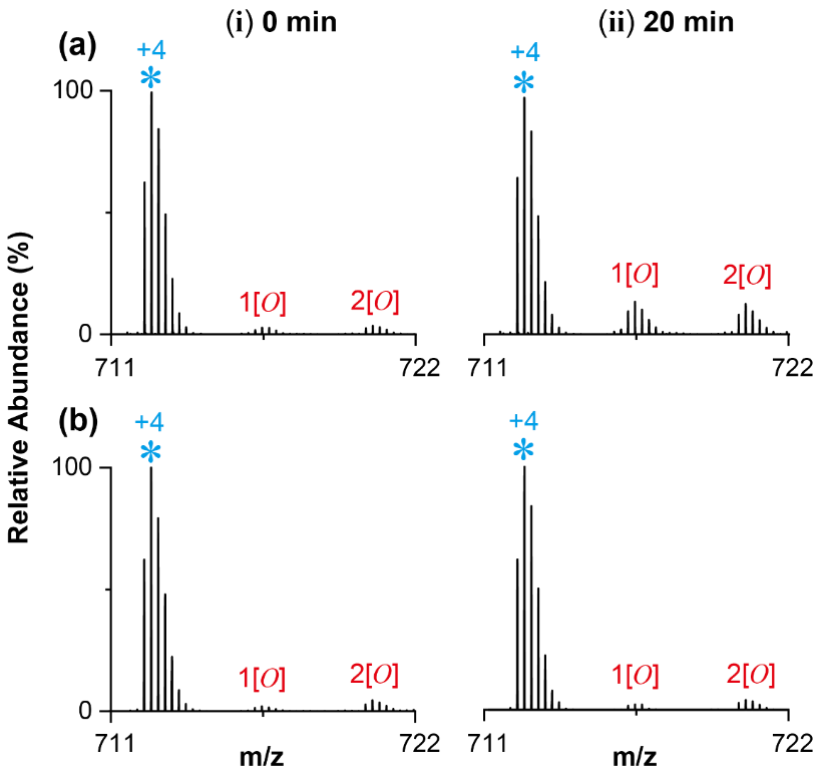

Figure 7.15. Mass spectra of melittin (10 μM) in 100 mM ammonium acetate aqueous solution using different ion sources. (a) High-pressure offline ESI using a platinum electrode. (b) High-pressure offline bipolar-ESI. The asterisk * denotes the unoxidized ion. *n*[*O*] denotes the oxidized species. Flow rate is ~80 nL/min.

Ferrocene

Figure 7.16 shows the comparison of standard ESI and bipolar ESI for the detection of molecular cations from the neutral ferrocene (Cp_2Fe). The tested solutions were i) pure acetonitrile, ii) 0.1 % trifluoracetic acid (TFA), and iii) 1 % formic acid (FA) in acetonitrile. Protonated species were not observed even with the use of acidic solutions. Only Cp_2Fe^+ was detected without fragmentation. Overall, the formic acid ACN solution yields the highest intensity for both ESI and bipolar ESI. The peak heights for Cp_2Fe^+ obtained using the standard ESI with metal capillary (Figure 7.16a) were approximately 30×, 12×, and 6× higher than the bipolar ESI with insulating capillaries (Figure 7.16b) for pure ACN, TFA, and FA solutions, respectively. Previously, the generation of Cp_2Fe^+ from ESI was attributed to the electrochemical oxidation (electron removal) at the interface of liquid-electrode. The result here verified that the electrolytic nature of the standard ESI indeed had a beneficial effect on the detection of $Cp2Fe^+$ because the ion signal using the metal capillary was always stronger than the one obtained using insulating emitters. However, the result also shows that electrochemistry was not the only oxidation route. Since the electrochemistry at the metal/liquid interfaces could not take place in the insulating sprayer, the considerable abundance of Cp_2Fe^+ generated by bipolar ESI must be due to other causes. Possible sources of contribution are as follows. i) Native oxidized ferrocenes in the sample solution. Although this possibility could not be completely ruled out, the measured sample was prepared from the freshly prepared stock solution (yellowish) and we had not observed any color change. The color of the ferrocene solution was known to turn blue-green upon oxidation. ii) Redox reaction in the electrosprayed droplet solution. The oxidation of ferrocene was known to take place in acidic solutions with the presence of oxygen[174]. A higher ion signal of Cp_2Fe^+ acquired from solutions containing TFA and FA (columns ii & iii in Figure 7.16) appeared to support this possibility. The redox reaction might also be enhanced by the high electrical field on the charged droplet[175]. iii) Gas phase oxidation by the electrospray plume. A related finding by Yu. S. Nekrasov *et al*. detected Cp_2Fe^+ by interacting the ferrocene vapor with the charged acetonitrile droplets from ESI and they proposed that the gas phase hydronium ions or a protonated ferrocene acted as an oxidant for the detected ferrocene molecular ions[176].

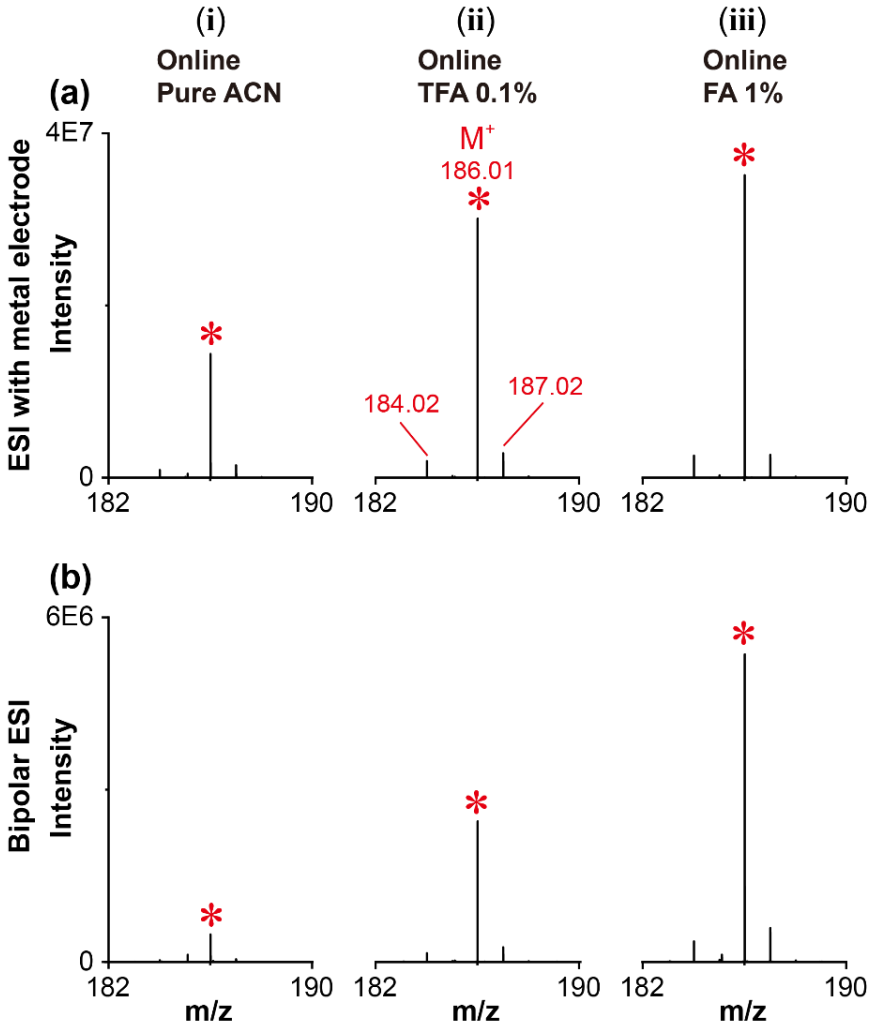

Figure 7.16. Mass spectra of 10 μM ferrocene in different solvents acquired using different ESI sources. (a) ESI with stainless steel capillary. (b) Online bipolar ESI. The solvents are pure acetonitrile (ACN) for column i, 0.1 % trifluoroacetic acid in ACN for column ii, and 1% formic acid in ACN for column iii. Flow rate for each emitter is 5 μL/min. Asterisk denotes the peak for Cp_2Fe^+.

Conclusions

The characteristics of the electrodeless bipolar electrospray are summarized as follows. i) Similar to the standard electrospray, bipolar electrospray also exhibited dripping, kHz pulsation, steady cone-jet, and multi-jet modes with increasing voltage. ii) A higher voltage was needed to complete the full transition from pulsation to cone-jet mode at both emitters. iii) Except for a wider quasi-stable stage, the I-V and I-Q relationships for bipolar ES are the same as the standard ES. iv) Offline operation had a different I-V from the online operation but they followed the same scaling law for I-Q. In conclusion, despite the absence of electrochemical reactions in the sprayer, the bipolar electrospray generated solely by the electrical field-induced ion separation was found to be stable in the steady cone-jet mode, attaining the ionization efficiency equivalent to a standard ESI. The electrodeless operation on the sprayer side eliminates the interferences originating from the electrochemical reactions such as the oxidation of analyte, solvent, and electrode in conventional ESI-MS. Potential applications include the analysis of compounds that are sensitive to the oxidation/reduction reaction and the comparative study of the electrolytic effect in the standard electrospray.

Chapter 8: New variation of near AP ESI for higher ion transmission: inlet tube ESI

Summary

In Chpater 8, endeavor was made to investigate the electrospray ionization inside the narrow channel of the ion inlet tube. An insulating emitter capillary made of fused silica with 0.2 mm outer diameter was inserted into the ion inlet tubes with 0.5 & 0.6 mm inner diameter to aspirate all the charged droplets. A custom-made ion inlet tube with two side holes near its entrance is used to observe the spraying condition. Spray current is measured and monitored during the MS acquisition using isolation amplifiers. Because the emitter is cylindrically surrounded in close proximity by the metallic inner wall, it is difficult to obtain a stable and symmetric Taylor cone with its apex at the center of the emitter. Instead, a stable operation under a flow rate of 1- 4 μL/min is found to be in the form of multi-cone-jet mode with two or more Taylor cones anchoring around the rim of the emitter. The emitted charged droplet jets are dragged from hitting the wall by the fast-flowing air inside the inlet tube. Comparison with the typical cone-jet and multi-jet mode operated several millimeters outside the inlet capillary shows signal enhancements for protein standards.

Introduction

The simplest electrospray electrode configuration is the needle-to-plane geometry where the potential field can be easily approximated by assuming a Taylor cone formed at the apex of a paraboloid[177], or a hyperboloid[178]. A perfect hydrostatic and electrostatic Taylor cone has an apex angle of 98.6°[11]. In practice, the cone angle decreases with the increase of the solution flow rate[36]. The rigorous theoretical treatment for the electrospray is yet available but the spray current and precursor droplets size can be estimated with good accuracy using existing scaling laws[24]. Upon the reach of cone-jet mode, further increase of emitter voltage turns the spray into two or multi-jet mode[25], a phenomenon recorded as early as 1915 by Zeleny[179]. Multiplexing the electrospray from a single liquid supply line reduces the size of the precursor charged droplets because the main flow rate is shared by

multiple jets[180]. However, the naturally occurring multi-jet mode is not as stable as the cone-jet mode, thus, not extensively utilized in industrial and analytical applications[181]. To stabilize the positions of the multi-jet, grooves or other microstructure are made on the emitter capillary to provide anchoring points for the liquid and the field enhancement[182,183]. High-density multi-jets had also be reported from thin disk[184], and insulating nozzle[185]. Multiplexed electrospray has also been performed using a multi-emitter system, in which each sprayer is operated at the cone-jet mode. Multi-emitter sprayers have been used in electrospinning, thin film deposition[186], as well as mass spectrometry. Ion signal enhancement has been reported using an ESI source that employs microchip-based multi-nozzles[187], linear and radial arrays of fused silica capillary[188,189], and multi-nozzles made on a single fiber[190]. Operation of nanoESI arrays with sheath gas assistance under the sub-ambient pressure is also reported to improve the ion transmission[191].

In addition to the "pure electrospray" where the formation of the jet is driven solely by electrical means, there exist variations of sprayers to assist the stable spraying of liquids. The widely used ESI sprayer, pneumatic-assisted ESI sources employs a nebulizer design, in which emitter capillary is placed at the center of another coaxial gas flowing tube[192]. Stability for high flow operation is improved by separating the charging and the jet formation processes. Besides assisting the nebulization, the gas flow prevents the undesirable spreading of liquid on the outer surface of the emitter tip, thus also found use in the microflow system. The standard operating pressure of ESI is 1 atm but has been expanded to greater than the atmospheric pressure for aqueous solutions and high-temperature operation[23,53,193], and sub-ambient condition for the enhancement of ion transmission[194]. Ultra-high vacuum operation of electrospray also exists for the generation of cluster beam for SIMS[195].

Notable ion interfaces are an orifice plate with counter-flow curtain gas, simple conic skimmer, glass ion transport capillary, and heated ion inlet tube[196]. The ion inlet tube design, initially used by Chait[197], later adopted in some commercial instruments, uses a heated metallic tube of ~0.5 mm i.d. for the desolvation of ions and the prevention of solvent clustering when they enter the first vacuum stage. The viscous laminar flow is important to transmit the ions and micro charged droplets through the narrow and long tube with high transmission[198,199]. Unlike the high-vacuum ion optics system, the fluidic consideration is important for designing an atmospheric ion sampling system as the gas drag can be strong enough to move the ions/charged droplets across the electrical potential

barrier[55,171]. Hydrodynamically optimized inlet with a funnel shape has also been used to prevent the occurrence of turbulence at the ion sampling entrance[200,201]. By placing the nanoESI close enough to the sampling aperture, it is possible to aspirate all ions/charged droplets into the vacuum for "total solvent consumption"[202]. McEwen and coworkers went even further by introducing the liquid sample directly inside the heated inlet tube using a fused silica tube[203]. The application of voltage to the liquid via the metallic union was reported to improve the detection of peptides and produce ESI-like mass spectra[204]. They named the method ESI-inlet (ESII) but noted the difference with the standard ESI that there was no spray onset threshold, and the electrical field was only to provide charge separation, and droplets formation is due to the fast-flowing hot gas through the heated MS inlet tube[204]. Quantitative analysis without LC was also reported using ESII-MS/MS[205]. Direct visual probing of the spraying condition was hindered by the fact it was placed inside a closed metallic tubing.

The main purpose of this chapter is to investigate if the commonly known electrospray mode can be stably operated inside the narrow channel of the MS ion inlet tube. The tested sprayer emitter is of a typical outer diameter of 0.2 mm which is placed within the inlet tube of 0.5~0.6 mm inner diameter with only 0.15~0.2 mm insulating gap. A specially fabricated inlet tube with two side holes, previously designed for an ESI-based string sampling system[206], is used to probe the electrospray mode under such conditions.

Experimental section

ESI emitter

The schematic of the ESI emitter used in this study is shown in Figure 8.1. Fused silica capillaries with polyimide coating (0.1mm i.d. and 0.2mm o.d. from Thermo Fisher Scientific, Tokyo, Japan) cut to ~30 mm were used as the default ESI emitter capillary. Stainless steel capillary (with 0.1mm i.d. and 0.2mm o.d. from Nilaco, Tokyo, Japan) was used for comparison but it was prone to electrical discharge and current leak. Two ion inlet tubes were used. One is the original heated inlet tube with a ~0.6 mm inner diameter. Another was a custom inlet tube made from a commercial straight-cut stainless-steel tube with 0.5 mm inner diameter. Two side holes (0.5 mm dia, 2 mm from the entrance) were fabricated along the axis orthogonal to the central axis of the ion path. The flowrates

of air aspirated from the atmospheric pressure into the vacuum (measured using mass flow meter) were 1.5 L/min and 1.0 L/min, respectively for the original and custom-made inlet tubes. The linear velocities of the gas flow in between the inlet and the capillary were estimated to be approximately 120 m/s for the original and 100 m/s for the custom-made inlet tubes. As in the pneumatically-assisted ESI, the fast-flowing gas was important in stabilizing the spray and the prevention of arcing. The fused silica capillary was connected to a metallic union using a polychlorotrifluoroethylene ferrule (Kel-F, i.d. 0.2 mm, Thermo Fisher Scientific). The emitter capillary was further protected by a sleeve tube (Fluorinated ethylene propylene, with 0.3 mm i.d. and 1.6 mm o.d. from GL Science, Tokyo, Japan) to prevent the vibration caused by the electrostatic force, airflow, and the propulsion of multi-jet electrospray. The protruded length of the fused silica capillary from the sleeve tube was approximately 6 mm. The fused silica tube was aligned to be at the center and coaxially with the inlet tube of a mass spectrometer using a precision 3-axis stage. An effort was made to ensure that the position of the fused silica tube could be flexibly adjusted relative to the inlet entrance without touching its inner surface. High voltage (HV) was applied to the zero dead-volume metallic union linking the tubing from an infusion pump to the fused silica capillary (ESI emitter). The DC high voltage was tuned from 0.6-3.0 kV. A syringe pump (PHD 4400, Harvard Apparatus, MA) was used for solution infusion and the flow rate was adjusted from 1- 4 μL /min.

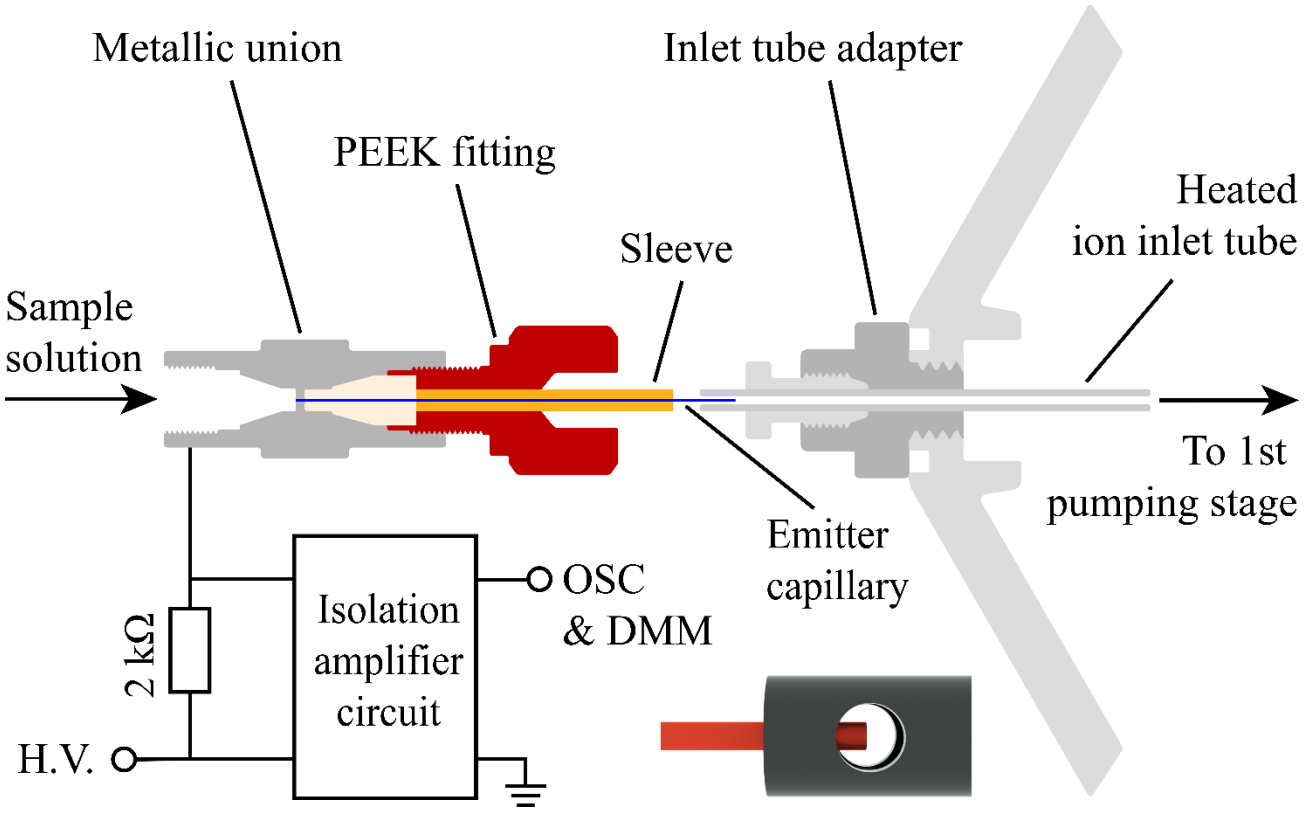

Figure 8.1. Schematic of the electrospray ion source. Inset shows the custom-made ion inlet used for the visualization of electrospray inside the ion inlet tube. OSC: oscilloscope. DMM: Digital multimeter.

Spray current & optical visualization

The spray current was measured by sensing the voltage drop across a 2 kΩ resistor connected in series with the metallic union using a custom-made isolation amplifier (ISO 121BG, Texas Instrument). The signal was coupled to the multimeter (Agilent 34461A) and oscilloscope (Agilent DSO-X 2014A). The current measurement was calibrated using a pico-ammeter (Keithley). A long-distance microscope (Infinity photo-optical) connected to a single-lens reflex camera (Canon EOS) was used to inspect the spraying condition. The routine inspection was performed using white-light LED. For laser illumination, the beam of a green laser (Nd:YAG, 2nd harmonics, 532 nm wavelength) was maneuvered to pass through the side holes. A razor blade was used to block the main beam in front of the microscope to capture the scattered light from the electrospray jet (Figure 8.2).

Mass spectrometry

The experiment was conducted using a benchtop Orbitrap mass spectrometer (Exactive, Thermo Fisher Scientific, Bremen, Germany). The original ESI source was removed and the interlock was overridden. Full-scan positive ion spectra were acquired and processed by the default software (Xcalibur). The mass spectra were constructed from the average of 6 single scan mass spectra acquired over ~6 s. The instrumental settings for the mass spectrometer were as follows: the temperature for the ion transport tube: 300 °C, the inlet capillary voltage was 140 V, the tube lens voltage was 130 V, and the skimmer voltage was 20 V. The maximum ion injection time was 50 ms. The pressure in the fore vacuum was 1.14 mbar.

Sample preparation

The LC grade methanol was purchased from Kanto Chemical. Bovine heart cytochrome c was purchased from Wako Pure Chemical Industries, Ltd. . Pure water was prepared using Simplicity UV (Millipore, Bedford, MA). All the chemicals were used without further purification. The Bovine heart cytochrome c was directly dissolved into a storage solution of 2.5×10^{-3} M by pure water and then diluted to 2.5×10^{-7} M, and 5×10^{-9} M in methanol aqueous solution. Formic acid was used for the

acidified solutions.

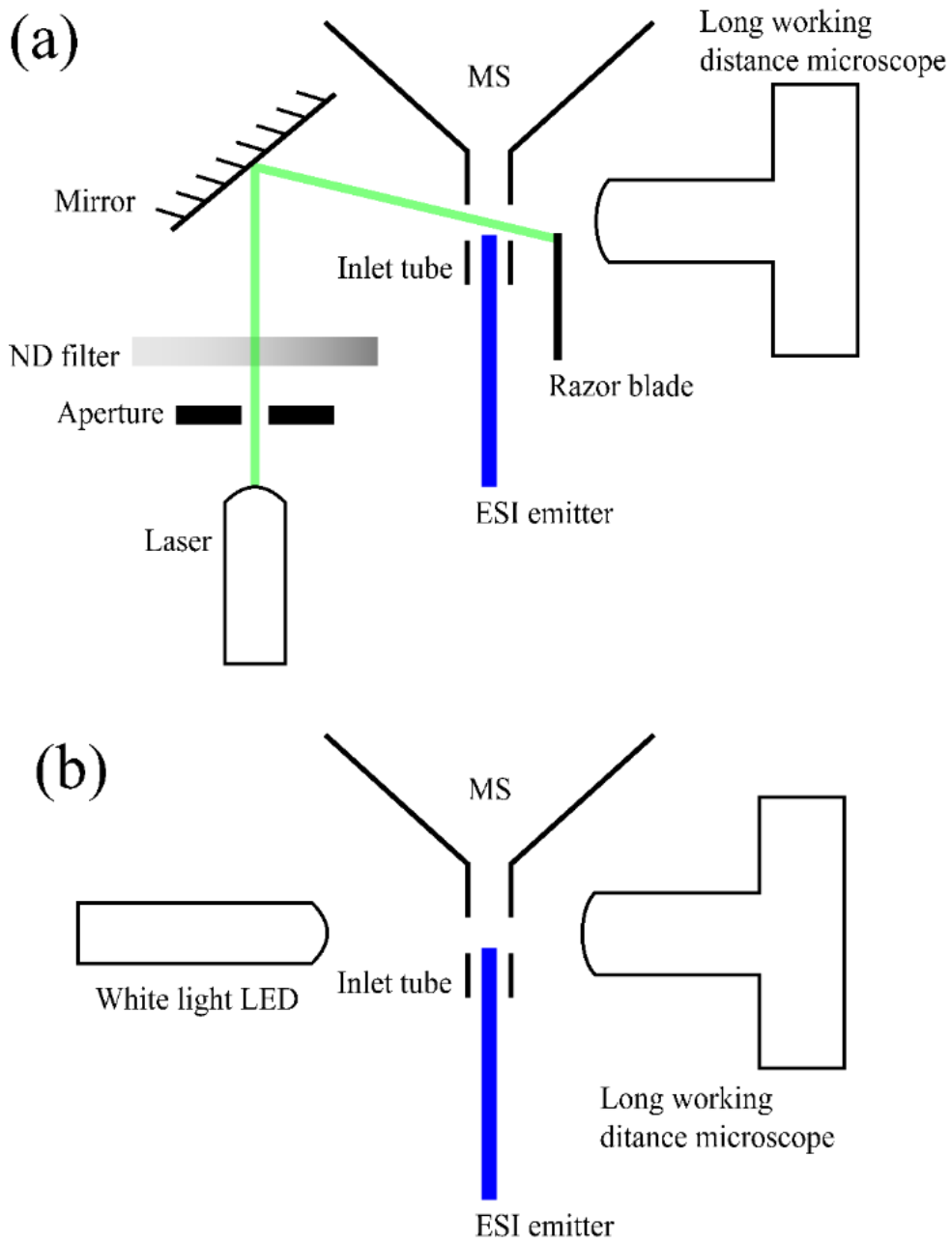

Figure 8.2. Schematics of the optical configuration for the visualization of the electrospray inside the ion inlet tube through the side holes. (a) Laser illumination. (b) White-light LED.

Results and Discussion

Under the typical needle-to-plane electrode configuration, the electrical field concentrates at the center of the tip of the emitter when the conductive liquid emerges from the emitter capillary. The net force acting on the emitter is at a direction parallel to the central axis of the emitter capillary. In the present experiment, an emitter capillary (fused silica) of 0.2 mm o.d. was inside the ion inlet tube with a gap of approximately 0.15 mm. When filled with conductive liquid applied at high potential, the electrical field was strongest at the rim of the opening of the capillary. Owing to the electrostatic force and the recoil from the ejected charged droplets, the force acting at the rim of the capillary had components that were perpendicular to the capillary axis. The use of a ~3 cm emitter capillary resulted in a vigorous vibration even if the capillary was precisely aligned to the center of the inlet tube. The vibration caused ion instability and short-circuit of the HV supply when the emitter tip touched the metallic inner wall. The capillary vibration also took place outside the inlet tube when the multi-jet mode was initiated. We found that the emitter capillary vibration could be effectively prevented or damped to a negligible level by adding a sleeve tube to the emitter capillary and keeping the unsleeved portion to a length of less than 10 mm.

Similar to ESI-inlet, the use of insulating emitter capillary such as fused silica tube was essential for the proper operation of ESI inside or at a distance less than 1 mm from the ion inlet. The reason was twofold. First, the liquid line needed to be electrically insulated from the metal surface to prevent the “short circuit”. Second, the insulating emitter prevented the arcing from the emitter itself, thus allowing the application of higher voltage to the liquid. A switch to a standard stainless-steel emitter caused the electrical discharge when the distance between the electrodes was less than 1 mm even with careful tuning of HV. A photo showing the filamentary discharge from the metallic emitter is shown in Figure 8.3. Nevertheless, a much higher HV could still cause the electrical discharge from the liquid surface particularly when dealing with high surface tension samples such as pure water. Thus, similar to the normal electrospray, the use of organic solvent was necessary for this work to initiate a stable spray.

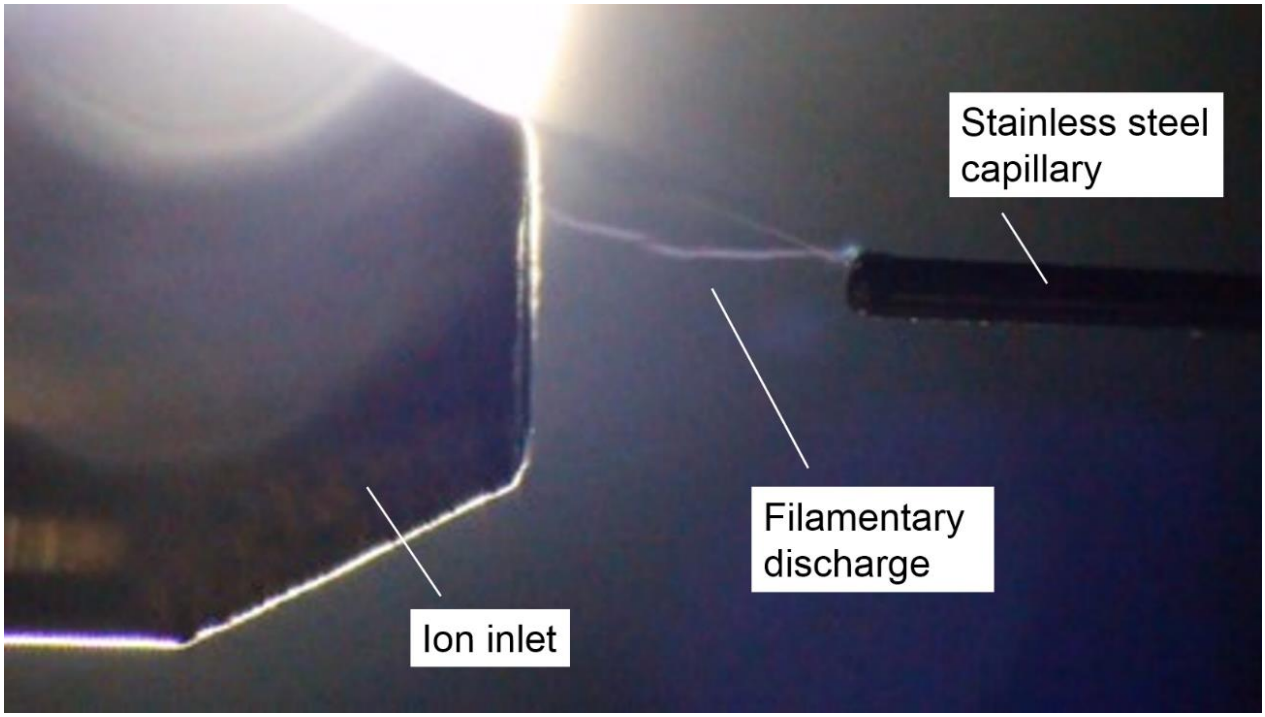

Figure 8.3. The occurring of filamentary discharge when the ESI capillary made of stainless steel is brought close to the ion inlet. The H.V. applied to the stainless-steel capillary is 1.5 kV. The distance between the capillary and the ion inlet is approximately 0.8 mm.

A custom-made inlet tube with two side holes of 0.5 mm was used to inspect the electrospray inside the inlet tube. The pressure in the region under inspection was slightly lower than the atmospheric pressure. The liquid was aspirated even without the application of voltage. Unlike the normal electrospray, we found that it was difficult to generate a symmetric cone-jet mode with its apex located at the center of the emitter. At the lowest HV for observing ion signal, the electrospray was in the pulsation mode with kHz oscillation in spray current. A stable mode under a flow rate of 1~4 μL/min was in the form of a multi-jet with two or more Taylor cones anchoring around the rim of the emitter capillary. Four Taylor cones can be seen in Figure 8.4a. As the emitter capillary was inserted further into the lower pressure region, the direction of the electrospray jets was dragged towards a direction parallel to the central axis of the inlet tube (Figure 8.4b, three Taylor cones), an effect due to Stoke's drag force induced by the fast-moving air. The observation of the emitted jet inside the inlet tube using a laser (532 nm) illumination for the spraying of 25 % methanol without acid is shown in Figure 8.4c. The Taylor cones in Figure 8.4c are too small to be identified but there are at least 5 emitting jets. The introduction of side holes for visualization inevitably affects the pattern of the airflow and the radial symmetricity of the electrical field. The absence of jets emanating towards the camera in Figure 8.4c may be due to the weaker electrical field in this direction. The pressure in the region under inspection should be lower and the air velocity should be higher for the actual condition without the side holes. The airflow from the side holes can be stopped using transparent components but it is not available in the present study. For comparison, we have fabricated another ion inlet tube with smaller side holes (0.3 mm in diameter). Similar observations were obtained but the direction of the jets appeared to be relatively parallel to the central axis compared to the one with 0.5 mm side holes (Figure 8.5).

Another microscopic observation was made using the original ion inlet tube. The flow rate of gas aspirated into the vacuum using this inlet tube was approximately 1.5 L/min. The electrospray was first operated at the multi-jet mode (6 jets) at a distance of 2 mm from the inlet and jets and the plume could be seen to be dragged towards the inlet (Figure 8.4d). As the emitter got closer to the inlet, the number of the jets increased to 8 due to the higher electrical field, and their direction became more parallel to the inlet axis (Figure 8.4e, 8.4f). The linear air velocity inside the tube was estimated to be greater than 100 m/s and the drag force was larger than that outside the inlet tube. Although the actual

spraying condition inside the inlet tube could not be visually probed directly, it should resemble those of Figures 8.4b and 8.4f, but with more parallel jets because the drag force was larger due to the higher linear velocity of air.

In the present work, the highest number of the observable jet is 4~5 jets for the acidic solution (conductivity = 9 mS/m) and 8~9 jets for the non-acidic solution (conductivity = 0.3 mS/m). Surface tension, electrical conductivity, permittivity, viscosity, solution flowrate, and space charge effect are known to influence the condition electrospray. A rigorous theoretical model for predicting the maximum number of jets for the multi-jet mode is not well established, but it should be related to the minimum flow rate that can be sustained by each jet. The number of jets in multi-jet mode generally increases with the applied voltage, but in practice, the maximum voltage is limited by the occurrence of discharge. The solution with high electrical conductivity is known to sustain high current discharge, whereas the less conductive solution is a current limiting resistor. In this work, the highest applicable voltage which was limited by the discharge was usually found to be lower than the less conductive solution, which may explain the observed smaller number of the jet in Figures 8.4a and 8.4b.

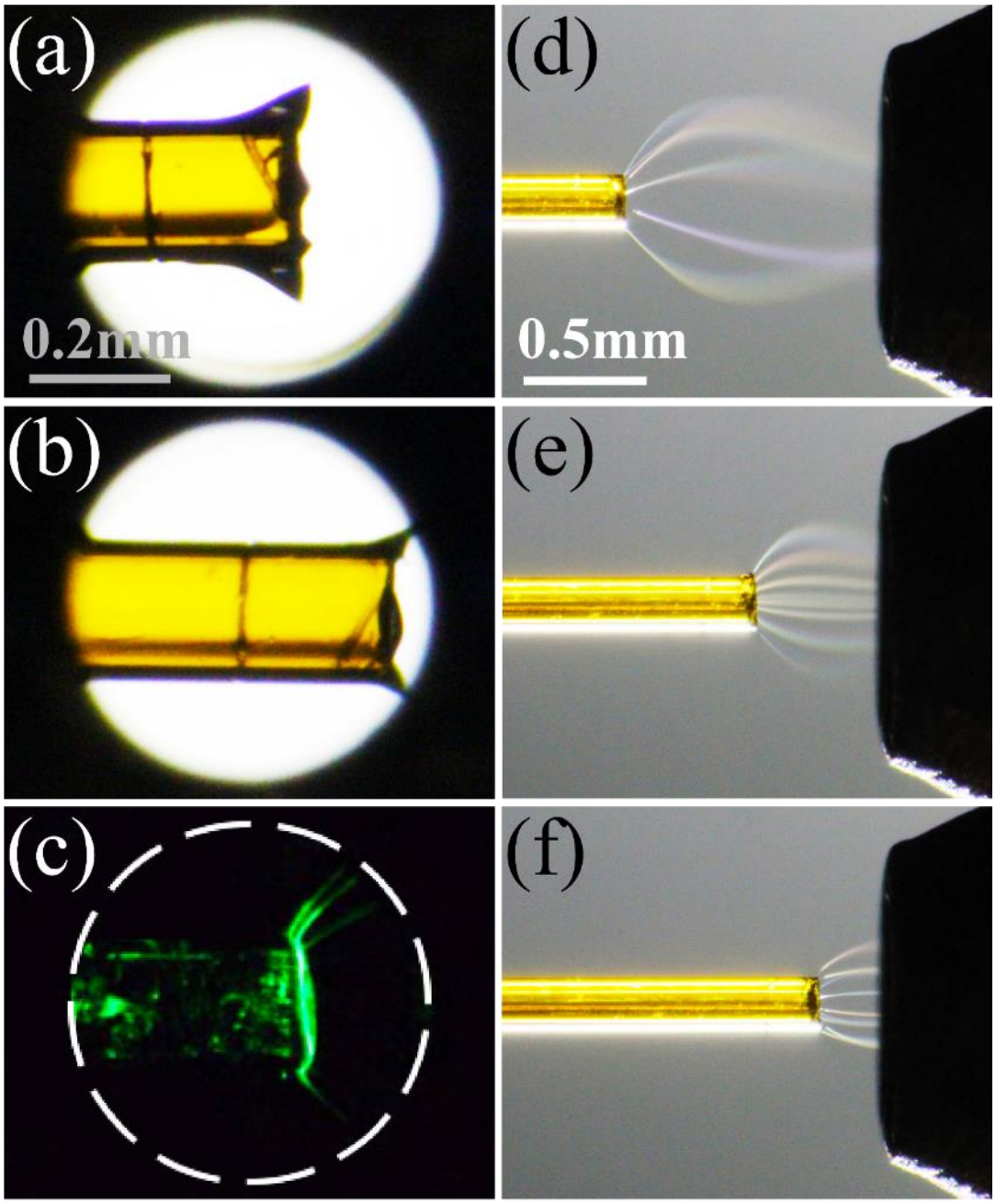

Figure 8.4. Microscopic inspection of Electrospray. (a) & (b) Images taken using the custom-made inlet tube with side holes with the emitter capillary at different positions. Spraying solution: 50 % v/v Ethanol in water with formic acid. (c) Image taken using laser illumination. Spraying solution: 25 % Methanol in water. The dashed line indicates the side hole. (d)-(f) Images taken using the original inlet tube with different distances between ESI Emitter and inlet entrance. (d) 1.00 mm, (e) 0.50 mm, (f) 0.25 mm.

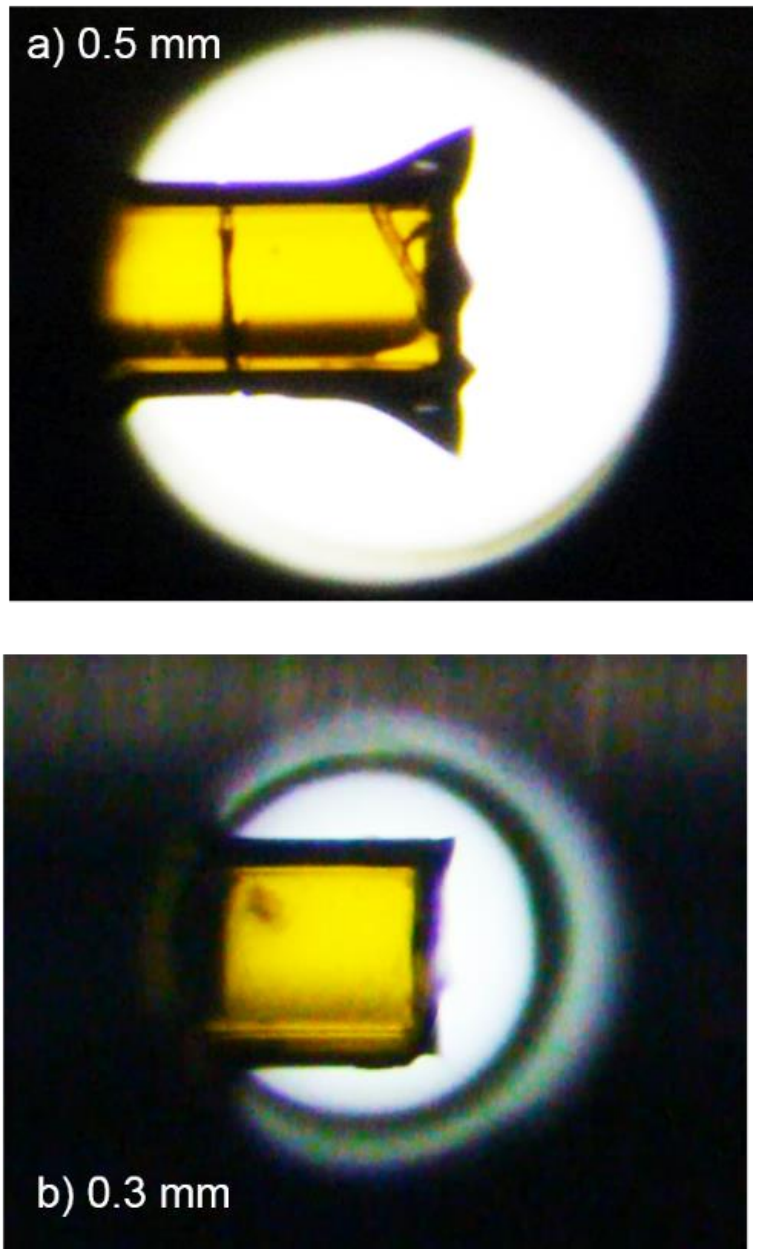

Figure 8.5. Observation of Taylor cone formed at the rim of the fused-silica capillary inside the ion inlet tube using side-holes of different sizes. a) Side holes diameter = 0.5 mm. b) Side holes diameter = 0.3 mm.

In addition to optical inspection, the spray current could be used to indicate the spraying mode inside the ion inlet tube. The spray current was measured by sensing the voltage drop across a 2 kΩ resistor placed in between the HV source and the metallic union. The use of an isolation amplification circuit allowed us to monitor the instantaneous spray current to determine the spraying mode and to ensure the spray stability during the MS acquisition. For all measurements in Figure 8.6, the HV was raised slowly to the highest value that the spray remained stable. Above that point, there was an erratic rise of instantaneous current up to several microamps, indicating a discharge taking place. Figure 8.6a shows the spray current measured for the emitter capillary placed just outside the inlet tube. The distance from the inlet entrance was 0.1 mm, and the measurement was performed with the microscopic inspection. The solution was 50% v/v methanol aqueous solution with 0.025% formic acid, and the flow rate was 1 μL/min. The stepwise increase of the spray current in Figure 8.6a was due to the change of electrospray mode from pulsation, cone-jet, two-jet, and multi-jet. Figure 8.6b shows the measurement performed at 1 mm inside the ion inlet. For a particular voltage, the electrical field and the spray current inside the inlet tube were higher than that outside the inlet tube (Figure 8.6a). Figures 8.6c and 8.6d show similar current measurements using the 25% v/v methanol aqueous solution without acid. The current reading that corresponded to the onset of multi-jet is at approximately 200 nA for acidic solution in Figure 8.6a and 20 nA for non-acidic solution in Figure 8.6c. These current levels provide a reference to the operating mode inside the tube. The same measurement performed with the emitter inside the ion inlet tube showed lower threshold voltages for the initialization of spray and multi-jet mode (Figure 8.6b & 8.6d). The increase of spray current with the voltage due to the increase in the number of jets is well documented for multi-emitter sprayers, as well as for the multi-jet mode of a single emitter[182,185,187,190]. For conductive solutions, the electrospray current follows the scaling law $I \propto \sqrt{Q}$, where Q is the solution flow rate[24]. If the flow rate is evenly divided by n individual jets, the total spray current I_n of multi-jets follows $I_n \propto \sqrt{n}$ for typical ESI solvents[187,190]. In Figures 8.6a and 8.6c, the current jump by a factor of approximately $\sqrt{2}$ when the single jet turns into two jets agrees reasonably with the scaling law.

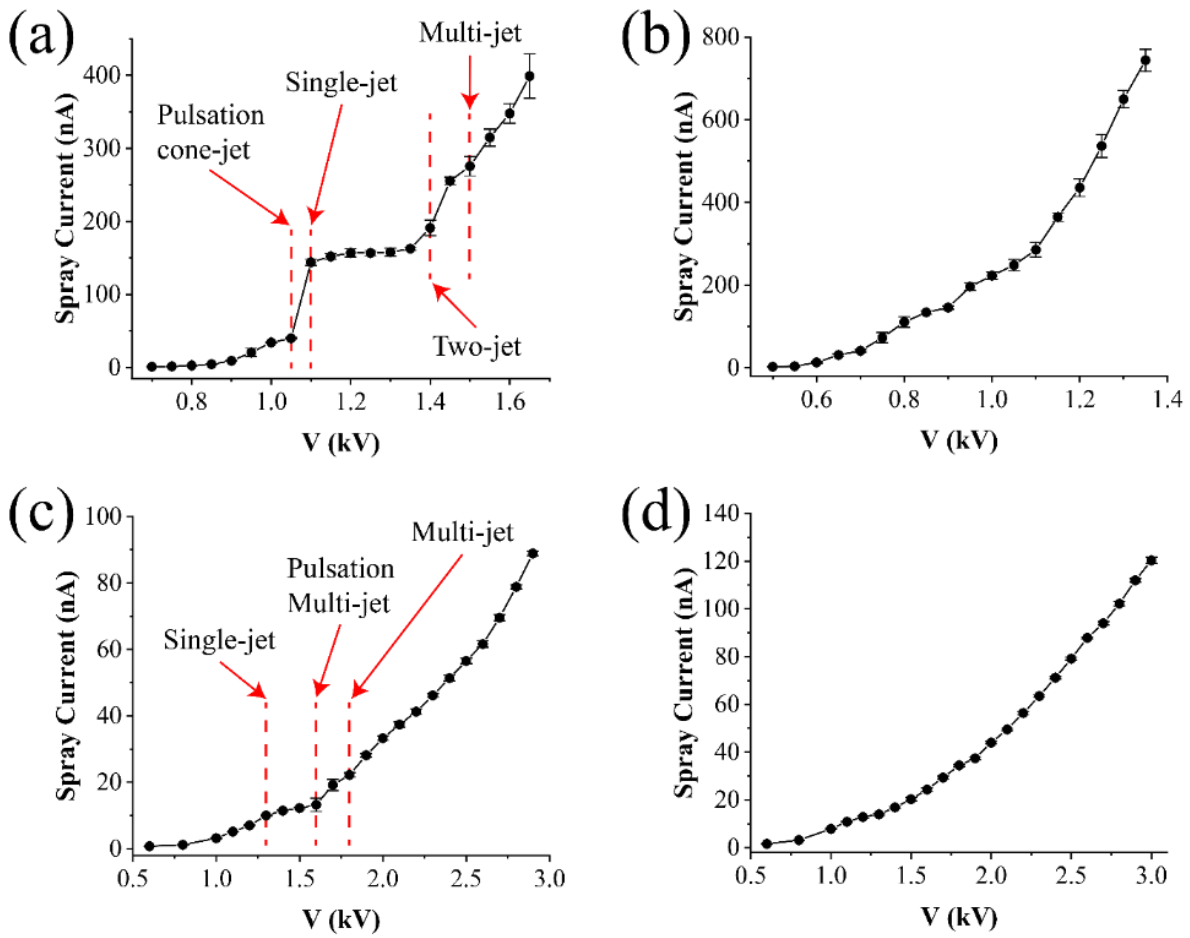

Figure 8.6. Plot of spray current versus the potential applied to the metallic union for (a & c) emitter positioned at 0.1 mm outside the ion inlet entrance, and (b & d) emitter positioned at 1 mm inside the ion inlet. Spray solutions are (a & b) 50 % methanol with 0.025 % v/v formic acid, and (c &d) 25% v/v methanol/water solution.

Figure 8.7a shows the change of spray current for the emitter capillary at different positions. The entrance of the inlet tube is assigned as the origin (0.0 mm). The sign is positive for the emitter inside the inlet tube and negative when for the position outside the inlet tube. The applied voltage was at a constant voltage of 1.4 kV. Under a constant emitter potential, the increase of spray current when it is brought closer to the inlet was due to the increase of the electrical field. The sprays outside the tube at -0.5 mm and -1.0 mm were in cone-jet modes. The transition to the multi-jet mode took place near the entrance, and the current increased to 650 nA at the 0.5 mm position. The spray current remained relatively unchanged after this point because the electrical field at the emitter tip is the same at any distance inside the ion inlet tube. Another measurement was made using a 25 %v/v methanol without acid (Figure 8.7b). The multi-jet mode was first initiated outside the inlet at -1 mm by applying 3 kV to the metallic union. The flow rate was 2.5 μL/min. A similar trend was observed but overall the current level was smaller. Here the emitter was aligned to the center and in parallel to the inlet axis, therefore the electrical field was the same at all distances inside the inlet tube. The spray current was found the be stabilized more easily inside the tube probably due to the fast-flowing gas that kept the outer surface of the fused capillary dry and carried away the charged droplet more quickly to reduce the space charge effect.

Figure 8.8 shows the change of total ion signal originated from 2.5×10^{-7} M cytochrome c in 25 % v/v methanol solution. The trend agrees with the spray current seen in Figure 8.6. Near and at the entrance, (position –0.5 mm and 0 mm), the fluctuation of ion signal was relatively large, an effect that might be associated with turbulence at the entrance of the inlet tube. The total ion current from cytochrome c reached a plateau when the emitter was at the position of 0.5 mm inside the inlet tube. Besides intensity, signal stability also improved owing to higher gas velocity and the reach of stable laminar flow. The increase of total ion current when the emitter was inside the ion inlet also implied an increase in ion transmission efficiency. Despite careful alignment, the orientation of the emitter capillary was not perfectly coaxial with the ion inlet tube. The initial position of the capillary was at the center of the entrance of the ion inlet. When the capillary was inserted deeper into the tube, the emitter tip could deviate from the center. The drop of ion abundance after 0.5 mm was caused by the deviation of the emitter from the central axis. The deviation was however less than 0.1 mm.

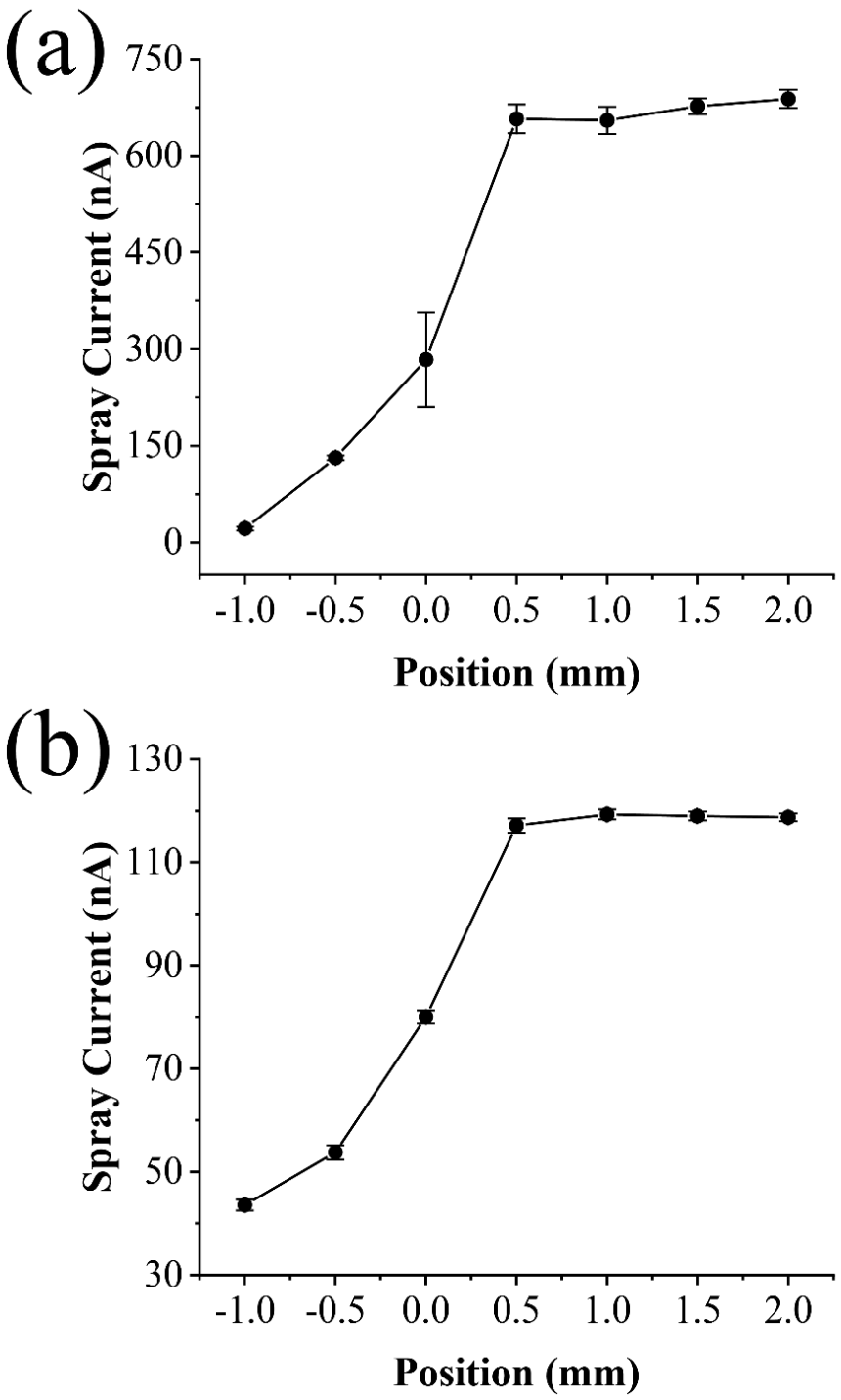

Figure 8.7. Plot of spray current versus emitter position for (a) 50 % v/v methanol with 0.025% v/v formic acid, and (b) 25 % v/v methanol without acid. The emitter potentials are 1.5 kV for (a) and 3kV for (b). The entrance of the inlet tube is assigned as the origin. The sign was positive when the emitter capillary is inside the inlet tube and negative when it is outside.

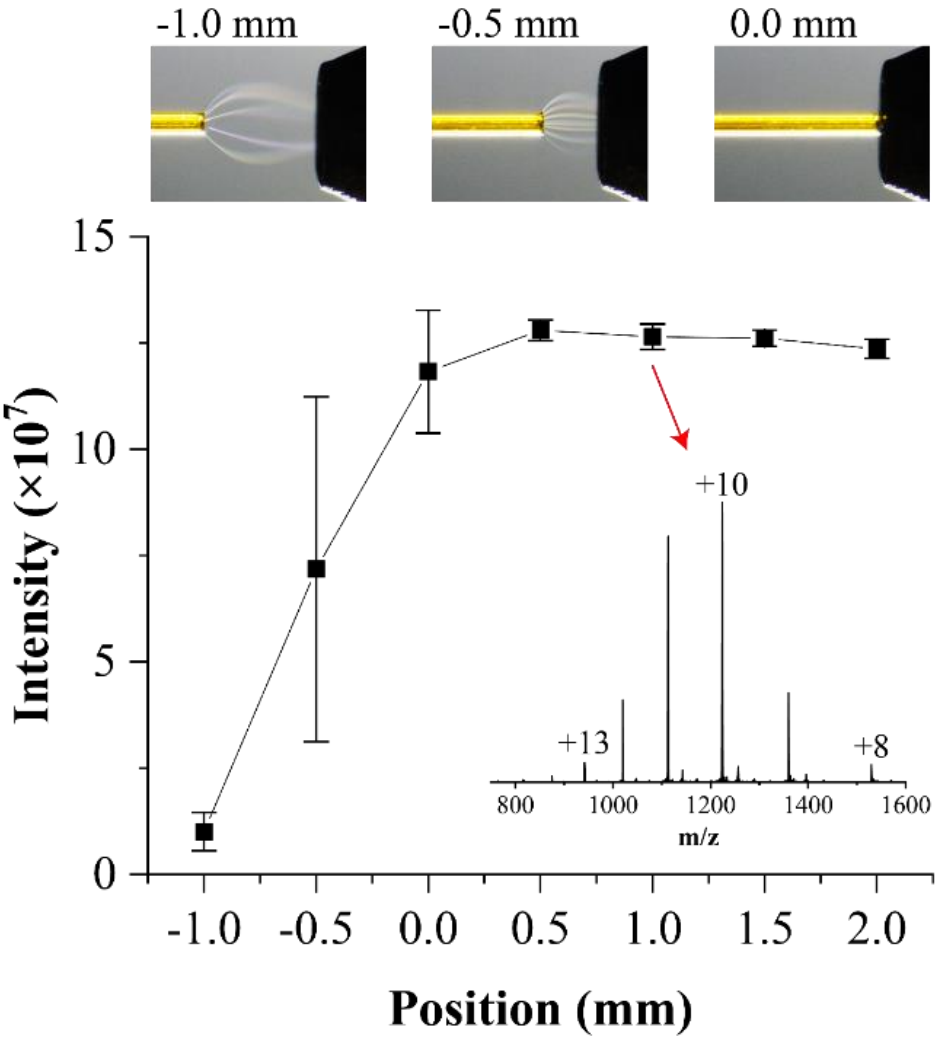

Figure 8.8. Total ion count for 2.5×10^{-7} M cytochrome c acquired at different emitter positions. Insets show the positioning of the emitter and the mass spectrum taken at position 1 mm.

The detections of cytochrome c from diluted solution with a concentration of 5×10^{-9} M are shown in Figure 8.9. Comparisons were made with the typical electrospray position at –2.0 mm outside the inlet and at 1.0 mm inside the inlet. Peaks originated from cytochrome c are labeled with red diamonds. Two types of solvents were used. One was a 50 % v/v methanol aqueous solution with 0.025% formic acid (Figures 8.9a & 8.9b, HV ~1.5 kV); another was 25 % v/v methanol aqueous solution (Figures 8.9c & 8.9d, HV ~ 3kV). At the position of –2 mm, the electrospray is in the single con-jet mode, and at +1.0 mm, it is in the multi-jet mode. Peaks related to the polyethylene glycol (PEG) contaminants with *m/z* 44 spacing) are present in Figures 8.9c and 8.9d. Those PEGs were not added intentionally and were detected only when dealing with samples of low concentration. Peaks from cytochrome c could be detected under the conditions in Figure 8.9a-8.9c, but not in Figure 8.9d. Following the scaling law,[207] the size of the precursor charged droplet for the solution without acid (Figure 8.9d) is larger than the one with acid (Figure 8.9b). For the same solution, the size of the precursor droplets is reduced by the formation of multiple jets when the emitter was inserted inside the inlet tube (Figure 8.9c). Since the average size of the precursor droplet is the largest in Figure 8.9d, the ion suppression effect, which is known to be more severe for larger droplets[43], was also a factor in addition to the ion transmission loss.

In sum, the sensitivity and the signal-to-noise ratio were improved by operating the ESI inside the tube, i.e. utilizing the multi-jet mode and, introducing all sprayed droplets into the vacuum. The improved ion transmission was in agreement with the results of ESII. It is noted that for ESII, Pagnotti et al reported an improved sensitivity when the fused silica emitter was touching the inlet tube walls or nearly touching rather than at the center position. Sweet spots were also observed in their work. That phenomenon is intriguing and one may wonder how could the electrospray be generated when the electrical circuit is “shorted” by touching the wall. However, if the surface temperature is high enough, the Leidenfrost effect can produce an insulating vapor layer which may explain the non-shorting condition. In our case, the surface temperature near the inlet entrance was relatively mild, (< 100 °C). When the emitter touched the wall, the electrospray stopped a greater than 1 μA current flowed through the circuit loop. For cytochrome c, even after readjusting the emitter to the center to re-initiate the spray, a significant amount of oxidation species (protein incorporated with oxygen atoms) was observed, indicating an electrochemical process during the short circuit. Future work is in progress

to replicate the results of Pagnotti et al.

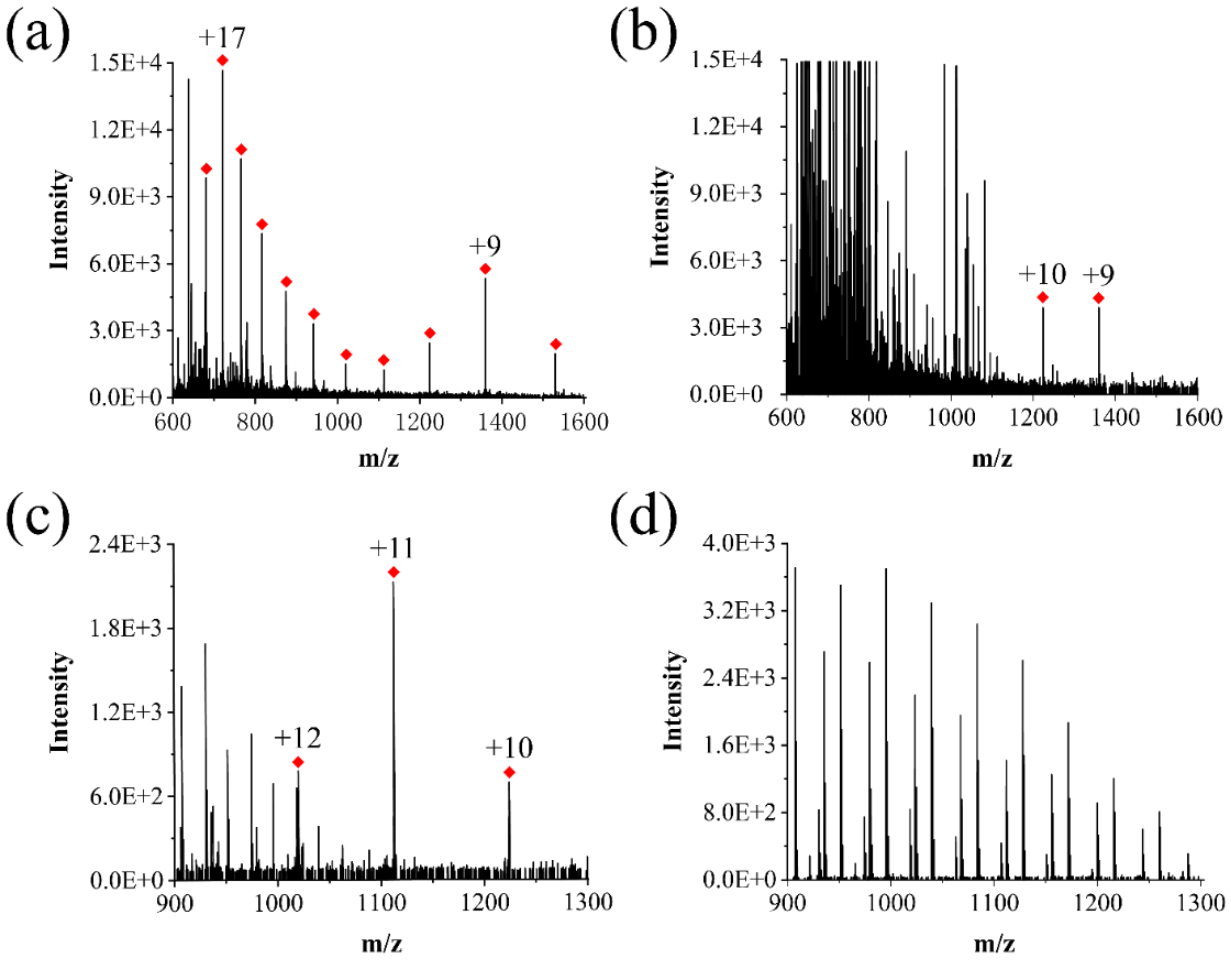

Figure 8.9. Mass spectra of 5×10^{-9} M cytochrome c acquired at 1.0 mm (a) & (c) and –2.0 mm (b) & (d). The solvents in (a) and (b) are 50 % v/v methanol aqueous solutions with 0.025% v/v formic acid. (c) & (d) are 25% v/v methanol aqueous solution. Peaks originated from cytochrome c are labeled with red diamonds. The mass spectra were constructed from the average of 6 single scan mass spectra.

Conclusions

Electrospray inside the MS ion inlet tube of 0.5~0.6 mm has been performed using an insulating emitter capillary. The stable and optimum condition for ion detection was found to be in the multi-jet mode. The present ion source can be seen as a standard microflow ESI with coaxial sheath gas, and the drag force from the fast-flowing gas prevented the ions and charged droplets from hitting the inner wall of the inlet tube before entering the first pumping stage. The precise alignment of the emitter, mechanical stability, and the electrical insulation were essential to ensure proper operation. Earlier works have reported the benefits of grooved or micro-structured emitters to provide anchoring points for the stabilization of the multi-jets and the enhancement of the electrical field[182]. Although our present study relied on the "naturally occurring" multi-jet mode, the surface defects on the rim of the capillary could act as the initial anchoring points and provide a local enhancement of the electrical field. The reproducibility of the multi-jet inside the ion inlet should be further improved with the micromachined structure on the emitter.

Chapter 9: Conclusion

In this thesis, we have developed atmospheric pressure & high pressure electrospray. The fundamental characteristic of the high pressure nano-electrospray ionization source was described in Chapter 2, focusing on the relationship between voltage, current, flow rate, and Taylor cone angle about ESI. The effect of flow rate on the ionization process was concentrated in Chapter 3. Chapter 4 introduced a new oxidation phenomenon that relies on high conductivity and extremely low flow rates. Chapter 5 introduced the phenomenon of acid-induced protein refolding observed by mass spectrometry. Studies on controlling the stability of electrospray using feedback Taylor cone angle and spray current at atmospheric pressure was presented in Chapter 6. Chapter 7 introduced a new electrospray without electrochemical: bipolar electrospray. Chapter 8 presented an ion source, Inlet ESI, that enhances the ion transmission efficiency.

In the chapter 2, stable Taylor cones with a half apex angle close to the theoretical Taylor angle have been generated for highly conductive aqueous solutions by operating the electrospray at spray currents near the minimal levels under a high-pressure condition. The formation of the aqueous Taylor cone from a large emitter capillary (i.d. 0.4 mm) that was typically difficult under atmospheric pressure was made possible under a super-atmospheric pressure condition. The emitter capillary was operated “off-line”, i.e. it was not connected to liquid pumps to maintain a zero-pressure difference between its both ends. The physical and ionization characteristics of this electrospray have been evaluated by the measurements of spray current, cone geometry, liquid flow rate, and mass spectrometry. The scaling law for spray current and flow rate which was previously established using a liquid pump-based system was found to be valid for the off-line system down to the nL/min flow regime. The flow rate in the present system was solely controlled by the applied potential and the choice of electrolytes, and the spray current was a reliable indicator of instantaneous liquid flow rate. The solution flow rate was finely tuned over the range of <0.2 nL/min to 120 nL/min using applied potential alone without changing the size of the emitter capillary. The spray current was used as the real-time indicator for the instantaneous flow rate and initial droplet size. High-resolution flow rate scanning and simultaneous acquisition of spray current and MS can also be performed to correlate the ionization results with the physical variables such as flow rate and initial droplet size with higher

precision. From the evidence of solution flow rate and mass spectrometric results, it was verified that the ultra-small size of the emitter is not an essential factor to produce the “true nanoelectrospray” equivalent ionization. Compared to the capillary-based methods, the present method allows the fine-tuning of flow rate and initial droplet size without changing the diameter of the emitter tip, which is beneficial for the fundamental study of the ionization mechanism. Artifacts originating from the surface interaction with the emitter can also be avoided when studying the physical chemistry of charged nanodroplets and liquid interface. The same working principle and the scaling law should also apply to smaller capillaries as long as the jet diameter is much smaller than the inner diameter.

In the chapter 3, an offline electrospray with a continuously varying flow rate in the nL/min regime had been developed to provide a more quantitative assessment of the nanoflow rate effect on the ionization response. The working principle based on the scaling law of spray current and flow rate is straightforward, and the technical requisites for scaling law to be valid: a large dimension ratio of emitter opening to the jet, operation in the cone-jet mode, and the absence of electrical discharge were met by operating the ion source in high-pressure. The dependence on flow rate for ion intensity, charge state distribution, peak spreading and oxidative modification shows that there is no universal optimum flow rate for all analytical purposes. A high throughput flow rate tuning within a flow rate window of several hundred pL/min to ~100 nL/min can thus be used to provide a full ionization response for the handling of analyte mixture, automatic searching for the flow rate best suited for each application, on-demand switching of flow regime, and the direct detection of protein from the high-salt buffer for native spectrometry. The present method also provides a platform to study electrospray-related phenomena taking place under a high electrical field at an extremely small flow rate.

In the chapter 4, we have demonstrated an efficient oxidation method that relies on the strong electrical field on the surface of a charged droplet or at the tip of a Taylor cone. The degree of oxidation was highly tunable by varying the flow rate of the electrospray, hence changing the size of the initial charge droplet and the radius of curvature at the tip of the Taylor cone. On-demand oxidation had been performed by precision tuning of the nano-flow rate using HV modulation with spray current as the feedback signal. The response of oxidation to the measured spray current was almost instantaneous. Using the scaling laws for electrospray, the threshold electrical field to induce the oxidation was found to be in the order of 1 V/nm. The isotope labeling showed that the oxygen atoms originated from the

gas phase. Ozone is commonly produced in electrical discharge but it was found not to be the final reactive oxygen species that reacted with the analytes. We postulate that the split oxygen atoms generated by electron activation under the strong electrical field reacted directly with the analytes to form the observed dominant oxidation species. The oxygen atom and the cogenerated ozone also reacted with water to form hydroxy radicals. The controlled oxidation can find application in the labeling of the analyte and the selective fragmentation that targets the oxygen-labeled location for structural analysis. As the present method only requires high electrical conductivity, the buffer solutions commonly used in the native electrospray to maintain a near physiological pH can be employed directly to perform native ESI-MS and oxidation analysis on the same sample in a single emitter. The use of electrical field strength, which can be estimated from the spray current, as the universal control parameter also improves the reproducibility across different emitters and solvent systems.

In the chapter 5, the high stability and improved desolvation of HP-ESI have enabled a mass spectrometric study of acid-induced compaction of protein at pH 1, a condition that was difficult for conventional atmospheric electrospray and nanoESI. The conformational change of protein standards induced by pH was manifested by the drastic shift of the dominant charge state to low charge, producing mass spectra resembling the condition of a native protein. Each protein also has its unique charge state response to the pH. Increasing the concentration of anions at pH 2 using ammonium chloride replicated the compaction phenomenon, supporting the role of anions as the main factor for this phenomenon. The compaction of protein was also found to take place in acidic organic solvent mixtures containing 50 % ethanol or acetonitrile. The dominant and the average charge of the compacted protein show dependency on the type of acid that is related to the propensity for the anion to cause compaction and charge reduction effect. In sum, the HP-ESI-MS has been demonstrated to be a potential tool for probing the acid-induced compaction phenomenon which is critical for our understanding of the science behind protein folding.

In the chapter 6, a simple iterative learning feedback control system has been developed for ESI-MS which provided an automatic correction to the emitter voltage to ensure the cone-jet mode operation throughout the course of the analysis. Spray current and optical image were used to determine the spraying mode and for performing the closed-loop control using a simple updating rule

to stabilize the apex angle or spray current to a user-defined value. The robustness of the feedback system was tested using emulated perturbation of flow rate, surface tension, and electrode distance. For an analysis involving changes in flow rate, and fluidic or electrostatic conditions, the locking of the Taylor cone ensured a steady cone-jet mode operation and overall ion signal stability. For an offline electrospray with constant fluidic variables, the locking of the spray current also stabilized the Taylor and the solution flow rate.

In the chapter 7, the characteristics of the electrodeless bipolar electrospray are summarized as follows. i) Similar to the standard electrospray, bipolar electrospray also exhibited dripping, kHz pulsation, steady cone-jet, and multi-jet modes with increasing voltage. ii) A higher voltage was needed to complete the full transition from pulsation to cone-jet mode at both emitters. iii) Except for a wider quasi-stable stage, the I-V and I-Q relationships for bipolar ES are the same as the standard ES. iv) Offline operation had a different I-V from the online operation but they followed the same scaling law for I-Q. In conclusion, despite the absence of electrochemical reactions in the sprayer, the bipolar electrospray generated solely by the electrical field-induced ion separation was found to be stable in the steady cone-jet mode, attaining the ionization efficiency equivalent to a standard ESI. The electrodeless operation on the sprayer side eliminates the interferences originating from the electrochemical reactions such as the oxidation of analyte, solvent, and electrode in conventional ESI-MS. Potential applications include the analysis of compounds that are sensitive to the oxidation/reduction reaction and the comparative study of the electrolytic effect in the standard electrospray.

In the chapter 8, electrospray inside the MS ion inlet tube of 0.5~0.6 mm has been performed using an insulating emitter capillary. The stable and optimum condition for ion detection was found to be in the multi-jet mode. The present ion source can be seen as a standard microflow ESI with coaxial sheath gas, and the drag force from the fast-flowing gas prevented the ions and charged droplets from hitting the inner wall of the inlet tube before entering the first pumping stage. The precise alignment of the emitter, mechanical stability, and the electrical insulation were essential to ensure proper operation. Earlier works have reported the benefits of grooved or micro-structured emitters to provide anchoring points for the stabilization of the multi-jets and the enhancement of the electrical field[182]. Although our present study relied on the “naturally occurring” multi-jet mode, the surface defects on

the rim of the capillary could act as the initial anchoring points and provide a local enhancement of the electrical field. The reproducibility of the multi-jet inside the ion inlet should be further improved with the micromachined structure on the emitter.

Reference

(1) Smyth, H. D.; Rutherford, E. Further Studies in Ionization: Hydrogen and Oxygen. *Proceedings of the Royal Society of London. Series A, Containing Papers of a Mathematical and Physical Character* **1924**, *105* (729), 116–128. https://doi.org/10.1098/rspa.1924.0008.

(2) Hogness, T. R.; Lunn, E. G. The Ionization Potentials of Hydrogen as Interpreted by Positive Ray Analysis. *Proceedings of the National Academy of Sciences* **1924**, *10* (9), 398–405. https://doi.org/10.1073/pnas.10.9.398.

(3) Dempster, A. J. LII. The Ionization and Dissociation of Hydrogen Molecules and the Formation of H 3. *The London, Edinburgh, and Dublin Philosophical Magazine and Journal of Science* **1916**, *31* (185), 438–443. https://doi.org/10.1080/14786440508635520.

(4) Munson, M. S. B.; Field, F. H. Chemical Ionization Mass Spectrometry. I. General Introduction. *J. Am. Chem. Soc.* **1966**, *88* (12), 2621–2630. https://doi.org/10.1021/ja00964a001.

(5) Munson, M. S. B. Proton Affinities and the Methyl Inductive Effect1. *J. Am. Chem. Soc.* **1965**, *87* (11), 2332–2336. https://doi.org/10.1021/ja01089a005.

(6) Munson, M. S. B.; Field, F. H. Reactions of Gaseous Ions. XV. Methane + 1% Ethane and Methane + 1% Propane. *J. Am. Chem. Soc.* **1965**, *87* (15), 3294–3299. https://doi.org/10.1021/ja01093a002.

(7) Karas, Michael.; Hillenkamp, Franz. Laser Desorption Ionization of Proteins with Molecular Masses Exceeding 10,000 Daltons. *Anal. Chem.* **1988**, *60* (20), 2299–2301. https://doi.org/10.1021/ac00171a028.

(8) Tanaka, K.; Waki, H.; Ido, Y.; Akita, S.; Yoshida, Y.; Yoshida, T.; Matsuo, T. Protein and Polymer Analyses up to m/z 100 000 by Laser Ionization Time-of-Flight Mass Spectrometry. *Rapid Communications in Mass Spectrometry* **1988**, *2* (8), 151–153. https://doi.org/10.1002/rcm.1290020802.

(9) Fenn, J. B.; Mann, M.; Meng, C. K.; Wong, S. F.; Whitehouse, C. M. Electrospray Ionization for Mass Spectrometry of Large Biomolecules. *Science* **1989**, *246* (4926), 64–71. https://doi.org/10.1126/science.2675315.

(10) Zeleny, J. The Electrical Discharge from Liquid Points, and a Hydrostatic Method of Measuring the Electric Intensity at Their Surfaces. *Phys. Rev.* **1914**, *3* (2), 69–91. https://doi.org/10.1103/PhysRev.3.69.

(11) Taylor, G. I. Disintegration of Water Drops in an Electric Field. *Proceedings of the Royal Society of London. Series A. Mathematical and Physical Sciences* **1964**, *280* (1382), 383–397. https://doi.org/10.1098/rspa.1964.0151.

(12) Rayleigh, Lord. XX. On the Equilibrium of Liquid Conducting Masses Charged with Electricity. *The London, Edinburgh, and Dublin Philosophical Magazine and Journal of Science* **1882**, *14* (87), 184–186. https://doi.org/10.1080/14786448208628425.

(13) Iribarne, J. V.; Thomson, B. A. On the Evaporation of Small Ions from Charged Droplets. *The Journal of Chemical Physics* **1976**, *64* (6), 2287–2294. https://doi.org/10.1063/1.432536.

(14) Dole, M.; Mack, L. L.; Hines, R. L.; Mobley, R. C.; Ferguson, L. D.; Alice, M. B. Molecular Beams of Macroions. *The Journal of Chemical Physics* **1968**, *49* (5), 2240–2249. https://doi.org/10.1063/1.1670391.

(15) Ahadi, E.; Konermann, L. Modeling the Behavior of Coarse-Grained Polymer Chains in Charged Water Droplets: Implications for the Mechanism of Electrospray Ionization. *J. Phys. Chem. B* **2012**, *116* (1), 104–112. https://doi.org/10.1021/jp209344z.

(16) Khristenko, N.; Rosu, F.; Largy, E.; Haustant, J.; Mesmin, C.; Gabelica, V. Native Electrospray Ionization of Multi-Domain Proteins via a Bead Ejection Mechanism. *J. Am. Chem. Soc.* **2023**, *145* (1), 498–506.

https://doi.org/10.1021/jacs.2c10762.
(17) Blades, A. T.; Ikonomou, M. G.; Kebarle, Paul. Mechanism of Electrospray Mass Spectrometry. Electrospray as an Electrolysis Cell. *Anal. Chem.* **1991**, *63* (19), 2109–2114. https://doi.org/10.1021/ac00019a009.
(18) Mora, J. F. de la; Van Berkel, G. J.; Enke, C. G.; Cole, R. B.; Martinez-Sanchez, M.; Fenn, J. B. Electrochemical Processes in Electrospray Ionization Mass Spectrometry. *Journal of Mass Spectrometry* **2000**, *35* (8), 939–952. https://doi.org/10.1002/1096-9888(200008)35:8<939::AID-JMS36>3.0.CO;2-V.
(19) Van Berkel, G. J.; Zhou, F.; Aronson, J. T. Changes in Bulk Solution pH Caused by the Inherent Controlled-Current Electrolytic Process of an Electrospray Ion Source. *International Journal of Mass Spectrometry and Ion Processes* **1997**, *162* (1), 55–67. https://doi.org/10.1016/S0168-1176(96)04476-X.
(20) Van Berkel, G. J.; Asano, K. G.; Schnier, P. D. Electrochemical Processes in a Wire-in-a-Capillary Bulk-Loaded, Nano-Electrospray Emitter. *J. Am. Soc. Mass Spectrom.* **2001**, *12* (7), 853–862. https://doi.org/10.1016/S1044-0305(01)00264-1.
(21) Van Berkel, G. J. Electrolytic Deposition of Metals on to the High-Voltage Contact in an Electrospray Emitter: Implications for Gas-Phase Ion Formation. *Journal of Mass Spectrometry* **2000**, *35* (7), 773–783. https://doi.org/10.1002/1096-9888(200007)35:7<773::AID-JMS4>3.0.CO;2-6.
(22) Van Berkel, G. J.; McLuckey, S. A.; Glish, G. L. Electrospray Ionization of Porphyrins Using a Quadrupole Ion Trap for Mass Analysis. *Anal. Chem.* **1991**, *63* (11), 1098–1109. https://doi.org/10.1021/ac00011a009.
(23) Chen, L. C.; Mandal, M. K.; Hiraoka, K. High Pressure (>1 Atm) Electrospray Ionization Mass Spectrometry. *J. Am. Soc. Mass Spectrom.* **2011**, *22* (3), 539–544. https://doi.org/10.1007/s13361-010-0058-8.
(24) Fernández De La, M., J.; Loscertales, I. G. The Current Emitted by Highly Conducting Taylor Cones. *Journal of Fluid Mechanics* **1994**, *260*, 155–184. https://doi.org/10.1017/S0022112094003472.
(25) Cloupeau, M.; Prunet-Foch, B. Electrohydrodynamic Spraying Functioning Modes: A Critical Review. *Journal of Aerosol Science* **1994**, *25* (6), 1021–1036. https://doi.org/10.1016/0021-8502(94)90199-6.
(26) Wilm, M.; Mann, M. Analytical Properties of the Nanoelectrospray Ion Source. *Anal. Chem.* **1996**, *68* (1), 1–8. https://doi.org/10.1021/ac9509519.
(27) Hong, C.-M.; Lee, C.-T.; Lee, Y.-M.; Kuo, C.-P.; Yuan, C.-H.; Shiea, J. Generating Electrospray from Solutions Predeposited on a Copper Wire. *Rapid Communications in Mass Spectrometry* **1999**, *13* (1), 21–25. https://doi.org/10.1002/(SICI)1097-0231(19990115)13:1<21::AID-RCM441>3.0.CO;2-7.
(28) Chen, L. C.; Nishidate, K.; Saito, Y.; Mori, K.; Asakawa, D.; Takeda, S.; Kubota, T.; Hori, H.; Hiraoka, K. Characteristics of Probe Electrospray Generated from a Solid Needle. *J. Phys. Chem. B* **2008**, *112* (35), 11164–11170. https://doi.org/10.1021/jp803730x.
(29) Nissilä, T.; Sainiemi, L.; Sikanen, T.; Kotiaho, T.; Franssila, S.; Kostiainen, R.; Ketola, R. A. Silicon Micropillar Array Electrospray Chip for Drug and Biomolecule Analysis. *Rapid Communications in Mass Spectrometry* **2007**, *21* (22), 3677–3682. https://doi.org/10.1002/rcm.3266.
(30) Liu, J.; Wang, H.; Manicke, N. E.; Lin, J.-M.; Cooks, R. G.; Ouyang, Z. Development, Characterization, and Application of Paper Spray Ionization. *Anal. Chem.* **2010**, *82* (6), 2463–2471. https://doi.org/10.1021/ac902854g.
(31) Aksyonov, S.; Williams, P. Electrospray Ionization Using Disposable Plastic Pipette Tips. *Rapid Commun Mass Spectrom* **2001**, *15* (19), 1890–1891. https://doi.org/10.1002/rcm.437.
(32) Han, Z.; Chen, L. C. High-Pressure nanoESI of Highly Conductive Volatile and Non-Volatile Buffer Solutions from a Large Taylor Cone: Effect of Spray Current on Charge State Distribution. *International Journal of Mass Spectrometry* **2022**, *476*, 116845. https://doi.org/10.1016/j.ijms.2022.116845.
(33) Han, Z.; Chen, L. C. Generation of Ions from Aqueous Taylor Cones near the Minimum Flow Rate: "True

Nanoelectrospray" without Narrow Capillary. *J. Am. Soc. Mass Spectrom.* **2022**, *33* (3), 491–498. https://doi.org/10.1021/jasms.1c00322.

(34) Forbes, R. G. Liquid-Metal Ion Sources and Electrosprays Operating In Cone-Jet Mode: Some Theoretical Comparisons And Comments. *Journal of Aerosol Science* **2000**, *31* (1), 97–120. https://doi.org/10.1016/S0021-8502(99)00036-1.

(35) Yamashita, M.; Fenn, J. B. Electrospray Ion Source. Another Variation on the Free-Jet Theme. *J. Phys. Chem.* **1984**, *88* (20), 4451–4459. https://doi.org/10.1021/j150664a002.

(36) Mora, J. F. D. L. The Effect of Charge Emission from Electrified Liquid Cones. *Journal of Fluid Mechanics* **1992**, *243*, 561–574. https://doi.org/10.1017/S0022112092002829.

(37) Chen, D.-R.; Pui, D. Y. H.; Kaufman, S. L. Electrospraying of Conducting Liquids for Monodisperse Aerosol Generation in the 4 Nm to 1.8 Mm Diameter Range. *Journal of Aerosol Science* **1995**, *26* (6), 963–977. https://doi.org/10.1016/0021-8502(95)00027-A.

(38) Gañán-Calvo, A. M.; Dávila, J.; Barrero, A. Current and Droplet Size in the Electrospraying of Liquids. Scaling Laws. *Journal of Aerosol Science* **1997**, *28* (2), 249–275. https://doi.org/10.1016/S0021-8502(96)00433-8.

(39) Fernández de la Mora, J. The Fluid Dynamics of Taylor Cones. *Annual Review of Fluid Mechanics* **2007**, *39* (1), 217–243. https://doi.org/10.1146/annurev.fluid.39.050905.110159.

(40) Gamero-Castaño, M.; Fernández de la Mora, J. Direct Measurement of Ion Evaporation Kinetics from Electrified Liquid Surfaces. *The Journal of Chemical Physics* **2000**, *113* (2), 815–832. https://doi.org/10.1063/1.481857.

(41) Wilm, M. S.; Mann, M. Electrospray and Taylor-Cone Theory, Dole's Beam of Macromolecules at Last? *International Journal of Mass Spectrometry and Ion Processes* **1994**, *136* (2), 167–180. https://doi.org/10.1016/0168-1176(94)04024-9.

(42) Gibson, G. T. T.; Mugo, S. M.; Oleschuk, R. D. Nanoelectrospray Emitters: Trends and Perspective. *Mass Spectrometry Reviews* **2009**, *28* (6), 918–936. https://doi.org/10.1002/mas.20248.

(43) Juraschek, R.; Dülcks, T.; Karas, M. Nanoelectrospray—More than Just a Minimized-Flow Electrospray Ionization Source. *J. Am. Soc. Mass Spectrom.* **1999**, *10* (4), 300–308. https://doi.org/10.1016/S1044-0305(98)00157-3.

(44) Schmidt, A.; Karas, M.; Dülcks, T. Effect of Different Solution Flow Rates on Analyte Ion Signals in Nano-ESI MS, or: When Does ESI Turn into Nano-ESI? *J Am Soc Mass Spectrom* **2003**, *14* (5), 492–500. https://doi.org/10.1016/S1044-0305(03)00128-4.

(45) Yuill, E. M.; Sa, N.; Ray, S. J.; Hieftje, G. M.; Baker, L. A. Electrospray Ionization from Nanopipette Emitters with Tip Diameters of Less than 100 Nm. *Anal. Chem.* **2013**, *85* (18), 8498–8502. https://doi.org/10.1021/ac402214g.

(46) Susa, A. C.; Xia, Z.; Williams, E. R. Native Mass Spectrometry from Common Buffers with Salts That Mimic the Extracellular Environment. *Angewandte Chemie International Edition* **2017**, *56* (27), 7912–7915. https://doi.org/10.1002/anie.201702330.

(47) Susa, A. C.; Xia, Z.; Williams, E. R. Small Emitter Tips for Native Mass Spectrometry of Proteins and Protein Complexes from Nonvolatile Buffers That Mimic the Intracellular Environment. *Anal. Chem.* **2017**, *89* (5), 3116–3122. https://doi.org/10.1021/acs.analchem.6b04897.

(48) Chernushevich, I. V.; Bahr, U.; Karas, M. Nanospray 'Taxation' and How to Avoid It. *Rapid Communications in Mass Spectrometry* **2004**, *18* (20), 2479–2485. https://doi.org/10.1002/rcm.1649.

(49) Cherney, L. T. Structure of Taylor Cone-Jets: Limit of Low Flow Rates. *Journal of Fluid Mechanics* **1999**, *378*, 167–196. https://doi.org/10.1017/S002211209800319X.

(50) Rahman, M. M.; Mandal, M. K.; Hiraoka, K.; Chen, L. C. High Pressure Nanoelectrospray Ionization Mass Spectrometry for Analysis of Aqueous Solutions. *Analyst* **2013**, *138* (21), 6316–6322. https://doi.org/10.1039/C3AN00699A.

(51) Rahman, M. M.; Chen, L. C. Analytical Characteristics of Nano-Electrospray Operated under Super-Atmospheric Pressure. *Analytica Chimica Acta* **2018**, *1021*, 78–84. https://doi.org/10.1016/j.aca.2018.03.026.

(52) Yin, Z.; Huang, J.; Miao, H.; Hu, O.; Li, H. High-Pressure Electrospray Ionization Yields Supercharged Protein Complexes from Native Solutions While Preserving Noncovalent Interactions. *Anal. Chem.* **2020**, *92* (18), 12312–12321. https://doi.org/10.1021/acs.analchem.0c01965.

(53) Chen, L. C.; Ninomiya, S.; Hiraoka, K. Super-Atmospheric Pressure Ionization Mass Spectrometry and Its Application to Ultrafast Online Protein Digestion Analysis. *Journal of Mass Spectrometry* **2016**, *51* (6), 396–411. https://doi.org/10.1002/jms.3779.

(54) Chen, L. C.; Naito, T.; Ninomiya, S.; Hiraoka, K. Hyphenation of High-Temperature Liquid Chromatography with High-Pressure Electrospray Ionization for Subcritical Water LC-ESI-MS. *Analyst* **2018**, *143* (22), 5552–5558. https://doi.org/10.1039/C8AN01113C.

(55) Chen, L. C. A Plug-and-Play High-Pressure ESI Source with an Emitter at Ground Potential and Its Application to High-Temperature Capillary LC-MS. *J. Am. Soc. Mass Spectrom.* **2020**, *31* (5), 1015–1018. https://doi.org/10.1021/jasms.0c00052.

(56) Rahman, M. M.; Hiraoka, K.; Chen, L. C. Realizing Nano Electrospray Ionization Using Disposable Pipette Tips under Super Atmospheric Pressure. *Analyst* **2013**, *139* (3), 610–617. https://doi.org/10.1039/C3AN01635H.

(57) Dutcher, C. S.; Wexler, A. S.; Clegg, S. L. Surface Tensions of Inorganic Multicomponent Aqueous Electrolyte Solutions and Melts. *J. Phys. Chem. A* **2010**, *114* (46), 12216–12230. https://doi.org/10.1021/jp105191z.

(58) Li, Y.; Cole, R. B. Shifts in Peptide and Protein Charge State Distributions with Varying Spray Tip Orifice Diameter in Nanoelectrospray Fourier Transform Ion Cycltron Resonance Mass Spectrometry. *Anal. Chem.* **2003**, *75* (21), 5739–5746. https://doi.org/10.1021/ac0301402.

(59) Mortensen, D. N.; Williams, E. R. Surface-Induced Protein Unfolding in Submicron Electrospray Emitters. *Anal. Chem.* **2016**, *88* (19), 9662–9668. https://doi.org/10.1021/acs.analchem.6b02499.

(60) Fernandez de la Mora, J. Electrospray Ionization of Large Multiply Charged Species Proceeds via Dole's Charged Residue Mechanism. *Analytica Chimica Acta* **2000**, *406* (1), 93–104. https://doi.org/10.1016/S0003-2670(99)00601-7.

(61) Kaddis, C. S.; Lomeli, S. H.; Yin, S.; Berhane, B.; Apostol, M. I.; Kickhoefer, V. A.; Rome, L. H.; Loo, J. A. Sizing Large Proteins and Protein Complexes by Electrospray Ionization Mass Spectrometry and Ion Mobility. *J Am Soc Mass Spectrom* **2007**, *18* (7), 1206–1216. https://doi.org/10.1016/j.jasms.2007.02.015.

(62) Emmett, M. R.; Caprioli, R. M. Micro-Electrospray Mass Spectrometry: Ultra-High-Sensitivity Analysis of Peptides and Proteins. *J Am Soc Mass Spectrom* **1994**, *5* (7), 605–613. https://doi.org/10.1016/1044-0305(94)85001-1.

(63) Li, H.; Allen, N.; Li, M.; Li, A. Conducting and Characterizing Femto Flow Electrospray Ionization. *Analyst* **2022**, *147* (6), 1071–1075. https://doi.org/10.1039/D1AN02190G.

(64) Tang, X.; Bruce, J. E.; Hill, H. H. Characterizing Electrospray Ionization Using Atmospheric Pressure Ion Mobility Spectrometry. *Anal. Chem.* **2006**, *78* (22), 7751–7760. https://doi.org/10.1021/ac0613380.

(65) Kostelic, M. M.; Hsieh, C.-C.; Sanders, H. M.; Zak, C. K.; Ryan, J. P.; Baker, E. S.; Aspinwall, C. A.; Marty, M. T. Surface Modified Nano-Electrospray Needles Improve Sensitivity for Native Mass Spectrometry. *J. Am.*

Soc. Mass Spectrom. **2022**, *33* (6), 1031–1037. https://doi.org/10.1021/jasms.2c00087.

(66) Prabhu, G. R. D.; Ponnusamy, V. K.; Witek, H. A.; Urban, P. L. Sample Flow Rate Scan in Electrospray Ionization Mass Spectrometry Reveals Alterations in Protein Charge State Distribution. *Anal. Chem.* **2020**, *92* (19), 13042–13049. https://doi.org/10.1021/acs.analchem.0c01945.

(67) Marginean, I.; Kelly, R. T.; Prior, D. C.; LaMarche, B. L.; Tang, K.; Smith, R. D. Analytical Characterization of the Electrospray Ion Source in the Nanoflow Regime. *Anal. Chem.* **2008**, *80* (17), 6573–6579. https://doi.org/10.1021/ac800683s.

(68) Marginean, I.; Tang, K.; Smith, R. D.; Kelly, R. T. Picoelectrospray Ionization Mass Spectrometry Using Narrow-Bore Chemically Etched Emitters. *J. Am. Soc. Mass Spectrom.* **2014**, *25* (1), 30–36. https://doi.org/10.1007/s13361-013-0749-z.

(69) Li, M.; Li, H.; R. Allen, N.; Wang, T.; Li, L.; Schwartz, J.; Li, A. Nested-Channel for on-Demand Alternation between Electrospray Ionization Regimes. *Chemical Science* **2021**, *12* (5), 1907–1914. https://doi.org/10.1039/D0SC06221A.

(70) Sterling, H. J.; Cassou, C. A.; Susa, A. C.; Williams, E. R. Electrothermal Supercharging of Proteins in Native Electrospray Ionization. *Anal. Chem.* **2012**, *84* (8), 3795–3801. https://doi.org/10.1021/ac300468a.

(71) Xia, Z.; Williams, E. R. Effect of Droplet Lifetime on Where Ions Are Formed in Electrospray Ionization. *Analyst* **2018**, *144* (1), 237–248. https://doi.org/10.1039/C8AN01824C.

(72) Hedges, J. B.; Vahidi, S.; Yue, X.; Konermann, L. Effects of Ammonium Bicarbonate on the Electrospray Mass Spectra of Proteins: Evidence for Bubble-Induced Unfolding. *Anal. Chem.* **2013**, *85* (13), 6469–6476. https://doi.org/10.1021/ac401020s.

(73) Rundlett, K. L.; Armstrong, D. W. Mechanism of Signal Suppression by Anionic Surfactants in Capillary Electrophoresis−Electrospray Ionization Mass Spectrometry. *Anal. Chem.* **1996**, *68* (19), 3493–3497. https://doi.org/10.1021/ac960472p.

(74) Yue, X.; Vahidi, S.; Konermann, L. Insights into the Mechanism of Protein Electrospray Ionization From Salt Adduction Measurements. *J. Am. Soc. Mass Spectrom.* **2014**, *25* (8), 1322–1331. https://doi.org/10.1007/s13361-014-0905-0.

(75) Chen, L. C.; Rahman, M. M.; Hiraoka, K. Super-Atmospheric Pressure Ion Sources: Application and Coupling to API Mass Spectrometer. *Mass Spectrometry* **2014**, *3* (Special_Issue), S0024–S0024. https://doi.org/10.5702/massspectrometry.S0024.

(76) Boys, B. L.; Kuprowski, M. C.; Noël, J. J.; Konermann, L. Protein Oxidative Modifications During Electrospray Ionization: Solution Phase Electrochemistry or Corona Discharge-Induced Radical Attack? *Anal. Chem.* **2009**, *81* (10), 4027–4034. https://doi.org/10.1021/ac900243p.

(77) Morand, K.; Talbo, G.; Mann, M. Oxidation of Peptides during Electrospray Ionization. *Rapid Communications in Mass Spectrometry* **1993**, *7* (8), 738–743. https://doi.org/10.1002/rcm.1290070811.

(78) Maleknia, S. D.; Chance, M. R.; Downard, K. M. Electrospray-Assisted Modification of Proteins: A Radical Probe of Protein Structure. *Rapid Communications in Mass Spectrometry* **1999**, *13* (23), 2352–2358. https://doi.org/10.1002/(SICI)1097-0231(19991215)13:23<2352::AID-RCM798>3.0.CO;2-X.

(79) Hambly, D. M.; Gross, M. L. Laser Flash Photolysis of Hydrogen Peroxide to Oxidize Protein Solvent-Accessible Residues on the Microsecond Timescale. *J. Am. Soc. Mass Spectrom.* **2005**, *16* (12), 2057–2063. https://doi.org/10.1016/j.jasms.2005.09.008.

(80) Lawal, R. O.; Donnarumma, F.; Murray, K. K. Electrospray Photochemical Oxidation of Proteins. *J. Am. Soc. Mass Spectrom.* **2019**, *30* (11), 2196–2199. https://doi.org/10.1007/s13361-019-02313-4.

(81) Tang, S.; Cheng, H.; Yan, X. On-Demand Electrochemical Epoxidation in Nano-Electrospray Ionization

Mass Spectrometry to Locate Carbon–Carbon Double Bonds. *Angewandte Chemie International Edition* **2020**, *59* (1), 209–214. https://doi.org/10.1002/anie.201911070.

(82) Bruggeman, P.; Schram, D. C. On OH Production in Water Containing Atmospheric Pressure Plasmas. *Plasma Sources Sci. Technol.* **2010**, *19* (4), 045025. https://doi.org/10.1088/0963-0252/19/4/045025.

(83) Tang, L.; Kebarle, P. *Effect of the conductivity of the electrosprayed solution on the electrospray current. Factors determining analyte sensitivity in electrospray mass spectrometry*. ACS Publications. https://doi.org/10.1021/ac00023a009.

(84) Enke, C. G. A Predictive Model for Matrix and Analyte Effects in Electrospray Ionization of Singly-Charged Ionic Analytes. *Anal. Chem.* **1997**, *69* (23), 4885–4893. https://doi.org/10.1021/ac970095w.

(85) Pei, J.; Hsu, C.-C.; Yu, K.; Wang, Y.; Huang, G. Time-Resolved Method to Distinguish Protein/Peptide Oxidation during Electrospray Ionization Mass Spectrometry. *Analytica Chimica Acta* **2018**, *1011*, 59–67. https://doi.org/10.1016/j.aca.2018.01.025.

(86) Konermann, L.; Silva, E. A.; Sogbein, O. F. Electrochemically Induced pH Changes Resulting in Protein Unfolding in the Ion Source of an Electrospray Mass Spectrometer. *Anal. Chem.* **2001**, *73* (20), 4836–4844. https://doi.org/10.1021/ac010545r.

(87) He, F.; Hendrickson, C. L.; Marshall, A. G. Unequivocal Determination of Metal Atom Oxidation State in Naked Heme Proteins: Fe(III)Myoglobin, Fe(III)Cytochrome c, Fe(III)Cytochrome B5, and Fe(III)Cytochrome B5 L47R. *J Am Soc Mass Spectrom* **2000**, *11* (2), 120–126. https://doi.org/10.1016/S1044-0305(99)00132-4.

(88) Chen, M.; Cook, K. D. Oxidation Artifacts in the Electrospray Mass Spectrometry of Aβ Peptide. *Anal. Chem.* **2007**, *79* (5), 2031–2036. https://doi.org/10.1021/ac061743r.

(89) Cheng, H.; Yang, T.; Edwards, M.; Tang, S.; Xu, S.; Yan, X. Picomole-Scale Transition Metal Electrocatalysis Screening Platform for Discovery of Mild C–C Coupling and C–H Arylation through in Situ Anodically Generated Cationic Pd. *J. Am. Chem. Soc.* **2022**, *144* (3), 1306–1312. https://doi.org/10.1021/jacs.1c11179.

(90) Wan, L.; Gong, G.; Liang, H.; Huang, G. In Situ Analysis of Unsaturated Fatty Acids in Human Serum by Negative-Ion Paper Spray Mass Spectrometry. *Analytica Chimica Acta* **2019**, *1075*, 120–127. https://doi.org/10.1016/j.aca.2019.05.055.

(91) Thomas, M. C.; Mitchell, T. W.; Blanksby, S. J. Ozonolysis of Phospholipid Double Bonds during Electrospray Ionization: A New Tool for Structure Determination. *J. Am. Chem. Soc.* **2006**, *128* (1), 58–59. https://doi.org/10.1021/ja056797h.

(92) Tang, S.; Chen, X.; Ke, Y.; Wang, F.; Yan, X. Voltage-Controlled Divergent Cascade of Electrochemical Reactions for Characterization of Lipids at Multiple Isomer Levels Using Mass Spectrometry. *Anal. Chem.* **2022**, *94* (37), 12750–12756. https://doi.org/10.1021/acs.analchem.2c02375.

(93) Zhang, X.; Barraza, K. M.; Upton, K. T.; Beauchamp, J. L. Time Resolved Study of Hydroxyl Radical Oxidation of Oleic Acid at the Air-Water Interface. *Chemical Physics Letters* **2017**, *683*, 76–82. https://doi.org/10.1016/j.cplett.2017.05.051.

(94) Zhang, X.; Ren, X.; Chingin, K.; Xu, J.; Yan, X.; Chen, H. Mass Spectrometry Distinguishing C=C Location and Cis/Trans Isomers: A Strategy Initiated by Water Radical Cations. *Analytica Chimica Acta* **2020**, *1139*, 146–154. https://doi.org/10.1016/j.aca.2020.09.027.

(95) Cao, W.; Ma, X.; Li, Z.; Zhou, X.; Ouyang, Z. Locating Carbon–Carbon Double Bonds in Unsaturated Phospholipids by Epoxidation Reaction and Tandem Mass Spectrometry. *Anal. Chem.* **2018**, *90* (17), 10286–10292. https://doi.org/10.1021/acs.analchem.8b02021.

(96) Lee, J. K.; Walker, K. L.; Han, H. S.; Kang, J.; Prinz, F. B.; Waymouth, R. M.; Nam, H. G.; Zare, R. N.

Spontaneous Generation of Hydrogen Peroxide from Aqueous Microdroplets. *Proceedings of the National Academy of Sciences* **2019**, *116* (39), 19294–19298. https://doi.org/10.1073/pnas.1911883116.

(97) Lee, J. K.; Han, H. S.; Chaikasetsin, S.; Marron, D. P.; Waymouth, R. M.; Prinz, F. B.; Zare, R. N. Condensing Water Vapor to Droplets Generates Hydrogen Peroxide. *Proceedings of the National Academy of Sciences* **2020**, *117* (49), 30934–30941. https://doi.org/10.1073/pnas.2020158117.

(98) Musskopf, N. H.; Gallo, A. Jr.; Zhang, P.; Petry, J.; Mishra, H. The Air–Water Interface of Water Microdroplets Formed by Ultrasonication or Condensation Does Not Produce H2O2. *J. Phys. Chem. Lett.* **2021**, *12* (46), 11422–11429. https://doi.org/10.1021/acs.jpclett.1c02953.

(99) Jr, A. G.; H. Musskopf, N.; Liu, X.; Yang, Z.; Petry, J.; Zhang, P.; Thoroddsen, S.; Im, H.; Mishra, H. On the Formation of Hydrogen Peroxide in Water Microdroplets. *Chemical Science* **2022**, *13* (9), 2574–2583. https://doi.org/10.1039/D1SC06465G.

(100) Mehrgardi, M. A.; Mofidfar, M.; Zare, R. N. Sprayed Water Microdroplets Are Able to Generate Hydrogen Peroxide Spontaneously. *J. Am. Chem. Soc.* **2022**, *144* (17), 7606–7609. https://doi.org/10.1021/jacs.2c02890.

(101) Qiu, L.; Psimos, M. D.; Cooks, R. G. Spontaneous Oxidation of Aromatic Sulfones to Sulfonic Acids in Microdroplets. *J. Am. Soc. Mass Spectrom.* **2022**, *33* (8), 1362–1367. https://doi.org/10.1021/jasms.2c00029.

(102) Qiu, L.; Cooks, R. G. Simultaneous and Spontaneous Oxidation and Reduction in Microdroplets by the Water Radical Cation/Anion Pair. *Angewandte Chemie* **2022**, *134* (41), e202210765. https://doi.org/10.1002/ange.202210765.

(103) Xiong, H.; Lee, J. K.; Zare, R. N.; Min, W. Strong Electric Field Observed at the Interface of Aqueous Microdroplets. *J. Phys. Chem. Lett.* **2020**, *11* (17), 7423–7428. https://doi.org/10.1021/acs.jpclett.0c02061.

(104) Han, Z.; Chen, L. C. A Subtle Change in Nanoflow Rate Alters the Ionization Response As Revealed by Scanning Voltage ESI-MS. *Anal. Chem.* **2022**, *94* (46), 16015–16022. https://doi.org/10.1021/acs.analchem.2c02997.

(105) Kotiaho, T.; Eberlin, M. N.; Vainiotalo, P.; Kostiainen, R. Electrospray Mass and Tandem Mass Spectrometry Identification of Ozone Oxidation Products of Amino Acids and Small Peptides. *J Am Soc Mass Spectrom* **2000**, *11* (6), 526–535. https://doi.org/10.1016/S1044-0305(00)00116-1.

(106) Xu, G.; Chance, M. R. Radiolytic Modification of Sulfur-Containing Amino Acid Residues in Model Peptides: Fundamental Studies for Protein Footprinting. *Anal. Chem.* **2005**, *77* (8), 2437–2449. https://doi.org/10.1021/ac0484629.

(107) Lloyd, J. A.; Spraggins, J. M.; Johnston, M. V.; Laskin, J. Peptide Ozonolysis: Product Structures and Relative Reactivities for Oxidation of Tyrosine and Histidine Residues. *The official journal of The American Society for Mass Spectrometry* **2006**, *17* (9), 1289–1298. https://doi.org/10.1016/j.jasms.2006.05.009.

(108) Sharma, V. K.; Graham, N. J. D. Oxidation of Amino Acids, Peptides and Proteins by Ozone: A Review. *Ozone: Science & Engineering* **2010**, *32* (2), 81–90. https://doi.org/10.1080/01919510903510507.

(109) Borotto, N. B.; Richards, T. K. Rapid Online Oxidation of Proteins and Peptides via Electrospray-Accelerated Ozonation. *J. Am. Soc. Mass Spectrom.* **2022**, *33* (11), 2078–2086. https://doi.org/10.1021/jasms.2c00182.

(110) Xing, D.; Meng, Y.; Yuan, X.; Jin, S.; Song, X.; Zare, R. N.; Zhang, X. Capture of Hydroxyl Radicals by Hydronium Cations in Water Microdroplets. *Angewandte Chemie* **2022**, *134* (33), e202207587. https://doi.org/10.1002/ange.202207587.

(111) Benedikt, J.; Hefny, M. M.; Shaw, A.; R. Buckley, B.; Iza, F.; Schäkermann, S.; E. Bandow, J. The Fate of

Plasma-Generated Oxygen Atoms in Aqueous Solutions: Non-Equilibrium Atmospheric Pressure Plasmas as an Efficient Source of Atomic O (Aq). *Physical Chemistry Chemical Physics* **2018**, *20* (17), 12037–12042. https://doi.org/10.1039/C8CP00197A.

(112) Gao, D.; Jin, F.; Kyoo Lee, J.; N. Zare, R. Aqueous Microdroplets Containing Only Ketones or Aldehydes Undergo Dakin and Baeyer–Villiger Reactions. *Chemical Science* **2019**, *10* (48), 10974–10978. https://doi.org/10.1039/C9SC05112K.

(113) Han, Z.; Komori, R.; Suzuki, R.; Omata, N.; Matsuda, T.; Hishida, S.; Shuuhei, T.; Chen, L. C. Bipolar Electrospray from Electrodeless Emitters for ESI without Electrochemical Reactions in the Sprayer. *J. Am. Soc. Mass Spectrom.* **2023**, *34* (4), 728–736. https://doi.org/10.1021/jasms.2c00382.

(114) Chowdhury, S. K.; Katta, V.; Chait, B. T. Probing Conformational Changes in Proteins by Mass Spectrometry. *J. Am. Chem. Soc.* **1990**, *112* (24), 9012–9013. https://doi.org/10.1021/ja00180a074.

(115) Mirza, U. A.; Cohen, S. L.; Chait, B. T. Heat-Induced Conformational Changes in Proteins Studied by Electrospray Ionization Mass Spectrometry. *Anal. Chem.* **1993**, *65* (1), 1–6. https://doi.org/10.1021/ac00049a003.

(116) Loo, J. A.; Loo, R. R. O.; Udseth, H. R.; Edmonds, C. G.; Smith, R. D. Solvent-Induced Conformational Changes of Polypeptides Probed by Electrospray-Ionization Mass Spectrometry. *Rapid Communications in Mass Spectrometry* **1991**, *5* (3), 101–105. https://doi.org/10.1002/rcm.1290050303.

(117) Goto, Y.; Calciano, L. J.; Fink, A. L. Acid-Induced Folding of Proteins. *Proceedings of the National Academy of Sciences* **1990**, *87* (2), 573–577. https://doi.org/10.1073/pnas.87.2.573.

(118) Goto, Y.; Takahashi, N.; Fink, A. L. Mechanism of Acid-Induced Folding of Proteins. *Biochemistry* **1990**, *29* (14), 3480–3488. https://doi.org/10.1021/bi00466a009.

(119) Fink, A. L.; Calciano, L. J.; Goto, Y.; Kurotsu, T.; Palleros, D. R. Classification of Acid Denaturation of Proteins: Intermediates and Unfolded States. *Biochemistry* **1994**, *33* (41), 12504–12511. https://doi.org/10.1021/bi00207a018.

(120) Mann, M. The Ever Expanding Scope of Electrospray Mass Spectrometry—a 30 Year Journey. *Nat Commun* **2019**, *10* (1), 3744. https://doi.org/10.1038/s41467-019-11747-z.

(121) Breuker, K.; McLafferty, F. W. Stepwise Evolution of Protein Native Structure with Electrospray into the Gas Phase, 10−12 to 102 s. *Proceedings of the National Academy of Sciences* **2008**, *105* (47), 18145–18152. https://doi.org/10.1073/pnas.0807005105.

(122) Fenn, J. B. Ion Formation from Charged Droplets: Roles of Geometry, Energy, and Time. *J. Am. Soc. Mass Spectrom.* **1993**, *4* (7), 524–535. https://doi.org/10.1016/1044-0305(93)85014-O.

(123) Donor, M. T.; Ewing, S. A.; Zenaidee, M. A.; Donald, W. A.; Prell, J. S. Extended Protein Ions Are Formed by the Chain Ejection Model in Chemical Supercharging Electrospray Ionization. *Anal. Chem.* **2017**, *89* (9), 5107–5114. https://doi.org/10.1021/acs.analchem.7b00673.

(124) Konermann, L.; Douglas, D. J. Unfolding of Proteins Monitored by Electrospray Ionization Mass Spectrometry: A Comparison of Positive and Negative Ion Modes. *J. Am. Soc. Mass Spectrom.* **1998**, *9* (12), 1248–1254. https://doi.org/10.1016/S1044-0305(98)00103-2.

(125) Konermann, L.; Douglas, D. J. Acid-Induced Unfolding of Cytochrome c at Different Methanol Concentrations: Electrospray Ionization Mass Spectrometry Specifically Monitors Changes in the Tertiary Structure. *Biochemistry* **1997**, *36* (40), 12296–12302. https://doi.org/10.1021/bi971266u.

(126) Konermann, L.; Douglas, D. J. Equilibrium Unfolding of Proteins Monitored by Electrospray Ionization Mass Spectrometry: Distinguishing Two-State from Multi-State Transitions. *Rapid Communications in Mass Spectrometry* **1998**, *12* (8), 435–442. https://doi.org/10.1002/(SICI)1097-

0231(19980430)12:8<435::AID-RCM181>3.0.CO;2-F.

(127) Kharlamova, A.; DeMuth, J. C.; McLuckey, S. A. Vapor Treatment of Electrospray Droplets: Evidence for the Folding of Initially Denatured Proteins on the Sub-Millisecond Time-Scale. *J. Am. Soc. Mass Spectrom.* **2012**, *23* (1), 88–101. https://doi.org/10.1007/s13361-011-0258-x.

(128) Fisher, C. M.; Kharlamova, A.; McLuckey, S. A. Affecting Protein Charge State Distributions in Nano-Electrospray Ionization via In-Spray Solution Mixing Using Theta Capillaries. *Anal. Chem.* **2014**, *86* (9), 4581–4588. https://doi.org/10.1021/ac500721r.

(129) Chen, L. C.; Mandal, M. K.; Hiraoka, K. Super-Atmospheric Pressure Electrospray Ion Source: Applied to Aqueous Solution. *J. Am. Soc. Mass Spectrom.* **2011**, *22* (12), 2108–2114. https://doi.org/10.1007/s13361-011-0253-2.

(130) Han, Z.; Omata, N.; Matsuda, T.; Hishida, S.; Takiguchi, S.; Komori, R.; Suzuki, R.; Chuin Chen, L. Tuning Oxidative Modification by a Strong Electric Field Using nanoESI of Highly Conductive Solutions near the Minimum Flow Rate. *Chemical Science* **2023**, *14* (17), 4506–4515. https://doi.org/10.1039/D2SC07113D.

(131) Chen, L. C. High-Pressure ESI-MS Made Easy Using a Plug-and-Play Ion Source and Its Application to Highly Conductive Aqueous Solutions. *Journal of Mass Spectrometry* **2021**, *56* (4), e4583. https://doi.org/10.1002/jms.4583.

(132) Lyu, J.; Liu, Y.; McCabe, J. W.; Schrecke, S.; Fang, L.; Russell, D. H.; Laganowsky, A. Discovery of Potent Charge-Reducing Molecules for Native Ion Mobility Mass Spectrometry Studies. *Anal. Chem.* **2020**, *92* (16), 11242–11249. https://doi.org/10.1021/acs.analchem.0c01826.

(133) Walker, T. E.; Laganowsky, A.; Russell, D. H. Surface Activity of Amines Provides Evidence for the Combined ESI Mechanism of Charge Reduction for Protein Complexes. *Anal. Chem.* **2022**, *94* (30), 10824–10831. https://doi.org/10.1021/acs.analchem.2c01814.

(134) Konermann, L. Addressing a Common Misconception: Ammonium Acetate as Neutral pH "Buffer" for Native Electrospray Mass Spectrometry. *J. Am. Soc. Mass Spectrom.* **2017**, *28* (9), 1827–1835. https://doi.org/10.1007/s13361-017-1739-3.

(135) Mirza, U. A.; Chait, B. T. Effects of Anions on the Positive Ion Electrospray Ionization Mass Spectra of Peptides and Proteins. *Anal. Chem.* **1994**, *66* (18), 2898–2904. https://doi.org/10.1021/ac00090a017.

(136) Gumerov, D. R.; Dobo, A.; Kaltashov, I. A. Protein—Ion Charge-State Distributions in Electrospray Ionization Mass Spectrometry: Distinguishing Conformational Contributions from Masking Effects. *Eur J Mass Spectrom (Chichester)* **2002**, *8* (2), 123–129. https://doi.org/10.1255/ejms.480.

(137) Verkerk, U. H.; Kebarle, P. Ion-Ion and Ion-Molecule Reactions at the Surface of Proteins Produced by Nanospray. Information on the Number of Acidic Residues and Control of the Number of Ionized Acidic and Basic Residues. *J. Am. Soc. Mass Spectrom.* **2005**, *16* (8), 1325–1341. https://doi.org/10.1016/j.jasms.2005.03.018.

(138) Ptitsyn, O. B. Protein Folding: Hypotheses and Experiments. *J Protein Chem* **1987**, *6* (4), 273–293. https://doi.org/10.1007/BF00248050.

(139) Frimpong, A. K.; Abzalimov, R. R.; Eyles, S. J.; Kaltashov, I. A. Gas-Phase Interference-Free Analysis of Protein Ion Charge-State Distributions: Detection of Small-Scale Conformational Transitions Accompanying Pepsin Inactivation. *Anal. Chem.* **2007**, *79* (11), 4154–4161. https://doi.org/10.1021/ac0704098.

(140) Pantano, C.; Gañán-Calvo, A. M.; Barrero, A. Zeroth-Order, Electrohydrostatic Solution for Electrospraying in Cone-Jet Mode. *Journal of Aerosol Science* **1994**, *25* (6), 1065–1077. https://doi.org/10.1016/0021-8502(94)90202-X.

(141) Nemes, P.; Marginean, I.; Vertes, A. Spraying Mode Effect on Droplet Formation and Ion Chemistry in

Electrosprays. *Anal. Chem.* **2007**, *79* (8), 3105–3116. https://doi.org/10.1021/ac062382i.
(142) Konermann, L.; Pan, J.; Wilson, D. J. Protein Folding Mechanisms Studied by Time-Resolved Electrospray Mass Spectrometry. *BioTechniques* **2006**, *40* (2), 135–141. https://doi.org/10.2144/06402TE01.
(143) Evans, C. A., Jr.; Hendricks, C. D. An Electrohydrodynamic Ion Source for the Mass Spectrometry of Liquids. *Review of Scientific Instruments* **1972**, *43* (10), 1527–1530. https://doi.org/10.1063/1.1685481.
(144) Gapeev, A.; Berton, A.; Fabris, D. Current-Controlled Nanospray Ionization Mass Spectrometry. *J Am Soc Mass Spectrom* **2009**, *20* (7), 1334–1341. https://doi.org/10.1016/j.jasms.2009.03.007.
(145) Marginean, I.; Kelly, R. T.; Moore, R. J.; Prior, D. C.; LaMarche, B. L.; Tang, K.; Smith, R. D. Selection of the Optimum Electrospray Voltage for Gradient Elution LC-MS Measurements. *J Am Soc Mass Spectrom* **2009**, *20* (4), 682–688. https://doi.org/10.1016/j.jasms.2008.12.004.
(146) Valaskovic, G. A.; Murphy, J. P.; Lee, M. S. Automated Orthogonal Control System for Electrospray Ionization. *J Am Soc Mass Spectrom* **2004**, *15* (8), 1201–1215. https://doi.org/10.1016/j.jasms.2004.04.033.
(147) Kien Nguyen, T.; Nguyen, V. D.; Seong, B.; Hoang, N.; Park, J.; Byun, D. Control and Improvement of Jet Stability by Monitoring Liquid Meniscus in Electrospray and Electrohydrodynamic Jet. *Journal of Aerosol Science* **2014**, *71*, 29–39. https://doi.org/10.1016/j.jaerosci.2014.01.004.
(148) Kang, S.; Chen, A. B.; Yu, T.; Yang, Y.; Gui, H.; Liu, J.; Chen, D.-R. A New Spray Current Control for the Reliable Operation of a Single-Capillary Electrospray. *Journal of Aerosol Science* **2022**, *166*, 106073. https://doi.org/10.1016/j.jaerosci.2022.106073.
(149) Bradski, G. The OpenCV Library. *Dr. Dobb's Journal: Software Tools* **2000**.
(150) Uchiyama, M. Formation of High-Speed Motion Pattern of a Mechanical Arm by Trial. *Transactions of the Society of Instrument and Control Engineers* **1978**, *14* (6), 706–712. https://doi.org/10.9746/sicetr1965.14.706.
(151) Arimoto, S.; Kawamura, S.; Miyazaki, F. Bettering Operation of Robots by Learning. *Journal of Robotic Systems* **1984**, *1* (2), 123–140. https://doi.org/10.1002/rob.4620010203.
(152) Owens, D. H.; Hätönen, J. Iterative Learning Control — An Optimization Paradigm. *Annual Reviews in Control* **2005**, *29* (1), 57–70. https://doi.org/10.1016/j.arcontrol.2005.01.003.
(153) Arakawa, R.; Yamaguchi, M.; Hotta, H.; Osakai, T.; Kimoto, T. Product Analysis of Caffeic Acid Oxidation by On-Line Electrochemistry/Electrospray Ionization Mass Spectrometry. *Journal of the American Society for Mass Spectrometry* **2004**, *15* (8), 1228–1236. https://doi.org/10.1016/j.jasms.2004.05.007.
(154) Severs, J. C.; Harms, A. C.; Smith, R. D. A New High-Performance Interface for Capillary Electrophoresis/Electrospray Ionization Mass Spectrometry. *Rapid Communications in Mass Spectrometry* **1996**, *10* (10), 1175–1178. https://doi.org/10.1002/(SICI)1097-0231(19960731)10:10<1175::AID-RCM636>3.0.CO;2-L.
(155) Kim, K.; Compton, P. D.; Toby, T. K.; Thomas, P. M.; Wilkins, J. T.; Mutharasan, R. K.; Kelleher, N. L. Reducing Protein Oxidation in Low-Flow Electrospray Enables Deeper Investigation of Proteoforms by Top down Proteomics. *EuPA Open Proteomics* **2015**, *8*, 40–47. https://doi.org/10.1016/j.euprot.2015.05.005.
(156) Lübbert, C.; Peukert, W. How to Avoid Interfering Electrochemical Reactions in ESI-MS Analysis. *Journal of Mass Spectrometry* **2018**, *54* (4), 301–310. https://doi.org/10.1002/jms.4315.
(157) Grimm, R. L.; Beauchamp, J. L. Field-Induced Droplet Ionization Mass Spectrometry. *J. Phys. Chem. B* **2003**, *107* (51), 14161–14163. https://doi.org/10.1021/jp037099r.
(158) Grimm, R. L.; Beauchamp, J. L. Dynamics of Field-Induced Droplet Ionization: Time-Resolved Studies of Distortion, Jetting, and Progeny Formation from Charged and Neutral Methanol Droplets Exposed to Strong Electric Fields. *J. Phys. Chem. B* **2005**, *109* (16), 8244–8250. https://doi.org/10.1021/jp0450540.

(159) Grimm, R. L.; Hodyss, R.; Beauchamp, J. L. Probing Interfacial Chemistry of Single Droplets with Field-Induced Droplet Ionization Mass Spectrometry: Physical Adsorption of Polycyclic Aromatic Hydrocarbons and Ozonolysis of Oleic Acid and Related Compounds. *Anal. Chem.* **2006**, *78* (11), 3800–3806. https://doi.org/10.1021/ac0601922.

(160) Chen, H.-K.; Chang, C.-K.; Wu, C.-C.; Huang, M.-C.; Wang, Y.-S. Synchronized Dual-Polarity Electrospray Ionization Mass Spectrometry. *J Am Soc Mass Spectrom* **2009**, *20* (12), 2254–2257. https://doi.org/10.1016/j.jasms.2009.08.014.

(161) Stark, A. K.; Schilling, M.; Janasek, D.; Franzke, J. Characterization of Dielectric Barrier Electrospray Ionization for Mass Spectrometric Detection. *Anal Bioanal Chem* **2010**, *397* (5), 1767–1772. https://doi.org/10.1007/s00216-010-3749-x.

(162) Huang, G.; Li, G.; Cooks, R. G. Induced Nanoelectrospray Ionization for Matrix-Tolerant and High-Throughput Mass Spectrometry. *Angewandte Chemie International Edition* **2011**, *50* (42), 9907–9910. https://doi.org/10.1002/anie.201103687.

(163) Usmanov, D. T.; Ninomiya, S.; Hiraoka, K.; Wada, H.; Nakano, H.; Matsumura, M.; Sanada-Morimura, S.; Nonami, H. Electrospray Generated from the Tip-Sealed Fine Glass Capillary Inserted with an Acupuncture Needle Electrode. *J. Am. Soc. Mass Spectrom.* **2018**, *29* (12), 2297–2304. https://doi.org/10.1007/s13361-018-2062-3.

(164) Qiao, L.; Sartor, R.; Gasilova, N.; Lu, Y.; Tobolkina, E.; Liu, B.; Girault, H. H. Electrostatic-Spray Ionization Mass Spectrometry. *Anal. Chem.* **2012**, *84* (17), 7422–7430. https://doi.org/10.1021/ac301332k.

(165) Pei, J.; Zhou, X.; Wang, X.; Huang, G. Alleviation of Electrochemical Oxidation for Peptides and Proteins in Electrospray Ionization: Obtaining More Accurate Mass Spectra with Induced High Voltage. *Anal. Chem.* **2015**, *87* (5), 2727–2733. https://doi.org/10.1021/ac503990a.

(166) Kim, O. V.; Dunn, P. F. Controlled Production of Droplets by In-Flight Electrospraying. *Langmuir* **2010**, *26* (20), 15807–15813. https://doi.org/10.1021/la102793j.

(167) Li, A.; Hollerbach, A.; Luo, Q.; Cooks, R. G. On-Demand Ambient Ionization of Picoliter Samples Using Charge Pulses. *Angewandte Chemie International Edition* **2015**, *54* (23), 6893–6895. https://doi.org/10.1002/anie.201501895.

(168) Kulyk, D. S.; Swiner, D. J.; Sahraeian, T.; Badu-Tawiah, A. K. Direct Mass Spectrometry Analysis of Complex Mixtures by Nanoelectrospray with Simultaneous Atmospheric Pressure Chemical Ionization and Electrophoretic Separation Capabilities. *Anal. Chem.* **2019**, *91* (18), 11562–11568. https://doi.org/10.1021/acs.analchem.9b01456.

(169) Li, A.; Zi, Y.; Guo, H.; Wang, Z. L.; Fernández, F. M. Triboelectric Nanogenerators for Sensitive Nano-Coulomb Molecular Mass Spectrometry. *Nature Nanotech* **2017**, *12* (5), 481–487. https://doi.org/10.1038/nnano.2017.17.

(170) Fernandez de la Mora, J.; Barrios-Collado, C. A Bipolar Electrospray Source of Singly Charged Salt Clusters of Precisely Controlled Composition. *Aerosol Science and Technology* **2017**, *51* (6), 778–786. https://doi.org/10.1080/02786826.2017.1302070.

(171) Chen, L. C.; Tsutsui, S.; Naito, T.; Ninomiya, S.; Hiraoka, K. Electrospray Ionization Source with a Rear Extractor. *Journal of Mass Spectrometry* **2018**, *53* (5), 400–407. https://doi.org/10.1002/jms.4072.

(172) Wyman, Jeffries. THE DIELECTRIC CONSTANT OF MIXTURES OF ETHYL ALCOHOL AND WATER FROM -5 TO 40°. *J. Am. Chem. Soc.* **1931**, *53* (9), 3292–3301. https://doi.org/10.1021/ja01360a012.

(173) Vazquez, G.; Alvarez, E.; Navaza, J. M. Surface Tension of Alcohol Water + Water from 20 to 50 .Degree.C. *J. Chem. Eng. Data* **1995**, *40* (3), 611–614. https://doi.org/10.1021/je00019a016.

(174) Bitterwolf, T. E.; Ling, A. C. Metallocene Basicity: II. Reaction of the Ferrocenonium Cation with O2 and

SO2. *Journal of Organometallic Chemistry* **1972**, *40* (1), C29–C32. https://doi.org/10.1016/S0022-328X(00)86974-0.

(175) Zhang, D.; Yuan, X.; Gong, C.; Zhang, X. High Electric Field on Water Microdroplets Catalyzes Spontaneous and Ultrafast Oxidative C–H/N–H Cross-Coupling. *J. Am. Chem. Soc.* **2022**, *144* (35), 16184–16190. https://doi.org/10.1021/jacs.2c07385.

(176) Nekrasov, Yu. S.; Borisov, Yu. A.; Skazov, R. S.; Rodionov, A. N.; Simenel, A. A.; Belousov, Yu. A. On the Mechanism of Ferrocene Oxidation under the Conditions of Electrospray Ionization. *Russ Chem Bull* **2009**, *58* (7), 1521–1523. https://doi.org/10.1007/s11172-009-0205-1.

(177) Taylor, G. I.; Van Dyke, M. D. Electrically Driven Jets. *Proceedings of the Royal Society of London. A. Mathematical and Physical Sciences* **1969**, *313* (1515), 453–475. https://doi.org/10.1098/rspa.1969.0205.

(178) Smith, D. P. H. The Electrohydrodynamic Atomization of Liquids. *IEEE Transactions on Industry Applications* **1986**, *IA-22* (3), 527–535. https://doi.org/10.1109/TIA.1986.4504754.

(179) Zeleny, J. On the Conditions of Instability of Electrified Drops, with Applications to the Electrical Discharge from Liquid Points. *proc.camb.phil.soc* **1915**, No. 18, 71–87.

(180) Noymer, P. D.; Garel, M. STABILITY AND ATOMIZATION CHARACTERISTICS OF ELECTROHYDRODYNAMIC JETS IN THE CONE-JET AND MULTI-JET MODES. *Journal of Aerosol Science* **2000**, *31* (10), 1165–1172. https://doi.org/10.1016/S0021-8502(00)00019-7.

(181) Ryan, C. N.; Smith, K. L.; Stark, J. P. W. Characterization of Multi-Jet Electrospray Systems. *Journal of Aerosol Science* **2012**, *51*, 35–48. https://doi.org/10.1016/j.jaerosci.2012.03.007.

(182) Duby, M.-H.; Deng, W.; Kim, K.; Gomez, T.; Gomez, A. Stabilization of Monodisperse Electrosprays in the Multi-Jet Mode via Electric Field Enhancement. *Journal of Aerosol Science* **2006**, *37* (3), 306–322. https://doi.org/10.1016/j.jaerosci.2005.05.013.

(183) Kang, J. S.; Park, I.; Jung, J. H.; Kim, S. S. Free-Surface Electrospray Technique Using a Multi-Hole Array. *Journal of Aerosol Science* **2013**, *55*, 25–30. https://doi.org/10.1016/j.jaerosci.2012.07.010.

(184) Wang, Z.; Tian, Y.; Zhang, C.; Wang, Y.; Deng, W. Massively Multiplexed Electrohydrodynamic Tip Streaming from a Thin Disc. *Phys. Rev. Lett.* **2021**, *126* (6), 064502. https://doi.org/10.1103/PhysRevLett.126.064502.

(185) Gu, W.; Heil, P. E.; Choi, H.; Kim, K. Generation of Stable Multi-Jets by Flow-Limited Field-Injection Electrostatic Spraying and Their Control via I–V Characteristics. *J. Phys. D: Appl. Phys.* **2010**, *43* (49), 492001. https://doi.org/10.1088/0022-3727/43/49/492001.

(186) Ueda, H.; Takeuchi, K.; Kikuchi, A. Effect of the Nozzle Tip's Geometrical Shape on Electrospray Deposition of Organic Thin Films. *Jpn. J. Appl. Phys.* **2017**, *56* (4S), 04CL05. https://doi.org/10.7567/JJAP.56.04CL05.

(187) Tang, K.; Lin, Y.; Matson, D. W.; Kim, T.; Smith, R. D. Generation of Multiple Electrosprays Using Microfabricated Emitter Arrays for Improved Mass Spectrometric Sensitivity. *Anal. Chem.* **2001**, *73* (8), 1658–1663. https://doi.org/10.1021/ac001191r.

(188) Kelly, R. T.; Page, J. S.; Tang, K.; Smith, R. D. Array of Chemically Etched Fused-Silica Emitters for Improving the Sensitivity and Quantitation of Electrospray Ionization Mass Spectrometry. *Anal. Chem.* **2007**, *79* (11), 4192–4198. https://doi.org/10.1021/ac062417e.

(189) Kelly, R. T.; Page, J. S.; Marginean, I.; Tang, K.; Smith, R. D. Nanoelectrospray Emitter Arrays Providing Interemitter Electric Field Uniformity. *Anal. Chem.* **2008**, *80* (14), 5660–5665. https://doi.org/10.1021/ac800508q.

(190) Fu, Y.; Morency, S.; Bachus, K.; Simon, D.; Hutama, T.; Gibson, G. T. T.; Messaddeq, Y.; Oleschuk, R. D. A Microstructured Fiber with Defined Borosilicate Regions to Produce a Radial Micronozzle Array for

Nanoelectrospray Ionization. *Sci Rep* **2016**, *6* (1), 21279. https://doi.org/10.1038/srep21279.

(191) Cox, J. T.; Marginean, I.; Kelly, R. T.; Smith, R. D.; Tang, K. Improving the Sensitivity of Mass Spectrometry by Using a New Sheath Flow Electrospray Emitter Array at Subambient Pressures. *J. Am. Soc. Mass Spectrom.* **2014**, *25* (12), 2028–2037. https://doi.org/10.1007/s13361-014-0856-5.

(192) Bruins, A. P.; Covey, T. R.; Henion, J. D. Ion Spray Interface for Combined Liquid Chromatography/Atmospheric Pressure Ionization Mass Spectrometry. *Anal. Chem.* **1987**, *59* (22), 2642–2646. https://doi.org/10.1021/ac00149a003.

(193) Chen, L. C.; Rahman, Md. M.; Hiraoka, K. High Pressure Super-Heated Electrospray Ionization Mass Spectrometry for Sub-Critical Aqueous Solution. *J. Am. Soc. Mass Spectrom.* **2014**, *25* (11), 1862–1869. https://doi.org/10.1007/s13361-014-0974-0.

(194) Page, J. S.; Tang, K.; Kelly, R. T.; Smith, R. D. Subambient Pressure Ionization with Nanoelectrospray Source and Interface for Improved Sensitivity in Mass Spectrometry. *Anal. Chem.* **2008**, *80* (5), 1800–1805. https://doi.org/10.1021/ac702354b.

(195) Ninomiya, S.; Chen, L. C.; Suzuki, H.; Sakai, Y.; Hiraoka, K. Vacuum Electrospray of Volatile Liquids Assisted by Infrared Laser Irradiation. *Rapid Communications in Mass Spectrometry* **2012**, *26* (7), 863–869. https://doi.org/10.1002/rcm.6181.

(196) Bruins, A. P. ESI Source Design and Dynamic Range Considerations. In *Electrospray ionization mass spectrometry: Fundamental, instrumentation and appliations*; Cole, R. B., Ed.; Wiley: New York, 1997; pp 107–136.

(197) Chowdhury, S. K.; Katta, V.; Chait, B. T. An Electrospray-Ionization Mass Spectrometer with New Features. *Rapid Communications in Mass Spectrometry* **1990**, *4* (3), 81–87. https://doi.org/10.1002/rcm.1290040305.

(198) Lin, B.; Sunner, J. Ion Transport by Viscous Gas Flow through Capillaries. *J Am Soc Mass Spectrom* **1994**, *5* (10), 873–885. https://doi.org/10.1016/1044-0305(94)87012-8.

(199) Bernier, L.; Pinfold, H.; Pauly, M.; Rauschenbach, S.; Reiss, J. Gas Flow and Ion Transfer in Heated ESI Capillary Interfaces. *J. Am. Soc. Mass Spectrom.* **2018**, *29* (4), 761–773. https://doi.org/10.1007/s13361-018-1895-0.

(200) Wu, S.; Zhang, K.; Kaiser, N. K.; Bruce, J. E.; Prior, D. C.; Anderson, G. A. Incorporation of a Flared Inlet Capillary Tube on a Fourier Transform Ion Cyclotron Resonance Mass Spectrometer. *The official journal of The American Society for Mass Spectrometry* **2006**, *17* (6), 772–779. https://doi.org/10.1016/j.jasms.2006.02.011.

(201) Pauly, M.; Sroka, M.; Reiss, J.; Rinke, G.; Albarghash, A.; Vogelgesang, R.; Hahne, H.; Kuster, B.; Sesterhenn, J.; Kern, K.; Rauschenbach, S. A Hydrodynamically Optimized Nano-Electrospray Ionization Source and Vacuum Interface. *Analyst* **2014**, *139* (8), 1856–1867. https://doi.org/10.1039/C3AN01836A.

(202) Schneider, B. B.; Javaheri, H.; Covey, T. R. Ion Sampling Effects under Conditions of Total Solvent Consumption. *Rapid Communications in Mass Spectrometry* **2006**, *20* (10), 1538–1544. https://doi.org/10.1002/rcm.2511.

(203) Pagnotti, V. S.; Chubatyi, N. D.; McEwen, C. N. Solvent Assisted Inlet Ionization: An Ultrasensitive New Liquid Introduction Ionization Method for Mass Spectrometry. *Anal. Chem.* **2011**, *83* (11), 3981–3985. https://doi.org/10.1021/ac200556z.

(204) Pagnotti, V. S.; Chakrabarty, S.; Harron, A. F.; McEwen, C. N. Increasing the Sensitivity of Liquid Introduction Mass Spectrometry by Combining Electrospray Ionization and Solvent Assisted Inlet Ionization. *Anal. Chem.* **2012**, *84* (15), 6828–6832. https://doi.org/10.1021/ac3014115.

(205) Chakrabarty, S.; Shelver, W. L.; Smith, D. J. Electrospray Ionization Inlet Tandem Mass Spectrometry: A

Hyphenated Method for the Sensitive Determination of Chemicals in Animal Tissues and Body Fluids. *J. Am. Soc. Mass Spectrom.* **2021**, *32* (1), 14–20. https://doi.org/10.1021/jasms.9b00114.

(206) Chen, L. C.; Iwano, T.; Ninomiya, S.; Koike, T.; Tanaka, Y.; Yoshimura, K. Miniaturized String Sampling Probe and Electrospray Extraction/Ionization within the Ion Inlet Tube for Mass Spectrometric Endoscopy. *J. Am. Soc. Mass Spectrom.* **2021**, *32* (2), 606–610. https://doi.org/10.1021/jasms.0c00366.

(207) Fernández De La Mora, J.; Loscertales, I. G. The Current Emitted by Highly Conducting Taylor Cones. *Journal of Fluid Mechanics* **1994**, *260*, 155–184. https://doi.org/10.1017/S0022112094003472.

List of Publications

Original paper

1. **Han, Z.**; Omata, N.; Chen, L. C.*. Probing acid-induced compaction of denatured proteins by high-pressure electrospray mass spectrometry. ***Analytical Chemistry***, 2023, ***Accepted.***

2. **Han, Z.**; Omata, N.; Matsuda, T.; Hishida, S.; Shuuhei, T.; Komori, R.; Suzuki, R.; Chen, L. C.*. Tuning oxidative modification by strong electric field using nanoESI of highly conductive solutions near minimum flow rate. ***Chemical Science***, 2023,14, 4506-4515.

3. **Han, Z.**; Chen, L. C.*. A subtle change in nanoflow rate alters the ionization response as revealed by scanning voltage ESI-MS. ***Analytical Chemistry***, 2022, 94, 46, 16015–16022.

4. **Han, Z.**; Hishida, S.; Omata, N.; Matsuda, T.; Komori, R.; Chen, L. C.*. Feedback Control of Electrospray with and without an External Liquid Pump Using the Spray Current and the Apex Angle of a Taylor Cone for ESI-MS. ***Analytical Chemistry***, 2023, 95, 10744-10751.

5. **Han, Z.**; Chen, L. C.*. Electrospray Ionization Inside the Ion Inlet Tube: Multijet Mode Operation. ***Journal of the American Society for Mass Spectrometry***, 2021, 32, 7, 1821–1828.

6. **Han, Z.**; Chen, L. C.*. Generation of Ions from Aqueous Taylor Cones near the Minimum Flow Rate: “True Nanoelectrospray” without Narrow Capillary. ***Journal of the American Society for Mass Spectrometry***, 2022, 33, 3, 491–498.

7. **Han, Z.**; Komori, R.; Suzuki, R.; Omata, N.; Matsuda, T.; Hishida, S.; Shuuhei, T.; Chen, L. C.*. Bipolar Electrospray from Electrodeless Emitters for ESI without Electrochemical Reactions in the Sprayer. ***Journal of the American Society for Mass Spectrometry***, 2023, 34, 4, 728–736.

8. **Han, Z.**; Chen, L. C.*. High-Pressure NanoESI of Highly Conductive Volatile and Non-Volatile Buffer Solutions from a Large Taylor Cone: Effect of Spray Current on Charge State Distribution. ***International Journal of Mass Spectrometry***, 2022, 476, 116845.

Conference

Oral presentation

1. **Han, Z.**; Chen, L. C.*. Electrospray ionization inside the narrow channel of ion inlet tube: multi-jet mode operation and total solvent consumption. 69th Annual Conference on Mass Spectrometry, Mass Spectrometry Society of Japan (MSSJ), Online, May 19, 2021.

2. **Han, Z.**; Chen, L. C.*. "TRUE NANOELECTROSPRAY" WITHOUT NARROW CAPILLARY BY GENERATION OF IONS FROM AQUEOUS TAYLOR CONES NEAR THE MINIMUM FLOW RATE. Workshop on ion chemistry and plasmas, Bratislava, Slovakia, August 30, 2022.

Poster presentation

1. **Han, Z.**; Chen, L. C.*. "True Nanoelectrospray" without Narrow Capillary by Generation of Ions from Aqueous Taylor Cones near the Minimum Flow Rate. 70th Annual Conference on Mass Spectrometry, Mass Spectrometry Society of Japan (MSSJ), Fukuoka, Japan, June 22, 2022.

2. **Han, Z.**; Omata, N.; Matsuda, T.; Hishida, S.; Komori, R.; Chen, L. C.*. Scanning nanoflow rate electrospray ionization for the precision tuning of oxidative modification by strong electric field. 71th Annual Conference on Mass Spectrometry, Mass Spectrometry Society of Japan (MSSJ), Osaka, Japan, May 17, 2023.

Acknowledgments

I thank the member of dissertation committee of this Ph.D. thesis, Prof. Dr. Lee Chuin Chen (陈　力勤), Prof. Dr. Satoshi Ninomiya (二宮　啓), Prof. Dr. Koji Yano (矢野　浩司), Prof. Dr. Kazuyuki Uno (宇野　和行), Prof. Dr. Tetsuo Kuwabara (桑原　哲夫), and Prof. Dr. Yoshiaki Ukita (浮田　芳昭).

Time flies by, and the end of my doctoral studies is approaching. The past three years of academic life have greatly enriched me. First and foremost, I would like to express my heartfelt gratitude to my supervisor, Prof. Dr. Lee Chuin Chen（陈　力勤）is an approachable person. Throughout the process of selecting the research topic, gathering materials, and writing, Prof. Dr. Chen has shown great care and encouragement. His rigorous approach to scientific research and unwavering pursuit of excellence will have a lasting impact on and inspire me throughout my life. I will forever cherish his care and guidance. I would like to take this opportunity to sincerely thank Prof. Dr. CHEN.

I am also grateful to Prof. Dr. Kenzo Hiraoka (平岡　賢三) for the encouragement and generous sharing of his comprehensive research and ideas with me. I am grateful to Prof. Dr. Satoshi Ninomiya (二宮　啓) for the assistance provided during the experiment. I thank Mr. Takato Hadori (服部　貴斗）for his help when I first arrived in Japan. I am grateful to Mr. Nozomu Omata (小俣　望), Mr. Shoki Hishida (菱田　將希), Mr. Ryoki Komori (小森　亮輝), Mr. Takeshi Matsuda (松田　健史), Mr. Shuuhei Takiguchi (滝口　修平）and Mr. Riku Suzuki (鈴木　理玖）for their mutual encouragement and support over the past three years. Through our collective efforts, we have maintained a positive and uplifting learning environment. It has been a great honor for me to be a part of such a team.

Finally, I thank the China Scholarship Council for its financial support.